Lasing and ion beam doping of semiconductor nanowires

Dissertation

zur Erlangung des akademischen Grades
doctor rerum naturalium (Dr. rer. nat.)

vorgelegt dem Rat der Physikalisch-Astromonischen Fakultät
der Friedrich-Schiller-Universität Jena

von Dipl.-Phys. Sebastian Geburt
geboren am 05.06.1982 in Göttingen

Laseremission und Ionenstrahl-Dotierung von Halbleiter-Nanodrähten

Halbleiter-Nanodrähte zeigen herausragende optische Eigenschaften wie stark lokalisierte Lichtemission nach optischer oder elektrischer Stimulierung und exzellente Wellenleitung bei einem Durchmesser kleiner als die Wellenlänge des geführten Lichts. Darüber hinaus stellt ihre Geometrie einen optischen Resonator dar, so dass durch die Kombination von Lichtemission, -führung und -verstärkung intensive Laseremission von Halbleiternanodrähten ermöglicht wird. Daraus ergeben sich unzählige Möglichkeiten für die Realisierung neuartiger nanoskalierter Lichtquellen. Auf dem Weg dorthin ist es jedoch unabdingbar, die fundamentalen Eigenschaften der kleinstmöglichen photonischen Lichtquellen zu erforschen und zu verstehen.

Optisch stimulierte Laseremission konnte bereits bei ZnO Nanodrähten bei hohen optischen Anregungsleitungen eindeutig nachgewiesen werden. CdS Nanodrähte bieten ebenfalls das Potential, Lichtverstärkung und Laseremission bei möglicherweise niedrigeren Anregungsleistungen zu generieren. In dieser Arbeit werden daher die optischen Eigenschaften von einzelnen CdS Nanodrähten bei niedriger und hoher Anregung untersucht. Das Auftreten von geführten Moden bei erhöhter optischer Anregung wird beobachtet und auch Laseremission kann oberhalb einer Schwellintensität von 10 kW/cm^2 bei Raumtemperatur eindeutig nachgewiesen werden. Die Emissionseigenschaften einzelner lasender CdS Nanodrähte werden charakterisiert und mit ihrer Morphologie korreliert, um im Vergleich mit lasenden ZnO Nanodrähten die fundamentalen Eigenschaften und Größenlimitationen photonischer Nanolaser zu erforschen.

Die optischen Eigenschaften von Halbleitern lassen sich zudem stark über die Dotierung mit geeigneten Leuchtzentren wie Übergangsmetallen und Lanthanoiden modifizieren. Neben der Erweiterung des Emissionsspektrums bietet sich vorallem die Möglichkeit, die optisch aktiven Leuchtzentren in der Resonatorkavität der Nanodrähte unterzubringen, wodurch ein nanoskalierter Festkörperlaser realisiert werden könnte, der aufgrund der langen Lebenszeiten der optischen Zentren eine Inversion und Lichtverstärkung bei noch niedrigeren Anregungleistungen als undotierte Nanolaser erreichen könnte. Der erste Schritt dorthin ist die Realisierung und Charakterisierung von dotierten Nanodrähten. ZnO Nanodrähte wurden erfolgreich mit Kobalt über Ionenimplantation dotiert. Eine intensive intra-3d Emission der Co^{2+} Ionen in den ZnO Nanodrähten wird beobachtet und die veränderten strukturellen und optischen Eigenschaften der dotierten Nanodrahtensemble sowie einzelner Nanodrähte charakterisiert.

Mn in ZnS Nanodrähten stellt ein weiteres interessantes Materialsystem zur Untersuchung der fundamentalen Wechselwirkungen von Leuchtzentren mit nanoskalierten Halbleitern dar. Das zeitliche Abklingen der Mn-Ionen wird im Wesentlichen von dem Energietransfer zwischen Mn-Ionen sowie der nichtstrahlenden Abregung durch die Interaktion mit Defekten beeinflusst. Zusätzlich beeinflusst die Nanostruktur das zeitliche Verhalten, da der Energietransfer unter bestimmten Bedingungen nur noch eindimensional entlang des Nanodrahts stattfindet. Das zeitliche Abkklingen kann durch ein modifiziertes Förster-Dipol-Dipol-Energietransfer-Modell beschrieben werden, welche für unterschiedliche Kombinationen der Mn Konzentration und Nanodraht Morphologie schon bestätigt wurde. In dieser Arbeit wird die Defektkonzentration in ZnS:Mn Nanodrähten über verschiedene Ansätze kontrolliert verändert und die Fähigkeit des Modells zur Beschreibung des zeitlichen Verhaltens der Mn-Defekt-Interaktion in ZnS Nanodrähten nachgewiesen.

Terbium dotiertes ZnS stellt ein hochinteressantes Materialsystem zur Realisierung von effizienten Elektrolumineszenz-Emittern dar. In der vorliegenden Arbeit konnten ZnS Nanodrähte erfolgreich über Ionenimplantation mit den gewünschten Tb-Konzentrationen dotiert werden. Eine intensive Tb intra-4f Emission der dotierten Nanodrähte wurde nach geeigetem Tempern beobachtet. Die Emissioneigenschaften der dotierten ZnS Nanodrähte werden als Funktion verschiedener Einflussparameter (Konzentration, Temperatur, Anregungsleistung) charakterisiert und daraus die optimalen Präparationsparameter bestimmt.

Die in dieser Arbeit erzielten Ergebnisse tragen wesentlich zum fundamentalen Verständnis der Nanolaser-Emissionseigenschaften bei und bilden wichtige Grundlagen für die spätere Realisierung von nanoskalierten Lichtquellen auf Basis dotierter Halbleiter-Nanodrähte.

Contents

1 Introduction

The technical progress in the last 50 years was significantly accelerated by semiconductors, which provide the basic material for the realization of mile stones like transistors, light emitting devices (LED) and solid state lasers. Since the realization of the first prototypes, their manifold properties have been extremely expanded by the shrinking of the structural sizes, which allowed the integration into electrical circuits and logic structures with high complexity and density [1]. This allowed the development of smart high performance devices, which can be found everywhere in our daily life, e.g. as (portable) computers and smartphones.

The technical development was enabled by the shrinking of the structural sizes down to the nanometer range, in which the properties of the materials start to deviate from their bulk counterparts. The influence of the surface is significantly enhanced due to the high surface-to-volume ratio [2]; and also the elastical [3], optical [4], electrical [5] and thermal [6, 7] properties of nanostructured materials change and new effects like quantization [8] and reduced dimensionality [9] appear.

The nanosized structures are usually processed by so-called *top down* approaches, in which the final structure is developed by many processing steps from the bulk. Despite the waste of a huge amount of material, those approaches have reached their physical size limits. A further shrinkage of the structural sizes is often only possible by the development of cost-intense new structuring processes. Those limitations can be overcome by the integration of self-assembled nanostructures, which can be synthesized in self-organized *bottom up* approaches [10].

Semiconductor nanowires are one class of self-organized nanomaterials, which are expected to be the future building-blocks for next-generation high performance devices [11]. A nanowire can be described in first approximation as a cylinder with a diameter in the nanometer range (1...1000 nm), while the length often approaches tens of micrometers, even up to millimeters [12]. Nanowires offer a high potential due to their ability to combine the functional with the electrical or optical connection element for new smart devices with enhanced properties. Examples have been demonstrated for nanowire field effect transistors (FET) [13], FET based high sensitive sensors [14], solar cells [15–17] as well as photonic devices like LEDs [18, 19], waveguides [20] and lasers [21].

Several methods have been developed to synthesize nanowires from diverse material systems by simple techniques like growth from wet chemical solutions [22], chemical vapour deposition [23, 24], pulsed laser deposition (PLD) [25] and more complex techniques like metal-organic vapour phase epitaxy (MOVPE) [26, 27] and molecular beam epitaxy (MBE) [28]. Beneath the technologically relevant synthesis on silicon substrates, all kinds of substrates including even transparent and flexible ones can be covered with nanowires [29]. A precise control of the final structure can be achieved by the smart pre-patterning of the substrate and choice of the appropriate growth conditions [30]. Nanowires can also synthesized in material combinations, which are incompatible for thin films due to the large lattice mismatch: The small footprints allow the relaxation of the induced strain and a growth of the nanowire with a very high crystal quality above [31]. By the incorporation of nanowires, new designs and layouts in three dimensions can be realized [32], which are not possible by standard processing techniques.

1.1 Nanowire photonics

The optical properties of semiconductor nanowires often exceed the properties of the bulk material by far. The resulting interest in research created a new field of science called *nanowire photonics* [33], which covers the investigation of the basic optical properties and realization of photonic and optoelectronic nanowire devices [34]. Several effects were also observed on the nanoscale like non-linear wave-mixing [35], second harmonic generation (SHG) [36, 37] and coupling to plasmonic nanoparticles [38]. Diverse applications have been demonstrated using nanowires as LEDs, waveguides, nanolasers, optical switches, beam splitters, interferometers, resonator structures, just to name a few examples [25, 34, 39, 40]. Most of the effects and applications are related to the basic optical properties of semiconductor nanowires:

Light emission The ability to emit photons upon optical or electrical stimulation originates from the semiconductor material itself. The nanowire structure can be used to examine the influence on the surface by different coatings like dielectrica and metals due to the large surface-to-volume ratio [41, 42]. Nanosized light sources from ensembles [18, 39, 43] and single nanowires [19, 44] could be realized, which offer highly localized and unidirectional emission.

Light confinement The high index of refraction of the semiconductors enables the efficient light confinement and waveguiding with low losses, even for nanowire diameters in the sub-wavelength range [20, 45, 46]. A strong light matter interaction results from the confinement and enables the investigation of polaritonic effects [47, 48]. Extreme light confinements could be realized by the coupling of semiconductor nanowires to plasmonic substrates [49, 50].

Light amplification The confined light is partially reflected at the nanowire ends or side facets due to high contrast of the refractive index. Thus, the nanowire structure acts as optical resonator. Dependent on the nanowire morphology, Fabry-Pérot or whispering gallery type resonator form a natural cavity [51–53], which provides a feedback for the confined light. Additionally, the semiconductor material can overcome the absorption losses and achieve gain, if a population inversion is achieved at high excitation [54]. The theoretically predicted high modal gain for light confined in nanowires [55] could be experimentally observed [56]. The combination of light emission, gain and feedback in the resonator enables the amplified stimulated emission [57–59] and even lasing oscillations in nanowires [21, 60].

1.2 Key challenges

Although a huge variety of different effects and concepts for nanoscaled light sources has already been demonstrated, most of the devices have the status of demonstrators or lack in a reproducible performance. To overcome this, three major key challenges remain for the successful and efficient integration of semiconductor nanowires in optoelectronic devices:

Fundamental properties and limits Many of the optical properties of semiconductor nanowires have only been investigated on ensembles, in which the properties of the individual nanowire is lost in the superposition [57–59]. For a basic understanding of e.g. diameter related effects and properties, single nanowires have to be investigated and their optical properties have to be correlated to the morphology [21, 51]. Such investigations are able to uncover the fundamental optical properties of the individual nanowires and will finally provide answers to the questions: What are the physical size limits for nanowire optics? What is the smallest photonic laser device possible?

Tayloring of the nanowire properties by doping   Although the intrinsic nanowires already exhibit unique and extraordinary optical qualities, doping could even extend these by new optical [61, 62], electrical [63–65], thermoelectrical [66, 67] and magnetical properties [68, 69], as well as combinations of these [70]. Especially for the optical properties, doping with optically active impurities like transition metals (TM) and rare earth (RE) elements enables the extension of the emission range from the intrinsic band gap of the semiconductor to the IR. Multi-wavelength and white light emission becomes possible from a single nanowire device by the combination of the suitable dopants. The nanowires doped with such impurities would also allow a smart realization of a solid state 4-level laser system on the nanoscale: The impurities embedded in the nanowire are utilized as light emitters, which can reach the population inversion necessary for gain at low pumping levels due to the long life times of the excited levels [71], while the nanowire provides the efficient waveguide and the resonator structure for the optical feedback. The approach could provide a solution to the drawback of undoped semiconductor nanolasers, as the population inversion is reached in the quasi-3 level laser system only at very high pumping intensities [21].

Doping of semiconductor nanowires with optically active impurities can be performed in two approaches: incorporation during growth and post-growth modification using ion implantation. The first method is difficult for VLS grown nanowires, as the growth process is sensitive to altered conditions [72, 73]. The low solubility and high melting points of the dopants (and their compounds) [74] hamper the successful incorporation [62, 75]. Doping of wet chemical synthesized nanowires and optical activation has been successfully demonstrated for several material combinations [75–77]. But the grown nanostructures exhibit rather poor aspect ratios [78–80] and the crystal quality is worse compared to VLS synthesized nanowires [81, 82]. Additionally, the control over the dopant distribution and concentration is limited and secondary effects like dopant segregation, accumulation at the surface and formation of secondary phases may occur [83, 84].

Ion implantation of nanowires as the alternative approach overcomes many of those limitation: nearly every element can be implanted in the desired lateral distribution and concentration, even above the solubility limit. Therefore, ion implantation advanced to a standard technique for semiconductor doping [85]. Despite all the benefits, one handicap is the creation of crystal defects due the nuclear stopping processes of the ion in the target [86]. The majority of the defects can be recovered by thermal annealing, but a simple application of bulk annealing conditions can lead to a dissolution of the nanostructures due to their reduced melting points [6]. Using adjusted annealing conditions for nanowires, successful incorporation and optical activation after annealing was already demonstrated for some nanowire ion combinations [9, 61, 62, 87]. The challenge is to find impurities, which can be efficiently excited by the host material and emit an intense intra-shell luminescence.

Elimination of the efficiency limiting processes   The creation of defects during growth or ion implantation directly points to another key challenge, which is the understanding and control of the processes limiting the efficiency of the optical emission [88–90]. This includes the investigation of the involved excitation processes of the impurity in the semiconductor matrix [91] as well as their interaction with defects [92, 93]. With an understanding of these processes, one will be able to uncover the loss processes and find optimized conditions for the impurity emission. Additionally, the doped nanowires interact with their surrounding. It is required to investigate and optimize the external influences like e.g. surface passivation [42, 94], electrical contacts [95] and the influence of the substrate on the optical emission properties [96].

1.3 Scientific goals

The outline of the thesis is structured as followed: Chapter 2 presents an overview on the properties, excitation and recombination processes of II-VI semiconductors in the low and high excitation regime as well as the optical properties specially related to semiconductor nanowires. A brief introduction to the properties of transition metals and rare earth elements in II-VI semiconductors is presented and the incorporation of transition metal and rare earth impurities in II-VI semiconductor nanowires is discussed.

The chapter 3 describes the sample preparation and experimental techniques used for characterization. A highlight is set on the properties of the micro-photoluminescence setup, which was developed, realized and established within in the scope of this thesis. The setup forms the basis for the widespread characterization of the emission properties of single nanowires. Additional technical information on the setup is available in appendix A.

Chapter 4 addresses the first key challenge: the structural properties of VLS grown ZnO and CdS nanowires are investigated and a special interest is given to the emission properties of single nanowires at low and high excitation conditions. Lasing oscillations at room temperature were proven above the threshold for single ZnO and CdS nanowires. The relation of the nanowire morphology to the emission properties is established in order to determine the physical size limits for CdS nanolasers. The influence of the substrate and the excitation polarization on emission properties was investigated for CdS nanolasers. The chapter is completed with a comparison of the lasing properties of ZnO and CdS nanowires, which allows the determination of the general physical requirements for II-VI semiconductor nanolasers.

Chapter 5 concentrates on the second key challenge by the modification of ZnO nanowires by implantation of cobalt as a suitable optically active transition metal. The morphology, stoichiometry and local structure of the implanted nanowires are investigated to determine the optimum preparation conditions. A comprehensive investigation on the emission and excitation properties of Co ions in ZnO nanowire ensembles are presented and the optical properties of single doped nanowires are highlighted.

Chapter 6 pays attention to the third key challenge by the investigation of the interaction of Mn ions with defects in ZnS nanowires. Several approaches were performed to alter and control the defect concentration of Mn implanted ZnS nanowires. The Mn-defect interaction is investigated by the temporal decay of the manganese luminescence and comparison of the experimental transients with the Förster dipole-dipole transfer model modified for 1D and 2D morphologies. The second part of chapter 6 focuses again on the doping of ZnS nanowires by implantation of terbium. The structural properties of rare earth implanted ZnS nanowires are described and a conclusive investigation on the optical properties of ensembles and single doped ZnS:Tb nanowires is presented.

Detailed motivations for the individual experiments are presented at the beginning of each chapter and important results are summarized at the respective chapter end. Chapter 7 summarizes the results in respect to the key challenges and conclusions are drawn for future experiments and the realization of devices.

2 Theory

The theoretical background presented in this thesis is split in two parts: the first part concerns the fundamental properties of II-VI semiconductors as well as their optical properties and emissions specifically related to nanowires. The second part covers a brief introduction to the properties of 3d- and 4f-element ions in II-VI semiconductors and the respective theoretical background on intra-shell transitions.

2.1 Semiconductor nanowires

2.1.1 Properties of II-VI semiconductors

Zinc oxide (ZnO) is a direct II-VI semiconductor with a wide band gap of $E_g = 3.44$ eV at T = 4.2 K [97]. Under normal ambient conditions, the wurtzite crystal structure is stable [98] in which every zinc atom is surrounded by four oxygen atoms and vice versa, as shown in the sketch of the unit cell in figure 2.1 (a). The lattice constants are $a = b = 0.329$ nm and $c = 0.524$ nm [99]. The non-centrosymmetric symmetry is C_{3v}, which results in a strong piezoelectric effect [100]. The tetrahedral coordinated bonding is formed by sp^3-hybrid orbitals with covalent bonding character. But the high difference in electronegativity of the two atom species results in a strong contribution of an ionic bonding, which is the origin of the high radiation hardness of ZnO. The magnitude of ionic bonding is 0.62 on the Phillips scale [101], which marks the border between ionic and covalent bonding.

The properties of the band gap are determined by the orbitals that contribute to the crystal bonding. Considering the ZnO as an ionic crystal, the top valence band is formed by the completely filled 2p-orbitals of the O^{2-} and the conduction band is formed by the empty 4s-orbitals of Zn^{2+} (see figure 2.1 (c)). In the covalent binding approach, the valence band is formed by the binding sp^3-hybrid orbitals, whereas the conduction band originated from the anti-binding hybrid orbitals. Both approaches deliver the same symmetries for the bands shown at the Γ point in figure 2.1 (c). Due to the crystal field and spin-orbit interaction of the O 2p-orbitals, the valence band (VB) is split into three sub-bands labelled A, B and C with increasing energy of the gap (compare figure 2.1 (c)). The energetic distance between the sub-bands is $\Delta E_{AB} = 4.9$ meV and $\Delta E_{BC} = 43.7$ meV [102]. The refractive index of ZnO is $n = 2.42$ at 385 nm (3.22 eV) [103] and the dispersion at this wavelength is $dn/d\lambda \approx$ -15 µm^{-1} [104].
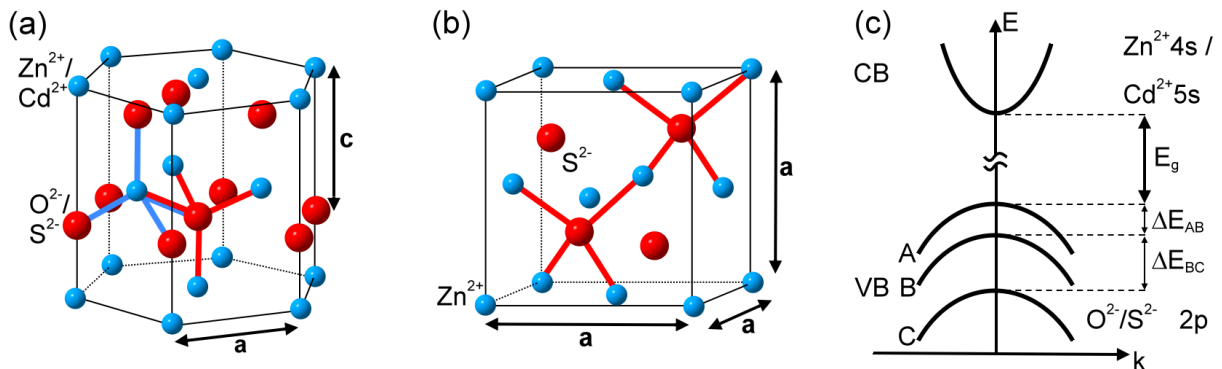

Figure 2.1: *(a) Sketch of the wurtzite unit cell of ZnO, ZnS and CdS: The positions of the anion (Zn/Cd) and cation (O/S) atoms are marked in blue and red, respectively. **a** and **c** label the lattice constants. (b) Sketch of the cubic unit cell of ZnS. (c) Schematic band structure showing the conduction and the threefold split (A, B and C) valence band around the Γ point.*

Zinc sulfide   Zinc sulfide (ZnS) is a direct wide band gap II-VI semiconductor which occurs in hexagonal (w-ZnS) as well as cubic configuration (c-ZnS) under normal conditions. The unit cell of the hexagonal phase has a wurtzite lattice structure with C_{3v} symmetry (compare figure 2.1 (a)). The band gap energy is E_g(wurtzite) = 3.91 eV at T = 19 K [105] and the lattice constants are a(wurtzite) = b = 0.382 nm and c = 0.626 nm [106]. The arrangement of the conduction and valence bands is similar to ZnO except for the symmetry of the valence sub-bands. The energetic spacing between the sub-bands is ΔE_{AB} = 28.9 meV and ΔE_{BC} = 87.6 meV [99]. The cubic configuration (shown in figure 2.1 (b)) crystallizes in a fcc lattice with zinc blend structure (T_d symmetry) with a lattice constant of a(cubic) = 0.541 nm [107]. The band gap energy of the cubic modification E_g(cubic)= 3.78 eV at T = 19 K [108] is smaller than in the wurtzite configuration and the top most valence band is only split in two sub-bands (A and B) with an energetic spacing of ΔE_{AB} = 70 meV [99].

Cadmium sulfide   Cadmium sulfide (CdS) is another II-VI semiconductor with a direct band gap of E_g(wurtzite) = 2.53 eV at room temperature [109]. As in the case of ZnO, the wurtzite phase is the most stable at ambient conditions and the lattice parameters are a = b = 0.416 nm and c = 0.676 nm [104, 107]. The structure and symmetry of the conduction and valence bands is similar to ZnO. The refractive index of the ordinary ray at 517 nm (2.40 eV) is n = 2.76 and the dispersion at this wavelength is $dn/d\lambda$ = -7.963 µm^{-1} [110].

2.1.2 Luminescence of II-IV semiconductors

After excitation by a fast electron or a photon with an energy larger than the band gap, an electron from the conduction band is lifted to the valence band creating an electron hole pair. The electron (hole) relaxes fast in the order of femto- to picoseconds to the bottom of the conduction band (the top of the valence band). Direct recombination of the carriers (band to band) would lead to the emission of a photon owning the band gap energy, but the direct recombination is unlikely in II-VI semiconductors.

Free excitons   Due to Coulomb interaction, the electron is attracted by the hole and vice versa, which leads to a bound state by formation of a quasi-particle called free exciton (FX). Analogue to the hydrogen atom, the exciton Bohr radius a_B is defined as the spacial expansion of the exciton, which is 1.8 nm for ZnO, 2.5 nm for ZnS [98] and 2.8 nm for CdS [111]. The free excitons are much larger than the unit cell and are therefore of Wannier type [112]. The energy of the emitted photon E_X is reduced by the binding energy E_B^{FX} of electron and hole (figure 2.2 (a)), which is 60 meV for ZnO [113], 36 meV for ZnS [114] and 28 meV for CdS [115] in the ground state n = 1. The binding energy is larger than the thermal energy at room temperature ($k_B T \approx$ 25 meV), so that the excitons are stable even at temperatures above. The lifetimes of excitons strongly depend on the crystal quality and are typically in the range of tens to hundreds of picoseconds [46, 58, 116–118].

Exciton-polariton   Excitonic excitations exhibit a strong coupling to the electromagnetic light field in II-VI semiconductors, therefore excitons and photons cannot be treated separately on the respective exciton and photon dispersion relation for states of equal energy. In other words, an impinging photon creates an electron-hole pair (exciton), which recombines by emission of a photon, creating an electron-hole pair and so on. The process is described by a quasi particle called exciton-polaration [119]. The parabola shaped dispersion (dashed line) of the longitudinal (E_L) and transversal exciton (E_0) shown in figure 2.2 (b) is crossed by the linear photon dispersion
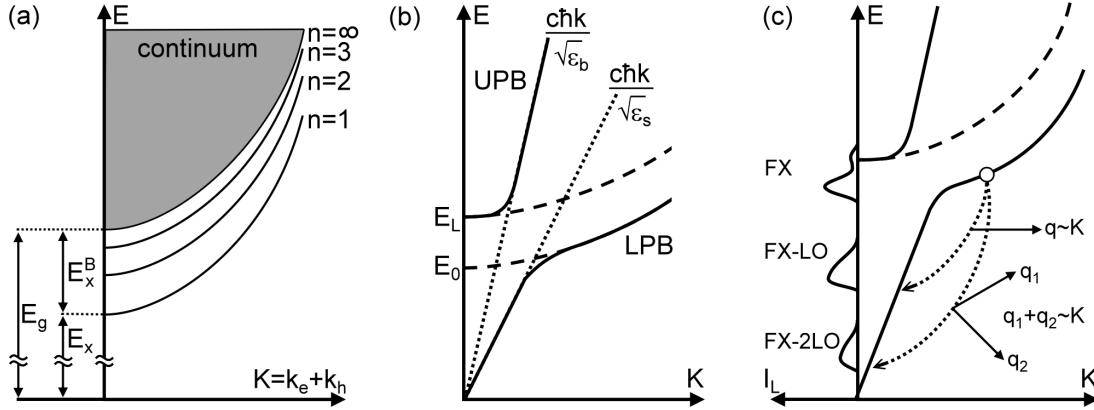
Figure 2.2: *(a) Sketch of the exciton dispersion relation showing the ground (n = 1) and higher excited states. (b) Sketch of the exciton-polariton dispersion relation including the dispersion for excitons (dashed) and photons (pointed). (c) Sketch of the recombination of a free exciton involving interaction with longitudinal optical phonons. The resulting photoluminescence emission is plotted on the left.*

(dotted line) with a slope influenced by the background (ϵ_b) and static dielectric function (ϵ_s). The continuous line describes the dispersion of the exciton polariton, which splits into the lower and upper polariton branch (UPB and LPB). The exciton-polaritons on the UPB follow the excitonic dispersion for small k and approach the photon dispersion for high k. On the LPB, the polaritons follow the linear photon dispersion for small k and advance to the excitonic dispersion for high k. Excitons with high or low energy therefore exhibit a photonic character. Excitation of the semiconductor with photons having energies much larger than the band gap results in the creation of excitons on the UPB, which can relax by scattering at optical and acoustical phonons into the LPB. The creation of excitons is always connected to polaritons, as both cannot be treated separately. The term "exciton", used in this thesis, is meant equivalent to the exciton-polariton.

Bound excitons and direct carrier recombination at impurities   The kinetic energy of excitons at low temperatures is small, which allows them to localise at imperfections in the crystal lattice. The binding to an impurity further lowers the energy of the exciton, leading to additional reduction of the photon energy equivalent to the binding energy. Such impurity sites can be intrinsic crystal defects like vacancies or interstitial atoms, but also extrinsic impurities like donors and acceptors [102]. Dependent on the type of impurities and their charge state, the excitons are labelled as neutral donor bound (DX), ionised donor bound (D^+X) or neutral acceptor bound excitons (AX). The complex of a negatively charged acceptor and an exciton is not stable and recombines in an electron and an neutral acceptor [120]. For ZnO and CdS, donors are the main impurities making the material intrinsic n-type [97, 121]. This is why e.g. the emission spectra at low temperature is mainly dominated by DX lines. As bound excitons do not exhibit any kinetic energy for their center of mass, the spectral emission lines appear very sharp in contrast to the emission lines from free excitons, that are broadened due to their kinetic movement.

Direct recombinations of free electrons from the conduction band with holes offered by e.g. acceptors (e,A) occur in ZnS [122, 123]. As the kinetic energy of the free electron can be large, the resulting emission is spectrally broad compared to bound exciton emissions. Direct recombination of electrons from donors with holes from the conduction band are possible as well.

Phonon interaction   During recombination, carriers interact with the crystal lattice and and a part of their energy can dissipate by the generation of one or more phonons [124]. Several phonon

modes (optical and acoustic) are possible for semiconductors with a textured basis, which are further divided to transversal and longitudinal vibration modes. The lattice atoms vibrate anti-phase in optical phonon modes, creating a dipole moment, which can interact with the light field. There is only very little coupling to acoustic modes as the atoms vibrate in phase. The most prominent mode is the longitudinal optical phonon (LO) with an energy of 72 meV [125] for ZnO, 43 meV [126] for ZnS and 38 meV for CdS [127]. Due to the interaction with phonons, excitons with high energies or high momentums can recombine optically as the momentum is conserved by the phonons [128]. The original emission (zero-phonon-line, ZPL) is then accompanied by an emission reduced by the energy of one or multiple phonons, as shown in figure 2.2 (c). The phonon replica emission is labelled by their origin and the active phonon mode.

Deep level recombination Crystals in the thermodynamic equilibrium always contain a certain amount of point defects [129], which induce additional states inside the band gap. Carriers can localize at these states and recombine by emission of a photon (deep level emission, DLE). The origin can be of intrinsic as well as extrinsic nature: Point defects like vacancies, interstitial atoms as well as anti-sites or defect complexes [97, 128, 130, 131] but also extended defects like dislocations can induce optical active levels [102]. The energetic position as well as the carrier recombination path for the defect levels are unclear in most cases and therefore heavily discussed in literature [97, 132–134]. Further complications are induced as defects can occur in several charge states having different energetic positions [135, 136]. In general, it is believed that the emission from recombinations at interstitial defects appear at higher energies than from vacancies states [137].
Extrinsic defects refer to impurity atoms on substitutional or interstitial sites, which are believed to generate optical active levels, like e.g. Cu in ZnO [138, 139] or Au in ZnS [140, 141]. The intrinsic and extrinsic defects induce distortions of the crystal lattice. The interaction with phonons is therefore strong and the direct recombination of carriers is often accompanied by phonon replica. The strength of the phonon-interaction is described for T $\rightarrow$ 0 by the Huang-Rhys-Factor S [142]. The direct emission (ZPL) is dominating for S < 1, while S > 1 corresponds to a reduced intensity of the ZPL accompanied by phonon replica. The ZPL is nearly suppressed for values of 10 or more and the phonon replica form a Gaussian like emission band.

Non-optical recombination Despite optical recombination, excited carriers can recombine non-radiative by transferring their energy to surface- and defect-related sites in the crystal [143]. As this reduces the emission intensity, those sites are sometimes called "killer centers". The energy dissipates fast as heat (via phonons) into the crystal lattice [144].

2.1.3 II-VI semiconductors at high excitation

All the recombination mechanisms described so far occur at low electron-hole pair concentrations n_p, so that the distance between carriers is large and interactions can be neglected. The emission intensity scales linear with the excitation power in the low excitation regime, if no saturation effects occur. A further increase of the electron-hole pair concentration lead to the situation that the Coulomb attraction between electron and hole gets more and more screened, and finally to the dissolution of excitons to free carriers. New recombination channels arise from the interaction between excitons and free carriers, as shown in figure 2.3 (a) and listed below. In general, the one-particle approximation is not valid any more in the medium and high excitation regime, which results in non-linear optical effects.
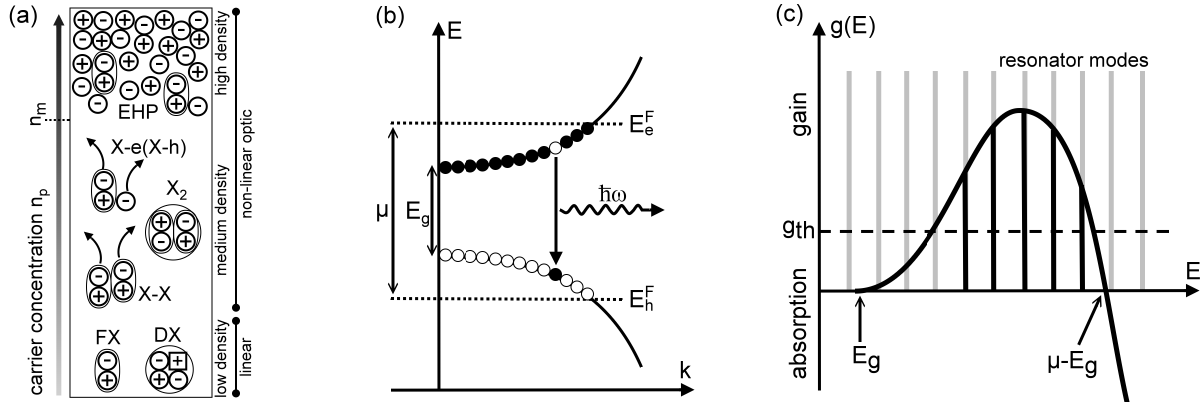
Figure 2.3: *(a) Interaction of excitons and free carriers at increasing electron-hole pair concentration n_p. (b) The valence and conduction band are filled with holes(electrons) up to the respective quasi Fermi energies in the electron-hole plasma. The carriers can recombine radiatively if momentum conservation is fulfilled, which results in a broad emission band. (c) Gain from an EHP is possible between E_g and $\mu - E_g$. Only resonator modes above the threshold g_{th} achieve gain.*

Exciton-exciton scattering and biexcitons   In the medium excitation regime, the excitons feel each others Coulomb interaction and elastic exciton scattering (X-X scattering) leads to a reduction of the exciton lifetimes [54]. If the excitons scatter inelastic, one is lifted to a higher excitonic state while the other is scattered to the photonic part of the LPB. This process results in the emission of the "P_n band" ($n = 2, ..., \infty$), which is labelled depending on the final state of the scattered exciton and appears at energies shifted below the emission of the free exciton by the exciton binding energy in maximum [145]. The exciton scattered into the excited state relaxes by phonon scattering back to the ground state $n = 1$ [146]. As the probability for exciton scattering increases superlinear with n_p, the emission intensity of the P band scales quadratic with the excitation power [147], although it is still regarded as a spontaneous emission processes [148]. High exciton concentrations allow the formation of a bound state of two excitons (biexciton, X_2), analogue to the H_2 molecule. The radiative recombination of a biexciton leads to the "M band" red-shifted by 12 - 20 meV compared to the emission of the free exciton [149, 150]. Exciton-electron(hole) scattering (X-e/X-h) becomes important at higher electron-hole concentrations [151].

Electron-hole plasma   A further increase of the electron-hole concentration decreases the mean exciton distance until the Coulomb screening and Pauli blocking initiates the dissolution of the excitons to free carriers [152]. The critical concentration n_M is related to the exciton volume (defined by the Bohr radius a_B) by $n_M \approx 1/a_B^3$. For concentrations above the Mott density n_M, the mean exciton distance is shorter than the Bohr radius and a bonding between particular carriers can no longer be defined, but an electron-hole plasma (EHP) is generated [153, 154]. Several effects appear in the high excitation regime: the carriers screen each other, leading to a monotonous shrinking of the band gap (band gap renormalization) [155, 156] with increasing carrier concentration n_p. The excitons also experience a screening effect, which decreases their binding energy. This just compensates the band gap renormalization, so that the emission of the free excitons remains constant at $E_g - E_B^{FX}$ [156]. The Mott density n_M defines the carrier concentration n_p, at which the renormalized band gap ($E_g(n_p)$) falls below the emission energy of the excitons. The transition is not sharp defined at room temperature due to the broadening of the excitonic emission and is in the range of $1 \cdot 10^{17} < n_M < 5 \cdot 10^{18}$ cm^{-3}. Mott densities have been determined to be $2.4 \cdot 10^{18}$ cm^{-3} for ZnO [128] and 2.5 - 2.8 $\cdot 10^{17}$ cm^{-3} for CdS [157, 158] at low temperatures.

The emission of an EHP originates from the radiative recombination of electrons and holes in the plasma (see figure 2.3 (b)). Valence and conduction band are filled with carriers up to the quasi Fermi levels E_F^h and E_F^e. This is a non-equilibrium state, which is only sustained by the continuous generation of carriers in the high excitation regime. The chemical potential μ is given by the difference of the quasi Fermi levels $\mu = E_F^e - E_F^h$ and depends on the exact impact power density. Radiative recombination can occur if momentum conservation is fulfilled, resulting into a broad emission band. The spectral width of the EHP emission is determined by $\Delta E = \mu - E_g(n_p)$. At increasing carrier concentration, the bands are higher filled with free carriers, which causes an enlargement of μ and therefore a broadening of the emission. As the band gap renormalization leads to a smaller band gap at the same time, the broadening appears at the low energy side for higher carrier concentrations.

Gain in II-VI semiconductors The intensity of light $I(E,l)$ with photon energy E travelling trough matter decreases exponentially with distance l due to scattering and absorption, as described by the Lambert-Beer law [159]: $I(E,l) = I_0 \cdot e^{-\alpha(E) \cdot l}$. I_0 is the original intensity and $\alpha(E)$ is the absorption coefficient, which depends on the energy of the photons. For highly excited semiconductors, the absorption coefficient can become negative, which equals gain and the light is amplified in the material: $g(E) = -\alpha(E)$. Gain can be achieved by spontaneous or stimulated radiative recombinations of carriers from the filled valence and conduction band. The situation sketched in figure 2.3 (b) can also be understood as a four-level system to describe the EHP gain mechanism: the high K states are the pump states, which allow absorption of photons with $\hbar\omega > E_g$. Electrons and holes relax fast ($\sim$ fs) by scattering with other carriers and phonons to lower K states, and finally recombine from these states by emission of photons. As the scattering processes are faster than the lifetime of states ($\sim$ ps) near $K = 0$, population inversion can be reached at sufficient high pumping. This enables light amplification in the range between $E_g(n_p)$ and $\mu - E_g(n_p)$ in the EHP. The chemical potential μ decreases at elevated temperature [160, 161], so that higher carrier concentrations are necessary to achieve gain at room temperature.

The emission process is called "amplified spontaneous emission" (ASE), as the emission overcomes the absorption. The intensity of the ASE increases exponentially with distance l in the gain medium. The $g(E)$ function describes the material gain and is a fundamental property of a semiconductor. The general course of $g(E)$ called gain bandwidth is shown in figure 2.3 (c): light with an energy below the band gap cannot be amplified, as the material is transparent. The gain $g(E)$ increases above $E_g(n_p)$ and the course is determined by the Fermi functions of electrons and holes and the combined density of states [54]. The transparency point is determined by the highest occupied states $\mu - E_g(n_p)$ at which $g(E_{tp}) = 0$ and strong absorption occurs above. The maximum material gain is in the range of $7 \cdot 10^3$ cm^{-1} for ZnO and up to $2.8 \cdot 10^4$ cm^{-1} for CdS [162].

Semiconductor lasers Embedding the gain medium in a resonator structure creates a feedback, which induces guided modes and enables further amplification of the emission, as used in a LASER [163]. The emission amplification is determined by the modal gain $g_{mod}(E)$ of the guided mode, which propagates through the gain medium:

$$g_{mod}(E) = \Gamma \cdot g(E). \tag{2.1}$$

The modal gain is connected to the material gain by the confinement factor Γ, which describes the overlap of the guided mode and the active medium and takes values between 0 to 1. The amplification of an emission mode can be achieved, when the gain overcomes the round trip losses in the oscillator induced by absorption and reflection losses at the resonator mirrors. The modal gain must overcome a threshold g_{th}, which takes the loss mechanisms into account [164]:

$$g_{mod}(E) > g_{th} = \alpha(E) + \alpha_W(E) + \alpha_M(E),\qquad(2.2)$$

where $\alpha(E)$ accounts for the additional loss mechanisms due to absorption and scattering, α_W describes the waveguide losses and $\alpha_M = 1/2L \cdot ln\,(1/(R_1 R_2))$ describes the mirror losses with the reflectivities $R_{1,2}$ at the ends of the resonator with length L. Only resonator modes above the threshold gain g_{th} will be amplified, as sketched in figure 2.3 (c). Typical edge emitting lasers have a low modal gain of 50 - 150 cm^{-1}, which results from a rather poor mode confinement of $\Gamma < 0.1$ [165].

2.1.4 Optical properties related to the nanowire

Waveguiding II-VI nanowires have been proven as excellent waveguides [20, 166], as they are able to guide light with a vacuum wavelength larger than their diameter with low losses. The principle follows a step-index fiber with a cladding (air, vacuum) extended to infinity. The guided light field exhibits a much stronger confinement compared conventional silica fibers due to the high difference in the refractive index of n_{NW} = 2.42 - 2.76 in the nanowire and $n_{sur.}$ = 1 - 1.5 for air or silica substrates. Below a critical radius, estimated by $d_{min} \sim \lambda/n$ [51] (λ: wavelength of the guided light, n: refractive index of the nanowire material), the light is not any more completely confined in the nanowire, but extends into the surrounding and propagates as evanescent field [20]. This is accompanied with increased waveguide losses.

At excitation above the band edge of the material, luminescence light is emitted and guided along the wire, so that an enhanced emission is observed at the facet ends. The emission is red-shifted with increasing distance compared to the emission at the excitation spot, which is explained by absorption and re-emission processes during the travel along wire, which acts like an active waveguide [166, 167]. For light with energies below the Urbach tail of the absorption profile [168], no red-shift occurs and the light is guided passively along the nanowire as described above.

Resonator effects The large difference in refractive index leads to the partial reflection of the guides modes at the nanowire facet ends. The reflected wave interferes with the incoming wave, thus creating a feedback in the form of standing waves in the nanowire resonator. This introduces a modulation superimposed to the emission spectrum in the form of sharp peaks at energies of constructive interferences. Straight nanowires with flat facet ends can be understood as Fabry-Pérot type resonators [51], while reflection at the side facets becomes also possible for large nanowire diameters in a whispering-gallery type resonator [53]. The type of the resonator can be distinguished by the mode spacing.

Finite-difference time-domain (FDTD) simulations show a strong dependence of the reflection coefficients on the guided mode, the refractive index change and the diameter of the wire [169]. Reflection coefficients up to 0.47 for the TE$_{01}$ mode could be evaluated for ZnO nanowires with diameters above 200 nm. Smaller diameter nanowires not only showed decreased reflection coefficients, but also exhibit enlarged waveguide losses due to a larger fraction of the light guided as evanescent field [21].

Gain The high confinement of the light field in the nanowire is not only attractive for waveguide applications, but also brings advantages as the nanowire can serve as optical gain medium itself. This brings a large overlap of the guided mode and the active medium with confinement factors up to $\Gamma \approx 1$. Nanowires with large diameters can even achieve confinement factors of $\Gamma \sim 1.2$, as the guided light not only travels along the wire axis, but can propagate in higher order modes not parallel to the wire axis. Such modes propagate at a longer distance than the nanowire length. Due to these factors, nanowires can achieve a high modal gain, which is in the same range as the material gain. A modal gain of up to 2500 cm^{-1} has been theoretically predicted for 150 nm diameter GaN nanowires [55]. The modal gain of ZnO nanowires as a function of diameter has been experimentally determined to 400 cm^{-1} for 200 nm thick wires and up to 5000 cm^{-1} for wires between 1.2 - 1.6 µm diameter [56].

Nanowire lasers Semiconductor nanowires with sufficient diameter therefore offer the essentials for a efficient nanoscaled light source: Luminescence is generated at excitation above the band edge, gain is achieved by the material at sufficient high pumping and the natural morphology of the nanowire provides the waveguide and resonator structure. Indeed, amplified spontaneous emission with sharp emission modes has been reported in many publications on ZnO, CdS and similar nanowires [57–59, 170–176], but a conclusive proof of lasing emission was missing. Zimmler et al. [21, 51] could observe the transition from ASE to lasing oscillations for ZnO nanowires and examined the lasing properties as a function of nanowire morphology. The proof for lasing oscillations in CdS nanowires will be provided in this thesis.

Influence of the large surface-to-volume ratio Although the nanowires behave similar to bulk materials from the electronic point of view, several differences appear in their optical properties related to the large surface-volume ratio of nanowires compared to bulk [37]. Additional states are induced close to the surface, at which excitons can localize (surface excitons, SX). Their recombination appears red-shifted to the free exciton emission [177]. This dominates the optical emission of ZnO nanowires thinner than 100 nm [178, 179].
Modifications of the surface alter strongly the emission properties. This arises from the pinning of the Fermi level at the surface of the n-type ZnO nanowires, which induces an upward bending of conduction and valence band [42]. In the untreated nanowire, holes at the surface can tunnel to deep states in the volume and activate the deep level recombination. Coating the nanowires with dielectrica and polymers lowers the upward bending [180, 181]. This reduces the tunnelling of the holes to defect states, while the emission of excitonic states near the surface (SX) is enhanced. On the other hand, coating the nanowire with metals induces additional gap states (MIGS) [41], which trap electrons. In this case, the DLE emission is enhanced by the recombination of holes with MIGS trapped electrons, while the recombination of surface excitons is hampered. Other treatments like dipping in isopropanol or surface modification by silanization [182] enhance the DLE emission as well, as similar processes are involved.

Lifetime and energy transfer The geometry of the nanowire shows an influence on the emission properties of embedded optical active impurities. For Mn in ZnS nanowires, a lifetime longer than the intrinsic lifetime for isolated ions in defect free bulk material was observed [183]. The explanation is given by the influence of the refractive index n of the host matrix on the transition probability, which is directly related to the lifetime of the ions (see chapter 2.2.2): the emission of Mn ions in ZnS nanostructures extends as evanescent field into the surrounding. The effective refractive index is therefore lowered and intermediate between the

bulk value and air/vacuum. This reduces the transition probability and elongates the lifetimes of ions in nanostructures.

Another influence of the nanowire geometry was found for the energy transfer between Mn ions and defects: The characteristic lengths of the Mn-Mn and Mn-defect interactions are typically in the nm range. A restriction in geometry as induced by the nanowire structure will therefore affect the energy transfer characteristics. The energy transfer was found to be quasi one-dimensional along the nanowire axis for ZnS nanowires with low Mn content [9].

2.2 3d- and 4f-impurities in II-IV semiconductors

Elements with partly-filled 3d(4f)-shells exhibit extraordinary properties due to the interactions of their unpaired electrons. Not only the resulting magnetic properties have drawn attention in research [184], but also their optical properties [185] making them suitable dopants for light emitters and laser crystals [186].

The term transition metal (TM) defines the elements with partly filled 3d-shell. The electronic configuration is $[Ar]4s^2 3d^n$. Embedded in solids, the ions typically appear in the 2+ or 3+ ionized state, changing the electronic configuration to $[Ar]3d^n$ with n = 1 for Sc^{2+} and n = 9 for Cu^{2+}. Typical coordination numbers are 4 or less, which accounts for a particular covalent bonding type.

Rare earth (or lanthanides, RE) label the elements with partly filled 4f-shell ranging. Their electronic structure is $[Xe]6s^2 5d^1 4f^n$. In solids, the elements occur dominantly in the triply ionized state ($[Xe]4f^n$) with n = 1 for Ce^{3+} to n = 13 for Yb^{3+}. The 2+ state is found for Eu, Yb and Gd (4+ for Ce) due to energetic reasons. The coordination number is 6 to 8, which is attributed to the more ionic character of the bonding to the ligands.

The filling of the 3d(4f)-shell can be explained according to Hund's rules, which predict that the state with the highest spin quantum number $S = |\sum m_s|$ ($m_s = \pm 1/2$) has the lowest energy. For states with equal S, the state with the highest angular momentum quantum number $L = |\sum m_l|$ ($m_l = -l, ..., l$) has the lower energy. The arising terms are labelled according to the Russell-Saunders scheme as ^{2S+1}L [187]. Taking spin-orbit coupling into account, L and S cannot be treated separately and couple to the total angular momentum $J = L+S, L+S-1, ..., |L-S|$, leading to a splitting of the term into the levels $^{2S+1}L_J$. The level with the smallest J is lowest in energy up to the half-filled shell, the level with the largest J otherwise. In this way, the ground state of the ions can be predicted.

The optical emissions of elements with partly filled shells have attracted interest in research since the first report by J. Becquerel in 1908 [188]. Fascinating was the fact that the radiative emissions, originating from electronic transitions within the 4f-shell, have dipole character [189, 190]. This was in contrast to the prediction of electrodynamics, which demand a change in parity between the initial and final state for dipole emission of electronic system in a spherically symmetric potential (Laporte's rule) [191]. A theory for the interaction of 3d(4f)-ions and the crystal field of the surrounding media was developed by Bethe [192], but could still not explain the radiative intra-shell emissions for rare earth. The solution was independently discovered by Judd and Ofelt [193, 194], who proposed an admixture of states with different parity through the crystal field, thus allowing *induced electric dipole* transitions for 4f-elements.

A short theoretical description of the energy level splitting and optical intra-shell transitions is provided for an understanding of the experimental data. The effects are discussed phenomenologically, the complete mathematical description is given e.g. in references [185, 195–199].

2.2.1 Splitting of the energy levels

Lanthanides and transition metals in solids can be handled according to the solution of the Schrödinger equation. The free ion is chosen as starting point and the influence of the host matrix treated as perturbation.

The free ion The energy levels of the free ion are determined by the eigenvalues of the Hamiltonian H_0, consisting of the summation of the kinetic and potential energy for each of the N 3d(4f)-electrons [185]. The potential energy is described by an effective potential Z^* for each electron at radius r_i, which includes the screening of the attractive nucleus by inner electrons:

$$H_0 = H_{kin} + H_{pot} = -\frac{\hbar^2}{2m_e}\sum_{i=1}^{N}\Delta_i - \sum_{i=1}^{N}\frac{Z^*e^2}{r_i} \tag{2.3}$$

Both the kinetic and potential term have spherical symmetry at this point, therefore the Schrödinger equation for H_0 is solved by a set of wavefunctions $\psi_{nlm_lm_s}(r,\theta,\phi)$, which are characterised by the quantum numbers n, l, m_l and m_s.

$$\psi_{nlm_lm_s}(r,\theta,\phi) = \frac{1}{r}R_{nl}(r)Y_{lm_l}(\theta,\phi)\chi_{m_s} \tag{2.4}$$

The energy levels for transition metals (rare earth) with $n = 3(4)$ and $l = 2(3)$ are highly degenerated, e.g. 3003-fold for the $Eu^{3+}4f^6$ configuration. The set of wavefunctions (equation 2.4) are chosen as the starting point for the application of perturbation theory, because the energy eigenvalues of the undisturbed system H_0 are much larger than the perturbations ($H_0 >> H_x$). This can be estimated from the binding energies of the 3d(4f)-electrons, which can be more that 1000 eV [200].

The strongest perturbation of the free ion is introduced by the electrostatic Coulomb interaction of the 3d(4f)-electrons H_C, which reduces the degeneracy and leads to a splitting into $(2S+1)(2L+1)$-fold degenerated levels labelled as $^{(2S+1)}L$ terms, as illustrated for Eu^{3+} in figure 2.4(a). Including spin-orbit coupling H_{SO}, L and S couple to J. The degeneracy is further lowered by the splitting of the terms into $^{(2S+1)}L_J$ multiplets [71], which are now $(2J+1)$-fold degenerated. It has to be noted that only Russell-Saunders coupling will lead to a pure $^{(2S+1)}L_J$ state, while the ground state in the case of jj-coupling (which is typically found for lanthanides) is characterised by a superposition of several $^{(2S+1)}L_J$ states, coupled by the coefficients of fractional parentage [201–204].

$$H_C = e^2\sum_i\sum_{j,j>i}\frac{1}{|r_j - r_i|} \qquad\qquad H_{SO} = \zeta\sum_i \mathbf{s}_i \cdot \mathbf{l}_i \tag{2.5}$$

Further perturbations, like the linear electrostatic two particle interaction H_{LC} [205], non-linear three-particle interactions H_{NLC} for more that two electrons [206], magnetic induced spin-spin and spin-other orbit interactions $H_{SS,SOO}$ [207] as well as electro static induced spin-orbit interactions H_{ECSO} [207, 208], will only shift the energy levels. The splitting of the energy levels and the relative strength of the interactions are visualized exemplarily for Eu^{3+} in figure 2.4 (a). The final Hamiltonian is characterised by up to 19 free ion parameters. Fitting of the energy levels is performed by parametrization of each interaction. The complete energy matrix is diagonalized and finally solved using numerical calculations. The resulting energy level structure is known as the "Dieke diagram" [195].
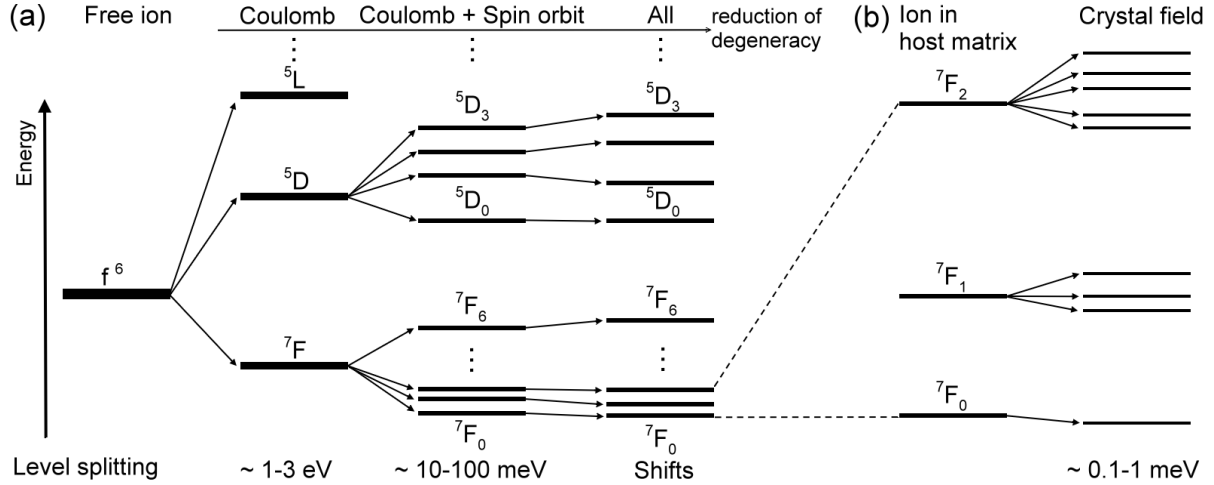
Figure 2.4: *(a) The energy levels of a free Eu^{3+} $4f^6$ ion are split by Coulomb and Spin-orbit interaction, the other interactions lead only to a relative shift of the levels. The degeneracy of the free ion is reduced by the interactions. The energy scale is arbitrary and intended to display the effects. (b) The energy levels of ions embedded in a host matrix are further split by the influence of the crystal field, removing their M_J degeneracy by the Stark effect.*

Influence of the crystal field   Incorporation of the 3d(4f)-ions into a solid matrix leads to an additional perturbation H_{CF} induced by the interaction with the crystal field. This lifts the degeneracy on m_J and splits the $^{(2S+1)}L_J$ multiplet into $2J+1$ levels by the Stark effect, shown in figure 2.4 (b). In a simple approach, the crystal field potential can be approximated as the superposition of point charges at the positions of the surrounding atoms (point charge electrostatic model) [192]. This is of course oversimplified as covalent bonding, ligand polarizations or overlap contributions are not regarded. More realistic models (e.g. like the ligand field model) were developed, which could describe the influence of the crystal field in better accuracy [197]. An overview for the numerical treatment of the crystal field interaction is presented in [71].

The crystal field potential is described by suitable parameters $B_q^{(k)}$ ($A_q^{(k)}$ in a different notation), which are restricted in that way that the crystal field Hamiltonian has to be invariant under all symmetry operations of the point group representing the site symmetry of the ion in the crystal. Only those crystal field parameters are non-zero that contain the symmetry elements of the respective point group [71]. From this parametrization, some selection rules can be directly derived. Further on, only the even parts are responsible for the splitting of the $^{(2S+1)}L_J$ multiplets, while the odd parts determine the intensities of the induced dipole transitions between multiplets [193, 194].

The evaluation of the energy matrix including the crystal field results in non-diagonal matrix elements with respect to the quantum number M_J, which require a relabeling of the levels split by the crystal field (Stark level). Racah [201] suggested the irreducible representation Γ_i (according to Bethe [192]) for rare earth elements, from which additional selection rules for polarization can be directly derived. Only unpolarized spectra were investigated in this thesis, therefore the relabeling of the multiplets was omitted. For transitions metals, which are stronger effected by the crystal field, the Mulliken symbols A, B, E and T [209] are introduced, which describe the degree of degeneracy of the crystal field level as well as some symmetry properties. A correlation between both sets of symbols is listed in [198].

Further contributions   Further contributions are introduced by the Kramers degeneracy [210]. For a system with an odd number of electrons, the energy levels are at least double degenerated, even in the presence of a crystal field [211]. This is a consequence of the invariance

of the Hamiltonian under time reversal. The degeneracy is only lifted by a magnetic field. Such double degenerated levels are labelled as *Kramers doublets*.

The positions of the atoms in the crystal lattice have been regarded as fixed so far. But from the interaction of the nuclear framework with the electrons arises another contribution: the symmetry at the site of the ion is distorted in order to achieve a lower energy state, known as the *Jahn-Teller effect* [212]. The effect originates from the displacement of the nuclei around their equilibrium positions induced by the interaction with the electrons [213]. The displacement causes a deformation of the 3d-orbitals, but no transitions between them. Due to this distortion, the degeneration of e.g. the ground state is lifted by the reduced local symmetry and the resulting states are labelled as "vibronic". Two types of the Jahn-Teller effect are known: the weak electron-nucleus coupling forces the system into a new stable nuclear configuration in the static Jahn-Teller effect. This is absent for the dynamic Jahn-Teller effect, as the system moves from one equilibrium configuration into another induced by stronger coupling. Both the Kramers degeneracy and the Jahn-Teller effect have to be regarded for the splitting of the energy levels, especially for transition metals in wide band gap semiconductors [214–217].

2.2.2 Intra-shell transitions

The electronic intra-shell transitions have electric dipole character, which is surprising, as electric dipole transitions are parity-forbidden in the 3d- and 4f-shell according to Laporte's rule [191]. This originates from the electric multipole tensor operator $\mathbf{m}^{(l)}$ of rank l ($l = 1$ for dipole and $l = 2$ for quadrupole radiation), which contains the electric dipole transitions operator $\mathbf{D}^{(l)}$ expressed by the position operator $\mathbf{r}$ of electron i [199]:

$$\mathbf{m}^{(l)} = -e\mathbf{D}^{(l)} = -e\sum_i \mathbf{r}^{(l)}(r_i, \theta_i, \phi_i) \tag{2.6}$$

The electron position operator $\mathbf{r}$ does not commute with the parity operator π [218]:

$$\langle i|\,\mathbf{r}\,|f\rangle = \langle i|\pi^+\pi\,\mathbf{r}\,\pi^+\pi|f\rangle = c_i c_f(-\langle i|\,\mathbf{r}\,|f\rangle) \tag{2.7}$$

The condition above is only fulfilled, if the initial state $\langle i|$ and the final state $|f\rangle$ have opposite parities, which is not found for the 4f-system. Judd and Ofelt showed that the occurrence of intra-4f-transitions can be explained by the admixture of states of opposite parity by the crystal field [193, 194]. The starting point for a treatment by perturbation theory is an arbitrary initial level, which is expanded with the disturbance of a configuration other than the 4f shell (e.g. $4f^{n-1}5d^1$) induced by the odd parts of the crystal field. The evaluation of the electric dipole operator is performed by parametrization of the perturbed levels. Finally, non-zero matrix elements are calculated for the *induced electric dipole transitions*.

In the same manner, the magnetic dipole transitions can be derived using the magnetic multipole operator $\boldsymbol{\mu}^{(l)}$, defined by the total spin $\mathbf{S}$ and total angular momentum operators $\mathbf{L}$ and the electron g-factor g_e:

$$\boldsymbol{\mu}^{(l)} = -\frac{e\hbar}{2m_e c}(\mathbf{L} + g_e \mathbf{S})^{(l)} \tag{2.8}$$

In contrast to electric dipole transitions, magnetic dipole transitions are parity allowed within intra-shell transitions and may occur even under inversion symmetry, but their intensity is more that one order of magnitude smaller that the induced electric dipole transitions. The selection rules can be derived from the final expressions of the transition intensities and are listed e.g. in [198]. It has to be mentioned that the transition rules are only valid for good quantum numbers, but e.g. the selection rules on M and S break down in the intermediate coupling scheme (applied

for transition metals) and the selection rule on J breaks down in the case of J-mixing (typical for rare earth).

For the evaluation of the transition probability and intensity, the dipole strength D is calculated from the absolute square of the matrix element of the respective dipole operator:

$$D = |\langle i|\mathbf{D}^{(l)}|f\rangle|^2 \tag{2.9}$$

The Einstein coefficients for spontaneous absorption, representing the transition probability, can be derived from the dipole strength. The Einstein coefficients for spontaneous emission are proportional to these, but the dipole strength has to be corrected by the susceptibility χ of the medium surrounding the ion (*local Lorentz correction* [199]), which can be approximated for electric (ED) and magnetic (MD) dipole transitions by

$$\chi_{ED} = \frac{n(n^2 + 2)^2}{9} \qquad\qquad \chi_{MD} = n^3 \tag{2.10}$$

with n being the refractive index of the host material. Taking the susceptibility χ into account, the Einstein coefficients for spontaneous emission at the frequency $\bar{\nu}$ between two individual Stark levels can be written as:

$$A(i \to f)_{Stark} = \frac{64\pi^4\bar{\nu}^3}{3h}\left[\chi_{MD}D_{MD} + \chi_{ED}D_{ED}\right] \tag{2.11}$$

The transition probability for a multiplet starting from the initial level i with J_i is essentially the average of the individual transition probabilities under the implicit assumption that the Stark levels are equally populated:

$$A(i \to f)_{Multiplet} = \frac{A(i \to f)_{Stark}}{(2J_i + 1)} \tag{2.12}$$

The local Lorentz field correction includes the correction factor $\bar{\nu}^3\chi$, which induces an interesting effect: For the same dipole strength, the transition probability in the ultraviolet is higher compared to transitions in the infrared. Additionally, χ contains the refractive index n of the host medium, which also depends on the frequency(wavelength) of the emission [219] and increases the effect for high frequencies (short wavelengths). This suggests that lanthanide or transition metal doped wide band gap semiconductors are promising UV and VIS emitters.

Influence of temperature   The 3d- and 4f-ions experience not only the influence of the static crystal field from the surrounding host matrix, but also electron-phonon interactions, which can be divided into acoustical and optical phonons. Each multiplet, sufficiently spaced from lower multiplets to prevent non-radiative relaxation and split by the crystal field, interferes with acoustical phonons so that the population of each stark levels is determined by the Boltzmann distribution. This is valid as the electron-phonon interaction takes place in a time scale of $<$ ps [91]; while the multiplets have typical lifetimes of µs to ms [91, 185], and therefore thermal equilibrium of the Stark multiplets can be assumed before the radiative intra-4f-transitions occurs [91]. A temperature dependent fractional thermal population can be derived from the interaction with acoustic phonons, which depends on the degeneracy and energy above the lowest level and results in a population of higher stark levels at elevated temperatures. This becomes visible in a temperature dependent emission energy shift and change in the spectral line shape.

The interaction with optical phonons is responsible for the non-radiative decay of a multiplet sufficiently spaced from other multiplets to prevent relaxation processes by acoustical phonons [220–

222]. A theoretical probability for non-radiative transitions involving multiple optical phonons is based on a transition rate model [223], which is governed by the energy of the phonon mode, the number of involved phonons, the mean thermal occupation of a vibrational mode determined by the Bose-Einstein distribution and the Huang-Rhys parameter [142], accounting for the magnitude of the electron-phonon interaction. The interaction with optical phonons determines not only the absence of a multiplet in a spectrum due to non-radiative decay, but also the temperature dependent intensities.

Exciation and de-excitation mechanisms Several different excitation mechanisms have been theoretically proposed and experimentally verified by PL and PL excitation spectroscopy [91], which can be divided in three categories:

1) The 3d(4f) levels can be directly (resonant) excited by photons, e.g. from a tunable laser or absorption of the host emission. The spectral line width are rather sharp (< 0.1 eV at low T) and this process has a rather small cross section due to the small transition probabilities.

2) The second process involves the excitation of an external center, followed by non-radiative energy transfer to the 3d(4f) ion and excitation of the respective inner shell. The external center can be acceptor like defect states of the host crystal, which transfer their excitation energy to the RE/TM ion typically acting as shallow donor. But also non-intrinsic impurities (sensitising centers) can be excited, followed by energy transfer to the RE/TM ion. The excitation bandwidth of such processed is usually broad (0.1 - 0.6 eV) and located below the band edge of the host material [91].

3) The external excitation source generates excitons or electron-hole pairs in the semiconductor host, which can be captured by the TM/RE ion and recombine via energy transfer, yielding into the excitation of the 3d(4f) electrons. This mechanism can be further subdivided into defect Auger recombination [224, 225] (trapping of a free or bound exciton and energy transfer to the ion upon exciton recombination) and the ion acting as trap to bind carriers. The charged complex attracts a carrier of the opposite species forming an exciton. The energy transfer is equivalent to the first case. The excitation is observed as a broad band around or above the band gap energy of the host.

Excitation by hot electrons (as used in cathodoluminescence) usually involves creation of the excitation of the host material by the creation of carriers (analogue to case 3), but also additional excitation mechanisms may occur: the hot electrons can scatter inelastic with the electrons of the 3d(4f)-shell, resulting in their excitation. The mechanism can be further subdivided into impact excitation [226, 227] and impact ionization [228], at which the transition metal/lanthanide ion is ionized by the impact of a hot carrier.

In an ideal inorganic solid, de-excitation occurs mainly by radiative decay and non-radiative transitions due to (multi-)phonon emission [221]. But in semiconductors, the de-excitation mechanisms are more complex, as additional processes involving energy transfer to neighbouring ions or non-radiative sites ("killer centers") are present [229, 230]. Such de-excitation processed can be divided into four groups [91]: a) intra-ion multiphonon transitions [231, 232], b) cross-relaxation processes (energy transfer between the 3d(4f) states of two TM(RE) ions) [233, 234], c) energy transfer to impurity states outside the 3d(4f) shell (provided that there is sufficient energetic overlap) [230] and d) Auger-type relaxation, in which the de-excitation energy is transferred to free carriers [235, 236].

Lifetime and energy transfer The theoretical lifetime of a state is the inverse of the transition probability. Taking into account all possible radiative channels trough which an excited

level i can decay, the theoretical lifetime is given by:

$$\tau(i) = \frac{1}{\sum_f A(i \rightarrow f)} \tag{2.13}$$

The experimental determined lifetime is often shorter due to non-radiative de-excitation mechanisms, the ratio of both determines the quantum efficiency $\eta = \tau_{experimental}/\tau_{theory}$ of the emission. Excited isolated ions in a perfect surrounding decay spontaneously, which results in a single exponential decay. The decay rate is usually difficult to determine, but it is direct proportional to the time-resolved luminescence intensity. A single exponential fit reproduces well the examined decay behaviour in this particular case. If ions in different surroundings (lattice sites or crystal phases) are present, the measured decay behaviour can be described by a multi-exponential function with the lifetime τ_i of each site:

$$I(t) = \sum_i I_{0,i} \cdot e^{-\frac{t}{\tau_i}} \tag{2.14}$$

Any deviation from this (single) exponential behaviour can be attributed to interaction with defects or energy transfer within the 3d(4f)-ion subsystem. The interaction with defects allows non-radiative de-excitation, which lead to a faster intensity decrease. Another shortening of the lifetime is induced by energy transfer within the ion, e.g. by population of an energetically lower multiplet.

For high ion concentrations, interactions in form of energy transfer in the ion subsystem becomes relevant. Several mechanisms have been observed [185], like resonant and phonon assisted transfer, cross-relaxation and dipole-dipole interaction. The latter process was first examined by Förster and Dexter [229, 230]. A modification of the theory can describe the energy transfer between triply ionized 4f-ions in bulk crystals [237]:

$$I(t) = I_0 \cdot exp\left[-\frac{t}{\tau_0} - \Gamma\left(1 - \frac{3}{s}\right)\frac{c}{c_0}\left(\frac{t}{\tau_0}\right)^{3/s}\right] \tag{2.15}$$

τ_0 labels the intrinsic lifetime of isolated ions in a perfect surrounding, c_0 a critical concentration which equals a mean ion-ion radius, at which radiative decay and energy transfer have equal probability and the parameter s, which describes the type of interaction (e.g. $s = 6$ for dipole-dipole interaction). A further modification of the original model was introduced for implanted semiconductor nanostructures [9, 183]. The influence of the nanostructure on the energy transfer characteristics is successfully described for the decay of Mn^{2+} and Tb^{3+} in ZnS nanowires (see chapter 6).

2.2.3 Differences of rare earth and transition metal elements

Although the optical emissions of transition metals and rare earth elements both originate from intra-shell transitions, several differences arise from the interaction of the partly filled shell with the host matrix.

For rare earth elements, the interaction with the surrounding is weak due to the strong shielding of the 4f-shell by the $5s^2$ and $5p^6$ orbits [185]. This results in a very similar chemical behaviour for all lanthanides.

The energy level splitting by spin-orbit coupling (typically ~ 250 meV) is stronger for rare earth than the influence of the crystal field (~ 10 meV) [198] in the weak coupling regime, therefore the energetic spacing of the electronic levels is nearly independent of the host material. A con-

sequence are the low transitions probabilities and very sharp emission lines. In addition, only marginal shifts are induced by elevated temperature and the sharp emissions appear even at room temperature.

Transition metals behave in a different manner as they feel a stronger influence of their surrounding due to the weaker shielding of the 3d-shell by the $3s^2$ and $3p^6$ orbits. The consequence is that the spin-orbit coupling is weaker than the crystal field influence in the moderate coupling regime ($H_C > H_{CF} > H_{SO}$) [238]. The 3d-level are broad, the energetic spacing varies with the host material [239] and the electron-phonon interaction is stronger compared to rare earth. The direct intra-3d-transition is often accompanied by phonon replica in a side band [239–241], which even become dominant at elevated temperatures while the direct transition declines. The temperature related de-excitation (thermal quenching) of transition metals is in many cases stronger compared to rare earth elements.

2.2.4 Doping of II-VI semiconductor nanowires

Doping of semiconductors is crucial for the tailoring of the electrical, magnetical and optical properties [238]. For semiconductor nanowires, this is still a challenging task as doping during growth is difficult and nearly impossible for some material dopant combinations. For Si and III-V compound nanowires, suitable precursors and methods have been developed with a lot of afford to achieve p- and n-type doping during VLS growth [27, 242–244]. But the dopant can have a strong influence on the nanowire growth and respective morphology [72]. Further on, the dopant concentration and location is not uniform: the incorporation during growth mainly occurs by VS growth on the nanowire sides, while the catalyst dot acts purifying on the core [245, 246]. Successful doping of II-VI semiconductor nanowires with optical active TM and RE ions during growth is even more difficult due to their low solubility, the lack of suitable precursors [72] and the high melting points of the TM/RE metals and compounds [74], which often exceeds the nanowire growth temperatures. Successful doping of e.g. ZnO nanorods with RE could achieved by wet chemical methods [78–82, 247, 248]. But the morphology, crystal quality and dopant concentration of the grown structures is usually poor compared to VLS grown nanowires.

Ion implantation was proven as a reliable method for the doping of nanowires, as all limitations induced by the VLS growth can be conquered [249, 250]: every element is possible and the choice of ion energy and fluence offers the precise control of the dopant location and concentration, even above the solubility limit. Successful doping with RE and TM by ion implantation has been proven for VLS grown ZnO and ZnS nanowires [62, 87, 251–253]. But despite all advantages, the ion implantation process is accompanied by the creation of crystal defects [254] and morphology changes [255, 256], which have to be recovered by suitable implantation and annealing methods.

3 Experimental details

The main details of the methods used in this thesis are described in a short summary. A (micro-)photoluminescence setup was developed and installed during this thesis, which is briefly described. Additional information are presented in appendix A.3.

3.1 Synthesis of II-VI semiconductor nanowires

II-VI semiconductor nanowires are typically synthesized using the Vapour-Liquid-Solid (VLS) mechanism first described by Wagner and Ellis for micrometer sized Si whiskers [257]. A catalyst (C) is required, which forms an eutectic with the source material (S) having lower melting point. Substrates covered with the catalyst (typically gold as thin film (< 10nm) or colloid) are heated to a temperature between the melting points of source material and catalyst. The catalyst becomes liquid and forms nanometer sized droplets. Source material supplied from the gas phase is preferentially absorbed at the surface of the catalyst droplet and forms the eutectic solution. Steady supply of source material from the gas phase increases the concentration of the source material in the droplet until supersaturation is reached and the source material nucleates as solid phase, typically by heteronucleation at the interface between catalyst droplet and growth substrate. The solubility of the catalyst in the source material is typically very low, therefore nearly no catalyst is incorporated and the catalyst droplet remains on top of the growing nanowire. The diameter is determined approximately by the size of the catalyst droplet, the length can be controlled by the time of source material vapour supply.

The VLS model using a quasi-binary phase diagram for catalyst and source material is to some extend oversimplified for compound semiconductors (like II-VI materials), as ternary phase diagrams has to be regarded [23]. Due to the low solubility of the non-metal component (oxygen or sulfur) in gold compared to the metal (zinc or cadmium) [258–260], it is assumed that the non-metal is incorporated by indiffusion at the interface between catalyst droplet and nanowire, similar to III-V nanowires [261]. A generalization of the VLS model for compound semiconductors was discussed in literature [262].

Growth occurs directly from the vapour phase (vapour-solid growth, VS) at high source material vapour supply and elevated temperatures. This mechanism strongly depends on the surface energies and therefore favours specific crystal directions [30, 263, 264], leading to tapered nanowires, nanosails [265] or the formation of nanobands with a height in the nanometer range and a width up to micrometers [266]. The growth rate of VS is in the order of some nm/min and therefore slow compared to VLS growth with up to µm/min.

ZnO, ZnS and CdS nanowires were synthesized in a self-assembled CVD reactor at a source material temperature of 1350°C (ZnO), 1050°C (ZnS) or 800°C (CdS), respectively. The evaporated material is transported by Ar gas towards the growth substrates (Si chips covered with a nominal 5 nm Au film) at the cooler end of the furnace, where nanowires grow at 1100-950°C (ZnO), 970-830°C (ZnS) and 700-600°C (CdS). Influences of the growth parameters as well as the optimum conditions for each material have been discussed in detail in foregoing studies [23, 24, 66, 267–273], except for CdS nanowires, which have been investigated within this thesis (chapter 4.3). The as-grown nanowires typically have random orientation towards the substrate and grow on top of VS grown structures. For some experiments, the nanowires were transferred to clean substrates either by the imprint technique (details see [249]) or by transfer via solution: the nanowires are dispersed in isopropanol by applying an ultrasonic bath and distributed from the solution on clean substrates.

3.2 Modification of nanowires

Doping is crucial for the modification of the optical, electrical and magnetical properties of semiconductors. As doping of VLS grown nanowires during growth is inhomogeneous and nearly impossible for certain elements, ion implantation can overcome such limitations.
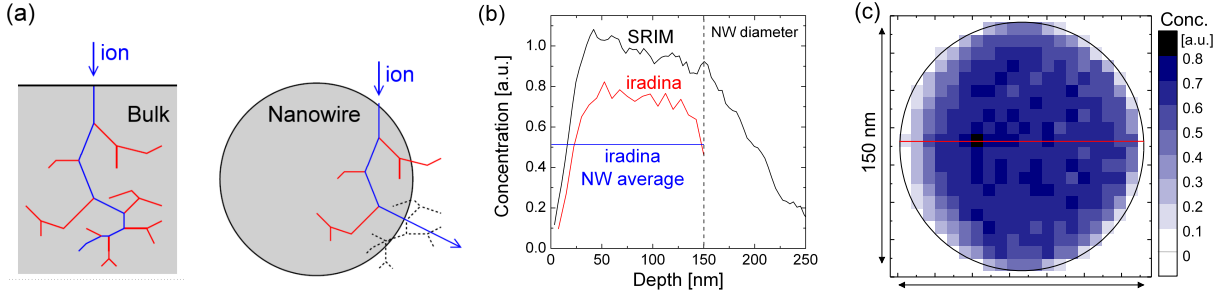
3.2.1 Simulation of ion implantation

Figure 3.1: *(a) The ion impinging on a target is decelerated by electronic and nuclear stopping and kicks out target atoms, creating a defect cascade. If the ion range is in the same order as the nanowire diameter, some ions can leave the nanowire target, which is not regarded in the bulk target. (Picture adapted from [274]). (b) The comparison of the ion implantation profiles calculated by SRIM and iradina using equal input parameter visualizes this effect. (c) iradina 2D map showing the homogeneous ion distribution for a 150 nm nanowire. The red line marks the line profile plotted in (b).*

As an energetic ion penetrates the target, its energy is reduced either by electronic stopping (excitation and ionization of electrons) or nuclear stopping (inelastic scattering with lattice atom nuclei). The latter can lead to the displacement of the atom from its lattice side and the creation of a vacancy. If the kinetic energy of knocked-out atom is still above the displacement energy, it can kick out further target atoms and a defect cascade is formed (figure 3.1 (a) top). These processes can be simulated using Monte Carlo codes like the *SRIM* (Stopping and Range of Ions in Matter) [86], which work well for ion implantation in bulk and layered targets. However, a bulk target geometry is not sufficient for an accurate simulation of the implantation processes in nanostructures [274]. If the ion range is in the same order as the nanowire diameter, some ions can leave the nanowire target (figure 3.1 (a) bottom), which is not regarded in the bulk target geometry.

The Monte Carlo code *iradina* (Ion Range and Damage in Nanostructures) was developed for this purpose [254], but was not available at the beginning of this thesis. The implantation profiles for the doping of nanowires were simulated using *SRIM* with bulk sample geometry and perpendicular ion incidence. The target material parameters are listed in the appendix in table B.1. The simulations were repeated later using *iradina* with equal parameters in order to judge the deviations due to the nanostructure. An example for Co implantation into ZnO nanowires is presented in figure 3.1. The used ion energies of the SRIM simulation were arranged to create a homogeneous concentration profile between 15 to 150 nm. The simulation data evaluated by iradina show also a homogeneous ion distribution within the nanowire (see figure 3.1 (b) and (c)), but the concentration in the line plot is only 60 to 80 % of the nominal SRIM value. Integration over the nanowire cross section delivers a more realistic concentration, which is in the order of 50 % of the nominal SRIM value. The explanation is given by the ions leaving the nanowire target, which is accounted in iradina [274], but not in SRIM. Therefore, the SRIM simulation overestimates the concentration. The deviation can be even larger for ion incidence angles smaller than 90°.

3.2.2 Ion beam doping

The ion beam doping of the nanowires was performed using the ion implanter ROMEO. The Cockcroft-Walton type accelerator (High Voltage Engineering Europe) allows implantation of nearly every element with ion energies from 10 to 380 keV and ion current up to tens of $\mu A/cm^2$. The desired element is introduced into the ion source either as gas or evaporated from the solid phase. The gas is ionized by a hot filament and the positive ions are extracted by a negative voltage and pre-accelerated with 10-30 keV. The ion beam is focused by electrostatic lenses and mass separated using a 90° bending magnet. The magnetic field applied perpendicular to the ion direction guides the charged ions on a curved path due to the Lorentz force. The strength of the magnetic field allows the selection of a certain mass/charge ration, which passes the separation slit behind the bending magnet. The isotope pure beam is further accelerated up to 350 keV, focused by ion optics and scanned across the sample in order to achieve lateral homogeneous implantations. The ion current on the sample is integrated in order to determine the ion fluency. All implantations were performed at high vacuum conditions ($< 5 \cdot 10^{-6}$ mbar).

The impact of an ion leads to the creation of up to 1000 defects (interstitial-vacancy pairs). Although a large number already annihilate at room temperature for certain materials, a significant amount is still left after the implantation which dominate the optical and electrical properties of the semiconducting nanowires. A reduction of the ion induced damage can be achieved by thermal treatment (annealing) enabling the recrystallization of the lattice and activation of the introduced dopants.

Post-implantation annealing at temperatures between 500 - 900°C in air (ZnO nanowires) and up to 600°C in high vacuum (ZnS nanowires) resulted in a sufficient reduction of the defect related emissions and optical activation of the dopants. As an alternative approach, high temperature implantations were performed. The higher mobility of the displaced atoms and therefore a higher annihilation rate of vacancies and interstitials leading to an increased in-situ recovery of the crystal lattice. Such an enhanced dynamic annealing was observed for nanostructures, as e.g. amorphization could be completely suppressed for Mn implanted GaAs nanowires by implantation at elevated temperatures [68, 274]. In this work, implantation of ZnO (ZnS) nanowires was performed up to 700°C (600°C).

3.3 Characterisation methods

3.3.1 Structural characterisation

Scanning electron microscopy (SEM)   As the diameter of nanowires is typically below the Abbe resolution limit of light microscopes, electron microscopy is used for structural characterisation as the shorter DeBroglie wavelength of the electrons provide the needed resolution in the nm range. Using scanning electron microscopy, an energetic electron beam is focused to a few nanometers and scanned across the sample. Imaging is performed by the correlation of the signal intensity of the sample response with the location of the electron beam. In this matter, different types of information can be obtained as e.g. the signal of secondary electrons reproduces well the morphology and while the backscattered electrons include additionally a mass contrast. The resolution is not only determined by the focus of the electron beam, but also strongly depends on the interaction volume of the electrons with the sample. Detailed information about this technique are given in [275, 276].

In this work, a JEOL JSM-6490 SEM equipped with a LaB_6 thermal electron gun was used for structural characterisation. The acceleration voltage could be altered between 1 to 30 keV and the system provides a resolution down to 10 nm. High resolution images were obtained using

the field emission column of a dual beam focused ion beam (FIB) system (FEI Helios NanoLAB 600i) with a resolution of 1 nm.

Transmission electron microscopy (TEM) Sub-nm imaging was performed using transmission electron microscopy. In contrast to SEM, the image is not formed by scanning across the sample, but a parallel high energetic electron beam (typically 300 keV) illuminates the sample. Several methods are available to generate an image: in bright field mode (BF), the parallel beam is imaged through the sample onto a screen or CCD camera. The contrast is generated by absorption of electrons in the sample ("mass-thickness contrast"). In dark field mode (DF), only electrons diffracted in a certain direction are used to generate an image. The structures diffracting the electrons in this certain direction appear bright ("diffraction contrast"). Increasing the magnification, single atom columns become visible in the high resolution mode (HR-TEM). The image is generated by the interference of the transmitted (undiffracted, forward scattered) electron reference wave and the diffracted wave. Therefore, information about crystal phases and lattice parameters can be obtained from fast Fourier transformation (FFT). To accentuate certain crystal directions, only certain reflexes can be selected and re-transformed (iFFT). Imaging of the electron diffraction pattern (DP) provides information about the crystalinity and sample structure. In selected area electron diffraction (SAED), the area for the generation of the diffraction pattern can be confined using an aperture. If a scanning unit is available, the focused beam can be positioned on a certain location or scanned across the sample (STEM). This is useful for the spacial high resolved investigation of the sample the combination with other methods. A good overview and more details on TEM imaging is presented in [277–280].

TEM investigations were performed at the Institute for Material Science Jena (IMT) using a JEOL JEM 3010 with a thermal LaB_6 electron gun at 300 keV offering a point resolution of 0.21 nm (lattice resolution 0.14 nm). The preparation for nanowires is fairly easy as they can be transferred to TEM specimen (copper grid with carbon foil) by imprint. In addition, nanowires are electron transparent up to a thickness of typically 100 nm.

Energy dispersive X-ray analysis (EDX) As high energetic electrons penetrate the sample, target atoms can be ionized. Bound electrons of upper shells fill the vacancy and the energy is dissipated as X-ray photon whose energy is characteristic for each element and transition. Analysis of the X-ray energy and intensity provides information about the elements and their stoichiometric composition (energy dispersive X-ray spectroscopy).

Both the JEOL SEM as well as the JEOL TEM are equipped with a nitrogen cooled Si(Li)EDX detector (typical energy resolution of 150 eV at 5.9 keV). The detection limit for elements heavier than carbon are typically in the order of 1 at.%. Point analysis at a selected location, along a direction (line scan) or mapping can be performed by monitoring the intensity of the element specific X-ray intensity as a function of the excitation position.

X-ray fluorescence (XRF) X-ray fluorescence is similar to EDX, but instead of energetic electrons, X-rays are used for the excitation of the sample. The advantage of this method is that nearly no disturbing background signal is present in contrast to excitation by high energetic electrons, which emit bremsstrahlung upon de-acceleration. The detection limit is therefore enhanced to ~ 0.1 at.% compared to EDX.

The investigations of single nanowires were performed in close collaboration with the group of Dr. Gema Matrinez-Criado at the European Synchrotron Radiation Facility (ESRF, Grenoble) at the beam line ID22NI. High lateral resolution was achieved by focusing the X-ray beam using a pair of Kirkpatrick-Baez multilayer coated Si mirrors down to a spot size of 50 x 50 nm^2. The

monochromated X-ray beam (using a Si(311) monochromator) with an energy between 3 - 27 keV excite the sample with a flux up to 10^{11} photons/s in the focal spot (at 17 keV, $\Delta E/E \approx 10^{-2}$). The intensity of the incident beam was monitored using a gas-filled ionization chamber. The emitted X-ray fluorescence was detected at 15° in respect to the sample surface by an energy dispersive silicon drift detector. The XRF spectra were analysed using the non-linear least-squared fit routine PyMca [281]. XRF maps were obtained at an excitation energy of 12 keV and a pixel size of 25 x 25 nm^2 with integration times of 500 ms per point. The information depth, determined by the penetration depth of the incident X-rays, the energy of the resulting fluorescence X-rays and the absorption of the sample, is 8.0 µm and 4.3 µm for the Zn and Co fluorescence photons at the used excitation energy [282], so the the contribution of the complete nanowire is detected. Detailed information about the beam line, instrumentation and technical parameters are given in [283–286].

X-ray absorption spectroscopy (XAS)   X-ray absorption spectroscopy (XAS) is performed by analysing the intensity of an emitted fluorescence X-ray energy (and therefore the X-ray absorption) as function of the excitation X-ray energy in high resolution (typically 1-5 eV). Two techniques are available for different purposes: X-ray absorption near edge spectroscopy (XANES) investigates the shape and structure of the absorption edge to gain information about chemical composition, charge states, lattice sites, crystal structure and quality. Extended X-ray absorption fine structure spectroscopy (EXAFS) investigates the energy range above the absorption edge. The XRF signal is modulated by the inference of the emitted X-ray photon waves and reflections at neighbouring atoms. Therefore, the local environment (first and second nearest neighbours) can be probed to obtain information about the direct surrounding of the probe atoms like interatomic distances and structural order. Details on the methods are given in [287, 288].
The high spacial resolution of the ID22NI beam line at the ESRF allowed XANES and EXAFS measurements at several different positions on one single nanowire using the equipment mentioned in the previous paragraph. XANES and EXAFS spectra were acquired in XRF mode with a excitation energy step size of 1 eV and integration times determined by the counting statistics. Data analysis was performed with the IFEFFIT package [289].

3.3.2 Optical characterisation

Luminescence is the spontaneous emission of radiation after an external non-thermal excitation [290]. Depending on the excitation source, it is further specified as photoluminescence (excitation by photons), cathodoluminescence (energetic electrons), chemiluminescence (chemical reactions) and so on. After excitation, the generated carriers can recombine and emit photons whose energy is related to the energy of electron and hole (and therefore the band edge E_g) or the energy levels of impurities or defects. Luminescence spectroscopy investigates these radiative recombinations in order to obtain information about exciton and acceptor/donor energies, impurities, defect states and recombination dynamics and can judge the material quality. The emissions of optical active impurities allow insights into donor-acceptor recombination dynamics as well as the properties of electronic intra-shell transitions.

Cathodoluminescence spectroscopy (CL)   Cathodoluminescence spectroscopy uses an electron beam to excite the sample by ionization or elastic and inelastic scattering, which is rather strong as one electron typically generates $E/3E_g$ electron-hole pairs [291, 292]. The emitted luminescence light is collected by a parabolic mirror and guided towards the detection system.

Figure 3.2: *Scheme of the CL system: The focused electron beam is used to excite the sample, the luminescence light is collected by a parabolic mirror and guided to the detection system. In panchromatic CL mode, the luminescence intensity is detected by the photomultiplier as a function of the excitation position. In monochromatic CL mode, the luminescence light is spectrally dispersed in the monochromator and detected by the photomultiplier (PMT) or CCD. Sample cooling using the cryostage is available down to 6 K.*
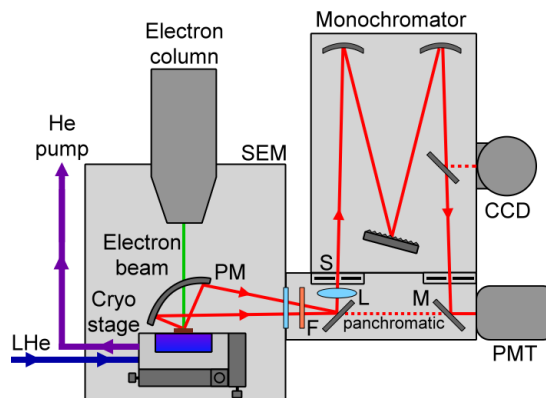
CL in combination with SEM is very valuable for the investigation of semiconductor nanostructures. The penetration depth and interaction volume of the electron beam can be adjusted to the dimensions of the nanostructures by lowering the acceleration voltage to 1 - 10 keV and allows depth resolved analysis of bulk samples. The electron-sample interaction can be simulated using the Monte Carlo code *CASINO* [293–296]. The latest version (v3.2) even takes 3D geometries into account [297]. The combination of optical with morphological and stoichiometric information (evaluated by the secondary electrons or EDX) is useful for the spacial resolved detection of e.g. impurity distributions. As a disadvantage, the light detection is global, this means that the exact position of the emission cannot be identified. A general review about cathodoluminescence, techniques and applications is provided by [291, 298]. An good overview of the possibilities for the investigation of nanostructures and related effects is given in [299, 300].

Cathodoluminescence measurements were performed with the JEOL SEM equipped with a GATAN MonoCL3+ system. Figure 3.2 shows the scheme of the system, which has be setup and established within the frame of this thesis. The sample is excited by the focused electron beam, the emitted light is collected by a parabolic Al mirror (PM) and guided to the detection system. A long pass filter (F) can be inserted to block unwanted emissions. Two detection modes are available: (1) The luminescence light is guided directly on the photomultiplier (PMT) detector in *pancromatic mode*. Therefore, the total light intensity is detected as a function of the electron beam position. (2) The light is guided by mirrors (M) and focused by a lens (L) onto the entrance slit (S) of the 300 mm monochromator for spectral resolved investigations in *monochromatic mode*. A 1200 l/mm (VIS) is installed as standard, a second grating can be exchanged according to the specific application. The spectrally dispersed light is focused onto the exit slit and guided to the photomultiplier detectors. A PMT with high sensitivity in the VIS range (Hamamatsu R943) and wide range IR PMT (Hamamatsu 5509) are available. For fast spectral acquisition, an additional mirror is inserted in the monochromator, which guides the light onto a CCD camera (Princeton Instruments Spec-10). This allows several acquisition modes: besides spectra recording by parallel (CCD) or serial (PMT) detection, monochromatic luminescence maps and hyperspectral images (complete spectrum at each point) can be recorded. A cryostage can be mounted in the SEM chamber, which allows sample temperatures between 6 K to 300 K at liquid He operation and 78 K to 300 K using cooled dry nitrogen. A quick load system allows the exchange of samples at low temperatures within typically 15 minutes. Power dependent measurements can be performed by variation of the electron beam current within $\sim$ 10 pA to more than 100 nA.

Photoluminescence spectroscopy (PL)   Photoluminescence is a complementary technique to CL, as it uses mono-energetic photons (usually provided by a laser) instead of the multi-energetic excitation by hot electrons. This brings the advantage of a more specific excitation
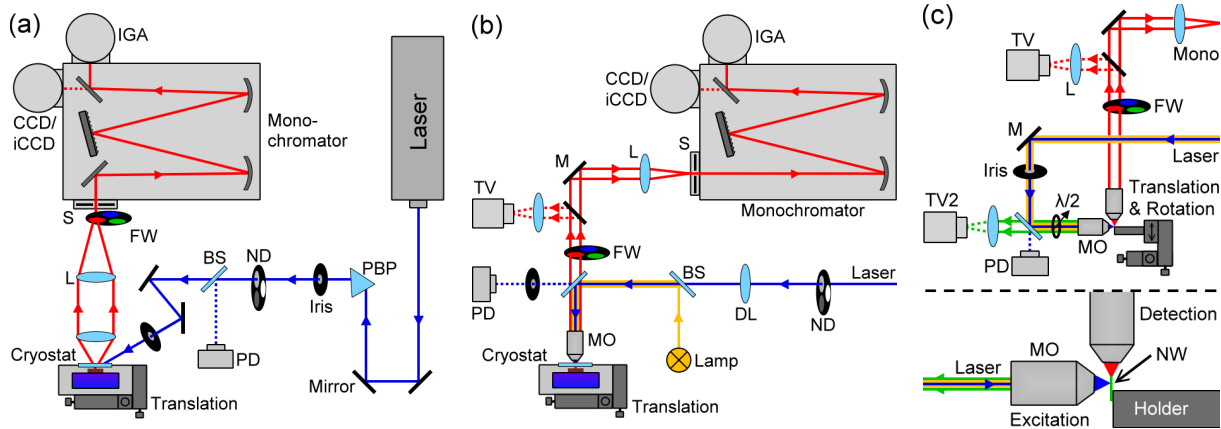
Figure 3.3: *(a) Scheme of the macro PL setup: The excitation laser (cw or pulsed) is guided by mirrors (M) through a pellin-broca prism (PBP) to separate the excitation wavelength from other harmonics. The laser intensity can be adjusted by neutral density filters (ND) and a part of the laser beam is guided by a beam splitter (BS) to a power diode (PD) for on-line monitoring. The luminescence from the sample mounted in a cryostat is collected by lenses (L) and focused onto the monochromator entrance. The laser and higher order diffractions are suppressed by a long pass filter wheel (FW). The dispersed luminescence is detected either by a CCD(iCCD) or an InGaAs array (IGA). (b) Scheme of the μPL setup used for the investigation of single nanowires: The laser beam is guided by a beam splitter and focused by a microscope objective (MO) onto the sample. The luminescence light is collected in backscatter geometry, passes the beam splitter and the filter wheel and is detected either by a TV camera (TV) for imaging or the detectors attached to the monochromator for spectral acquisition. White light can be coupled to the beam path for bright field illumination. (c) The modified "Head-On" μPL setup enables the detection of the direct nanowire (NW) emission by the decoupling of excitation and emission. A λ/2 wave plate is used to adjust the polarization of the excitation laser beam.*

conditions by the choice of the excitation energy. In low excitation conditions, the absorption of a photon creates only one electron hole pair and the heat generation is less compared to electron excitation, where most of the energy dissipates as phonons. Micro-photoluminescence (μPL) uses a focused laser beam for a localized excitation and provides high excitation powers. In contrast to CL, the detection of the emitted light by confocal techniques is local and excitation and detection path can be separated, but the spacial resolution is worse compared to CL. In the scope of this thesis, a (micro-)photoluminescence setup was developed, installed and established. The setup sketched in figure 3.3 was designed to investigate single wide band gap semiconductor nanowires with a spacial resolution of 1 μm in the temperature range of 4 - 300 K at excitation powers of mW to MW/cm^2. A macro PL setup provides fast characterization of as-grown nanowires as well as thin film semiconductors used in photovoltaics.

Macro PL setup Figure 3.3 (a) shows the detailed scheme of the macro PL setup. Excitation is provided by a cw laser (Kimmon HeCd, 325 nm, 33 mW and Polytec HeNe, 633 nm, 5 mW) or nanosecond pulsed laser (Innolas Spitlight Nd:YAG, 266 - 1064 nm, up to 5 mJ at 200 Hz, 10 ns pulses). The laser beams are guided by dielectric high performance mirrors and separated by a Pelin-Broca Prism (PBP) from higher harmonics and unwanted wavelength. The intensity of the laser beam can be adjusted by neutral density filters (ND) by 8 orders of magnitude. A beam splitter (BS) can be inserted for on-line monitoring of the laser power using a Si photo diode (PD). The laser beam illuminates the sample mounted in a liquid He flow cryostat (Janis ST-500) offering sample temperatures from 4 K to 475 K. The luminescence emission is collected by lenses (L) and focused onto the side entrance slit (S) of a 500 mm monochromator (Princeton Instruments SP-2500i). The laser beam and higher order diffractions can be suppressed by long pass filters in the filter wheel (FW). The luminescence light is dispersed at one of the three gratings installed at an interchangeable turret in the monochromator, providing resolution down

to 0.05 nm. The dispersed light is detected by a LN2 cooled front-illuminated CCD (Princeton Instruments Spec-10, 200 - 1100 nm) in the UV-VIS range or a LN2 cooled InGaAs photodiode array (IGA, Princeton Instruments OMA V, 800 - 1700 nm) in the IR, providing a detection range from 200 - 1700 nm. The CCD can be exchanged to a Peltier cooled intensified CCD (iCCD, Princeton Instruments PI-MAX 3), providing temporal resolution down to ns in the range of 200 - 900 nm. Technical details on the lasers, gratings and detectors are summarized in the appendix (chapter A.3).

µPL setup A self-built epifluorescence microscope was realised for the investigation of the emission properties of single nanowires. The scheme of the micro-photoluminescence setup is displayed in figure 3.3 (b). Flipping away a mirror of the macro setup, the laser beam is guided to a beam splitter and focused by a microscope objective (MO) to a spot of a few µm diameter. The laser beam transmitted through the beam splitter can be used for on-line power monitoring using the Si photo diode (PD). For lasing experiments, a defocussing lens (DL) can be inserted into the beam path which enlarges the laser spot to ~ 30 µm diameter. A white light lamp can be coupled into the beam path by a beam splitter for bright field illumination of the sample. The luminescence light of the sample mounted in the cryostat is collected in backscatter geometry by the same microscope objective and passes the beam splitter in straight direction. The backscattered laser is blocked by long pass filters in a filter wheel (FW). The image of luminescence emission is detected on a TV camera. For spectral resolved detection, a mirror is flipped away and the luminescence light is focused by a lens (L) on the front entrance slit (S) of the monochromator described above. Additional technical information on the available microscope objectives and the optical resolution of the system are available in the appendix (chapter A.3.5).

For investigations of the direct power output and the on-axis far field emission of a nanowire, excitation and detection have to be decoupled. A modified "Head-On" µPL setup was realized for this purpose, which is shown in figure 3.3 (c). The excitation laser beam is guided by a mirror (M) and a beam splitter (BS) to the excitation microscope objective. The position of the focused laser spot on the sample can be adjusted by tilting the laser beam with the beam splitter and re-positioning of objective by a 3-axis stage. The white light source coupled into the excitation path provides bright-field illumination of the sample. The image of the sample and the laser spot is recorded by a TV camera (TV2). The detection microscope objective is matched with the focal spot of objective A and collects the on-axis emission of a nanowire. The sample is adjusted by a 3-axis stage in combination with a rotary stage. A $\lambda/2$ wave plate in front of the excitation objective is used to rotate the polarization axis of the laser beam.

Time resolved photoluminescence spectroscopy (TRPL) Time resolved photoluminescence measurements (TRPL) were performed in collaboration with Uwe Kaiser and the group of Prof. Dr. Wolfram Heimbrodt at the Philipps University in Marburg [88] (figure 3.4 (a)): the fundamental wavelength (1064 nm) of a pulsed Nd:YAG laser (Quantel Brilliant, repetition 10 Hz, pulse width FWHM 3.5 nm, pulse energy up to 50 mJ) was frequency tripled (355 nm) for excitation. The intensity of the laser can be varied by several orders of magnitude by insertion of attenuating glass plates into the beam. The laser beam was dispersed by a UV fused silica prism and the desired wavelength passes an iris aperture and was guided by mirrors onto the sample mounted in a LHe bath cryostat (Oxford Optistat) at temperatures between 10 - 300 K. The luminescence light was collected by a pair of convex lenses, focused on the 250 mm monochromator (Oriel MS257), dispersed either by a 300 l/mm (blaze 500 nm) or 600 l/mm (blaze 400 nm) grating and detected by an intensified CCD camera (iCCD, Andor iStar). The iCCD was synchronized with the laser allowing luminescence detection from a few nanoseconds
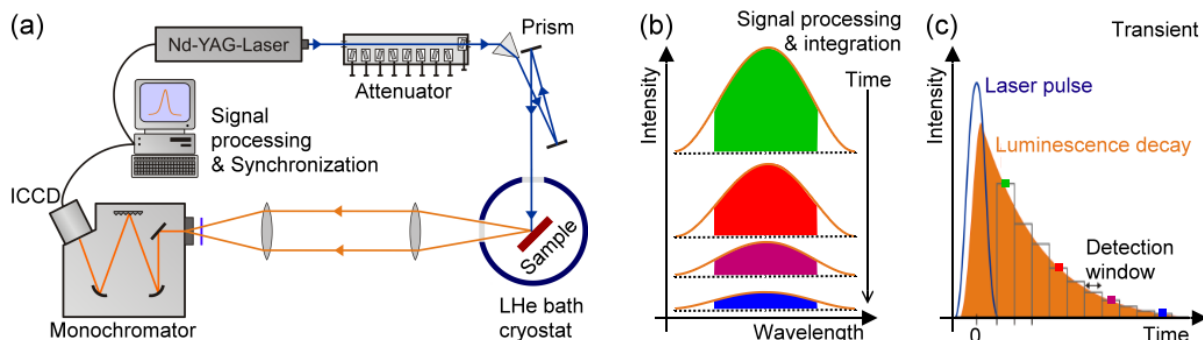
Figure 3.4: *(a) Scheme of the TRPL setup: a pulsed Nd:YAG laser excites the sample in a cryostat, the luminesence light is collected and detected by a iCCD camera synchronized to the laser. (b) The spectra at different times are processed by background removal and signal integration. (c) The integrated signal is plotted at the center of the detection window as a function of the time delay and to obtain the transient. Pictures adapted from the University of Marburg.*

up to 100 ms. The minimum integration time was 5 ns. The detected PL signal was processed by removal from noise and the background of superimposed emission bands. The intensity was normalized by the detection time window (figure 3.4 (b)). The integrated PL signal is plotted at the center of the detection window as a function of the delay to the laser pulse in order to obtain the transient, which represents the decay of the luminescence after the excitation pulse.

Photoluminescence excitation spectroscopy (PLE) For photoluminescence excitation measurements (PLE), the luminescence intensity at a fixed wavelength is detected as a function of the excitation wavelength. This allows the determination of excitation pathways and the excited states of optical active ions. PLE measurements were also performed in collaboration at the University Marburg. The scheme of the PLE system is shown in 3.5. The light of either a 450 W Xenon high pressure lamp or a 300 W halogen lamp was focused onto a 320 mm excitation monochromator (Jobin-Yvon Triax 320). The monochromated light was focused using a pair of UVFS lenses onto the sample mounted in a optical helium flow cryostat (T = 10 - 300 K). The luminescence light was collected at 90° to the excitation path and focused onto the detection monochromator (Zeiss 311507). A longpass filter in front of the monochromator suppressed the excitation light. The detection was performed using a high sensitivity photomultiplier (Hamamatsu R943) in combination with chopper wheel and lock-in amplifier (Stanford research SR830), as this reduces the disturbing influences at low light levels. The system is controlled by a self-assembled LabView programm.
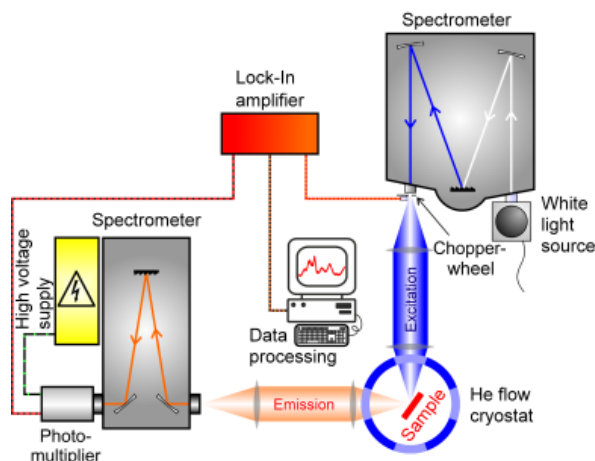

Figure 3.5: *Scheme of the PLE setup at the University of Marburg: The light of a Xe or Halogen lamp is monochromated by the excitation spectrometer and focused onto the sample in the cryostat. The emitted light is focused on the monochromator and detected by a photomultiplier. For better signal-to-noise ratio, lock-in technique is used. Picture adapted from the University of Marburg.*

4 Lasing in undoped ZnO and CdS nanowires

This chapter displays the structural and the optical properties of ZnO and CdS nanowires at low and high excitation conditions. ZnO nanowires were synthesized in collaboration with Martin Gnauck and Andreas Thielmann. The details have been published in [23] and the respective diploma theses [268, 271, 301, 302]. The synthesis of CdS nanowires was performed in collaboration with Michael Kozlik, Amanda McDonnell, Julian Kühnel and Andreas Thielmann (see the diploma theses [270, 272, 302, 303]). The structural as well as optical characterization are presented in this chapter. The lasing properties of single CdS nanowires were investigated in close collaboration with Andreas Thielmann and Robert Röder (see diploma theses [302, 304]). Parts of this work are published in [305].

4.1 Motivation

Miniaturized light sources are the key point for the development of smaller and more efficient optoelectronic devices with enhanced properties and functions [306]. Semiconductor nanowires are promising candidates as they combine all necessary functions of the active part with the connecting element: light emission by electrical (or optical) excitation, excellent waveguide properties and light amplification by stimulated emission and lasing.

ZnO as a direct wide band gap semiconductor [98] exhibits a high exciton binding energy [113], which allows intense excitonic light emission in the near UV at room temperature [152]. The synthesis of ZnO nanowires is fairly easy [30] and offers accurate control for the nanowire dimensions [307], which dragged a lot of interest on the investigation of their optical properties as LED and photonic waveguide [19, 20, 36, 44, 308, 309]. Evidence for amplified stimulated emission under optical excitation was reported by many groups [170, 173–175] and the transition to laser oscillations in single ZnO nanowires could be observed [51], but a drawback for the integration into future devices are the high lasing threshold of ~ 300 kW/cm^2 [21] and the lack of stable and reproducible p-doping for ZnO [97, 128]. This might be solved by the incorporation of optical active 3d- and 4f- ions into the ZnO nanowire cavity, which promises lower thresholds and enhanced properties like multi-wavelength emission depending on the choice of the dopant. ZnO nanowires are ideal suited for the modification by ion implantation doping due to the high radiation hardness of ZnO [310]. In order to judge the modifications introduced by the ion implantation process and the dopants, the properties of the untreated ZnO nanowires have been investigated first and are described in this chapter.

CdS nanowires are also promising for optoelectronic applications in the VIS range, as light emission at electrical excitation [311], efficient waveguiding [166] and stimulated emission [57–59] have been observed as well as evidence for lasing at low temperatures [171]. A hybrid photonic plasmonic nanowire laser with extreme light confinement could be realized by coupling of CdS nanowires to a plasmonic substrate [49], but the high optical losses of the plasmonic structure only allows light amplification at very high pumping powers in the order of some MW/cm^2. A future integration of CdS nanowires into devices needs the investigation of two key points: conditions for a controllable and reliable synthesis of high quality nanowires and the systematic study of their emission properties related to the nanowire dimensions. Although a lot of afford was already spent on CdS nanowire synthesis since several years ([312] and references therein), a comprehensive diagram of the VLS synthesis parameter has only been reported recently [305]. In addition, most previous experiments on the light amplification properties have been carried out on nanowire ensembles [57–59], so that the properties of the individual nanowire is lost in
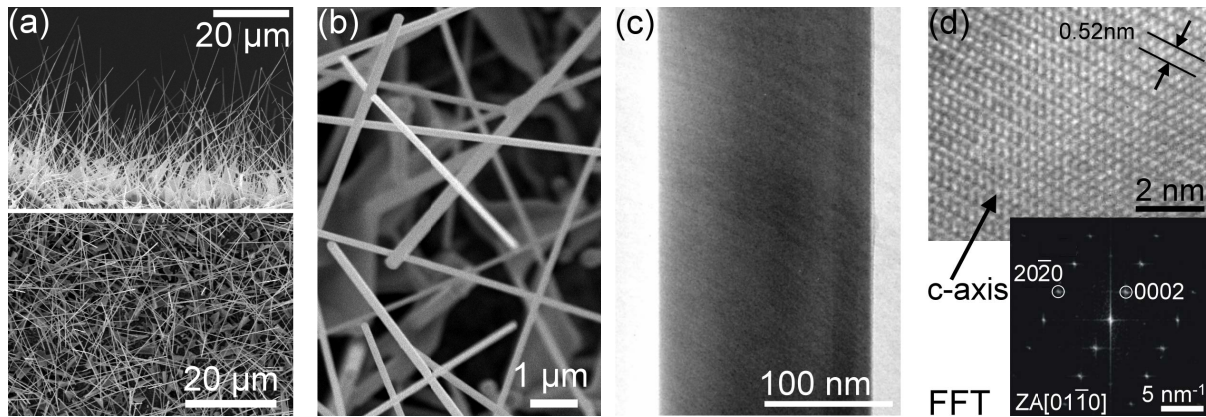
Figure 4.1: *(a) SEM images of a typical as-grown ZnO nanowire ensemble at side and top view show the homogeneous coverage with nanowires up to 50 µm length above underlying ZnO structures. (b) Nanowire diameters between 100-500 nm are estimated from the high magnification SEM image. (c) The survey TEM image shows the straight nanowire surface without imperfections. (d) The HR-TEM image reveals the high quality of the wurtzite ZnO crystal structure. The FFT image shown below indicates growth along the [0002] direction. (TEM data from [268].)*

the superposition of the ensemble. A clear proof for lasing oscillations in individual CdS nanowires as well as its relation to the morphology, as it is available for ZnO nanowires [21, 51], has not been reported yet. These two key points are addressed in this thesis: the nanowire growth parameter were systematically varied to achieve a reproducible routine for the synthesis of high quality CdS nanowires (see chapter B.1), whose individual optical properties were studied with respect to their morphology and compared to the properties of ZnO nanowires in this chapter.

4.2 ZnO nanowires

4.2.1 Morphology of ZnO nanowires

ZnO nanowires were synthesized using a CVD process in a horizontal tube furnace at high growth temperatures between 1100 and 950°C [23, 268]. Figure 4.1 (a) shows the as-grown substrates, which are homogeneously covered with long and straight nanowires growing above sail-like formed ZnO nanostructures. The nanowires grown with random orientation at angles between 15° and 75° towards the substrate surface exhibit diameters in the range of 100 to 500 nm (figure 4.1 (b)). The length of the as-grown nanowires is up to 50 µm, thus having a high aspect ratio up to 500 [271].

The survey TEM image in figure 4.1 (c) presents the very smooth and nearly defect free surface of the as-grown ZnO nanowires. The homogeneous contrast suggests a structure without extended defects. The high resolution TEM image (figure 4.1 (d)) shows the high quality lattice structure. No evidence of stacking faults, dislocations or other defects could be observed within the single crystalline nanowires [301]. In the fast-fourier transformed (FFT) image below in figure 4.1 (d), sharp and equidistant reflexes are observed at 3.99 nm^{-1} and 7.24 nm^{-1} in respect to the central spot, which matches well the spacing of the (0002) and (20$\bar{2}$0) planes of the wurtzite ZnO crystal phase. The according zone axis is [01$\bar{1}$0]. The plane spacing of 0.52 nm in the HR-TEM image is in good agreement with the literature value for the spacing of the ZnO c-planes [99]. The growth of the ZnO nanowires is along the [0001] direction (c-axis) [268], which is typically observed for ZnO nanowires [307, 313, 314]. The side surface could be assigned to the {10$\bar{1}$0} planes [301] also in agreement with literature [30, 315]. A remaining catalyst dot was observed at the tip of some ZnO nanowires after growth. EDX analysis in the TEM (not shown) could confirm the stoichiometry of the catalyst dot to pure Au without any traces of other impurities; whereas, the
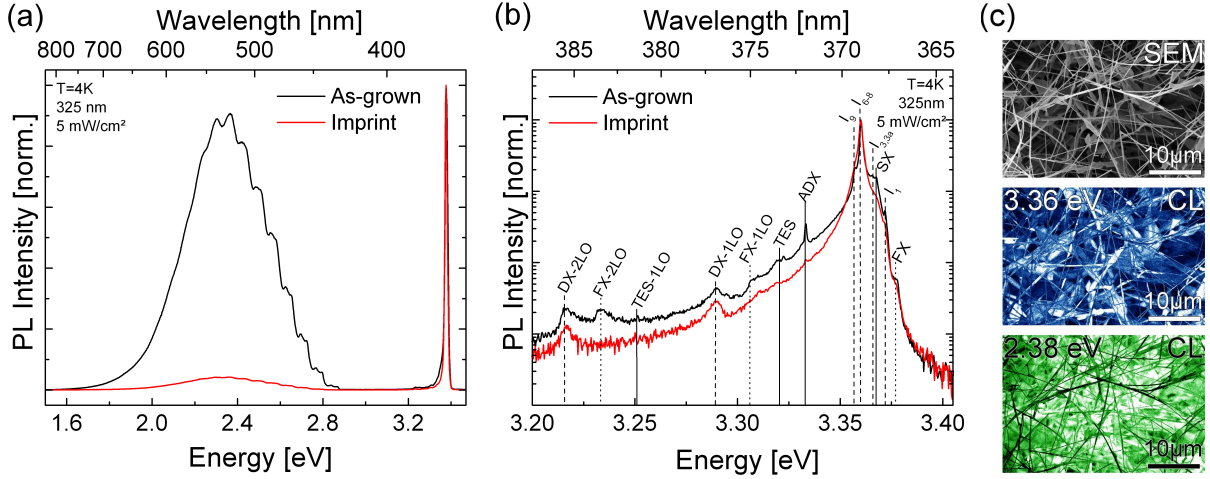
Figure 4.2: *(a) Photoluminescence spectra of an as-grown ZnO nanowire ensemble compared to nanowires imprinted to a clean Si substrate. (b) High resolution photoluminescence spectra of the near band edge emission show the presence of free and bound exciton recombinations. (c) Monochromatic CL images reveal that the defect emission mainly originates from the ZnO structures below the nanowires.*

nanowire body consists of ZnO in stoichiometric ratio. These findings confirm the growth of the ZnO nanowires by the VLS mechanism [23].

4.2.2 Luminescence at low temperatures

Photoluminescence spectroscopy at low temperatures under low power cw excitation was used to study the optical properties of a typical as-grown ZnO nanowire ensembles, which includes the ZnO nanowires and underlying nanostructures (see e.g. figure 4.1 (a) and (b)) as well as an imprint ensemble of the respective sample, which consists of bare nanowires transferred to a clean Si substrate [249]. Figure 4.2 (a) presents the survey luminescence spectra, which have been normalized to equal intensity. A sharp peak centered at 3.36 eV appears in the UV, which is attributed to the near band edge emission (NBE). A broad structured band centered at 2.38 eV is observed in the VIS region, which is related to the deep level emission (DLE).

The high resolution spectra of the NBE (figure 4.2 (b)) are dominated by a sharp emission peak at 3.360 eV (labelled I_{6-8}), which is attributed to several emission lines of neutral donor bound excitons (D^0X) [102, 316] and can not be resolved due to the limited resolution of the spectrometer. The emissions of free excitons are observed at 3.377 eV as a shoulder at the high energy side of the DX emissions [99], which has a slightly lower intensity for the imprint ensemble sample. The $I_{6,6a}$ emission line at 3.361 eV is related to aluminium acting as a shallow donor [102], which probably originates from the Al_2O_3 boats and tubes in the synthesis furnace. The I_8 emission line at 3.359 eV is typically attributed to Ga as donor impurity, which is a possible contamination of the ZnO source powder used for synthesis. The emission at 3.367 eV (labelled I_1) is related to the I_8 line [317] and is interpreted as the recombination of an exciton bound to an ionized Ga donor (D^+X). Slight intensity deviations between the as-grown and imprint ensemble are observed at 3.366 eV, which is typically attributed to interstitial zinc acting as intrinsic donor ($I_{3,3a}$ at 3.3660 eV) [136, 318, 319]. The interstitial zinc probably results from the slightly oxygen deficient growth conditions using pure ZnO powder without additional oxygen gas [268]. The $I_{3,3a}$ emission is superimposed to a emission band centered at 3.3670 eV, which is only observed for nanostructured ZnO and assigned to surface bound excitons (SX) [320, 321]. The SX intensity increases in intensity with decreasing nanowire diameter [177], it is therefore unlikely that the increased SX emission of the as-grown ensemble originates from the larger structures below the nanowires (compare figure 4.1 (b)). A higher concentration of interstitial zinc in the as-grown

ensemble is a more reasonable explanation.

Another peak is observed on the low energy side of the DX emission at 3.357 eV (labelled I_9), which is related to a further extrinsic impurity and could be assigned to In as donor [322], a typical contamination of the used ZnO powder [323]. The sharp line at 3.333 eV is related to excitons bound to structural defects (ADX) [102]. The higher intensity of the as-grown sample is a hint for a higher defect concentration of the structures below the nanowires, as this line is only weak for the bare nanowires in the imprint. A shoulder at 3.320 eV is commonly explained as a two-electron-satellite (TES) [102, 324], which occurs when the neutral donor is excited from the 1s ground state to a higher state (like 2s, 2p, etc.) after recombination of the bound exciton [54]. Several additional peaks appear on the low energy side. The spacing of 72 meV allows the assignment to the longitudinal optical phonon replica (LO) of the free and donor bound excitons, respectively [99].

The DX emission shows a strong intensity decrease with increasing sample temperature and is totally quenched at 90 - 110 K [325]. The localization energy of excitons at the donors equals the thermal energy at these temperatures, so that all bound excitons dissociate and ionized donors remain at temperatures above [102]. The free exciton and its phonon replica is enhanced and dominates the emission at room temperature [24] (compare spectra in figure 4.3 (a)). It shows a red-shift due to the temperature dependence of the band gap, which can be described by the Varshni formula [326].

Several defect related ZnO emission bands have been observed between 1.5 to 2.9 eV [132, 133, 327], but the origin of defect emissions is still controversial discussed in literature (see e.g. [97, 128, 327]). Several models have been suggested to explain the defect related emission involving Cu_{Zn} as extrinsic defect [138, 139, 328], intrinsic defects like interstitials and vacancies [132, 329–334] and more complex defects [335–337]. The basic ideas of the suggested models and their drawbacks are discussed in [301]. The broad emission band centered at 2.4 eV (FWHM 470 meV) with a periodic fine structure on the high energy side ("green defect band") is typical for as-grown ZnO nanowires and clearly visible in figure 4.1 (a). The emission properties and its temperature behaviour can be described by a configuration coordinate model [338] involving a transition from the conduction band or a donor to a deep level [336]. The deep center exhibits local vibrational states, which are characterized by a local phonon energy [339, 340]. The shape and width of the emission can be explained by a series of donor - deep center transitions. The fine structure at low temperature can be understood by the assumption, that the transition originates from two shallow donors with an energetic spacing of 30 meV to the same deep center [337], which is accompanied by generation of longitudinal optical phonons [336]. The fine structure is present only at low temperatures and vanishes above 100 K [268]. To explain the temperature behaviour, it is assumed that the transition mainly originates from the donor states at low temperatures. Around 100 K, the donors are ionized (as observed for the donor bound excitons) [325] and the fraction of band to deep level transitions increase and are finally the main emission channel at temperatures above.

Several assumptions have been made for the nature of the involved defects. Intrinsic defects like vacancies (V_{Zn} and V_O), interstitials (Zn_i and O_i) and antiside defects (O_{Zn} and Zn_O) are more likely than extrinsic defects, as the first are usually generated either during growth or in huge amounts due to the ion implantation process. Oxygen vacancies V_O are often suggested as origin for the green defect emission [329–332]. Annealing in an oxidizing atmosphere (air / O_2) should therefore reduce the V_O concentration in the nanowires and lower the defect emission, but the opposite was observed and a higher defect emission is present for annealed ZnO nanowires, especially after ion implantation and subsequent annealing. In addition, oxygen vacancies as well as interstitial oxygen in tetrahedral sites ($O_{i,th}$) and zinc on oxygen sites (Zn_O) [136, 318, 341]

introduce deep donor states into the band gap [341, 342], so that the participation of these species cannot describe the emission behaviour for ZnO nanowires for the assumed model [301].

A reasonable assumption for the involved shallow donor state is zinc on tetrahedral and octahedral interstitial sites [136, 318]. The donor bound exciton emission line $I_{3,3a}$ is related to Zn_i [102, 319] and shows as strong emission intensity decrease around 100 K as the donors are ionized; therefore, this can also explain the temperature behaviour of the fine structure. In addition, the binding energy of the shallow donor levels are 31 and 61 meV [318, 343], which fits well to the nature of the observed fine structure at low temperatures.

Several defects like zinc vacancies (V_{Zn}), interstitial oxygen on octahedral sites ($O_{i,oc}$) and oxygen on zinc sites (O_{Zn}) are assumed as deep acceptors [136, 318, 334, 344, 345] and are therefore possible assignments for the involved deep centers [61]. The participation of V_{Zn} is unlikely, as their concentration is usually low due to the high concentration of Zn_i [334]. Additional to this, the implanted TM and RE ions usually occupy Zn lattice cites [346, 347], so that no significant amount of V_{Zn} is generated by the implantation. But the energy levels of the remaining two species are suitable [136, 318, 345] to assume these to be the deep centers [61, 335].

For oxygen rich ZnO nanowire or thin film growth conditions, an additional defect band centered at 1.9 eV is observed [302, 348, 349]. This "red defect band" also appears after ion implantation and annealing in an oxidizing atmosphere [335, 350], which gives rise to the assumption, that the origin is an oxygen related defect: during growth (or annealing), the recombination of oxygen interstitials with vacancies competes with the indiffusion of oxygen from the ambient [329, 330], which results in a remarkable reduction of the oxygen vacancy, but interstitial oxygen remains in the lattice. A thermal activation energy of 1.9 eV was determined for oxygen at tetrahedral interstitial sites by ESR measurements [351], which allows the assignment of the band to this defect. The emission properties allow an explanation of the emission by the configuration coordinate model [336] with a transition from a shallow donor to a deep acceptor [132].

Comparing the as-grown ZnO nanowire ensemble to the bare nanowires from the imprint in figure 4.2 (a), it is obvious that the defect emission especially of the green defect band is much stronger for the as-grown ensemble sample. To investigate the origin, monochromatic CL imaging in an as-grown ensemble was performed at liquid helium temperature, as shown in in figure 4.2 (c). The SEM image is correlated with the spacial resolved emission intensity at 3.36 eV (corresponding to the NBE emission maximum due to donor bound excitons) and at 2.38 eV (corresponding to the defect emission maximum). A strong NBE emission is detected from the ZnO nanowires as well as some nanostructures below, while the defect emission mainly originates only from the sail-like nanostructures below the nanowires, while these remain dark in the monochromatic CL image. This leads to the conclusion that the as-grown ZnO nanowires exhibit a strong NBE and low defect emission, pointing out their very good optical quality. The strong defect emission observed in the as-grown ensemble spectra originates from the nanostructures below the nanowires. A comparison of CL and PL spectra of ZnO nanowire ensembles at similar excitation power reveals the same emission features in similar intensities (not shown). The CL spectra show a larger number of phonon replica of the FX and DX lines (up to 6), which can be explained by the stronger electron-phonon interaction due to the excitation with hot electrons [291]. The hot electrons not only create highly excited electron-hole pairs, but also a significant amount of their energy dissipates by elastic collisions with electrons and nuclei, generating phonons and thereby heating up the sample [292].

The experimental conditions for CL examination have to be chosen with care, especially for nanowire ensembles, as e.g. a larger excitation voltage enables a longer penetration depth of the electrons in matter and therefore influences the depth of the excitation. This results in a stronger defect emission of as-grown ZnO nanowire ensemble samples at higher electron acceleration volt-
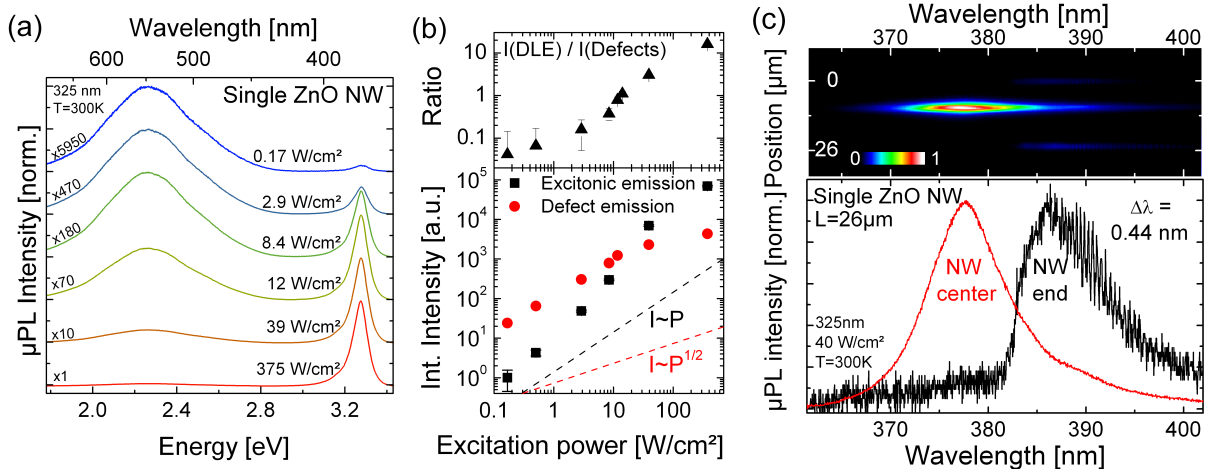
Figure 4.3: *(a) The µPL luminescence spectra of a single ZnO nanowire show mainly the defect emission at low power, while the near band edge emission becomes more dominant at higher excitation power. (b) The integrated PL intensities reveal a linear dependence with excitation power for the excitonic emission, while the defect emission scales sublinear. (c) The spacial and spectral resolved image of a 26 µm long ZnO nanowire (diameter ∼ 300 nm) shown the strongest emission from the position of the laser spot. Due to wave guiding of the light inside the nanowire, the emission at the nanowire facet ends is red-shifted and shows a modulation, which occurs due to the reflections of the sharp ends.*

ages (U > 10 keV), as the electrons deposit their energy mainly in the defect rich structures below the ZnO nanowires [293]. Reasonable results have been obtained at acceleration voltages between 5 - 10 keV, at which the electron penetration depth is in the order of the nanowire diameter (compare chapter A.2).

4.2.3 Single nanowire luminescence

The luminescence of single ZnO nanowires was investigated using µPL spectroscopy at low temperature and moderate cw excitation by the HeCd laser. The single nanowire emission (not shown) basically shows the same features as the imprint ensemble spectra (compare figure 4.2 (a) and (c)). Only slight deviations on the intensity of the DX lines and the defect emission could be observed for different nanowires, which can be attributed to different excitation powers depending on the power variation in the laser spot as well as the positioning of the laser spot on the nanowire. This observation is in well agreement with literature claiming that the emission properties of single as-grown ZnO nanowires are well reflected by the imprint ensemble spectra [179]. A systematic study of the emission properties as a function of the nanowire diameter demonstrates a stronger contribution of the surface bound exciton (SX) with decreasing diameter ($I_{SX} \sim 1/d_{NW}$) [177]. Here, a model was developed that defines a surface sensitive layer of 11 nm thickness mainly influencing the SX emission properties. In additions, slightly stronger contributions of free excitons were observed compared to the ensemble emission [321].

The normalized µPL emission spectra of a typical single ZnO nanowire at room temperature are plotted in figure 4.3 (a) at different cw excitation intensities. At low emission powers, the luminescence is dominated by the broad green emission band centered at 2.2 eV. The near band edge emission centered at 3.27 eV, which originated from the radiative recombination of free excitons and their phonon replica, has a significantly lower emission intensity by more that one order of magnitude. By increasing the excitation power, the emission intensity of the excitonic emission increases linear with power (I ∼ P) and dominates the spectrum above 10-20 W/cm², as plotted in figure 4.3 (b). Whereas, the intensity of the defect emission increases only sublinear with power (approximately I ∼ P$^{1/2}$) up to 10 W/cm² and saturates above. At excitation powers above 100 W/cm², deviations from the linear behaviour of the excitonic emission occur, which

are attributed to local heating effects of the cw laser.

The behaviour can be understood regarding the lifetime of excitons and radiative defects transitions: the lifetimes of free excitons is strongly influenced by the crystal quality. Typical free exciton lifetimes in ZnO nanowires at moderate excitation densities are $\sim$ 350 ps at 4 K and up to 480 ps at 60K [352], which are comparable to lifetimes of free excitons in high quality bulk material ($\sim$ 300 ps at 4 K [117] and 900 ps at 300 K [116, 353]). The green defect emission has a lifetime in the range of micro- up to milliseconds [354, 355], which is several orders of magnitude larger. At low excitation power, the carriers recombine mainly at defect states. Increasing the generation rate of carriers by higher excitation power, the defect emission intensity increases only sublinear due to the very limited number of defect centers in the good quality nanowire lattice, which become saturated due to the longer lifetimes [46, 356]. The excitonic emission still increases linear with power due to the significant shorter lifetime.

The spacial and spectral resolved luminescence of a single ZnO nanowire of 26 µm length (diameter $\sim$ 300 nm) is shown in figure 4.3 (c). The strongest emission originates from the position of the focused laser spot (diameter $\sim$ 5 µm) at the center of the nanowire. The respective spectrum measured at the center (shown below in red in figure 4.3 (a)) reproduced well the excitonic emission at 40 W/cm^2. Whereas, the emission from the nanowire ends (black spectrum) is red-shifted by 10 nm (85 meV) compared to the emission at the position of the laser spot. The origin of the red-shift is found in the characteristics of active light transport in semiconductor nanowire waveguides: The strong exciton-phonon coupling in polar semiconductors (like CdS or ZnO) leads to the formation of an Urbach tail, which extends the absorption profile into the energy gap due to the broadening of the exciton resonance [168, 357]. The excitonic emission guided along the nanowire can be re-absorbed by the band tails, and is re-emitted at lower energy (and so on). This absorption-emission-absorption process may occur several times, each causing a red-shift of the emitted photon. The process can be also understood as strong exciton-polariton interaction [167]. When the energy of the emitted light is below the Urbach tail, the semiconductor becomes transparent and the light propagates as electromagnetic wave along the passive nanowire waveguide with low losses [20].

At a close look, modulations of the emission equidistantly spaced by 0.44 nm can be observed on the low energy side above 388 nm, which are not present in the emission of the nanowire center. The light in the nanowire waveguide is reflected at the flat nanowire facet ends due to the sharp refractive index contrast, leading to feedback and thereby creating standing light wave in a resonator structure. The modulations of the luminescence intensity occur at positive interference conditions. The spacing of the modulations matches the nanowire length assuming Fabry-Pérot type cavity [358]. The nanowire diameter further rules out a whispering gallery mode resonator type [53].

4.2.4 Lasing of ZnO nanowires

Luminescence investigations of single ZnO nanowires were performed at high excitation conditions using the 355 nm nanosecond pulsed Nd:YAG laser. The laser spot was defocussed to $\sim$ 25 µm diameter for a uniform excitation of the complete nanowire. High resolution spectra of the near band edge emission of a single ZnO nanowire (length 16 µm, diameter $\sim$ 250 nm) at room temperature are presented in figure 4.4 (a). At moderate excitation power up to 200 kW/cm^2, a broad emission band around 378 nm (3.28 eV) is observed, which is attributed to the recombination of the free excitons and their phonon replica [359]. The luminescence originates mainly from the nanowire body at the position of the laser spot, as shown in the inset in figure 4.4 (a). The inhomogeneous emission intensity along the nanowire axis is attributed to the intensity
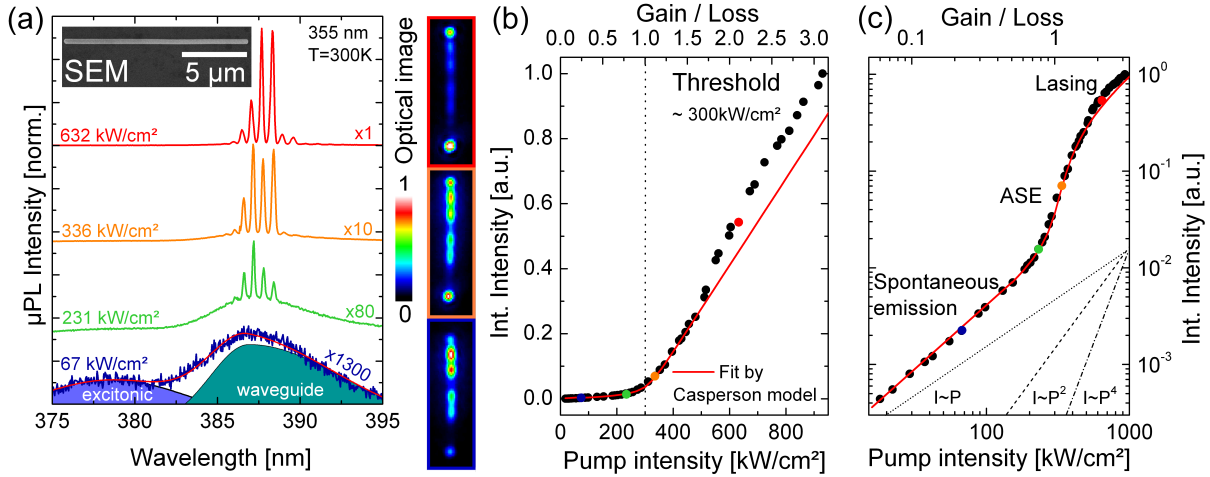
Figure 4.4: *(a) µPL high resolution spectra of a single ZnO nanowire at high excitation by the pulsed laser. Sharp peaks appear superimposed to the broad spontaneous emission, which dominate the spectra at high excitation power. The optical image shows the normalized emission intensity at the respective excitation power. The inset is an SEM image of the nanowire. (b) The integrated PL intensity shown in the linear plot can be fitted using a multimode laser model [360] with $x_0 = 0.25$. In the double logarithmic plot, the transition from spontaneous to amplified spontaneous emission and lasing clearly proofs lasing of the ZnO nanowire.*

distribution of the defocussed laser spot (compare figure A.7). The emission from the nanowire ends corresponds to an asymmetric band centered at 388 nm (3.20 eV), which is red-shifted by $\sim$ 10 nm to the excitonic emission (compare to previous chapter). Increasing the excitation power to 200 - 250 kW/cm^2, the emission from the nanowire ends becomes more intense and sharp, equidistant spaced peaks appear superimposed to the waveguide emission. Further enhanced excitation (above 300 kW/cm^2) is followed by a strong emission intensity increase and the domination of the sharp peaks in the spectrum (FWHM $\sim$ 0.15 nm). The main emission originates from the nanowire ends.

The integrated µPL intensity is plotted as a function of pump intensity in linear scale in figure 4.4 (b). The emitted intensity raises slowly with pump power up to 200 kW/cm^2. The appearance of the sharp modes is accompanied by a strong intensity increase. Above 300 kW/cm^2, the emission intensity increases again approximately linear with excitation power, but at a steeper slope. Plotting the data in double logarithmic scale provides more information in figure 4.4 (c): at moderate low excitation, the emission intensity increases approximately linear (I $\sim$ P), as typically observed for spontaneous emission. A deviation from a true linear behaviour originates from amplified spontaneous emission (ASE), which is enhanced by the nanowire waveguide and becomes dominant between 200 - 300 kW/cm^2. The appearance of the sharp modes is accompanied with a super-linear intensity increase (I $\sim$ P^4), as the gain in the nanowire resonator can overcome the losses at the facet ends. As the sharp modes dominate the spectrum (above 300 kW/cm^2), the integrated intensity increases again linear with the pump intensity, which is typically for lasing oscillations above the threshold. A further kink appears at 500 kW/cm^2, which probably originates from additional lasing modes at the lower energetic part of the mode spectrum further enhancing the emission intensity. This becomes obvious by comparing the emission spectra at 336 and 632 kW/cm^2.

The experimental values in fugire 4.4 (b) of the integrated PL intensity can be fitted using an analytical model developed for multi-mode laser oscillators [361]. The model calculates the total emission intensity of the competing laser modes as a function of the gain/loss ratio, which is connected to the pump rate. The course of the emission intensity is strongly determined by the parameter x_0, which describes the fraction of spontaneous emission in the lasing emission.

Smaller x_0 values correspond to a stronger kink in the emission intensity above the lasing threshold, equivalent to a more pronounced s-shaped curve in the double logarithmic plot. Additional information of the multimode model are given in chapter B.2. For the data given in figure 4.8 (b), a good fit is obtained for $x_0 = 0.25$. The lasing threshold is determined from the fit, where the pumping intensity equals a gain/loss ratio of 1, which is ~ 300 kW/cm^2 for the examined ZnO nanowire in figure 4.8. Similar thresholds are observed for other ZnO nanowires with comparable diameter and length.

Zimmler et al. first observed the transition from ASE to lasing oscillations in ZnO nanowires and characterized the emission properties in relation to the nanowire morphology [21, 51]. A threshold of ~ 270 kW/cm^2 was observed, which is comparable to the threshold of all examined ZnO nanowires in this thesis. In addition, spectral shape and fit parameter are similar to the reported values.

Several gain mechanisms have been proposed to explain the observed light amplification above the threshold in nanowires. Both bi-exciton recombination and inelastic exciton scattering can achieve gain [308], but those mechanisms only occur at low temperatures. Exciton-electron scattering is present above 100 K, this mechanism can be excluded at room temperature due to its temperature dependence, as the X-e scattering emission is shifted to energies smaller than the laser emission at room temperature [128]. Gain at room temperature by an inverted electron-hole plasma (EHP) is possible at sufficient excitation intensities in an energy range, which matches the observed nanolaser emission energy [152]. The presence of an EHP could be experimentally verified at excitation intensities comparable to those used in the above measurements [362] and is therefore supposed as the light amplification mechanism for lasing of ZnO nanowires at room temperature [363].

4.3 CdS nanowires

4.3.1 Structural properties of CdS nanowires

CdS nanowires were synthesized by a CVD method using a horizontal tube furnace using a process similar to the synthesis of ZnO nanowires. The investigation of the growth parameter and their optimization for a reliable CdS nanowire synthesis is described in the appendix (chapter B.1). High quality CdS nanowires with diameters between 50 - 700 nm were synthesized with lengths up to 50 µm, resulting in a high aspect ratio. Many nanowires show a remaining catalyst dot at the top after growth.

Figure 4.5 (a) shows a survey TEM image of a straight CdS nanowire with a smooth surface. The homogeneous contrast of the nanowire body suggests a crystal without extended imperfections. The catalyst dot on top the nanowire as well as the nanowire body were examined by catalyst droplet was identified as pure Au without residuals of the source material, which confirms VLS as the growth mechanism [257, 312]. The composition of the nanowire body is close to stoichiometric CdS without traces of the Au catalyst or other elements. The crystal structure was investigated using HR-TEM and SAED. Figure 4.5 (c) shows the SAED pattern of the nanowire body. The appearance of many diffraction spots reveals the high quality of the crystalline lattice. The spots were assigned by evaluation of the angles and the distances to the central spot and match well the spacing of the (0002) and (0$\bar{2}$20) denoted planes looking from the zone axis [10$\bar{1}$0] in wurtzite CdS with lattice parameters of $a = 4.16$ Å and $c = 6.76$ Å [364]. The comparison of the SAED pattern with the TEM image (figure 4.5 (a)) suggests growth of the nanowire along the c-axis ([0001] direction), as typically observed for VLS growth CdS nanowires [59, 365]. The high resolution TEM image in 4.5 (d) show the high quality single crystalline lattice structure
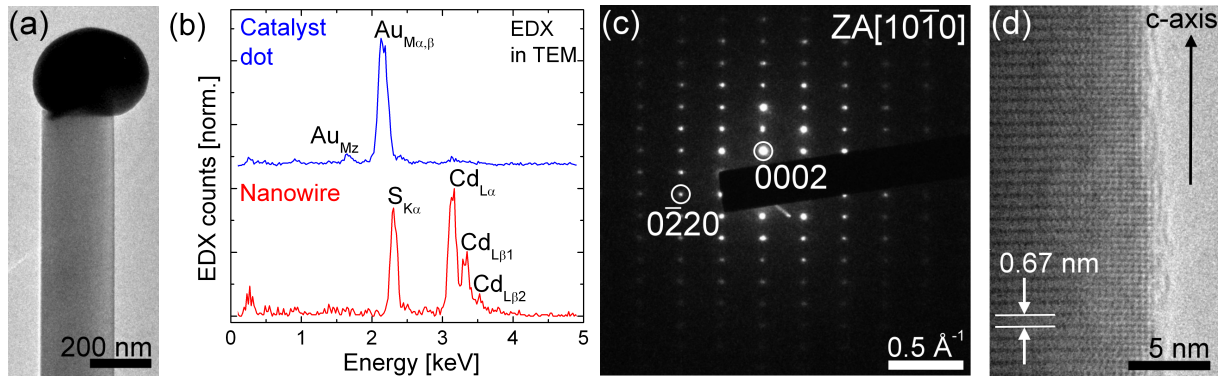
Figure 4.5: *(a) The survey TEM image shows a straight CdS nanowire with a smooth surface without extended imperfections.(b) EDX measurements in the TEM identify the catalyst dot as pure Au and stoichiometric CdS at the nanowire body. (c) The SAED image reveals many sharp reflexes revealing a high quality lattice. The reflexes could be attributed to the spacing of the $\langle 0002 \rangle$ and the $\langle 0\bar{2}20 \rangle$ planes (zone axis $[10\bar{1}0]$), indicating nanowire growth along the c-axis of the wurtzite CdS lattice. (d) The HR-TEM image can resolve the high quality crystal structure. No hints for extended defects were observed.*

with a plane spacing of 0.67 nm along the c-axis in good agreement with the literature value. A very flat surface is observed (roughness $<$ 1 nm) and no hints for extended defects such as stacking faults or dislocations were found, revealing the high quality crystal structure of the CdS nanowires.

For the unambiguous identification of the growth direction, another CdS nanowire was aligned by tip and tilt to a low index zone axis in TEM diffraction mode. The recorded SAED pattern and the corresponding bright field image are shown in 4.6 (a). The positions of the diffraction spots match well the denoted planes of the wurtzite CdS lattice with a $[10\bar{1}0]$ zone axis and the nanowire appears to be aligned with the c-axis. To ensure this and that the nanowire is not tilted towards the direction of observation, it was rotated by 30° around its axis (see illustration) and another SAED pattern was recorded, shown in figure 4.6 (b). The spot of the diffraction pattern can be identified very well with the spacing of the denoted planes assuming a $[1\bar{1}00]$ zone axis and occur exactly as expected for rotation of the wurtzite CdS lattice by 30° around the c-axis. This unambiguously confirms the growth of the CdS nanowires along the [0001] direction (c-axis).
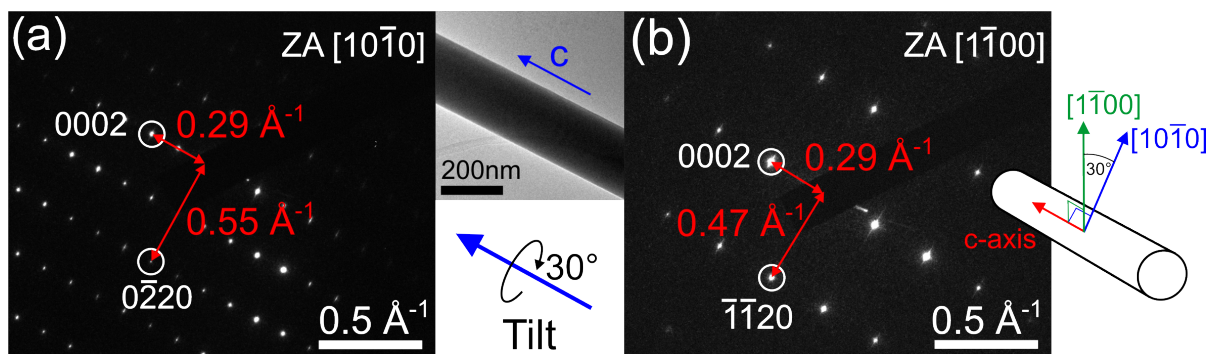
Figure 4.6: *Unambiguous evaluation of the CdS nanowire growth direction: (a) The SAED pattern shows diffraction spots, which match well the spacings of the denoted lattice planes. The TEM bright field image shows the respective area of the CdS nanowire, which seems to be aligned with the c-axis. Afterwards, the nanowire is rotated by 30° around this axis (illustration below) and another SAED pattern was recorded. (b) The identified diffraction spots and zone axis occur exactly as expected for a rotation of a wurtzite lattice by 30°; therefore clearly identifying the c-axis as growth direction.*

Figure 4.7: *(a) Low temperature photoluminescence spectra of a CdS nanowire imprint ensemble. The inset shows the high resolution spectra of the NBE, which dominates the emission. (b) Power dependent µPL spectra of a single CdS nanowire at room temperature and moderate excitation power showing the near band edge and defect related emission. (c) The near band edge emission increases linear in power and therefore stronger than the defect emission.*

4.3.2 Optical emission at low excitation power

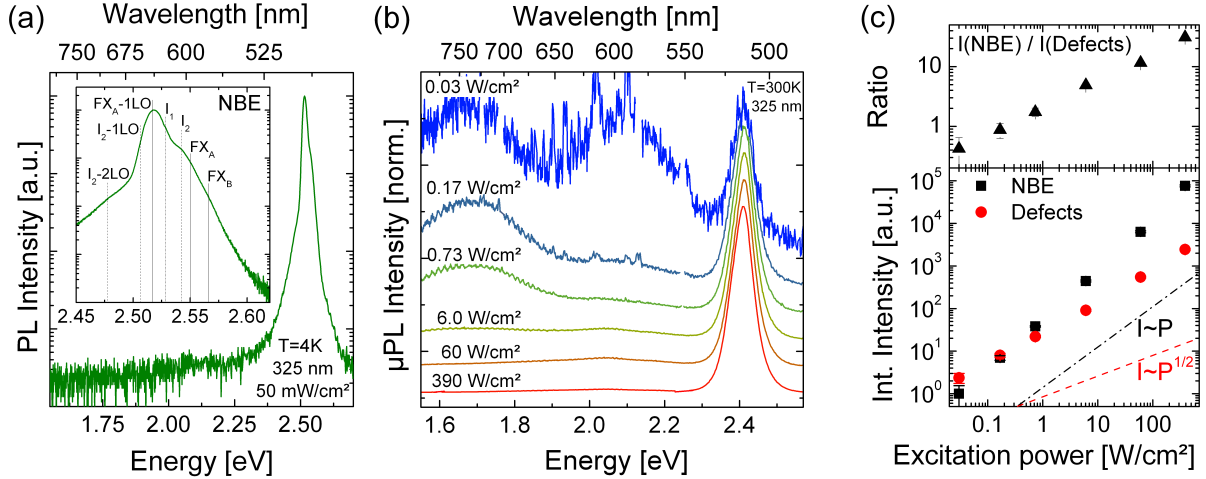Low temperature photoluminescence spectra of a CdS nanowire ensemble transferred via imprint to a clean Si substrate is shown in figure 4.7 (a). The emission is dominated by the near band edge emission (NBE) around 2.52 eV. Nearly no emission of defects is detected even at the low excitation power of 50 mW/cm^2, which points out the low defect concentration of the CdS nanowires. The inset in figure 4.7 (a) shows a high resolution spectrum of the NBE, in which several features could be assigned: The emission shoulders at the high energy side are attributed to recombinations of free excitons ($FX_B = 2.568$ eV and $FX_A = 2.550$ eV) [115, 366, 367]. the emission of donor bound excitons (labelled I_2) appears at 2.543 eV as well as acceptor bound excitons (labelled I_1) at 2.531 eV [121, 368]. The most intense peak in the high resolution spectrum appears 38 meV red-shifted to the emission of the free exciton FX_A and is therefore assigned to its phonon replica FX_A - 1 LO at 2.508 eV [127]. The shoulders at 2.508 eV and 2.477 eV are attributed to the first and second phonon replica of the donor bound excitons I_2 [369]. The low intensity of the bound excitons compared to the free exciton emissions is a hint for the low doping levels of the CdS nanowires [370].

The luminescence emissions of a single CdS nanowire was investigated using µPL spectroscopy at room temperature. For excitation, the laser beam of a 325 nm HeCd laser was focussed to a spot of ∼ 10 µm diameter. The spectral resolved emissions are shown in figure 4.7 (b). Three emission bands were observed at low excitation power of a few mW/cm^2. The emission centered at 2.41 eV is attributed to the near band edge (NBE) recombination of free excitons and their phonon replica [371, 372], which appears red-shifted by 11 meV due to the elevated temperature. The two bands at lower energies are assigned to the radiative recombination of carriers at intrinsic defects (deep level emission, DLE). The emission band at 2.1 eV is attributed to a transition from donor levels involving Cadmium interstitials (Cd_i) to the valence band [373–376]. The emission centered at 1.7 eV is typically attributed to a transition involving sulfur vacancies (V_S) [377, 378]. The sharp peaks in the spectra, especially at low excitation power, originate from stray light of the fluorescent lamp room lightning.

The defect emissions are the main contribution at low excitation conditions. The NBE intensity raises linear with the excitation power (I ∼ P, slope ∼ 1 in the double logarithmic plot shown in figure 4.7 (c)) and becomes more dominant above 300 mW/cm^2 while the defect emissions
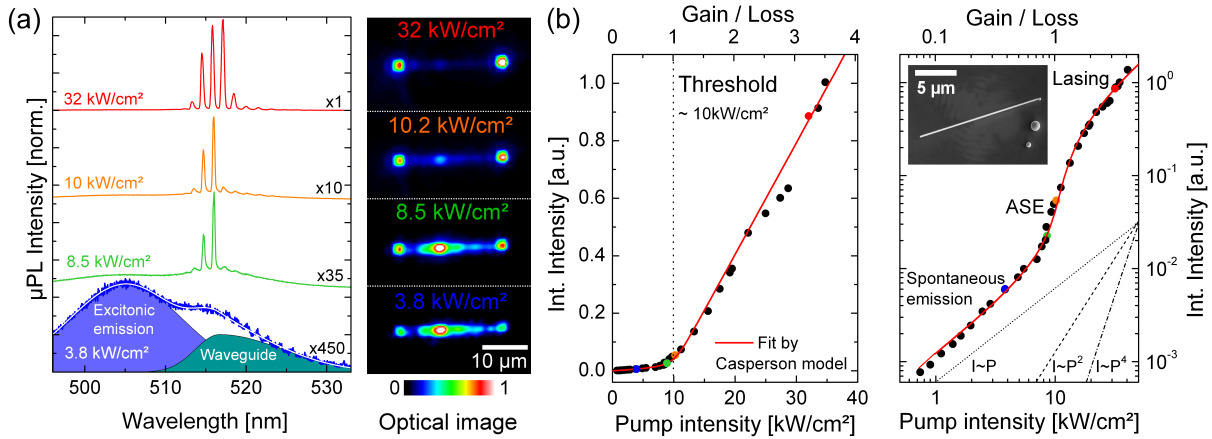
Figure 4.8: *(a) μPL spectra and optical image of a single CdS nanowire at high excitation. Sharp peaks appear superimposed to the broad spontaneous emission, which dominate the spectra at high excitation power. (b) The integrated PL intensity shown in linear plot can be fitted using a multimode laser model [360] with an $x_0 = 0.03$. In the double logarithmic plot, the transition from spontaneous to amplified spontaneous emission and lasing clearly proofs lasing of the CdS nanowire (SEM picture in inset).*

increase sublinear with a slope of ~ 0.5 ($I \sim P^{1/2}$). This behaviour can be understood as the lifetime of the carriers recombining at defects is several orders of magnitude larger (tens of μs) [379] compared to the lifetime of the free excitons (≤ 0.1 ns) [160, 380]. Due to the low defect concentration in the nanowires, the defect levels become saturated at elevated continuous excitation leading to the sublinear power behaviour. The generated carriers can still recombine via excitonic emission, therefore the NBE intensity scales linear with excitation power. This observed behaviour points out further more the high crystal quality of the CdS nanowires.

4.3.3 Lasing of CdS nanowires

Luminescence investigations at high excitation conditions were performed using the 355 nm nanosecond pulsed Nd:YAG laser with a defocussed spot of ~ 25 μm diameter for the uniform excitation of the nanowires. High resolution spectra of the near band edge emission and the corresponding optical PL image of a single nanowire are presented in figure 4.8 (a). At moderate excitation power (up to 7 kW/cm^2), a nearly Gaussian shaped emission band around 505 nm (2.455 eV) is attributed to the recombination of the free excitons and their phonon replica [371, 372]. The luminescence is mainly observed from the location of the laser spot. Additional emission from the nanowire ends corresponds to an asymmetric emission band, which is red-shifted by ~ 10 nm. Its origin can be explained as in the case of ZnO nanowires by the nature of active light transport in semiconductor nanowires. The absorption profile is extended by the Urbach tail below the band gap [168, 357], thus allowing absorption-emission-absorption processes of the excitonic emission, which explain the observed red-shift of the facet end emission. The asymmetric shape of the facet end emission is caused by the overlap of the absorption profile with the excitonic emission [166, 381]. Additionally, the intensity of the facet end emission is modulated. The contrast in refractive index between CdS and the surrounding air leads to the a partial reflection of the guided light at the flat facet ends, which creates a feedback and induces constructive interference for wavelengths fitting to the cavity. The CdS nanowires therefore combine waveguide and resonator properties [38, 166, 382].

Increasing the excitation power above 8 kW/cm^2, the emission from the nanowire ends become stronger and sharp peaks appear on the high energy side of the resonator induced modulations superimposed to the red-shifted waveguide emission. Further enhanced excitation (above 11 kW/cm^2) is followed by the domination of the sharp, equidistant spaced modes in the emission

spectrum. The optical image shows main emissions from the nanowire ends. The integrated µPL intensity is plotted as a function of pump intensity in linear scale in figure 4.8 (b): the emitted intensity raises moderate with pump power, but a strong intensity increase appears above the threshold of ~ 10 kW/cm^2 accompanied by the appearance of the sharp modes. Plotting the data in double logarithmic scale provides more information: at moderate low excitation, the emission intensity increases linear (I $\sim$ P), as typically observed for spontaneous emission. The appearance of the sharp modes is accompanied with a superlinear intensity increase (I $\sim$ P^4) originating from amplified spontaneous emission (ASE) [383]. As the sharp modes dominate the spectrum, the integrated intensity increases again linear with the pump intensity, which is typically observed for lasing action above the threshold. The evaluated power dependency of the optically pumped CdS nanowires therefore includes all characteristics of classical macroscopic lasers [163].

The experimental values of the integrated PL intensity were fitted using the analytical model developed for multi-mode laser oscillators [361]. Details of the model are described in chapter B.2. For the data given in figure 4.8 (b), a good fit is obtained for $x_0 = 0.03$. Comparing this value the results of Oulton et al. [49] for lasing CdS nanowires at low temperatures, similar values were found for CdS nanowires on silica substrates. The power dependence of nanowires on plasmonic substrates could be fitted using larger x_0 values in the range of 0.1 to 0.4 resulting from a higher fraction of spontaneous emission in the lasing mode, which is typical for the strong confinement in the hybrid system.

The threshold of the lasing CdS nanowires was derived from the fit of the experimental determined values as the excitation power at which the gain/loss ratio equals 1. For the 15 µm long nanowire of ~ 180 nm diameter, a threshold as low as 9.3 kW/cm^2 was determined. Nanowires with imperfection on the nanowire ends or deviations from a straight morphology (by e.g. tapering) also showed sharp emission peaks and the transition from ASE to lasing oscillations, but higher excitation densities are necessary, reflected by the determined thresholds in the range of 10 to 60 kW/cm^2.

The gain for the light amplification of CdS nanowires at room temperature probably also originates from an inverted electron-hole plasma [58], as the pump intensity should be sufficient to achieve carrier densities in the range of $\sim 10^{18}$ - 10^{19} cm^{-3}, which are above the Mott density [157]. A further hint is the stronger intensity increase of lower energy resonator modes at increased pump intensities (compare spectra in figure 4.8 (a)), which can be well explained by shift of the gain maximum to lower energies due to the renormalized band gap [158, 158].

Head-On measurements   The epifluorescence setup (chapter 3.3.2) used for the CdS nanolaser characterisation collects only the luminescence light scattered at 90° to the nanowire axis, which prevents the exact determination of the nanowire output and a full characterisation of the excitation conditions, as scattering effects from the substrates cannot be excluded. A µPL setup in "Head-On" geometry was developed for this purpose, which avoids such drawbacks by the decoupling of the excitation and detection pathways (see figure 4.9 (a)). The direct light output of a 17 µm long CdS nanowire of ~ 700 nm diameter partially suspended in air (shown in figure 4.9 (b) as inset) was detected as a function of the pump power. The nanowire output was measured by integration of the PL signal in the detection system (monochromator + CCD), which was calibrated using the reflection of the focussed spot of a 532 nm laser of known power simulating the nanowire emission and subsequent conversion of the spectral data. The wavelength difference between nanowire and calibration laser is negligible as the detector response is nearly equal for both wavelengths. To verify this method, direct measurements using a calibrated powermeter directly attached behind the microscope objective were performed and show good agreement
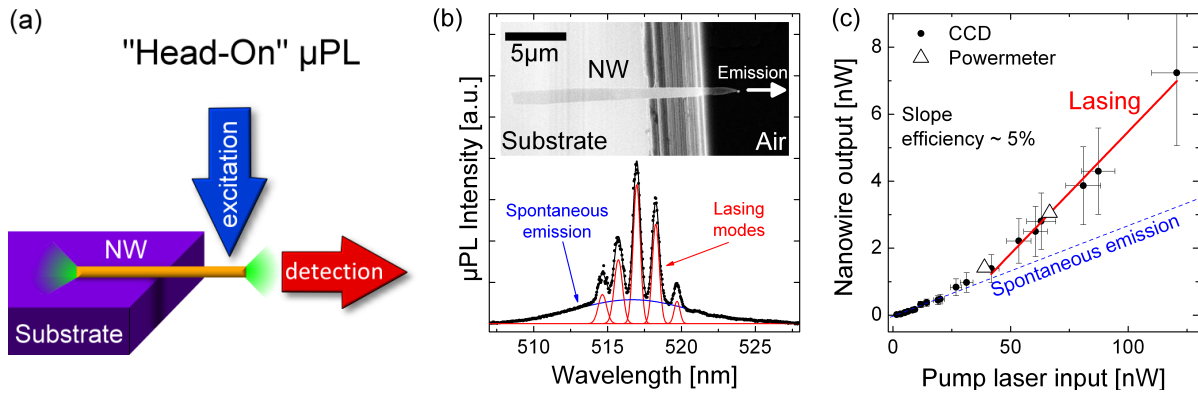
Figure 4.9: *(a) Schematic drawing of the µPL measurements in Head-On geometry for the direct detection of the nanowire emission. (b) µPL spectra of the direct nanowire emission contains the broad spontaneous emission superimposed with the lasing modes. The inset shows an SEM image (top view) of the free standing CdS nanowire. (c) Direct measurement of the nanowire output power as a function of pump laser input power.*

with the indirect measurement using the spectroscopic CCD.

Only broad spontaneous emission originates from the nanowire and the intensity increases linear with pump power up to an average power of 40 nW. Above this value, sharp peaks appear superimposed to the broad spontaneous emission (figure 4.9 (b)). A "kink" is observed in the power dependency (figure 4.9 (c)), which is typical for the lasing action above the threshold. The ratio of nanowire output to excitation laser input power increased from ~ 1 % for spontaneous emission to a slope efficiency of 5-10 % for the lasing nanowire, regarding only the emission from one nanowire facet end.

Polarization dependent excitation   The geometry of nanowires is highly anisotropic and makes them sensitive to the polarization of the excitation light, as observed for ZnO, CdS, CdSe and InP nanowires [381, 384–388]. Experiments on dispersed ZnO nanowires could also show an effect for the lasing of ZnO nanowires by rotating the wire in the polarized laser spot, but the measurement uncertainties induced by the need for the repositioning of the nanowire after rotation limited a conclusive interpretation [302].

  The Head-On µPL setup offers a reliable possibility to examine the lasing properties of single CdS nanowires as a function of the polarization direction of the excitation laser towards the nanowire axis. The nanowire suspended in air eliminates disturbing effects by scattering of the substrate and the measurement geometry enables illumination perpendicular to the nanowire axis. The direct emission of the nanowire along the nanowire axis is measured instead of the scattered emission in [302]. The electric field component of the polarized laser could be rotated by a $\lambda/2$-wave plate placed directly in front of the 15x excitation microscope objective (see figure 3.3.2 (c)). A polarization ratio of the excitation laser was determined to be 100:1 by detection of the laser power transmitted through a Glan-Thompson polarizer placed after the microscope objective .The laser power as well as the position of the laser spot remained constant within the experimental uncertainties at rotation of the wave plate without the additional polarizer, so no disturbing effect is introduced by the microscope objective.

Figure 4.10 displays the emission of 12.5 µm long CdS nanowire (diameter ~ 500 nm) at excitation above the lasing threshold detected in Head-On geometry. The domination of sharp emission modes superimposed to the broad spontaneous emission and the evaluated power dependency prove lasing oscillations in the CdS nanowire. The nanolaser spectra were recorded at constant excitation power as a function of the polarization angle α, which denotes the angle between the electric field component $\vec{E}$ of the polarized laser light and the nanowire axis, as shown in the
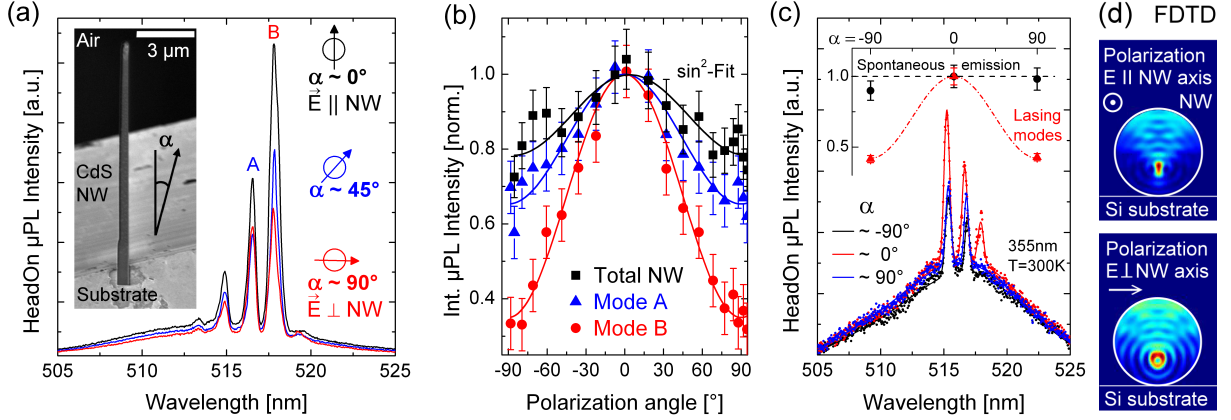
Figure 4.10: *(a) The intensity of the lasing emission of a CdS nanowire determined in Head-On geometry (shown in the inset) depends on the polarization of the electrical field component towards the nanowire axis. (b) The integrated nanowire emission intensity is strongest for polarization parallel to the nanowire axis. The angle dependence can be described by a $\sin^2$-fit. The emission modes (labelled A and B) reveal a different sensitivity to the excitation polarization. (c) The spontaneous emission is nearly insensitive to a change in excitation polarization. (d) The absorption profiles simulated by FDTD for a 500 nm nanowire at plane wave excitation parallel and perpendicular to the nanowire axis exhibits significant differences.*

inset of figure 4.10 (a). A maximum emission intensity was found at $\alpha = 0°$, which accounts for polarization parallel to the nanowire axis, as typically observed for nanowires [381, 384–386]. A deviation from this excitation condition results in a decreased emission intensity and a minimum was found for $\alpha = 90°$ (polarization of the electric field component perpendicular to the nanowire axis). The integrated total nanowire emission is plotted as a function of the polarization angle α in figure 4.10 (b). The data can be fitted using a $\sin^2$-function with a period of 180° revealing the expected polarization behaviour. A polarization ratio $\rho = (I_{||} - I_{\perp})/(I_{||} + I_{\perp})$ was determined to $\rho = 0.19 \pm 0.06$ for the overall nanowire emission in the lasing regime.

Taking a close look to the intensity of different emission modes in figure 4.10 (a), significant differences in their emission intensity depending on the polarization angle appear as they experience a different sensitivity to the polarization angle. The integrated intensity of single modes (labelled "A" and "B") was extracted by fitting the spectral data with Gaussian functions using the program "Fityk" [389]. The integrated intensity of each mode is displayed in the polar plot in figure 4.10 (b). The polarization angle dependent behaviour is similar for all modes and comparable to the behaviour of the total nanowire emission, but normalized intensities are lower for $\alpha = 90°$ and reach values down to $I_{\perp} \sim 0.3 \cdot I_{||}$ for mode A compared to $I_{\perp} \sim 0.7 \cdot I_{||}$ for mode B. thus, the polarization ratios vary from $\rho_A = 0.21 \pm 0.06$ to $\rho_B = 0.54 \pm 0.04$ and are larger compared to the total nanowire emission, as this also includes the spontaneous emission background, thus further limiting the polarization ratio for the total emission.

The experiment was repeated by adjusting the excitation power at several polarization angles to reach comparable nanowire emission intensities. The lowest excitation power of ~ 80 nW was found at $\alpha = 0°$, which had to be increased to more than 100 nW at $\alpha = 90°$. It can be concluded from this measurement that the lowest lasing threshold can be reached for excitation polarization parallel to the nanowire axis. The nanowire emission intensity at polarized excitation with fixed power just above the threshold in the ASE regime is displayed in figure 4.10 (c). As in the former experiments, a more intense nanowire emission was found for polarization parallel to the nanowire axis compared to the situation with perpendicular polarization. But it is remarkable that only the sharp resonator modes exhibit a clear angle dependency, while the broad spontaneous emission remained at an almost constant emission intensity.

To understand the impact of the absorption properties of CdS nanowires on this sensitivity to

the excitation polarization, a collaboration with Robert Buschlinger from the group of Prof. Ulf Peschel at the University of Erlangen was initiated to perform finite-difference time-domain (FDTD) simulations of the experimental realized conditions. The absorption of a free standing CdS nanowire with a spherical diameter of 500 nm was calculated by Robert Buschlinger for plane wave excitation at 355 nm polarized parallel and perpendicular to the nanowire axis. The assumption of a spherical nanowire diameter is valid as high resolution SEM and TEM images (figure 4.5) showed only little facetting of the nanowires. The absorption profiles are displayed in figure 4.10 (d). For polarization of the electric field component of the incoming plane wave along the nanowire axis, the absorption is strongly concentrated inside the nanowire, which is attributed a "lens effect" of the spherical nanowire cross section focussing the incident light in the material. The absorption for excitation polarization perpendicular to the nanowire axis is more homogeneous distributed inside the nanowire and the calculated absorption per unit length is slightly higher compared to the parallel case, reflecting the differences of the absorption coefficients parallel and perpendicular to the c-axis of wurtzite CdS [390]. The simulated absorption cannot explain the experimental observations for a 500 nm nanowire. The absorption was also simulated for smaller nanowire diameters and a stronger absorption for excitation polarization parallel to the nanowire axis was found for nanowires thinner than 180 nm, which is in agreement with the results from literature evaluated by simulation using pointing vector analysis [387]. The excitation polarization anisotropy of semiconductor nanowires is explained by the large dielectric contrast between the nanowire and the surrounding media (air) [169, 384]. The nanowire can be treated as an infinite dielectric cylinder, as the wavelength of the excitation light inside the nanowire is significantly shorter compared to the nanowire length. For polarization of the incident light parallel to the nanowire axis, the electric field inside the cylinder is not reduced. But the electric field is attenuated for incident polarization perpendicular to the nanowire axis according to $E_i = 2\epsilon_0/(\epsilon_m + \epsilon_0) \cdot E_e$ [391], with E_i being the electric field inside the cylinder, E_e is the excitation field and $\epsilon_m(\epsilon_0)$ is the dielectric constant of the cylinder (surrounding media). The different sensitivity of the single emission modes to the polarization direction of the incident light probably results from the differences in the absorption profiles, as certain resonator modes benefit stronger from the more concentrated absorption and are therefore better stimulated.

Geometry dependent properties   Lasing nanowires show a diverse in mode spacing depending on their length, as shown in figure 4.11 (a). Long nanowires exhibit many resonant lasing modes with small spacing and sharp peaks, while the mode spacing and FWHM is enlarged for shorter wires. The mode spacing of several lasing nanowires was determined for each peak and the mean value $\Delta\lambda$ was plotted as a function of the inverse nanowire length L in figure 4.11 (b). The data follow the linear relation $\Delta\lambda = \frac{1}{L}\left[\frac{\lambda^2}{2}\left(n - \lambda\frac{dn}{d\lambda}\right)^{-1}\right]$, which extrapolates to 0 nm for $L \to \infty$ and is typical for Fabry-Pérot type cavities [163]. The formula includes the refractive index of CdS $n = 2.76$ at 517 nm [110] and $dn/d\lambda$ labels the dispersion, which was extracted from the fit to $dn/d\lambda = $ -7.4 $\pm$ 0.8 μm^{-1}. This is in very good agreement with the literature value of $dn/d\lambda_{lit.} = $ -7.963 μm^{-1} for CdS at 517 nm [110]. Only a few data points show small deviations from the linear relation: Those wires are not completely regular shaped (e.g. tapered or connected to another wire) and a superposition of different resonator cavities was observed in the spectra.

Lasing oscillations can be achieved when the round-trip gain inside optically pumped CdS nanowires overcomes the round-trip losses [163]: $\Gamma g_{th} \geq \alpha_W + \alpha_M$, as mentioned in chapter 2.1.3. For nanowire lasers, the mirror losses exceed the waveguide losses due to the short cavity length and the limited reflection coefficients ($\alpha_M >> \alpha_W$) in contrast to conventional semiconductor lasers [392]. The nanowires ability for laser emission, determined by the threshold gain, is therefore
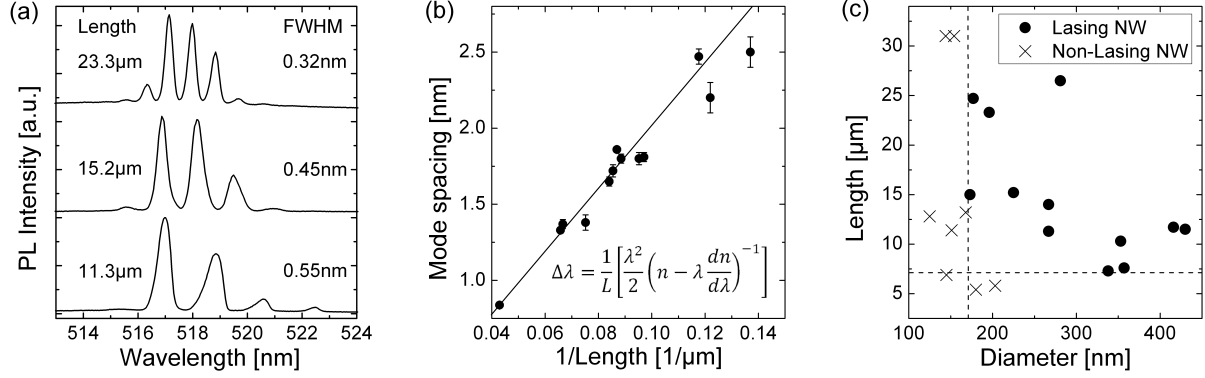
Figure 4.11: *(a) μPL emission spectra of CdS nanowires with different length showing different mode spacing. (b) The mode spacing plotted as a function of the inverse length results in a linear relation. (c) The length and diameter limits for lasing CdS nanowires.*

a strong function of the nanowire diameter D and its length L. Several CdS nanowires were investigated for their lasing ability at ~ 50 kW/cm^2 pump power and the results were plotted as a function of length and diameter in figure 4.11 (c). No lasing oscillations were found even for large nanowire diameters below a critical nanowire length of 7 μm. Above this value, the resonator cavity length enables a sufficient gain compensating the mirror losses. Another limit was found for nanowires of diameter smaller than 170 nm: although well defined resonator modes appear on the strong ASE peak at those wires, the insufficient gain limits their lasing ability, as they did not reach the threshold independent on the nanowire length. This can be understood as the reflection coefficient R is directly related to the confinement of light inside the waveguide [392]. FDTD simulations for ZnO nanowires in a similar geometry could show that for the lowest order mode at 500 nm, the fraction of power confined in the nanowires drops from ~ 80 % for D = 200 nm to less than 2 % for D = 100 nm [20]. It can be assumed that CdS nanowires exhibit similar waveguiding properties [166]. For nanowires with diameters below the critical limit, the light confinement is strongly reduces and the modes propagate as evanescent wave around the waveguide [51, 169]. This not only increases the waveguide losses, but also strongly reduces the reflection coefficient at the end facet, thereby suppresses gain and therefore lasing. The minimum diameter can be estimated by a rule of thumb as $d_{min} \approx \lambda_0/n$ with λ_0 being the vacuum wavelength of the guided light. The calculated value of ~ 174 nm for CdS is in good agreement with the experimentally determined data in figure 4.11 (c). Lasing at smaller diameters can be achieved [49], but the pumping threshold increases inversely to the decreasing diameter.

The performance of the nanowire resonator is characterized by the ratio of the stored to the dissipated energy per oscillation cycle [358, 393]. This is typically characterized for optical resonators by the quality factor $Q = \lambda_0/\Delta\lambda$, which was determined for each lasing mode using the central wavelength λ_0 divided by the spectral mode width ($\Delta\lambda$ = FWHM). For evaluation, the broad background was subtracted and each mode was fitted using a Gaussian function. In the lasing regime, the Q factors were evaluated from the spectra at a gain/loss ratio of 2, which allows a reasonable comparison between different nanowires. Typical Q factors of 1000 - 1600 are determined that can reach up to 2000. This is in the same order as Q factors evaluated for CdS nanoribbon lasers with rectangular cross section [394]. A general trend was found that the Q factor increases with the nanowire length, as shown in figure 4.12 (a). The explanation is quite obvious, as longer active media in the resonator cavity can offer higher gain [21] and therefore better compensates the waveguide and reflection losses at the facet ends. Further on, the observed threshold decreases with increasing Q factor of the nanowire cavity. The population inversion, which enables gain and is necessary for lasing, is reached at a lower pump power due to the lower energy dissipation per oscillator cycle resulting from the better resonator quality.
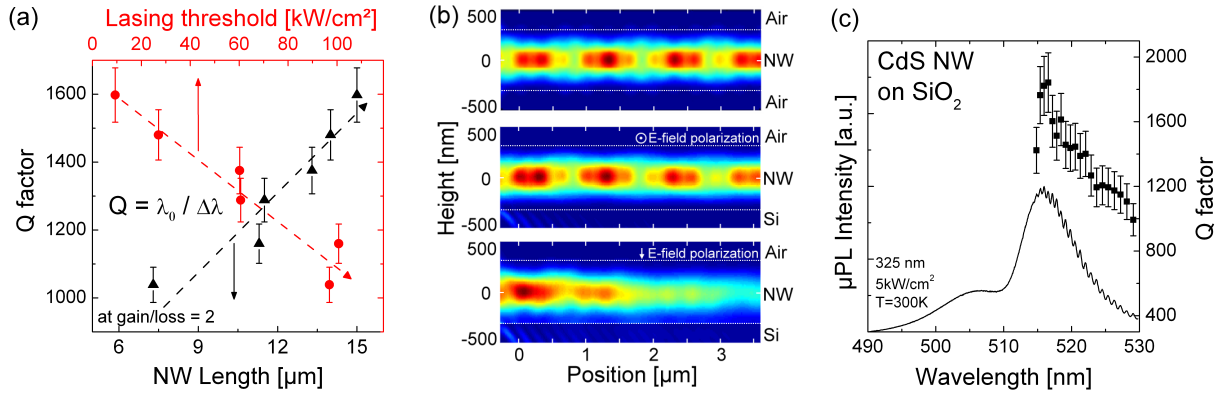
Figure 4.12: *(a) Mean Q factors for lasing CdS nanowires on Si substrates at gain/loss = 2 increase with the length of the nanowire. The estimated threshold is also correlated to the quality of the resonator. (b) The visualizations of FDTD simulation show the intensity distribution of the electric field in a 500 nm CdS nanowire . Very good multi mode waveguiding properties are observed for the nanowire surrounded by air (n = 1), while a strong leakage of the electric field occurs for a nanowire on a Si substrate (n ∼ 4.2). (c) A CdS nanowire on a 1.5 µm SiO₂ layer on Si shows enhanced waveguiding effects. The Fabry-Pérot modes can be observed even in the spontaneous emission regime, resulting in higher Q factors compared to CdS nanowires on Si.*

No correlation could found between the Q factor and the nanowire diameter. Thus it is assumed, that the lasing modes are nearly completely confined inside the nanowire at diameters between 175 and 600 nm, similar to ZnO nanowires [21]. The quality of the resonator is then mainly determined by the shape of the facet ends (reflectivity) and the length of the nanowire.

The substrate was found to have a strong influence on the resonator and emission properties. The experiments on CdS lasing and the determination of the Head-On and geometry dependent properties have been performed on CdS nanowires dispersed on Si substrates with a natural oxide layer of $\sim$ 4 nm. To gain more information on the waveguide and emission properties of CdS nanowires in such a geometry, FDTD simulations of the experimental realised conditions were performed by Robert Buschlinger (see chapter B.3). A CdS nanowire with a spherical diameter of 500 nm was modelled in 3D to explore the effects induced by the substrate and gold dots at the facet ends on the waveguiding. Figure 4.12 (b) visualizes the intensity of the electric field distribution in free CdS nanowire surrounded by air. After Gaussian-shaped excitation, several modes are guided with strong confinement inside the nanowire. Placing the CdS nanowire on a Si substrate (with natural oxide layer) induces a shift of the guided modes in the waveguide, as expected. Additional to this, a strong leakage of the electric field into the substrate was observed, which is stronger for electric field components polarized perpendicular to the substrate surface than parallel to it. The guided light field effectively couples from the CdS nanowire (n_{CdS} = 2.76) [110] to the Si substrate with a higher refractive index of n_{Si} = 4.2 at the respective wavelength of 515 nm [395], which induces the strong losses. The natural oxide layer was found to be to thin to prevent the leakage as the evanescent field extends deeper into the substrate.

µPL investigations of the waveguide and resonator properties below the laser threshold were repeated with CdS nanowires placed on Si substrates with a 1.5 µm thermal grown oxide layer. Even at medium cw excitation, a much stronger contribution of waveguide effects could be observed, which was obviously suppressed by the leakage into Si substrates in previous experiments. Figure 4.12 (c) shows the emission spectrum of a single CdS nanowire at room temperature. The red-shifted waveguide emission is much stronger compared to the free exciton emission (compare figure 4.8) and a set of sharp Fabry-Pérot modes is observed at the low energy side. Q factors of up to 1800 could be evaluated in the waveguide regime, which can be correlated to the reduced substrate losses and therefore improved resonator quality. µPL investigations at higher excita-

tion could observe lasing emission from larger fraction of CdS nanowires on SiO_2 substrates than from nanowires of comparable geometry and morphology on Si substrates. CdS nanowires with a non-perfect resonator can reach a sufficient gain for lasing as the waveguide losses were strongly reduced.

4.4 Comparison of CdS and ZnO nanolasers

CdS nanowire are able to reach sufficient gain and show laser oscillations at pumping above the threshold, similar to ZnO nanowires examined by Zimmler et al. [21, 51]. Despite the different emission wavelengths (385 - 390 nm for ZnO nanolaser and 515 - 520 nm for CdS nanolaser), both systems were found to have Fabry-Pérot type resonators, which are responsible for the observed mode spacing characteristics. The mode profile and emission intensity dependence are comparable and mainly related to the same resonator type. The fitting of the emission intensity with the theoretical multi mode laser model resulted in comparable fractions of spontaneous emission on the laser emission (x_0).

Some differences appear in the geometrical limits for lasing action. Although CdS should enable a stronger light confinement due to the higher index of refraction compared to ZnO [99], the minimum diameter of 150 nm for lasing in ZnO nanowires is smaller due to their shorter emission wavelength [21]. The minimum length of 7 µm for CdS is thereby comparable to ZnO nanowire lasers. The geometrical limits are therefore similar and mainly governed by the waveguide properties and the Fabry-Pérot type resonator.

The striking point is to explain the low threshold for lasing of CdS nanowires ($\approx 10 \text{ kW/cm}^2$), which are more than one order of magnitude lower compared to ZnO nanowires ($\approx 100 \text{ kW/cm}^2$). One major difference could originate from the Au catalyst dot, which often remains at the top end of CdS nanowires, while nearly no ZnO nanowires with attached Au dot were observed after imprint. The Au dot at the facet end enhances the reflectivity of the guided modes. This assumption is based on the observation, that the quality factor of a CdS nanowire in the waveguide regime could be enhanced by more than 50% by placing a Ag colloid close to the nanowire end [38]. The Ag colloid reflects the emission from the facet end and thereby reduces the mirror losses, thereby increasing the quality of the resonator. A similar enhancement of the Q factors could also be observed for ZnO nanowires with Al coated facet ends [396]. FDTD simulations of a CdS nanowire with and without Au dot are currently performed by the group of Prof. Ulf Peschel to gain further insights and quantify the enhancement.

An additional explanation for the lower lasing threshold could be the longer emission wavelength of CdS: the population inversion in 4-level laser systems, necessary for gain and lasing, is related to the Einstein coefficients for spontaneous and stimulated emission [163]. The ratio for stimulated to spontaneous emission scales inversely proportional to the wavelength square for a 3D system [397]. As a consequence, higher pumping thresholds are necessary to establish the inversion for shorter wavelength. Nevertheless, it has to be taken into account that this dependency is not that strong for a 1D system due to the reduced density of states of optical modes [305].

In ZnO nanowires, the gain is achieved by radiative recombinations of an electron-hole plasma (EHP) [362], which can be also assumed for CdS nanowires, because the Mott density n_M necessary for the formation of the EHP is reached at lower carrier concentrations due to the larger Bohr radius of the CdS excitons ($a_B^{CdS} = 2.8$ nm [98] and $a_B^{ZnO} = 1.8$ nm [111]). This is reflected by the experimental determined values of $n_M^{CdS} = 2.5 - 2.8 \cdot 10^{17}$ cm^{-3} at low temperatures [157, 158], which is nearly one order of magnitude lower than for ZnO $n_M^{ZnO} = 2.4 \cdot 10^{18}$ cm^{-3} [128]. The chemical potential μ is reduced at elevated temperatures, which increases the Mott densities. But the value for CdS at room temperature can be estimated to $0.6 - 2 \cdot 10^{18}$ cm^{-3}

[160, 383, 398] and is therefore still lower than the estimated Mott density of 3 - 5.7 $\cdot$ 10^{18} cm^{-3} for ZnO [154, 162]. This means, that the EHP can be established at lower pumping power in CdS nanowires.

In addition, a higher material gain was found for CdS (up to 2.8 $\cdot$ 10^4 cm^{-1}) compared to ZnO (up to 5.6 - 6.4 $\cdot$ 10^3 cm^{-1}) at equal excitation conditions [162]. If similar large confinement factors Γ are assumed as for ZnO nanowires, modal gain values in the same order as for ZnO [56] or even larger are possible at lower excitation power. This agrees well with the results from the direct power measurements in the head-on geometry. The slope efficiency of $\sim$ 5 % regarding the emission from only one CdS nanowire facet end is significantly higher compared to the value reported for ZnO nanowires of $\sim$ 1 % [51].

Summarizing the observations, none of the mentioned effects can explain the lower lasing threshold of CdS nanowires alone, but a combination is a very reasonable assumption. The attached Au catalyst dot enhances the resonator quality, thus lowering the threshold. The establishment of an EHP in combination with a similar gain enables lasing, even of slightly more irregular shaped (e.g. tapered) CdS nanowires compared to ZnO nanowires, at lower pumping powers.

4.5 Summary

The morphology and properties of as-grown ZnO nanowires were characterized. The emission properties of the as-grown sample was compared to a bare nanowire ensemble. Monochromatic CL measurements could show that main defect emission originates from the structures below the high quality nanowires. Single nanowire µPL measurements could show the saturation of defect emission intensity at moderate excitation intensities of $\sim$ 20 W/cm^2. Spacial and spectral resolved measurement reveal that the waveguide characteristic is dominated by active light transport in the nanowire for excitation above the band edge. A strong enhancement of the emission intensity and sharp emission peaks due to lasing oscillations appear in the high excitation regime above 300 kW/cm^2.

The morphology of CdS nanowires was characterized and related to the synthesis parameters in order to establish a comprehensive growth phase diagram. The structural and optical properties of the high quality nanowires were further examined. The nanowire ensemble shows a strong excitonic emission at low temperature, indicating a low defect concentration. The defect emission of single nanowires at room temperature saturated at low excitation densities of $\sim$ 100 mW/cm^2. Only excitonic emission was observed at moderate excitation. Nanosecond pulsed excitation at higher pumping power lead to sharp emission modes superimposed to the broad spontaneous emission and a super-linear intensity increase is observed. Laser oscillations were proven in the high excitation regime above 10 kW/cm^2. The direct light emissions of a CdS nanowire were characterized in "Head-On" geometry and the efficiency slope determined to 5-10 % in the lasing regime. The quality of the optical resonator was estimated to Q $\approx$ 2000 and related to nanowire length and threshold characteristics. The influence of polarized excitation was investigated in the ASE and lasing regime. Polarization of the electric field component parallel to the nanowire axis is more efficient due to higher absorption and more effective stimulation of resonator modes. A negative influence of the Si substrate was found for the CdS nanolaser emission and were investigated by FDTD simulations. The emission properties could be improved using SiO$_2$ substrates. The fundamental limits for CdS nanowire lasing were determined to a minimum length of 7 µm and a minimum diameter of 170 nm. A comparison of ZnO and CdS nanolasers was conducted and possible explanations for the lower threshold highlighted. Evidence for gain due to an inverted electron-hole plasma in CdS nanowires above the lasing threshold is provided from comparison of material properties with literature.

5 Cobalt implanted ZnO nanowires

This chapter reports on the structural and optical properties of cobalt (Co) implanted ZnO nanowires. Structural investigations were performed in collaboration with the group of Dr. Gema Martinez-Criado (European Synchrotron Radiation Facility, Beamline ID22NI). Parts of these results are published in [399, 400]. The time resolved and photoluminescence excitation measurements were performed in close collaboration with Uwe Kaiser from the group of Prof. Dr. Wolfram Heimbrodt (Phillips-Universität Marburg).

5.1 Motivation

Undoped ZnO and CdS nanowires exhibit extraordinary optical properties like light amplification and even lasing oscillations, as presented in the previous chapter. Nevertheless, these effects can only be stimulated at high optical pumping levels in the order of 10 - 300 kW/cm^2 [51, 305]. For the integration of nanowires into electrically driven devices, new approaches have to be found in order to enhance the emission properties of semiconductor nanowires and lower the threshold for lasing. A promising approach is doping with transition metals (TM) or rare earth elements (RE), which show spectral sharp intra-3d(4f) emissions when embedded in a suitable host material [401–410]. Several macroscopic system are realized with this approach, like the wide used Nd:YAG [411] and Ti:Saphhire lasers [412–414]. The realization of such an impurity LED or laser on the nanoscale could be achieved by doping of ZnO nanowires with optical active 3d- and 4f-elements: The nanowire provides the resonator structure in form of efficient waveguiding [20] and partial reflection of the guided light at the facet ends [392] (thus working as mirrors), while the impurities act as light emitters and provide gain due to the population inversion, which can theoretically be reached at low thresholds due to low transition probabilities and resulting long lifetimes of the excited states [186, 189, 190].

Doping of nanowires with transition metals or rare earth elements during VLS synthesis turned out to be difficult [62, 72, 75] due to the low solubility [415–417] and high melting points of the dopants and their compounds [418]. The presence of oxygen in the synthesis conditions could lead to the oxidation of the source materials and formation of secondary phases, hampering the incorporation of the element [75]. Even if doping during growth was achieved, a inhomogeneous dopant concentration was observed, as the dopands were mainly incorporated by VS growth on the nanowire sides instead of VLS growth in the core [245, 246]. The VLS mechanism is further on very sensitive to a change in the growth conditions, which are altered by the addition of dopants [72, 75].

Alternative approaches for the synthesis of doped ZnO nanostructure are wet chemical methods, in which the dopants are directly incorporated during growth. Successful doping could be achieved for several elements [78–82, 419] in ZnO nanocrystals and nanorods, but still the control of the morphology and the dopant concentrations remains challenging. For the wet-chemical synthesized nanostructures, the crystal quality is often limited by the low reaction temperatures compared to the VLS grown nanowires [23].

The doping of high quality VLS grown ZnO nanowires can be realized using ion implantation, which is a widely used and well established technique for the doping of semiconductors. The drawbacks of other doping methods can be avoided, as every element can be implanted with the desired lateral and depth homogeneity and concentrations well above the solubility limit. A disadvantage of this method is the generation of defects due to the interaction of the energetic ions with the target, which can be mainly recovered using appropriate annealing techniques [251].

ZnO nanowires are ideal suited for doping by ion implantation due to the high radiation hardness of ZnO [310, 420], as the materials is not amorphizied even at high ion fluences [421, 422] and shows a very good crystal recovery upon annealing. Optical activation was observed for several dopants in implanted ZnO nanowires [61, 62, 249, 252].

A promising doping elements is the transition metals cobalt (Co), which shows sharp intra-3d emission in ZnO [214, 239, 423]. Intra-3d emission has been observed for wet-chemical synthesized doped nanostructures [419, 424–428] as well as TM implanted ZnO nanowires [61]. Besides the promising optical properties, doping with TM offers interesting magnetic properties. Even ferromagnetism was predicted for TM doped ZnO [429–431] and has been observed [432, 433], although the origin of the magnetism is still not clear and a topic of discussion [434–439]. The combination of the optical properties with the magnetic and electric properties would even enhance the functionality [70].

5.2 Structure and morphology of Co implanted ZnO nanowires

5.2.1 Scanning electron microscopy

As-grown ensembles as well as imprint transferred ZnO nanowires have been implanted with Co using a combination of ion energies of 40 to 380 keV, resulting in a homogeneous implantation profile up to a nanowire diameter of 170 nm at maximum ion range of 350 nm. The ion fluences were adjusted from $7.8 \cdot 10^{14}$ - $1.3 \cdot 10^{17}$ ions/cm^2, resulting in nominal concentrations of 0.05 - 8.0 at.% evaluated by *SRIM* and more realistic concentrations of 0.02 - 4 at.% evaluated by *iradina*. After implantation, the samples have been annealed in air at temperatures of 500°C to 900°C for 30 to 240 min in order to recover the implantation related crystal damage and activate the Co impurities.

The morphology of transition metal doped ZnO nanowire ensembles was analysed using SEM after Co implantation and annealing at 700°C for 30 min in air. Figure 5.1 (a) displays the morphology of the ZnO nanowires after implantation of $7.8 \cdot 10^{14}$ ions/cm^2 (corresponding to a nominal concentration of 0.05 at.% Co), which appears unaltered compared to the as-grown ensemble (see figure 4.1). After implantation of $1.6 \cdot 10^{15}$ ions/cm^2 (equals 0.1 at.% Co, figure 5.1 (b)), the thinner nanowire tips are bended upwards while the thicker parts are still straight, which is also observed for ZnO nanowires implanted with Ar at similar fluences [274]. Implantation of higher Co ion fluences results into stronger bending also for thicker nanowires, as shown in figure 5.1 (c) for a fluence of $1.6 \cdot 10^{16}$ ions/cm^2 (1.0 at.% Co). Most of the nanowires are bended upward (towards the direction of the ion beam) and the nanowires appear thinner compared to the lower Co fluences, although all investigated samples originate from the same mother sample. Simulations of the Co ion implantation were performed using *iradina* to understand the bending mechanism of Co implanted ZnO nanowires. Figure 5.1 (d) shows the simulated ion distribution in the cross section of a 150 nm diameter ZnO nanowire at an ion incidence angle of $\sim$ 45° to the nanowire axis, which is derived from the SEM images in figure 4.1 as the average angle of the nanowires to the ion beam. The Co ions are homogeneously distributed across the nanowire. As the nanowire bending was also observed after implantation of ZnO nanowires with Ar at similar ion energies and fluences [256, 273], the additional incorporation of the implanted species can be ruled out to be the origin of the bending.

For Ar implanted ZnO nanowires, the bending was found to be related to the defects created during the implantation process [256, 273, 274]. Therefore, the vacancy and interstitial distribution was simulated for Co implantation using *iradina*. Although a significant amount of the defects already recombines during implantation at room temperature [420], the remaining defect
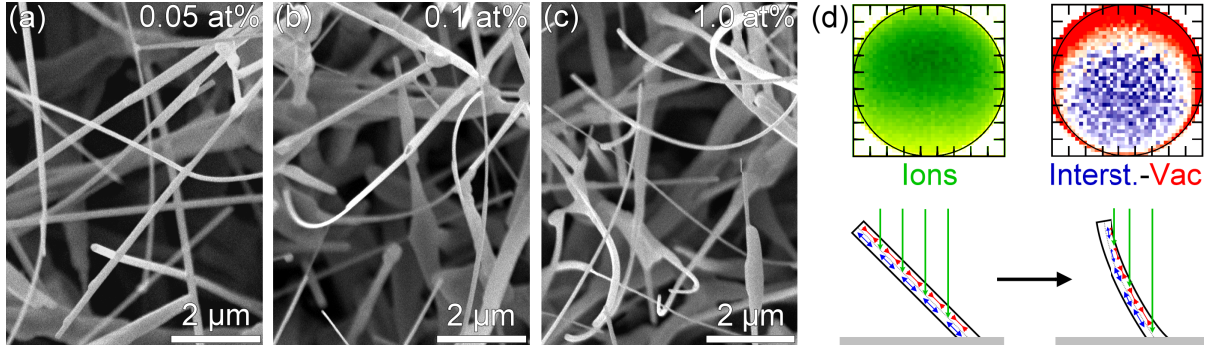
Figure 5.1: *Representative SEM images of ZnO nanowires after implantation of (a) $8 \cdot 10^{14}$ ions/cm^2 Co (nominal 0.05 at.%) and annealing. (b) Implantation of $1.6 \cdot 10^{15}$ ions/cm^2 Co (nom. 0.1 at.%) induces an upward bending of the nanowire tips. (c) The bending of the nanowires towards the direction of the ion beam is increased at a Co ion fluence of $1.6 \cdot 10^{16}$ ions/cm^2 (nom. 1.0 at.%). (d) Bending of the nanowires is not caused by the implanted Co ions as the implantation profile shows a homogeneous concentration. The remaining defects, calculated from the interstitial-vacancy distribution, induces compressive strain due to an excess of vacancies at the upper part and tensile strain due to the excess of interstitials in the lower part of the nanowire cross section, thus leading to the bending into the direction of the ion beam [274].*

distribution, evaluated by the difference of interstitials - vacancies, is inhomogeneous, as shown in figure 5.1 (d). This originates from the defect creations process: when the impinging ion hits a target atom and knocks it from its lattice site, a vacancy remains at this position or is occupied by an implanted Co atom. The interstitial atoms are preferentially driven deeper into the nanowire in the ion beam direction due to the momentum transfer from the Co ions. This process creates an excess of vacancies inducing compressive stress in the upper part of the nanowire, while the lower part exhibits an excess of interstitial atoms, resulting in tensile stress. As a consequence, the nanowire tries to minimize the internal stress by bending upwards to the direction of the ion beam, as sketched in figure 5.1 (d). As the angle between the ion beam and the nanowire declines, the projected range of the ions decreases and the defect distribution is shifted to the upper part of the nanowire cross section. This reverses the stress conditions conditions, so that the nanowire tip is finally aligned to the ion beam direction.

The bending of larger diameter nanowires at higher TM ion fluences occurs as sputtering becomes important above $\sim 5 \cdot 10^{15}$ ions/cm^2 [256]. The effect of sputtering and the influence on the nanowire morphology was investigated in [325]. The sputter yield was calculated using SRIM as an approximation for ion energies between 30 to 380 keV and incidence angles of 0° to 70° towards the surface normal. The sputter yield was calculated to be in the range of 5 - 10 atoms/ion for Co ions impinging perpendicular to the nanowire surface, which is about a factor of 2 less than the sputter yield calculated for rare earth ions [440] and can be obviously attributed to the lighter mass of the transition metal ions. The surface binding energy of ZnO is not well known and was therefore varied in the calculations between 2 to 6 eV, which influenced by calculated sputter yield by a factor of 5. The sputter yield increases for larger incidence angles, as the damage cascade induced the the impinging ion is tilted towards the surface [441], enhancing the energy transfer to surface atoms [325]. Target atoms are preferentially removed from the nanowire surface facing the ion beam, so that the defect distribution is shifted deeper into the nanowire, resulting in the bending of the nanowire parts, which remained straight at lower fluences.

ZnO nanowire ensembles were implanted with different Co fluences and the nanowires were transferred to a clean Si substrate by imprint after annealing. The morphology of Co implanted ZnO nanowires is shown in figure 5.2 (a). No morphological changes were observed up to a transition metal fluence of $1 \cdot 10^{15}$ ions/cm^2, in agreement with the conclusions described above. At higher
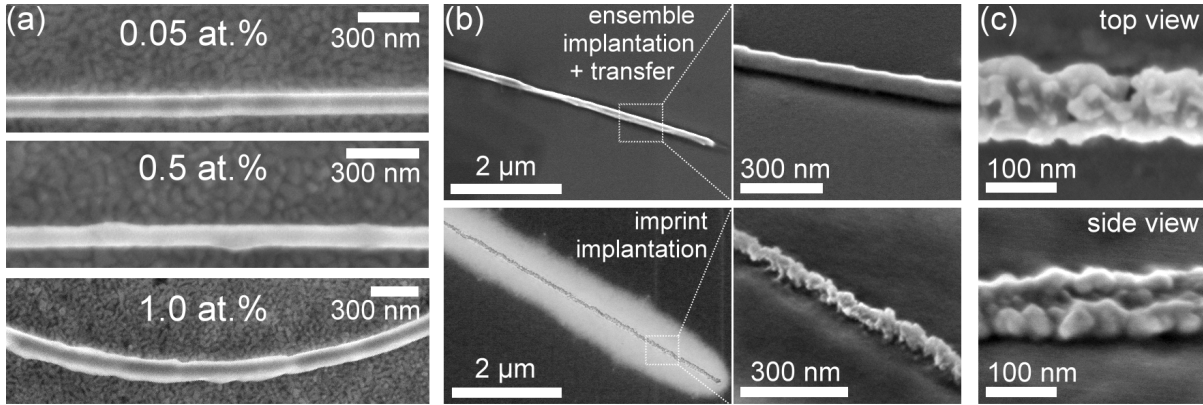
Figure 5.2: *(a) The nanowires exhibit an unaltered surface after implantation of 0.05 at.% Co, but kinks appear in the nanowires at higher concentrations. (b) The ZnO nanowires implanted on the ensemble sample and transferred to a new substrate afterwards show a rather smooth surface with some kinks along the nanowire axis, while the surface of ZnO nanowires implanted on the imprint is strongly roughened. (c) The nanowire height is stronger reduced due to sputter effects than its width.*

ion fluences, kinks developed and resulted in a roughening of the nanowire surface. The effect is well observed above a fluence of $5 \cdot 10^{15}$ ions/cm^2 and increases strongly for higher fluences. Their appearance is related to the statistical nature of sputtering of surface atoms. Although the mean sputter yield was calculated to 5-10 atoms/ion, some ions sputter more than 100 atoms [325], which causes a surface inhomogeneity. The higher surface curvature at the inhomogeneity enhances the sputter yield [441] and the removal of material. Redeposited atoms can diffuse on the surface and re-establish on energetically favourable crystal planes, which has a flattening effect. The interplay of both processes lead to the creation of regularly shapes kinks. Thinner nanowires experience a stronger impact of the sputter effects, as their surface has a stronger curvature at the smaller diameter, which enhances the sputter yields as well [325]. The length of transferred nanowires was shorter compared to the nanowires on the implanted ensemble. The ion implantation causes damage in the crystal structure, which reduces the elastic properties [442–445] and makes the nanowires more brittle, causing them to break into smaller pieces upon imprint transfer.

The effect of the preparation sequence was investigated by preparing a comparison sample by imprint from an as-grown nanowire ensemble and subsequent implantation with $1.6 \cdot 10^{16}$ cm^{-2} Co ions. After annealing, the morphology of those nanowires was compared to ensemble implanted nanowires transferred after annealing in figure 5.2 (b). The nanowires of the ensemble implanted sample are still quite smooth and only some regular kinks are observed, whereas the imprint implanted nanowires show a very different morphology. Those nanowires are not bended even at high fluences as the strong Van-der-Waals forces attach the nanowires to the substrate [446]. However, the nanowire surface is significantly stronger roughened and many kinks are present as well. Their appearance is more irregular and a roughness of 30 nm was estimated for the presented 150 nm nanowire. At a close look on figure, it seems like the implanted nanowires are on an elevated island, while material from the area around the nanowires was removed by sputtering. A stronger thinning of the nanowires was observed in the direction of the ion beam as perpendicular to it, as shown in figure 5.2 (c) by comparing the top and side view SEM image. The stronger damage on nanowires in contact with the substrate compared to free standing nanowires was also observed for rare earth implanted ZnO nanowires [62]. The free standing nanowires experience damage by directly hitting ions [447, 448], where the impact energy dissipates slowly due to the nanoscopic volume of the nanowire and the missing thermal contact to the surrounding, thus enhancing the in-situ recovery of the created defects. The nanowires
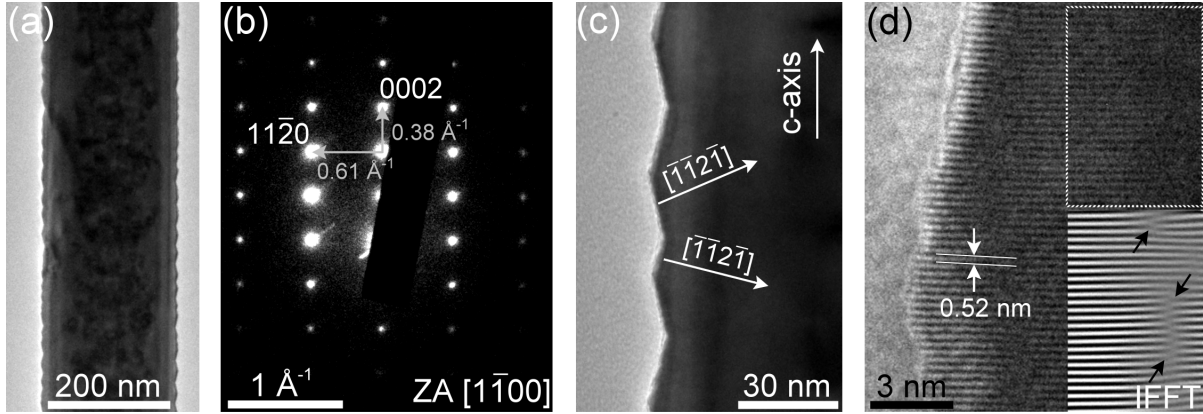
Figure 5.3: *(a) TEM survey micrograph of an implanted ZnO nanowire (1.0 at.% Co) showing a in-homogeneous contrast on the nanowire body. The surface is roughened due to the interaction with the ion beam. (b) The SAED pattern reveals single crystalinity of the Co implanted ZnO nanowire without signs of amorphization or secondary phases. (c) The ion beam induced kinks on the surface show a nearly periodic spacing. The surface could be assigned to the {11$\bar{2}$1} planes. (d) The HR-TEM micrograph reveal a high crystalinity of the {0001} planes up to the a surface with low roughness typically below 1 nm. A few remaining dislocations are observed in the IFFT of the c-plane reflexes.*

in contact with the substrate experience a better dissipation of the ion impact energy, which reduces the dynamic annealing. In addition, those nanowires receive transferred energy of ions hitting laterally close to the nanowire, which enhances the sputtering.

5.2.2 Transmission electron microscopy

Figure 5.3 (a) presents a TEM survey micrograph of a representative ZnO nanowire with 210 nm diameter implanted with a nominal concentration of 1.0 at.% Co and subsequent annealing at 750°C for 240 min. The nanowire body shows an inhomogeneous contrast, which was also observed for RE implanted ZnO nanowires [61, 62, 325]. The origin is probably related to the roughening of the surface or defects in the crystal structure. No evidence for precipitations, segregation or voids has been observed, which is in agreement with previous studies [301, 440, 449]. The selected area electron diffraction pattern presented in figure 5.3 (b) shows that the nanowire remain single crystalline even after implantation of $1.6 \cdot 10^{16}$ ions/cm^2. No signs of amorphizations or secondary phases were found for all examined nanowires. The sharp diffraction spots are a hint for a high crystal quality and could be assigned by evaluation of the angles and distances to the central spot. A good match was found for the spacing of the spots at 0.38 Å^{-1} and 0.61 Å^{-1} to the central spot, which correspond to the (0002) and (11$\bar{2}$0) denoted planes looking from the zone axis [1$\bar{1}$00] in undoped wurtzite ZnO with lattice parameters of $a = 3.29$ Å and $c = 5.24$ Å [99]. The nanowire axis is parallel to the [0002] direction (c-axis), which was assigned to the growth direction of the ZnO nanowires [23, 268]. Kinks appear on the roughened surface of the nanowire in figure 5.3 (a), which is displayed at higher magnification in figure 5.3 (c). A nearly periodic kink spacing of about 30 nm at a depth of 5 nm was observed and originates from the implantation process, as the as-grown nanowires exhibit a very smooth surface without irregularities (compare figure 4.1). The roughened surface is terminated with {11$\bar{2}$1} planes, which seems to be energetically favourable. The high quality crystal structure reaches up to the surface. A microscopic roughness of less than 1 nm is present in the HR-TEM micrograph in figure 5.3 (d), which was also observed for Ar implanted ZnO nanowires [450]. The plane spacing of 0.52 nm matches the assignment to undistorted (0002) planes, which is in agreement with the SAED results. The area marked by the white frame was Fourier transformed and the inset shows the inverse transform (IFFT) of the (0002) reflexes. Some remaining dislocations could
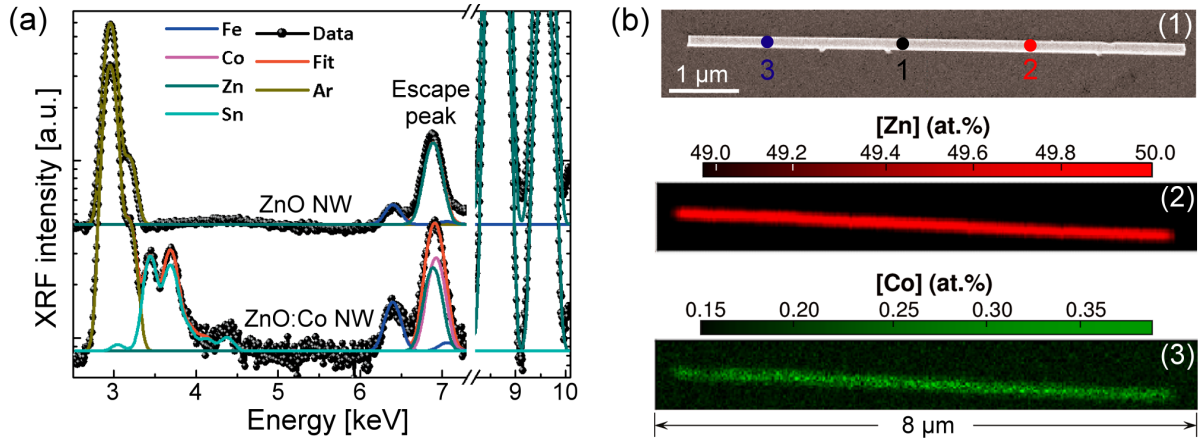
Figure 5.4: *(a) Normalized nanoXRF spectra of a single as-grown and a Co implanted ZnO nanowire. (b) SEM image (1) and elemental XRF mappings for Zn (2) and Co (3) of a single Co implanted ZnO nanowire collected at 12 keV X-ray energy. The respective atomic fraction estimated by XRF quantification is labelled in the colored scale bars. The points mark the positions for XANES and EXAFS investigations. Results are published in [399].*

be observed, which were created during the implantation and are not recovered by the annealing [61, 251, 449]. No formation of secondary phases was observed, as this is expected for higher TM concentrations above 4 at.% [301, 451, 452].

5.2.3 Stoichiometry

The stoichiometry of the Co implanted and annealed ZnO nanowires ensemble samples was investigated using EDX in the SEM. The EDX spectra (not shown) exhibit the expected Zn K_α X-ray emission line centered at 8.63 keV, Zn K_β emission line at 9.62 keV, Zn L emission line at 1.02 keV as well as the O K emission line at 0.53 keV [453]. The quantitative analysis reveals a stoichiometric composition for ZnO at low Co concentrations within the experimental errors. No other elements but the C K emission line at 0.28 keV (carbon contamination on the surface) the Si K emission line at 1.74 keV (low density of nanowires on the growth substrate) were detected. Above the experimental limits of 1 at.%, the Co K_α emission line at 6.92 keV and the Co K_β emission line at 7.65 keV reveal the successful doping of the ZnO nanowires via ion implantation. The Co L emission line was observed as a shoulder at 0.78 keV on the low energy side of the Zn L emission line. The integrated Co K_α X-ray emission intensity was extracted from the spectra and scaled approximately linear within the experimental errors with the Co concentration.

The stoichiometric investigation of the ensemble samples is not representative for the properties of single implanted ZnO nanowires, as their properties are lost in the superposition of the nanowire ensemble and the underlying ZnO background structures. Co implanted ZnO nanowires were therefore imprint transferred to Si substrates and the stoichiometry and local structure of single nanowires was examined using scanning XRF and XAS at the hard X-ray nanoprobe at the ESRF beamline ID22NI. Nano-XRF measurements were performed at 17 keV X-ray energy and a spot size of 50 x 50 nm^2. Figure 5.4 (a) presents the XRF spectra averaged for the scan area of a single as-grown ZnO nanowire (diameter 300 nm, length 15.5 μm) in comparison with a Co implanted nanowire (diameter 180 nm, length 7.7 μm) (nom. 1.0 at.%) [399]. The spectra were normalized to the intensity of the Zn K_α peak at 8.63 keV. The Zn K_α and K_β fluorescence line clearly originates from the ZnO nanowire. The XRF signals of the Ar K_α and K_β fluorescence are detected at 2.96 keV and 3.19 keV, which are generated from the Ar atmosphere surrounding the sample. Escape peaks are produced by the Si drift detector at 1.74 keV below the Zn parent lines. In the same energy range, an additional contribution was detected for the implanted ZnO

nanowire, which could be clearly identified as the Co K_α fluorescence by deconvolution and fitting of the XRF spectra using the PyMca code [281]. The quantification evaluates an average Co content of 0.3 ± 0.1 at.% [400], which is slightly less than the calculated Co concentration using *iradina*.

Gallium was found as additional trace impurity localized in the as-grown as well as in the implanted nanowires. The Ga probably originates from the contaminations of the ZnO source powder used for the nanowire synthesis [323], so that Ga might be incorporated during nanowire growth due to the high solubility in ZnO [454, 455]. This is also reflected by the strong PL intensity of the I_8 donor bound exciton (see figure 4.2 (b)), which is attributed to Ga acting as shallow donor [102]. XRF signals from residual Fe and Sn are also present in the spectra. Lateral resolved measurements revealed an uniform occurrence all over the examined area, pointing out that the signals originate from the substrate or contaminations on the sample and those elements are not incorporated in the nanowire [399].

To examine the elemental uniformity, a 12 keV focussed X-ray nanobeam of 100x100 nm^2 was scanned across several nanowires with a step size of 25 nm. Elemental maps were recorded at 500 ms/point integration time, which are displayed for Zn and Co together with a SEM image of the examined nanowire in figure 5.4 (b). The colour scale represents the XRF intensity at the respective point, which was rescaled by the quantification. The Zn map reproduces well the general morphology of the ZnO nanowire observed by the SEM. The Co fluorescence could also be laterally resolved and reflects a homogeneous Co presence in the ZnO nanowire, without agglomerations or signatures of clusters. The uniform Co incorporation was found for all examined nanowires at the length scale of the X-ray beam size and suggests a co-localization of Zn and Co in the nanowires within the experimental limits, thus a homogeneous doping by ion implantation was achieved.

5.2.4 X-ray absorption spectroscopy

The high lateral resolution of the X-ray nanoprobe was used to examine the local structure of the Co implanted ZnO nanowires by XANES and EXAFS at several positions marked in figure 5.4 (b). The linear polarization of the synchrotron X-ray beam could be used to detect the preferential orientation of defects induced by the ion implantation [456]: the XANES spectra of wurtzite ZnO depend on the crystallographic orientation [457] to the polariztion of the X-ray beam, as both are linked by the the scalar product of the photon polarization vector $\vec{e}$ and the position vector of the electron $\vec{r}$ in the matrix element of the absorption cross section: $M = \langle \phi_{1s} \, | \, \vec{e} \cdot \vec{r} \, | \, \phi_f \rangle$. If the electric field of the absorbed photons is perpendicular to the c-axis, only transitions from the $1s$ to the p_{xy} states are allowed, which probes symmetry of the p_{xy} conduction band states in the ab-plane of the wurtzite lattice. The XANES spectra recorded with the c-axis of the nanowires oriented perpendicular to the electric field vector of the synchrotron beam ($E \perp c$) are displayed in the top half of figure 5.5 (a). The spectral features of the Zn K edge are very similar at the examined positions and reflect the wurtzite structure of the ZnO crystal lattice [458]. The line shape and peak energies provide no evidence for structural disorder in the radial direction of the ZnO nanowires and no signatures of metallic Zn precipitates formed the ion implantation are observed. The spectra in the lower half of figure 5.5 (a) were recorded with the nanowire c-axis oriented parallel to the electric field vector of the synchrotron beam ($\vec{E} || c$), which probes the symmetry p_z conduction band states in the c-plane. The peaks in the spectra originate from the hexagonal lattice structure and no evidence of lattice damage are found along the nanowire. The XANES spectra of the Zn K edge reveal the high structural order in the crystal lattice along the radial as well as the axial direction of the Co implanted ZnO nanowires.
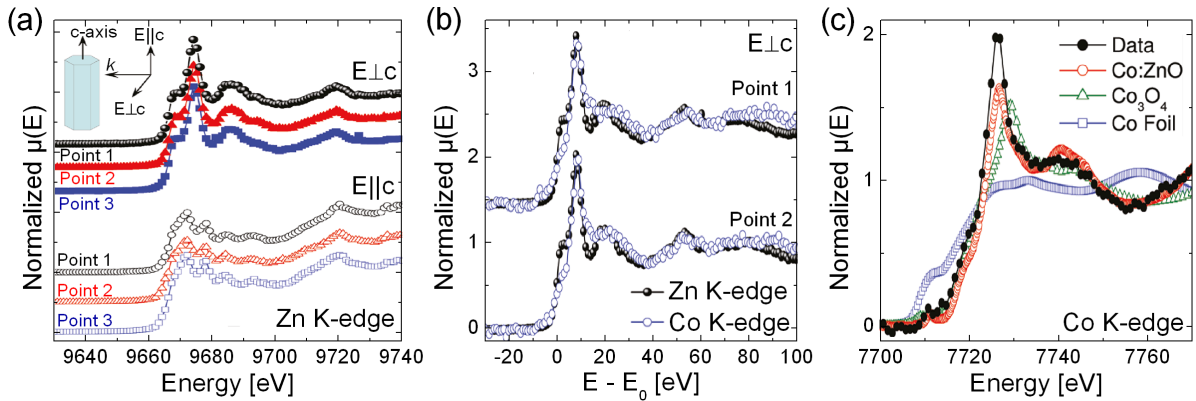
Figure 5.5: *(a) XANES spectra of the Zn K-edge recorded at selected points on the nanowire with the perpendicular (top) and parallel orientation (bottom) of the electric field vector of the polarized X-ray nanobeam to the nanowires c-axis. The spectra have been shifted vertically for visualization. (b) XANES spectra around the Zn and Co K-edge taken at points 1 and 2. The energy was rescaled to the respective absorption K edges. (c) Comparison of the average XANES spectra of the Co implanted nanowire with a high quality wurtzite $Zn_{0.9}Co_{0.1}O$ film [458], a mixed valence Co_3O_4 sample and a metallic Co foil. Data published in [400].*

Figure 5.5 (b) presents the superposition of the XANES spectra around the Zn K edge and the Co K edge measured in $E \perp c$ geometry at positions 1 and 2. The energy has been rescaled to the respective K absorption edge calculated by the first derivative of the XANES data for the direct comparison. Despite the higher noise due to the low Co content, the features of the Co K edge XANES spectra reproduce well the oscillations of the Zn K edge spectra with minor differences above 70 eV at both examined positions. This is a strong evidence for the incorporation of Co ions on Zn sites in the wurtzite ZnO host lattice. The chemical configuration was examined by comparison of the average XANES spectra of the Co implanted ZnO nanowire around the Co K edge with the spectra of a high quality wurtzite $Zn_{0.9}Co_{0.1}O$ epitaxial film [458], a mixed valence Co_3O_4 sample and a metallic Co foil in figure 5.5 (c). The nanowire data show a good match with the spectra of the ZnCoO film, which suggests the 2+ oxidation state for the Co ions in the nanowire. No contributions of metallic Co or mixed valence Co_3O_4 were observed. The weak preedge at 7710 eV is attributed to the hybridization of the Co 3d and 4p orbitals by the influence of the tetrahedral crystal field in the non-centrosymmetric ZnO lattice structure [459, 460]. A strong pre-edge would be typical for the presence of CoO particles as secondary phase [459], but the observed nanowire data support the assumption that the Co ions are substitutionally incorporated in the ZnO lattice.

The local structure was further examined by EXAFS around the Zn K edge at several position on the nanowire. Figure 5.6 (a) displays the k^3-weight EXAFS oscillations and their best fits in the k-space interval of 0 - 8.1 Å^{-1} using a Hanning window. The data were analysed by ab initio modelling of the absorption cross section using the FEFF code [461]. The theoretical backscattering amplitudes and phase shifts for all single and multiple scattering paths have been calculated using hexagonal ZnO model clusters with $a = 3.289$ Å and $c = 5.315$ Å [462]. The ARTEMIS routine [289] was used to fit the Fourier transformed data in R space within the interval 0 - 3.7 Å, which includes the first and second coordination shells. A fit of the third coordination shell was omitted due to the high signal noise above 8 Å^{-1}, which is related to the low counting rate from the investigated nanoscopic volume of the nanowire. A fixed coordination of 4 O nearest neighbour atoms and 12 second nearest neighbour atoms was chosen at the basis of X-ray diffraction data from Co implanted ZnO single crystals [463]. The interatomic distances R_i and the Debye-Waller factors σ_i^2 of the first and second coordinate shell were fitted using a fixed
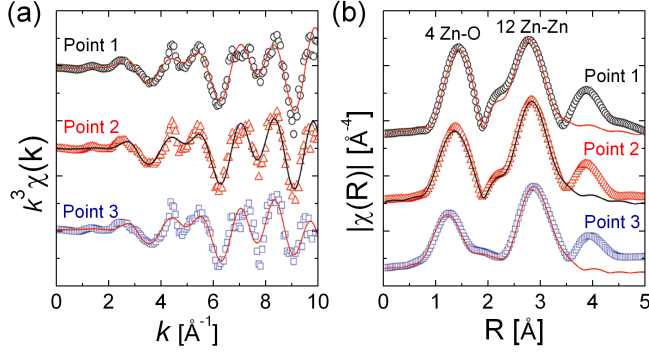
Figure 5.6: *(a) k^3-weight EXAFS oscillations taken a different points on the nanowire accompanied by their best fits in the interval k = 0 - 8.1 $\mathring{A}^{-1}$. (b) Magnitude of the Fourier transforms of the EXAFS function with their best fits for the first (Zn-O) and second (Zn-Zn) neighbour shell. The spectra have been shifted for clarity.*

Table 5.1: *Interatomic distances R_i (in $\mathring{A}$), Debye-Waller factors σ_i^2 (in $10^{-3}\mathring{A}^2$) and R factors obtained from the fit of the Fourier transformed EXAFS data using a fixed amplitude of $s_0 = 0.7307$. EXAFS data and fits are published in [400].*

Point	1	2	3
$\mathbf{R}_{Zn-O}$	1.97±0.02	1.98±0.02	1.98±0.02
σ^2_{Zn-O}	2.3±1.6	3.7±1.6	9.3±2.0
$\mathbf{R}_{Zn-Zn}$	3.25±0.02	3.25±0.01	3.25±0.01
σ^2_{Zn-Zn}	5.0±1.4	4.5±1.3	7.4±1.5
$\mathbf{R}$	0.016	0.011	0.011

amplitude of $s_0^2 = 0.7307$ determined from a metallic Zn foil. The structural parameter derived from the fits are listed in table 5.1. Figure 5.6 (b) shows the magnitude of the Fourier transforms of the EXAFS functions at the respective positions accompanied by the fits. The spectra are dominated by the peaks related to the first O- and second Zn-neighbour shell in agreement with the wurtzite structure model. All examined points show similar contributions and a slight decrease of the first shell amplitude at the different positions. No change in the first and second neighbour distances was detected within the experimental accuracy and the values match well the Zn-O and Zn-Zn spacings of pure ZnO [464]. No evidence of amorphization was observed and the undistorted cation-anion first neighbour distance reflects the low Co doping content, as estimated by the XRF measurements. The reduced amplitude of the nearest O-neighbour shell at the positions 2 and 3 was attributed to a higher static disorder. This is also reflected by the increased Debye-Waller factors especially at position 3, indicating a weakening of the bonding e.g. by the presence of oxygen vacancies. No local atomic distortion was found around the Zn sites, although the Debye-Waller factors increased as well for the respective positions. The analysis of the EXAFS results indicate no significant contribution of ion implantation related defects like secondary phases, vacancy accumulations or significant contributions of interstitials and confirms the good recovery of the ZnO lattice by the thermal annealing after ion implantation, in agreement with the TEM results.

5.3 Optical properties

Directly after ion implantation, only a weak luminescence is detected from the ZnO nanowires, although a large fraction of the created defects already recombines at room temperature [420]. However, the remaining defects limit the optical emission. Thermal treatment at 500°C and above strongly enhances the ZnO emission intensity and provides a sufficient recovery of the crystal lattice, as the displaced atoms can rearrange due to the increased mobilities at elevated temperatures.

Implantation of noble gas atoms leads only to the creation of damage, but no incorporation of the ions, as they are expected to diffuse out of the crystal at the latest during annealing. The remaining crystal damage results in a reduction of the NBE emission intensity and strong enhancement of the green and red defect band, which can be attributed to the presence of interstitial zinc and oxygen vacancies. The ratio between the two defect bands show nearly no dependence on the noble gas concentration [301]. Implantation of other elements than noble
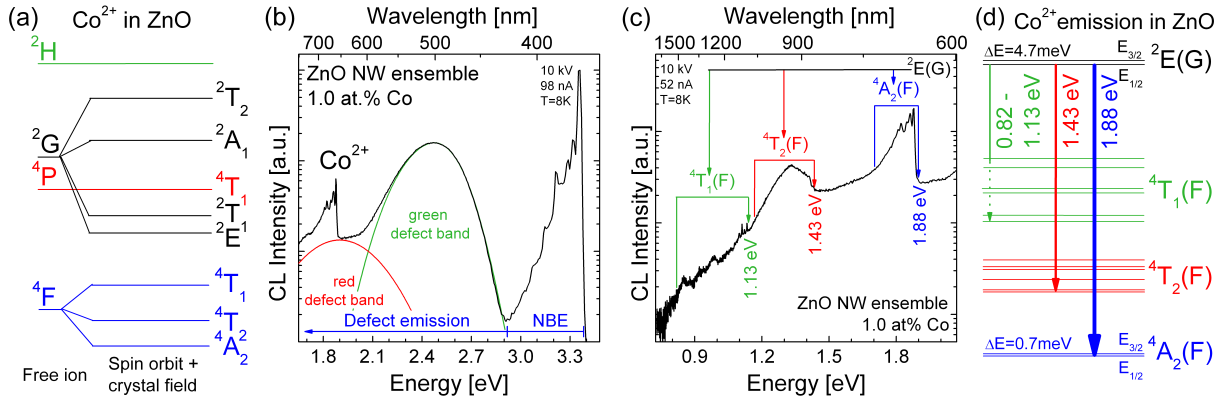
Figure 5.7: *(a) The Co^{2+} levels of the free ion split under the influence of the ZnO crystal field [239, 423]. (b) CL survey spectrum of an implanted and annealed ZnO nanowire ensemble (nom. 1.0 at.% Co) showing the ZnO related near band edge (NBE) and defect emissions. The Co^{2+} luminescence is superimposed to the red defect band. (c) Several Co^{2+} intra-$3d^7$ emissions are detected in the VIS to NIR and could be assigned according to the emission term scheme presented in (d).*

gases usually leads to their incorporation, which is accompanied by further effects. The dopants are mainly incorporated substitutional on zinc lattice sites [346, 347, 465–467], leading to an increased fraction of interstitial zinc and thereby enhancement of the green band intensity.

5.3.1 Co^{2+} luminescence in ZnO nanowires

Co in ZnO is typically incorporated in the divalent oxidation state on substitutial Zn lattice sites [400, 459], in which the Co^{2+} ion has a $3d^7$-configuration. The Co^{2+} free ion levels consist of the ^4F ground state followed by the ^4P as well as the ^2G excited state, as sketched in figure 5.7 (a). For ions embedded in ZnO, the states are mainly degenerated by the influence of the tetrahedral coordinated crystal field (T_d symmetry) [214, 239, 240, 423]. The free ion ground term splits into the $^4T_1$(F) at 0.78 - 1.13 eV and the $^4T_2$(F) terms at 0.45 - 0.55 eV above the $^4A_2$(F) ground term, as determined by absorption measurements [239, 423]. Additional degenerations arise form the trigonal crystal field due to the non-centrosymmetric C_{3v} symmetry of the wurtzite lattice [468], which can treated as a perturbation of the T_d symmetry, as well as spin-orbit interaction. Jahn-Teller interactions play a minor role as the Co^{2+} ions are stabilized by the axial crystal field components [423]. The $^4A_2$(F) ground term is two-fold degenerated and forms two Kramers doublets with a spacing of 0.7 meV in between [423].

The ^4P is not split by the tetragonal crystal field, but transforms into $^4T_1$(P), which degenerates under the influence of the trigonal crystal field components and spin orbit interaction into at least six sublevels at 2.01 - 2.12 eV above the ground term [239, 423]. The ^2G term is located above for the free ion, but splits into the four levels under the influence of the tetragonal crystal field, of which the ^2E(G) at 1.88 eV and the $^2T_1$(G) at 1.93 - 1.98 eV are below the $^4T_1$(P) level, while the $^2A_1$(G) at 2.187 eV and the $^2T_2$(G) at 2.24 - 2.36 eV are located above. The $^2T_2$(G) and $^2T_1$(G) are three-fold degenerated by the trigonal crystal field components and spin-orbit interaction while the $^2A_1$(G) level is not further split [239]. The ^2E(G) term splits into two Kramers doublets separated by 4.7 meV [423].

The CL emission spectra of implanted ZnO nanowires with a nominal Co concentration of 1.0 at.% is presented in figure 5.7 (b). The emission consists of the intense excitonic recombination and the respective phonon replica (NBE) between 3.37 and 2.9 eV as well as the unstructured green defect band around 2.5 eV and the red defect band centered at 1.9 eV. An additional band is superimposed to the red defect band at 1.74 - 1.88 eV, which is assigned to the $^2E(G) \rightarrow ^4A_2$(F) transition accompanied by a phonon side band on the low energy side [239, 240, 423]. The CL
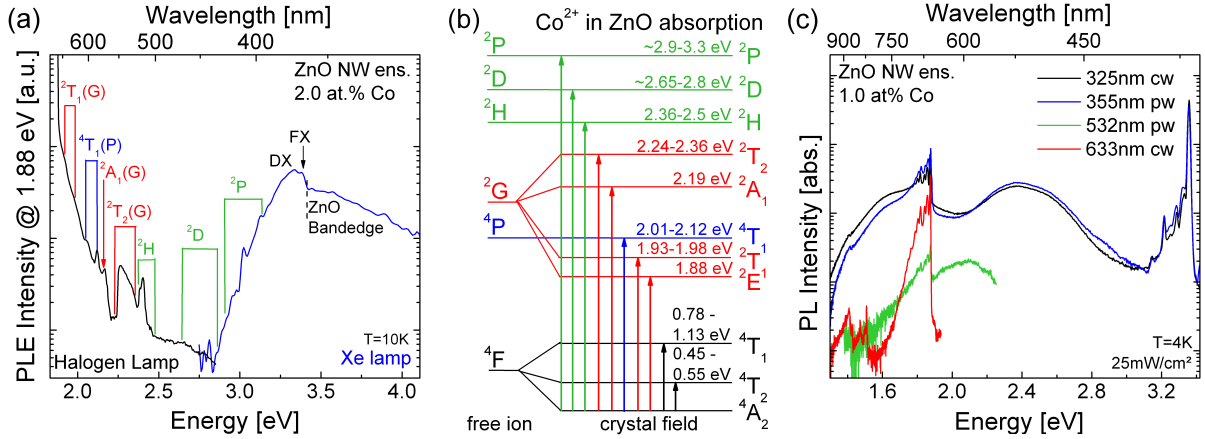
Figure 5.8: *PLE spectra of ZnO:Co nanowires reveal excitation of the incorporated Co^{2+} ions by energy transfer from the ZnO host matrix. (b) Several excited levels could be detected and assigned according to the absorption term scheme. [239, 240] (c) Absolute emission intensity of a ZnO nanowire ensemble (1.0 at.% Co) using different cw and pulsed lasers for excitation above and below and below the ZnO band edge.*

spectrum in figure 5.7 (c) shows several emissions in the NIR range. The emission at 1.43 eV is assigned to the $^4T_2(\text{F}) \rightarrow ^4A_2(\text{F})$ transition accompanied by a phonon side band. The peaks at 0.82 - 1.13 eV are attributed to the $^2E(G) \rightarrow ^4T_1(\text{F})$ transition. The observed Co^{2+} related transitions are sketched in the emission scheme shown in figure 5.7 (c), which includes additional information like the sublevel spacing and assignments derived from absorption measurements [214, 423].

The excitation of the Co^{2+} ions in a ZnO nanowire ensemble (nom. 2.0 at.%) was examined using PLE spectroscopy at low temperatures. The emission intensity of the $^2E(G) \rightarrow ^4A_2(\text{F})$ transition at 1.88 eV was detected as a function of the excitation wavelength using a halogen lamp in the VIS and a Xe high pressure lamp in the UV range. The spectra in figure 5.8 (a) are corrected for the system response, but not for the absolute intensity of the respective excitation source. Several pathways are present for the excitation of Co^{2+} ions: The strong PLE signal intensity above 3.0 eV reveals an efficient energy transfer from the ZnO host lattice to the Co ions. The modulations of the PLE signal are assigned to direct excitation of higher Co^{2+} levels, which decay non-radiative to the $^2E(G)$ level. Figure 5.8 (b) shows a diagram with the energetic positions of the Co^{2+} levels and possible direct excitations from the $^4A_2(\text{F})$ ground state to the higher levels [239, 240], which have been marked in the spectra in figure 5.8 (a). The strong intensity increase below 2.0 eV is attributed to a very efficient excitation via the $^2T_1(G)$ level and non-radiative relaxation as well as resonant absorption of the $^2E(G)$ state. The excitation efficiency at different wavelengths is reflected in the PL spectra plotted in absolute intensity in figure 5.8 (c), which were recorded using excitation by several cw and pulsed lasers with energies above and below the ZnO band gap. The excitation intensity was adjusted to an equal mean power of 25 mW/cm^2 for all lasers. Similar PL spectra are obtained for cw and pulsed excitation above the ZnO band gap, which show the same spectral features compared to the CL spectrum presented in figure 5.7 (a). The slight deviations are attributed to the higher peak power within the nanosecond excitation pulses of the Nd:YAG laser. The intensity of the phonon side band is slightly higher for pulsed excitation, whereas, the overall Co^{2+} emission intensity is nearly comparable. In contrast, pulsed excitation with 532 nm photons is not very efficient, as the Co^{2+} emission intensity is more than one order of magnitude lower compared to excitation above the ZnO band gap. However, continuous excitation at 633 nm is promising as this offers a strong Co^{2+} emission by the resonant excitation of the $^2T_1(G)$ level and nearly

complete suppression of the ZnO defect emission.

CL emission spectra of the main Co emission were recorded in high resolution and analysed in detail in figure 5.9 (b). The two sharp emission lines at 1.884 eV and 1.879 eV can be assigned to the transition from the ^2E(G) $E_{1/2}$ and $E_{3/2}$ level to the $^4A_2$(F) ground levels. The ground term splitting cannot be resolved with the CL setup, but was observed using high resolution PL spectroscopy (not shown). The intra-3d emission is accompanied by a phonon side band at the low energy side [214, 239, 240, 423]. Several ZnO phonon modes could be identified in the spectra in figure 5.9 (b) [125, 240, 469, 470]: (1) the E_2^{low}[Γ] mode at 12.5 meV (101 cm^{-1}) to the respective zero phonon line (ZPL), (2) the E_2(TO)[Γ] mode at 22.3 meV (180 cm^{-1}), (3) the E_2^{high}[Γ] mode at 53.4 meV (437 cm^{-1}), (4) the LO[Γ] at 62.1 meV (501 cm^{-1}) and (5) the TA+TO[H,M] at 76.5 meV (617 cm^{-1}). The shoulders at 1.853 eV and 1.848 eV (marked with e^*) do not fit any ZnO phonon mode. The emission probably results from electronic transitions from excited levels, which were distorted by electron-lattice interaction, resulting in a broad multiphonon band [239, 471]. The appearance of the phonon side band is attributed to disorder in the ZnO lattice due to the incorporated Co ion, which introduced a deviation of the bonding strength so that local ZnO phonon modes, which are forbidden for the pure ZnO crystal, become allowed [239, 240].

5.3.2 Optimization of the preparation conditions

Figure 5.9 presents normalized CL survey spectra of ZnO nanowires ensembles with nominal Co concentrations ranging from 0.05 - 8.0 at.% after annealing at 700°C for 30 min in air. A weak Co emission is observed for the lowest concentration, but increases with concentration and reaches a maximum at the highest concentration of 8.0 at.%. The defect emission intensity increases compared to near band edge emission due to the increase of the remaining implantation defects. High resolution spectra of the $^2E(G){\rightarrow}^4A_2$(F) transition after subtraction of the ZnO defect background are presented in figure 5.9 (b). The emission is dominated by the intra-3d transition accompanied by a phonon side band of low intensity for low Co concentrations. Increasing the Co content, the intensity ratio between the transition from the $E_{1/2}$ and the $E_{3/2}$ level of the ^{2}E(G) term to the ground state stays almost constant, meaning that the population is independent on the Co content. The intensity of the phonon side band increases with Co concentration, which indicates higher structural disorder at the increased Co content [301]. The emission intensities of the near band edge (NBE) emission, defect (DLE) as well as Co^{2+} emission were extracted from the CL survey spectra by integration of the respective energy range and normalization for the integration bandpass. As the Co emission is superimposed to the ZnO defect band, a linear background was fitted and subtracted in the respective energy range. The evaluated intensities were normalized to the lowest Co concentration and are plotted as a function of the Co concentration in figure 5.9 (c). The intensity of the defect emission remains nearly constant up to 1.0 at.% and increases slightly above. The NBE emission intensity decreases slightly for low concentrations and shows a stronger decrease above 1.0 at.% Co. The behaviour of the ZnO emission can be understood regarding the damage creation processed upon ion irradiation: Up to a Co fluence of $\sim 2 \cdot 10^{15}$ ions/cm^2 (0.1 at.%), the implanted Co fluences matches the damage stages I and II [310], in which the ion created damage can be nearly completely recovered by annealing. Higher fluences up to $\sim 2 \cdot 10^{16}$ ions/cm^2 (1.0 at.%) correspond to the damage creation stage III [420], in which the fraction of the remaining damage increases with the fluence, which is reflected by with the slight aggravation of the nanowire optical emission properties. Higher fluences correspond to the damage stage IV [420], in which complex defects are created and not recovered by annealing at moderate temperatures. Thus, the crystal quality decreases stronger at high Co
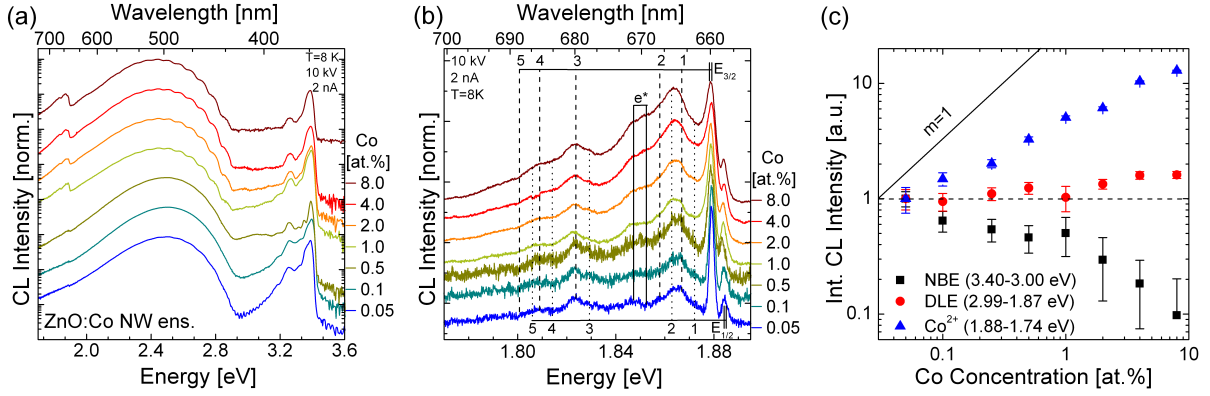
Figure 5.9: *(a) Normalized CL survey spectra of implanted and annealed ZnO nanowires with nominal Co concentrations of 0.05 - 8.0 at.%. (b) The direct Co^{2+} $^2E(G) \rightarrow ^4A_2(F)$ transition in the high resolution CL spectra is accompanied by a phonon sideband, which increases in intensity with Co concentration. Several local ZnO phonon modes (1-5) could be assigned according to literature [61]. (c) Integrated intensity of the near band edge (NBE), defect (DLE) and Co emission normalized on the lowest Co concentration.*

fluences, which is reflected by the lower nanowire NBE emission. This observation is in good agreement with TEM investigations of TM implanted ZnO nanowires: a nearly perfect recovery with only a few remaining extended defects was observed after annealing for a Co concentration of 1 at.% (compare previous section), while a significant amount of disorder remained at higher Co concentrations in the range of 4 at.% [301].

The Co^{2+} emission intensity increases with increasing implanted fluence and no hints for a saturation behaviour ("concentration quenching") were observed up to 8.0 at.%, which is in agreement with the emission behaviour observed for wet chemically grown ZnO:Co nanowires [419] and ZnO:Co nanoparticles [425, 426] with similar Co contents. The emission intensity scales sub-linear with the Co content, which means that not all incorporated Co^{2+} ions are optically activated or are de-excited non-radiatively to killer centers, whose concentration increases also with the implanted ion fluence. The optimum doping fluence is in the range of 1 at.%, as a reasonable Co^{2+} emission intensity is achieved, while the implantation related defects in the nanowires can be mainly recovered by annealing.

The annealing parameters were optimized for a Co implanted ZnO nanowire sample (1.0 at.%), which was split into several parts and annealed in air at different temperatures from 500 - 900°C for 30 min each. CL and PL spectroscopy at low temperatures was used to investigate the morphological and optical properties. The integrated emission intensities of the excitonic recombination (NBE), defect emission (DLE) and Co intra-3d luminescence (Co^{2+}) are displayed in figure 5.10 (a). Annealing at 500°C was sufficient for a recovery of the ZnO defect band with minor contribution of the NBE. After annealing at 700°C, the excitonic emission intensity increased accompanied by the decrease of the defect emission, which can be attributed to a recovery of the implantation related damage. Higher annealing temperatures of 900°C could not improve the optical properties of the ZnO nanowire. Although the red defect band, attributed to interstitial oxygen [348–350, 472] decreased strongly after annealing at this temperature, the excitonic emission intensity degraded, too. The intensity of the green defect band significantly enhances after annealing at temperatures above 800°C. No change of the nanowire morphology was observed up to this temperature, but severe changes occurred for annealing temperatures approaching the growth conditions of T $\geq$ 950°C [271].

An activation of the implanted Co ions at 500°C in form of a broad and unstructured band at 1.88 eV of low intensity was observed. The Co emission increases by a factor of 2 and the sharp emission peaks of the $^2E(G) \rightarrow ^4A_2$(F) transition accompanied by the phonon side band appear in the spectra after annealing at 700°C (compare figure 5.9 (b)). No further enhancement of the
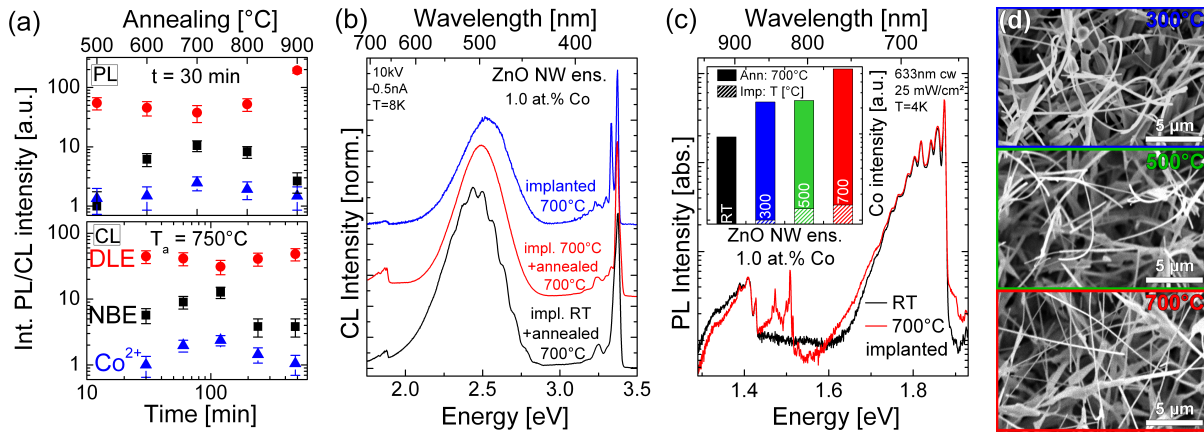
Figure 5.10: *(a) Impact of different annealing conditions on the emission intensity of Co implanted ZnO nanowires. (b) Comparison of CL survey spectra of 700°C to room temperature implanted ZnO:Co nanowires (1.0 at.%). (c) PL high resolution spectra of the $Co^{2+2}E(G) \rightarrow {}^4A_2(F)$ transition under near-resonant excitation show comparable emission intensities for room temperature and 700°C implanted ZnO:Co nanowires. The inset displays the increase of the Co^{2+} emission intensity after implantation at elevated temperatures and annealing.(d) SEM images reveal a significantly reduced bending for nanowires implanted at 700°C.*

Co emission intensity could be achieved at higher temperatures. The sharpening of the intra-3d transition accompanied with the decrease of the phonon side band indicates a higher structural order in the surrounding of the Co ions [249]. The slight decrease of the intra-3d emission intensity is probably related to the formation of CoO or segregation of implanted ions to the surface, as TM ions become mobile at temperatures above 750°C [473].

A Co implanted nanowire ensemble sample (1.0 at.%) was annealed in air at 750°C for different times. An enhancement of the NBE and Co emission intensity was observed up to 120 min annealing time, while the defect emission intensity decreased, especially for the UV band. The sharpening of the Co emission and reduction of the phonon side band intensity indicates that 120 min at the moderate temperature are also sufficient for an effective recovery of the disorder in the lattice. No improvement was found for longer annealing times.

Although ZnO nanostructures have an intrinsic high radiation hardness [310, 421, 422], ion implantation at elevated temperatures could additionally reduce the implantation induced damage due to an enhanced dynamical annealing [68]. To investigate this effect, one ZnO nanowire ensemble sample was split into several parts and implanted at 300°C, 500°C and 700°C with a Co fluence matching nominally 1.0 at.%. The PL emission directly after implantation as well as after annealing at 700°C is compared in figure 5.10 (a) to a equally prepared sample implanted at room temperature. Directly after implantation, the room temperature implanted sample shows no PL emission in contrast to the hot implanted ZnO nanowires. The NBE is dominated by the strong DX emission intensity accompanied by the strong phonon replica, which can be attributed to the remaining disorder in the crystal lattice after the implantation at high temperatures. A broad and unstructured Co^{2+} related emission band of low intensity is observed at 1.88 eV directly after implantation. This directly proves the decreased implantation damage of the ZnO nanowires at elevated implantation temperatures compared to room temperature implantation. Subsequent annealing of the sample at 700°C for 30 min in air (equivalent to the RT implanted sample) further improved the Co^{2+} emission intensity by more than one order of magnitude. The excitonic emission sharpens after the annealing treatment and the intensity of the phonon replica were significantly reduced, indicating a drastic lowering of the interstitial zinc fraction. The green defect band emission was red-shifted by 40 meV. Interestingly, none of the hot implanted samples showed the characteristic modulation of the green defect band, which this was present for

the unimplanted reference area and the room temperature implanted and subsequent annealed sample. The comparison of CL survey spectra in figure 5.10 (b) shows the strong enhancement of the Co^{2+} emission intensity for the hot implanted sample. This is reflected by the integrated Co emission intensity, which are compared for the RT and hot implanted samples in the inset of figure 5.10 (c), both after the subsequent annealing step. A positive influence on the intra-3d emission intensity was already found even for implantation at only 300°C and was further enhanced for higher implantation temperatures. Figure 5.10 (c) presents a direct comparison of the Co^{2+} emission spectra of the 700°C with the room temperature implanted nanowire ensemble taken with 633 nm excitation. The high resolution spectra show the $^2E(G){\rightarrow}^4A_2(F)$ transition at 1.88 eV as well as the $^4T_2(F){\rightarrow}^4A_2(F)$ transition at 1.43 eV, both accompanied by phonon side bands. Additional intra-3d transitions were observed from the resonantly excited $^2T_1(G)$ to the $^4T_2(F)$ at 1.46 - 1.53 eV for the hot implanted sample. Although a significantly decreased Co emission intensity was observed for the room temperature implanted sample at excitation with electrons or photons with energies above the ZnO band edge, resonant excitation by the HeNe laser yields into comparable emission intensities. The comparison proves the different energy transfer efficiencies from the ZnO host to the Co ions depending on the preparation. The room temperature implanted sample probably exhibits more defects, which trap carriers after excitation, thus limiting the efficient excitation of the 3d-impurities.

Another positive aspect was found for the morphology of the implanted ZnO nanowires: the ion beam induced nanowire bending, which was strongly present for room temperature implanted nanowires (compare figure 5.1 (c)), was significantly reduced for implantation at 500°C and a nearly straight morphology was sustained for implantation at 700°C (figure 5.10 (d)). This was also observed for ZnO nanowires implanted at 700°C with a comparable Ar fluence in reference [273, 274]. The elevated temperatures during implantation enhance the mobilities of the ion generated vacancies and interstitials [474, 475], which allow a better compensation of local inhomogeneities of the vacancy and interstitial distribution, thus a bending momentum is effectively reduced and the nanowire remains at its straight morphology.

5.3.3 Dependence on pumping power and temperature

The influence on pumping power was studied using CL and macro PL spectroscopy for an optimized implanted and annealed ZnO ensemble (1.0 at.% Co) (spectra not shown). Within the examined range of 10 mW/cm^2 to 10 W/cm^2 the intensities of all emission features scaled linear with the excitation power, as expected in the low excitation regime. A slight broadening of the NBE emission was observed in the CL spectra, which was attributed to local heating of the sample at high electron currents.

The influence of sample temperature on the optical emission properties was investigated for a ZnO:Co nanowire ensemble (1.0 at.% Co). Figure 5.11 (a) presents the normalized CL survey spectra at several temperatures between 12 to 290 K. The NBE is dominated by the DX emission at 3.36 eV at low temperatures, which decreases rapidly in intensity with increasing temperature and is completely quenched around 110 K, as the donors are ionized around this temperature [325]. The free excitons and their phonon replica govern the NBE at higher temperatures and the emission maximum is red-shifted, which can be described by the empirical Varshni relation [326]. The green defect emission is not shifted, but broadens at elevated temperatures in agreement with the configuration coordinate model (see chapter 4.2.2). The intensity of the red defect band decreases compared to the green defect band at elevated temperatures. The most intense Co^{2+} luminescence is observed at low temperatures. Only slight changes of the emission intensity are present up to 150 K. Higher temperatures lead to an intensity decrease of the intra-3d lumines-
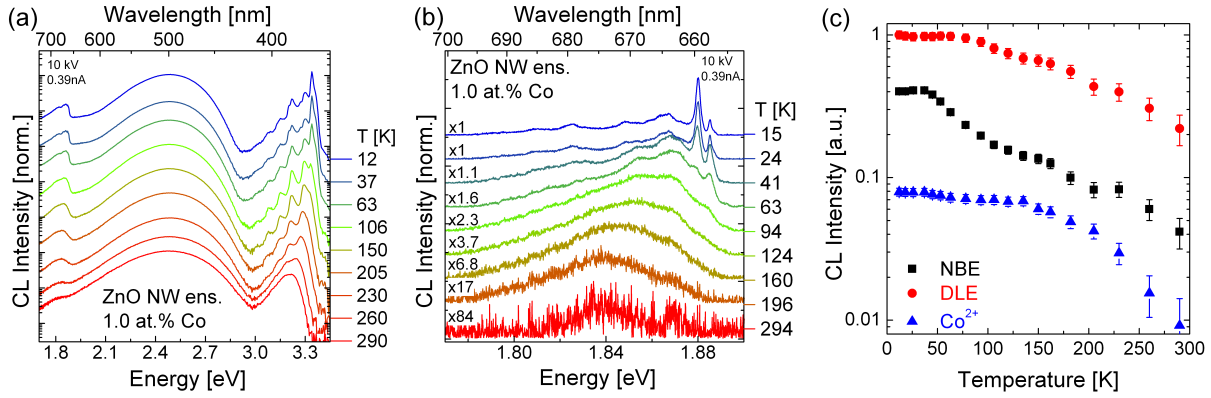
Figure 5.11: *(a) Normalized CL survey spectra of Co implanted ZnO nanowires at temperatures between 12 - 290 K reveal the Co^{2+} emission up to room temperature. (b) High resolution CL spectra show the intensity decrease of the direct $^2E(G) \to {}^4A_2(F)$ transition up to 100 K. The phonon side band dominates the emission at temperatures above. (c) Integrated NBE, DLE and Co^{2+} emission intensity as a function of sample temperature.*

cence, but it can still be observed up to room temperature.

High resolution spectra of the $^2E(G) \to {}^4A_2(F)$ transition are displayed after subtraction of the ZnO defect background at several temperatures in figure 5.11 (b). The Co^{2+} emission is dominated by the radiative intra-3d transition at low temperatures. The intensity of the direct transition decreases strongly up to 60 K and vanishes around 90-100 K. The intensity of the phonon side band is enhanced up to 40 K and dominates the emission at temperatures above, which is related to a stronger phonon coupling at elevated temperatures. The modulation of the phonon side band due to local phonon modes is reduced and only a broad unstructured band is observed above 120 K, which is red-shifted by 40 meV at elevated temperatures.

The integrated emission intensities of the NBE, DLE and Co^{2+} emission were normalized and plotted as a function of temperature in figure 5.11 (c). The intensities of the NBE emission remains constant up to 50 K, decreases by a factor of 2 due to the thermal ionization of the donor bound excitons at temperatures between 60 - 100 K follows the temperature dependence of the free exciton emission up to room temperature [326]. The DLE emission intensity is nearly constant up to 70 K and decreases by a factor of 5 up to RT. The Co^{2+} intensity also remained nearly constant up to 40 K and decreases up to 70 K. At higher sample temperatures, the Co^{2+} descented only slightly up to 150 K, but a strong intensity decrease is observed above. At low temperatures, the Co^{2+} ions can be excited the recombination of exciton bound to the Co ions as well energy transfer from defect states. The slight intensity decrease above 70 K can be interpreted that the excitation by the excitons is less effective at higher temperatures, as e.g. the bound excitons are thermally ionized [102]. Above this temperature, the excitation is mainly due to the less efficient energy transfer from defect states. Above 150 K, enhanced non-radiative de-excitation occurred by phonon interaction or energy transfer to killer centers. A similar temperature behaviour was observed for the emission properties of wet-chemical grown ZnO:Co nanowires and nanorods [419, 424] as well as the absorption properties of Co doped ZnO crystals [214].

5.3.4 Temporal decay of the Co luminescence

The temporal decay of the Co^{2+} $^2E(G) \to {}^4A_2(F)$ transition was investigated for Co implanted ZnO nanowire ensemble (1.0 at.%). Figure 5.12 (a) presents the normalized TRPL spectra at 5 ns integration time for different delays after the excitation pulse. Technical restrictions limited the investigation earlier than 35 ns after the excitation pulse. The spectra show the
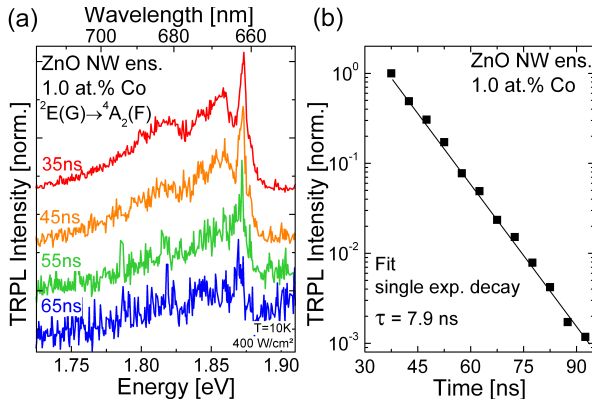
Figure 5.12: *(a) Normalized PL spectra of the Co^{2+} $^2E(G){\rightarrow}^4A_2(F)$ transition of a ZnO nanowire ensemble (1.0 at.% Co) at different delays after the excitation pulse. The spectral shape remains constant at the investigated time scale. (b) The transient can be fitted with a single exponential decay assuming a lifetime of 7.9(4) ns.*
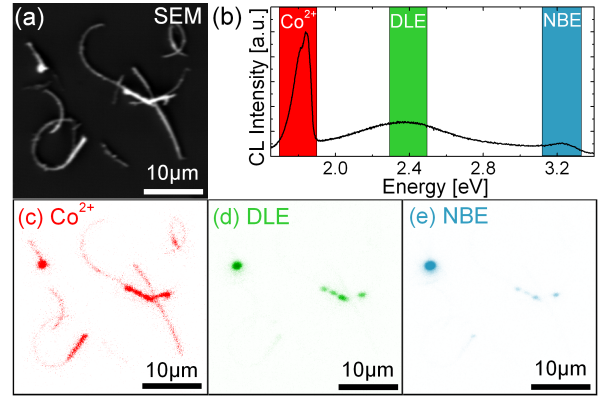
Figure 5.13: *((a) SEM image of dispersed ZnO:Co nanowires, which show a strong Co^{2+} emission in the CL spectrum (b). Monochromatic CL images show the homogeneous Co^{2+} emission (c) of single nanowires. The DLE (d) and NBE (e) emission is localized at thicker nanowire parts, which have not been completely implanted.*

direct $^2E(G){\rightarrow}^4A_2(F)$ transition accompanied by the phonon side band. The emission features are comparable to the high resolution spectra recorded using steady-state excitation conditions (compare figure 5.9 (b)). The spectral shape of the emission does not change within the investigated time range, as it is expected for a intra-3d transition. The integrated PL intensity after subtraction of the ZnO defect background is plotted normalized to 35 ns delay in figure 5.12 (b). The transient can be well fitted using a single exponential function with a radiative lifetime of 7.9 $\pm$ 0.4 ns. The temporal decay of the Co luminescence of ZnO nanowires with nominal 8.0 at.% (not shown) could also be fitted with single exponential decay using a similar lifetimes of 10.2 $\pm$ 0.9 ns. The Co^{2+} ions in ZnO nanowires show a slightly faster decay compared Co^{2+} ions in a single ZnO crystal ($\sim$ 15 ns) with low doping content (10 ppm) [476]. This can be attributed to the higher doping level, at which energy transfer between ions become important and allow fast non-radiative de-excitation. In addition, a higher defect concentration can be assumed for the ZnO nanowires due to the implantation. The short lifetimes indicate that the $^2E(G){\rightarrow}^4A_2(F)$ is a strongly allowed electric dipole transition for Co ions in ZnO [477]. The examined lifetimes for ZnO nanowires are almost one order of magnitude faster as lifetime ($\sim$ 65 ns) reported for wet chemical synthesized ZnO:Co nanocrystals [428]. Due to the small size of the nanocrystal ($\sim$ 3 nm), the Co ions experience a huge contribution of the surrounding in the case of emission, which lowers the effective refractive index, resulting in a reduced transition probability and thus elongates the lifetime (see chapter 2.2.2).

5.3.5 Emission properties of single ZnO:Co nanowires

The emission homogeneity of Co implanted ZnO nanowires was investigated using monochromatic CL at low temperatures, as presented in figure 5.13. The SEM image (a) shows dispersed ZnO nanowires with a nominal 2.0 at.% Co, which were imprinted to a clean Si substrate. The corresponding CL spectrum (b) reveals a strong Co^{2+} emission compared to the rather low intensity of the NBE and defect emission. Monochromatic CL images of the Co^{2+} emission recorded at 1.8 eV (c) with a bandpass of 0.2 eV reflect the strong and homogeneous intra-3d luminescence from the implanted nanowires. Thicker nanowires appear brighter as more ions are present in the excitation volume of the electron beam and contribute to the luminescence. Within the experimental uncertainties, no doping inhomogeneities are observed from the CL images. The DLE and NBE emission (recorded at 2.4 eV (d) and 3.25 eV (e)) are only observed from thicker
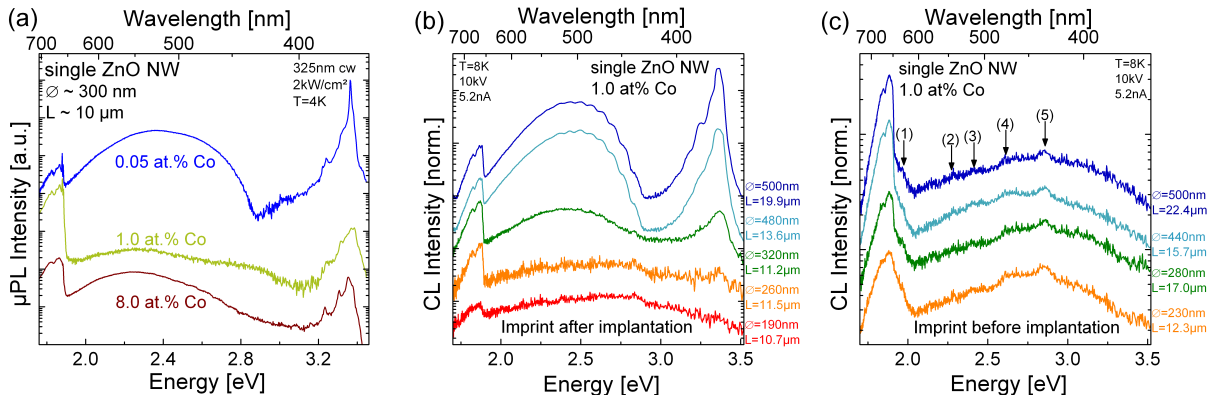
Figure 5.14: *(a) Representative µPL survey spectra single ZnO nanowires with nominal Co concentrations of 0.05 - 8.0 at.% show the strong Co^{2+} emission. (b) CL spectra of single ZnO nanowires transferred to a clean substrate after Co implantation show a strong influence of the nanowire diameter on the emission characteristics. (c) CL spectra of single ZnO nanowires transferred to a clean substrate before implantation exhibit a more homogeneous emission.*

nanowires or attached sail-like structures, which are probably not completely implanted and exhibit undoped ZnO parts.

Figure 5.14 presents typical µPL spectra of single Co implanted ZnO nanowires with nominal 0.05, 1.0 and 8.0 at.% at low temperatures under moderately high cw excitation. The nanowires have comparable dimensions with diameters around 300 nm and length of about 10 µm. For the low Co concentration, the ZnO emission dominates the spectra and is comparable to the implanted ZnO nanowire ensemble emission, but the Co emission is significantly stronger. The Co^{2+} emission dominates the emission spectrum of ZnO nanowires with 1.0 at.% and is significantly more intense than the NBE and DLE emission. The nanowire with nominal 8 at.% has a similar emission spectrum, but the intensity of the phonon side band is stronger as observed before in the ensemble measurements and the defect emission is increased, probably due to the higher defect concentration remaining after implantation and annealing.

The impact of the nanowire diameter on the emission properties was investigated for single Co implanted ZnO nanowires (1.0 at.%), which have been implanted as ensemble and transferred via imprint to a clean Si substrate afterwards. The spectra and the respective nanowire dimensions (diameter and length) are displayed in figure 5.14 (b). For thin nanowires (< 300 nm), the Co^{2+} emission dominated the spectrum and only a minor ZnO related emission was detected. At diameters above, the ZnO emission becomes more prominent and is the strongest contribution for nanowires above 400 nm diameter. The effect can be clearly correlated to the calculated Co ion range in ZnO: The maximum penetration depth at 380 keV ion energy is about 350 nm, which explains well the observation. Thinner nanowires are therefore completely implanted while thicker nanowires exhibits undoped ZnO parts, which are responsible for the increased contribution of the ZnO emission in the spectrum. The length of the nanowires transferred after implantation were in the range of 5 to 20 µm, which are therefore shorter than as-grown and not implanted nanowires transferred by imprint. Although the majority of the implantation related defects have been recovered, the remaining defects weaken the elastic properties of the crystal and shrink e.g. the Young modulus [444, 478], making the nanowires more brittle. Besides this, no influence of the nanowire length was found on the emission spectra.

The optical properties of the imprint sample, which was imprinted first and than implanted, was investigated using CL with equal excitation conditions. No intra-3d luminescence was detected from the Co implanted Si substrate. The CL spectra of single ZnO:Co nanowires with diameters between 230 - 500 nm are plotted in figure 5.14 (c). The Co^{2+} emission bestrides the spectra comparable to the nanowires transferred after implantation and no contribution of the ZnO
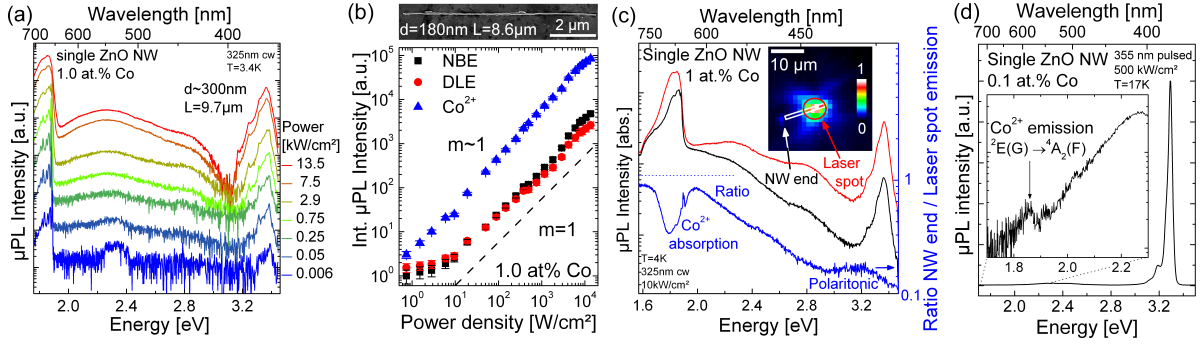
Figure 5.15: *(a) µPL survey spectra of a single ZnO:Co nanowire (1.0 at.%) at different excitation intensities. (b) The evaluated Co^{2+} intensities reveal a linear increase with excitation power. The inset presents an SEM image of the examined nanowire. (c) Lateral resolved µPL spectra of a single ZnO:Co nanowire from the position of the laser spot as well as from the waveguided emission at the nanowire end. (d) µPL spectrum of a single ZnO:Co nanowire at high excitation using the pulsed Nd:YAG laser.*

NBE was observed, even for thick nanowires with diameters in the range of 500 nm. The difference can be explained by the impact of the preparation, as described in section 5.2. The nanowires on the imprint sample experience a stronger damage due to the implantation [62], as the sputter coefficient is enhanced and more material is removed from the nanowires. As a consequence, the diameter is stronger reduced as for free standing nanowires and the nanowires are finally completely implanted (compare figure 5.2 (c)). Additional difference compared to the µPL investigations appear in the single nanowire CL spectra in form of the slight intensity modulations in the range of 1.95 - 2.9 eV, which might originate from radiative intra-3d transitions from higher excited levels to the $^4A_2(F)$ ground state, which are directly excited by hot electrons. The arrows in figure 5.14 (c) mark possible transitions at $(1) = {}^2T_1(G) \rightarrow {}^4A_2(F)$ at 1.95 eV , $(2) = {}^2T_2(G) \rightarrow {}^4A_2(F)$ at 2.27 eV, $(3) = {}^2H \rightarrow {}^4A_2(F)$ at 2.41 eV, $(4) = {}^2D \rightarrow {}^4A_2(F)$ at 2.63 eV and $(5) = {}^2P \rightarrow {}^4A_2(F)$ at 2.86 eV, which have been assigned by comparison of CL spectra with PLE data (figure 5.8 (a)) and absorption data from literature [214, 239, 423, 479].

The emission properties of one single nanowire with ~ 180 nm diameter and 8.6 µm length (1.0 at.% Co) has been investigated using µPL at different cw excitation powers in the range between $1 - 10^4$ W/cm^2. Figure 5.15 (a) presents the µPL survey spectra as a function of excitation power. The respective nanowire is shown in the SEM image in the inset of (b). The Co emission clearly dominates the spectrum at low excitation levels and the NBE and DLE emission are only minor contributions. Note: the elevated PL intensity between 2.25 and 2.4 eV is a system artefact related to the background correction of the CCD camera. At elevated excitation levels around 1 kW/cm^2, the NBE emission broadens as more carriers are generated. The phonon side band of the Co^{2+} emission also gains intensity and dominates the emission above 7 kW/cm^2, which is attributed to local heating of the nanowire by the laser beam at high excitation powers [309]. Figure 5.15 (b) presents the integrated µPL intensities as a function of the excitation power. The emission intensities of the NBE and DLE emission raise sub-linear in intensity up to 10 W/cm^2, following by a linear slope above. A similar behaviour is seen for the defect emission. The Co emission scales linear over a wide range of excitation powers, a slight deviation from this behaviour and sub-linear increase is observed above 3 kW/cm^2. The local heating is expected to enhance the non-radiative excitation at the high power levels.

Waveguide emission could be observed on the nanowire ends for some implanted ZnO nanowires, especially for thick nanowires (diameter ≥ 400 nm) of the hot implanted sample. Lateral resolved µPL spectra of the nanowire emission at the position of the laser spot as well as the waveguide emission from the nanowire facet end is presented in figure 5.15 (c). The emission at the position of the laser spot is characterised by the typical emission features of Co implanted ZnO nanowires

(compare figure 5.14 (a)). The emission from the facet end is less intense, but shows the same luminescence features. The NW end to laser spot emission ratio plotted below the µPLspectra in the 5.15 (c). A high ratio ($\sim$ 80 %) of the light with photons energies between 1.6 and 2.0 eV is guided with low losses from the laser spot to the nanowire end. The defect emission at energies below or above the Co^{2+} emission is less reduced than the intra-3d emission itself, which can be attributed to resonant re-absorption and emission processes of Co^{2+} ions in the nanowire [239, 423]. At higher energies, the ratio decreases nearly exponentially (linear decrease in logarithmic scale) at higher photon energies, as the ZnO waveguide has a higher self-absorption due to defect states in this range. A deviaton from this behaviour is found between 2.9 and 3.3 eV, which can be attributed to the properties of active (polaritonic) light transport in the ZnO nanowire [167].

The light transport properties are strongly related to the nanowire diameter, as the light is only guided with good confinement inside the nanowire above a critical diameter, as observed for undoped ZnO and CdS nanowires in chapter 4.3.3. The critical diameter for the Co^{2+} emission can be estimated to $\sim$ 340 nm, assuming the wavelength at the maximum of the Co intra-3d emission ($\sim$ 670 nm) and a refractive index of n = 1.98 [110] at the respective wavelength. This gives a reasonable explanation for the observation of waveguide effects only implanted nanowire of large diameters as well as the observed linear slope in the power dependent measurement, as the diameter of the examined nanowire was well below the critical diameter to enable efficient waveguiding and possible light amplification.

The emission properties in the high excitation regime were investigated using nanosecond pulsed excitation at 355 nm. The emission intensity of the implanted ZnO nanowires was significantly lower upon pulsed compared to cw excitation, which probably results from the short temporal response of the nanowire luminescence. A measurable intra-3d PL intensity from implanted ZnO nanowires was only observed at significantly higher excitation powers in the range of 300 kW/cm^2, at which unimplanted ZnO nanowires typically show a very intense emission by lasing oscillations (see previous chapter 4.2.4). The µPL spectrum of a single Co implanted ZnO nanowire (0.1 at.%) at high pulsed excitation was dominated by the ZnO near band edge emission with minor contributions of the defect emission (figure 5.15 (d)). The Co emission intensity is significantly less intense compared to cw excitation (µPL spectrum of the single NW with 0.05 at.% in figure 5.14 (a)). The observation points to a saturation behaviour of the Co emission at high pumping levels, as all Co ions are excited within the time scale of the excitation pulse and the additionally created carriers recombine via excitonic recombinations in the ZnO lattice. Although the majority of the implantation related defects have been recovered (see TEM and XAS data), the implanted nanowires seem to be limited in their ability for light amplification. This probably results from a stronger absorption of the implanted ZnO crystal. A similar observation was found for ZnO nanowires, whose facet ends were modified using the focussed ion beam microscope (FIB) [302]. Although the nanowire ends were irradiated by the Ga ion beam, a significantly weaker emission intensity and no light amplification was observed, even after annealing of the samples.

5.4 Summary

ZnO nanowires were doped with Co using ion implantation and subsequent annealing. The implantation of the free standing nanowires in the ensemble results in surface roughening and bending of the nanowires at high fluences in the range above $5 \cdot 10^{15}$ ions/cm^2. Nanowires in contact with the substrate suffer from a higher related implantation damage due to increased sputtering. The implantation related damage can be mainly recovered using appropriate annealing conditions, so that the implanted nanowire retain their high quality single crystalline

structure. Even the bending can be avoided at elevated implantation temperatures. EDX and nanoXRF measurements on single nanowires reveal successful doping with the desired concentrations. Lateral resolved XAS spectroscopy reveals the presence of Co ions in the 2+ oxidation state in a nearly perfect surrounding.

The optical activation of the Co^{2+} ions was observed after annealing above 500°C. Sharp and intense emission peaks were observed at low temperatures, which could be attributed to several Co^{2+} intra-$3d^7$ transitions. The Co ions can be excited by energy transfer from the ZnO host or via near-resonant optical stimulation. The Co concentration and annealing conditions were optimized for an intense Co luminescence. No saturation of the Co emission was found up to nominal 8 at.% Co, although the defect emission increased strongly above 1 at.% due to the creation of extended defects at the high fluences necessary, which cannot be recovered by annealing. For room temperature implanted samples, the best emission properties were found for annealing at 750°C for 120 min in air. Implantation at elevated temperatures could improve the Co^{2+} emission intensity by one order of magnitude. The sharp Co luminescence is most intense at low temperatures. At elevated temperatures, the Co emission intensity decreased by a factor of about 100 and only a broad phonon side band is observed in the spectra. A linear relation between the emission intensity and the pumping power was observed in the low excitation regime. TRPL spectroscopy could determine a lifetime of 10 ns for Co in ZnO nanowires, which is slightly faster compared to ZnO:Co single crystals. The emission properties of single implanted nanowires are governed the intense intra-3d emission. The emission properties for free-standing implanted nanowires depend on their diameter, which is related to the ion range. Power dependent measurements on one single nanowire show a linear power dependence for cw excitation up to 10 kW/cm^2. Waveguide effects were observed for large diameter nanowires at local cw excitation. A saturation of the Co luminescence was noticed for pulsed excitation in the high power regime (> 100 kW/cm^2).

6 Manganese and Terbium implanted ZnS nanowires

This chapter discusses the structural and optical properties of manganese (Mn) and terbium (Tb) implanted ZnS nanowires. ZnS nanowires were synthesized in close collaboration with Michael Kozlik and Franziska Riedel. Details of the growth process are published in their respective diplomas theses [24, 267, 269, 270, 480]. The investigation of Mn implanted ZnS nanowires was performed in collaboration with the group of Prof. Dr. Wolfram Heimbrodt (Phillips-Universität Marburg). Experiment design and sample preparation was executed in Jena, the optical experiments were performed by Uwe Kaiser in Marburg [88]. The data were interpreted in close collaboration. Parts of the results are published in [481, 482]. The experiments on terbium implanted ZnS nanowires were carried out in close collaboration with Franziska Riedel as well as Uwe Kaiser and Sebastian Gies (Phillips-Universität Marburg) [480, 483]. The work is partly published in [482].

6.1 Motivation

Zinc sulfide doped with manganese (Mn) and terbium (Tb) are well known phosphors and exhibit intense intra-3d(4f) luminescence from the impurities [484, 485]. The energy transfer from ZnS to the impurity states is very efficient, so that the excitonic ZnS emission can be completely quenched for high concentrations (typically > 1 at.%) [486]. Intense impurity emission by electroluminescence was observed for both dopants [484, 485], which made those elements interesting for the realization of thin film electroluminescence (TFEL) devices [487, 488]. The full colour range can be covered by the choice of the suitable dopant [233, 489, 490].

Doped ZnS nanocrystals even showed an increased emission intensity compared to bulk crystals and thin films [491], which was attributed to the increased quantum efficiency [492, 493]. So far, only doped ZnS nanocrystals have been realized as phosphors [494–496], but Mn or Tb doped ZnS nanowires would exhibit enhanced properties. The incorporation of the dopants into VLS grown nanowires is difficult (as described in chapter 5.1), but doping via ion implantation was proven to be successful [9, 497]. The impurities would act as light emitter while the nanowire geometry provides an efficient waveguide [20]. The combination of impurities and nanowires could yield into an electrically driven highly localized unidirectional emitting impurity LED. Making use of the resonator properties of ZnS nanowires [176], even electrically driven impurity nanolasers seem possible.

Mn^{2+} in ZnS shows an intense emission around 2.14 eV (580 nm), originating from an intra-$3d^5$ transition from the excited $^4T_1$(G) (S = 3/2) to the $^6A_1$(S) (S = 5/2) ground state [498] for ions incorporated substitutionally on a Zn site [499]. The internal transition is spin forbidden for the free ion, but the incorporation into the ZnS host matrix partly lifts the selection rules due to the reduction of local symmetry and s,p-d hybridization in the formation of the electronic band structure [500, 501]. Due to the low transition probability, isolated Mn ions in a nearly defect-free ZnS host matrix show a single exponential decay with a very long intrinsic lifetime of 1.8 ms [502]. The presence of defects in the closer surrounding of an excited Mn ion leads to strong non-exponential decay behaviour [498]: The Mn ions can de-excite by energy transfer to a defect related non-radiative site ("killer center"). This fast process therefore shortens the lifetime of the excited ions. Additional Mn ions in the closer surrounding of the excited ion promote the reduction of the Mn lifetime: resonant energy transfer between Mn ions becomes possible and the fast energy migration within the Mn subsystem makes it more probable for an excited ion to interact with a killer center. The Mn lifetime at a given defect concentration is

thereby further reduced, as more killer centers are involved. The temporal behaviour is therefore determined by the interplay of the two length scales, the mean Mn-defect distance (influenced by the defect concentration) and the mean Mn-Mn distance (influenced by the Mn concentration). Both scales are typically in the nanometer range (1-100 nm), therefore geometrical restrictions induced by e.g. ZnS nanostructures will have an additional effect on the temporal decay of the Mn ions [9].

A significant influence of the sample morphology and the Mn concentration on the temporal intra-3d decay was proven for implanted ZnS nanowires and nanobands with otherwise same properties and preparation [9, 183, 325]. The transients can be described by a model, which modified the Förster dipole energy transfer and its extension [230, 503] for 1D and 2D sample geometries [9]. The model takes into account three major contributions: resonant energy transfer (migration) between Mn ions, the interaction between Mn ions and killer centers as well as the dimensionality of the host nanostructure. The dimensionality results from the length scales of the mean Mn-Mn and Mn-defect distances in comparison to the nanowire diameter and length. Using correct parameter and dimensionality, the temporal behaviour of the luminescence can be correctly described from a few microseconds to several milliseconds [504]. Different ZnS nanostructure morphologies and Mn concentrations combinations covered the successful verification of the modified Förster model for these two contributions [9, 183]. In the experiments performed in this thesis, the Mn-defect interaction will be addressed by systematic variation of the defect concentration and the model verified for this parameter [88, 481].

Tb^{3+} in ZnS shows an intense green emission due to electronic intra-$4f^8$ transitions. High efficient electroluminescence devices were realized based on ZnS:Tb thin films [505]. For ZnS nanostructures, successful Tb doping was only reported for wet chemical grown nanocrystals [491, 493, 495] of otherwise rather poor crystal quality. The incorporation of Tb and other rare earth elements into high quality ZnS nanowires by ion implantation would open new possibilities. The experiments in this thesis investigate the structural and optical properties of the Tb implanted ZnS nanowires. The understanding of the emission properties of ensembles and single nanowires are crucial for the future realization of nanoscaled electroluminescence devices, which could be based on the adaption of thin-film electroluminescence concepts [233, 505] for ZnS:Tb nanowires.

6.2 As-grown ZnS nanowires

ZnS nanowires were synthesized by a CVD process using a horizontal tube furnace [270, 480]. The growth parameter were tuned to achieve reliable synthesis and optimized nanowire morphologies. Growth of ZnS nanostructures was found between 970 to 830°C. High temperatures and high transport gas pressure around 300 mbar lead to the formation of belt like structures with length up to 100 µm, width of 1 to 10 µm and a thickness of about 50 nm. At intermediate temperatures (around 900°C) and pressures around 100 mbar, long and straight ZnS nanowires were synthesized with diameters between 100 - 400 nm and length up to 100 µm, as shown in the SEM image in figure 6.1 (a). Further reduction of the pressure promotes the synthesis of nanowires with smaller diameters between 50 - 100 nm.

The morphology and crystal structure was examined using TEM. Figure 6.1 (b) shows a low magnification image of a typical ZnS nanowire with a smooth surface without observable imperfections. A droplet is often attached to the wire end. Stoichiometric analysis by EDX (not shown) identified Au from the catalyst, thus confirming the VLS growth of the ZnS nanowires. Residual Zn but no S is found in the Au catalyst droplet [270], which approves the assumption that the metal component (Zn) is incorporated via the liquid catalyst while the non-metal component (S) is incorporated at the interface between catalyst and nanowire [261]. The nanowire body was
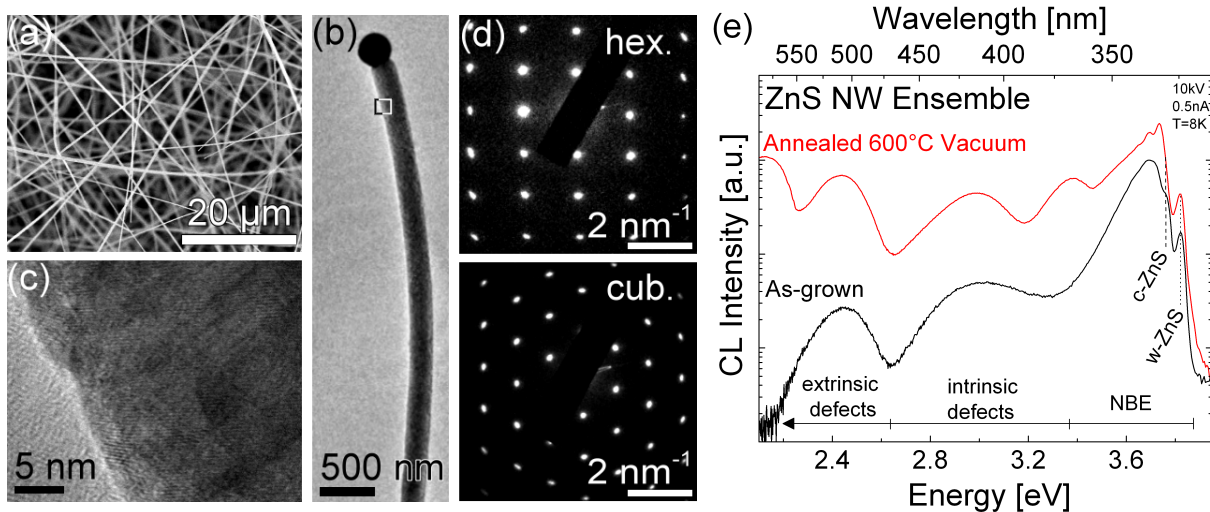
Figure 6.1: *(a) SEM image of an as-grown ZnS nanowire ensemble. (b) TEM image showing the smooth surface of a straight ZnS nanowire with catalyst dot. (c) HRTEM reveals the high quality lattice with different crystal phases. (d) SAED images show the occurrence of both the cubic and the hexagonal crystal phase in the ZnS nanowires. (e) CL overview spectra of the as-grown and annealed ZnS nanowire ensemble.*

found to be stoichiometric ZnS without any other impurities within the detection limits. High resolution images, as shown in figure 6.1 (c), reveal a high quality crystal lattice. Irregularities in the crystal structure are present, which do not originate from defects or dislocations. SAED investigations (figure 6.1(d)) can explain this by the presence of both the cubic and wurtzite phase, as typically observed for ZnS nanowires [267, 270]. The cubic lattice structure is usually more stable at temperatures below 1020°C [506], but the nanoscaled dimensions allow the occurrence of the wurtzite phase at temperatures similar to the growth temperatures [7]. The nanowires are therefore no single crystals, but often show a preferential crystal direction.

Optical investigations of an as-grown ZnS nanowire ensemble using CL at low temperatures show three emission bands (figure 6.1 (e)): The most intense emission between 3.3 and 3.9 eV is attributed to the recombination of carriers by donor bound (DX, 3.77 eV) [507] and acceptor bound excitons (AX, 3.73 eV) [508, 509] as well as direct recombinations of electrons with ionized acceptors (e,A, 3.62 eV) [122, 123]. The modulation of the band on the low energy side can be explained by the occurrence of longitudinal optical phonon replica (LO) with an energetic spacing of 43 meV [126]. A distinct peak appears on the high energy side at 3.87 eV is attributed to the recombination of the wurtzite phase [106]. The CL measurements further confirm the presence of both the cubic and wurtzite crystal phase in the nanowires.

The two emission bands at lower energies are assigned to intrinsic and extrinsic defects: The emission centered at 2.96 eV is related to recombination of carriers at zinc and sulfur interstitials and vacancies [130, 131]. A distinct assignment of the origins is excluded due to the band width of ~ 640 meV without specific features, but the recombination at vacancy states is regarded at lower energies to the interstitial states [137]. The origin of the band centered at 2.44 eV is still a point of discussion in literature. Its appearance in nominal undoped ZnS bulk material and nanostructures allows the assignment to intrinsic defects [510–512], like interstitial zinc in tetrahedric and octahedric sites. But an alternative interpretation is the recombination at extrinsic defects caused by unintentional doping with other transition metals (e.g. Ag, Cu, Al, Mn), as their emissions are typically observed in the same energy range [498, 513, 514]. As those elements are usually not incorporated into the nanowire during VLS growth, but accumulate in the catalyst dot, it is more likely that the defect emission originated from incorporated Au itself [140, 141].

Annealing of the as-grown ZnS nanowire ensemble in high vacuum atmosphere at 600°C for 30 min was performed, as these conditions were determined for a sufficient recovery of ion implanted ZnS nanowires [497]. The effects on the luminescence were investigated using equivalent CL conditions (figure 6.1 (d)). The intensity of the emissions band change slightly and a new band centered at 3.39 eV appears at some samples, which is assumed to originate from a DAP transition caused by unintended contamination with an impurity acting as a donor [267]. The stronger emission of the DX supports this assumption. Other samples show an additional emission band centered at 1.9 eV, especially for long annealing times. The appearance of the band is correlated to the incorporation of oxygen close to the surface [88, 515].

6.3 Mn implanted ZnS nanowires

6.3.1 Mn^{2+} luminescence in ZnS nanowires

ZnS nanowires with diameters of 100 - 300 nm and length up to 50 µm were transferred by isopropanol solution to clean Si substrates and implanted with Mn using different ion energies (20-380 keV) to establish a homogeneous concentration profile within the nanowire diameter. The ion fluencies were chosen to arrange Mn concentrations of $0.14 \cdot 10^{-3}$ and 0.14 at.%, corresponding to low and high Mn doping conditions with minor and major migration effects, respectively. Good optical activation of the Mn was found for subsequent annealing at 600°C for 30 min in vacuum [497]. Electron spin resonance (ESR) measurements could confirm the location of the Mn ions on Zn lattice sites [516]. Spacial resolved CL measurements proof Mn^{2+} intra-3d-luminescence originating only from the implanted ZnS nanowires [325]. Three approaches were used to alter the concentration of killer centers: 1) implantation at elevated temperatures, 2) post-implantation annealing and 3) implantation of additional Ne ions.

The samples were investigated using TRPL with 355 nm excitation at a temperature of 10 K. A series of processed and normalized spectra of the Mn luminescence taken at different times after the excitation pulse is plotted in figure 6.2 (a). The given time values correspond to the delay time from the excitation pulse at the center of the integration time window (value in brackets). Delay and window time were gradually extended to follow the Mn decay: the integration time window was set to 0.1 µs for early delay times up to 2 µs and extended to 1 µs up to 20 µs delay. 10 µs integration time was used between 20 and 200 µs, 100 µs up to 2 ms finally 1 ms integration time windows for later delay times. A single broad emission centered at 2.14 eV can be observed from some hundred nanoseconds up to several milliseconds. The spectral shape does not change for all investigated times, which is characteristic for the intra-$3d^5$ transition of Mn^{2+} ions. The integrated Mn PL intensity is plotted as a function of the delay time in figure 6.2 (b) for the sample implanted at 600°C with low Mn content. The transient shows a fast reduction of the Mn luminescence intensity at short times followed by a slow but nearly single exponential decay later. The rapid intensity decrease at early times is caused by fast energy transfer from excited Mn ions to killer centers. After those ions have been de-excited, the decay at later times is dominated by isolated ions and therefore nearly single-exponential. The observed behaviour can be well described by the modified Förster model (equation 6.1) [9, 183]. The model described the energy transfer by dipole-dipole interaction between the Mn ions and killer centers, which is proportional to R^{-6}, with R being the distance between the excited Mn ion and energy acceptor (Mn ion or defects). $R_0 = 4.85$ nm is the critical length at which radiative recombination and dipole-dipole energy transfer has equal probability for the excited Mn ion. The length was determined from experiments analyzing the PL decay of spherical ZnS:Mn nanoparticles with diameters below 10
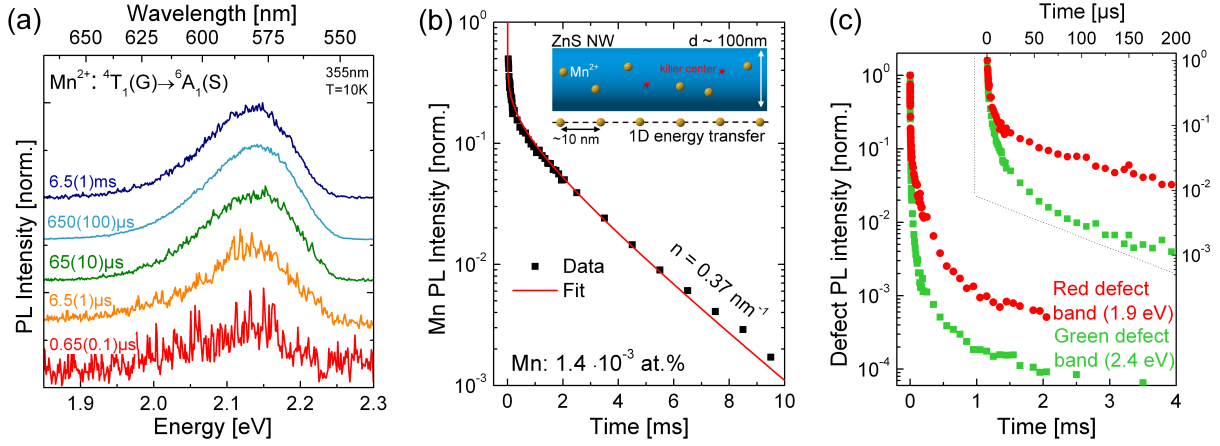
Figure 6.2: *(a) Luminescence spectra of the Mn implanted ZnS nanowires (1.4·10⁻³ at.-%) after annealing at 600°C. The spectral shape of the Mn^{2+} $^4T_1 \rightarrow ^6A_1$ transition does not change at different delay (integration) times. (b) The transient Mn decay of the ZnS nanowires can be fitted using the modified Förster model for D = 1, which is interpreted as preferential energy transfer along the nanowire axis. (c) Transients of the red and green defect band: the intensity of the red defect band limits the reliable data acquisition at short times especially for the low Mn samples.*

nm [504]. The normalized transient $\langle I(t)/I_0 \rangle$ can be fitted by

$$\left\langle \frac{I(t)}{I_0} \right\rangle = exp\left(-\frac{t}{\tau_{Mn}}\right) \cdot exp\left(-\alpha \cdot n^D \cdot R_0^D \cdot \left(\frac{t}{\tau_{migr}}\right)^{D/6}\right), \qquad (6.1)$$

where τ_{Mn} is the radiative lifetime of isolated Mn ions. A value of 2.5 ms was derived from the single exponential tail of the transient at large delay times, which is larger than the lifetime of 1.8 ms for Mn ions in a defect free bulk surrounding [502]. An explanation is given by the influence of the refractive index n of the surrounding media on the transition probability (and therefore lifetime) of the excited ion (see chapter 2.2.2): the emission of excited ions extends as evanescent field into the surrounding of the nanostructure. Due to this effect, the ion experiences a refractive index, which is intermediate between the bulk value and the surrounding air/vacuum ($n \cong 1$) [9]. The reduced effective refractive index decreases the transition probability and thereby extends the radiative lifetimes of the excited ions in nanostructures. The parameter D accounts for the dimensionality of the system and $n = N/R_g$ is a defect line density with N defects within the sample extension R_g in one, two or three dimensions. $\alpha = 1.129, 1.354$ or $\sqrt{\pi}$ is a factor calculated from a Γ-function depending on the dimensionality $D = 1, 2$ or 3. The migration time τ_{migr} accounts for the effectiveness of the excitation migration by energy transfer within the Mn subsystem. For isolated ions without migration effects, it has an upper limit of the natural Mn lifetime ($\tau_{migr} = \tau_{Mn}$). Higher Mn concentrations (shorter mean Mn-Mn distance) make excitation migration more effective (and faster), leading to a smaller value of τ_{migr}.

The transient for the low Mn content sample shown in figure 6.2 (b) can be perfectly fitted by the modified Förster model (equation 6.1) using $D = 1$, $n = 0.37$ nm⁻¹ and the parameter given in table 6.1. A migration time of $\tau_{Migr} = 1.4$ ms has to be employed, which is smaller than the natural lifetime τ_{Mn}. The value was estimated by interpolation from a model [517, 518] and

Table 6.1: *Sample details and parameter used for the fit by the modified Förster energy transfer model.*

Mn [at.%]	Mn [cm⁻³]	d_{MnMn} [nm]	R_0 [nm]	τ_{Mn} [ms]	τ_{Migr} [ms]	D	α
$1.4 \cdot 10^{-3}$	$6.9 \cdot 10^{17}$	11.3	4.85	2.5	1.4	1	1.129
$1.4 \cdot 10^{-1}$	$6.9 \cdot 10^{19}$	2.4	4.85	2.5	1.0	2	1.354

literature values taken from similar samples [9, 88]. The reduction of τ_{Migr} confirms that the majority of the Mn ions cannot be considered as isolated ions and energy migration is already present at this Mn concentration. The employed dimensionality $D = 1$ can be understood by comparison of the length scales: the Mn concentration of $1.4 \cdot 10^{-3}$ at.% corresponds to a mean Mn-Mn distance of 11.3 nm, which is more than a tenth of the estimated nanowire diameter (100 nm), but the nanowire length (> 10 µm) is large compared to these values. The arrangement of the Mn ions can be assumed as a linear chain in the nanowire and energy transfer occurs along this chain, preferentially in the direction of the nanowire axis (compare inset in figure 6.2 (b)). The system is quasi one dimensional for energy transfer and justifies the fit using $D = 1$, thus confirming that the restricted dimension of the nanowire morphology has a strong impact on the Mn decay dynamics. The defect line density of $n = 0.37$ nm^{-1} can be converted to a volume density by projection onto the cross-sectional area of the nanowire by n$_{volume} = n/\pi R^2$ for $D = 1$ [88]. The volume defect density is calculated assuming a 100 nm diameter nanowire and $D = 1$ for all samples with low Mn content. The evaluated line corresponds to a volume defect density of n$_{killer} = 4.7 \cdot 10^{16}$ cm^{-3}, similar to n$_{killer} = 1 \cdot 10^{17}$ cm^{-3} observed for the remaining defect density of implanted ZnS nanowires with low Mn content and good defect recovery by annealing [325]. The evaluated volume defect density corresponds to a mean defect distance of 28 nm, which in a similar order of magnitude as the mean Mn-Mn distance compared to the nanowire diameter. Thus, both characteristic lengths are about the same, which is an important condition for the application of the Förster model [503]. However, some restrictions have to be addressed for the defect concentration evaluation: The value is representative only for a 100 nm diameter nanowire. But the defect concentration strongly depends on the diameter, so the given value is an overestimation e.g. by 50 % for 300 nm diameter nanowires. Further on, the Förster model takes only defects into account, which are energetically lower than the excited Mn $^4T_1$ level and allow non-radiative recombination. The real defect concentration will be therefore higher than evaluated by this model.

The transient of the high Mn content sample (0.14 at.%, see e.g. figure 6.3 (b) transient for 600°C) can also be fitted with the modified Förster model. But a higher dimensionality $D = 2$, a smaller migration time $\tau_{Migr} = 1.0$ ms and a defect line density of $n = 0.175$ nm^{-1} have to be used. The effect of the increase in dimensionality at high Mn concentration was observed before [9] and is attributed to the smaller mean Mn-Mn distance of 2.4 nm. The comparison of the length scales now shows that this value is small compared to the nanowire diameter. The dimensionality of $D = 2$ should not understood as if the energy transfer occurs in a plane, but the system can be considered as intermediate between one- and three-dimensional. The energy transfer occurs not only along the nanowire axis, but also perpendicular to it. Due to the nanowire morphology, a preferential direction of energy transfer is preserved. The justification for the dimensionality of $D = 2$ is further given by the increased defect concentration of $n = 0.175$ nm^{-1}. It can be converted to the volume defect concentration via n$_{volume} = n_{line}^2/R$ for $D = 2$. A nanowire diameter of 100 nm was assumed for all samples with high Mn content to allow the comparison between samples. The calculated volume defect density n$_{killer} = 6.1 \cdot 10^{17}$ cm^{-3} corresponds to a mean defect distance of 12 nm, which is now also significant smaller compared to the nanowire diameter. The high defect concentration probably results from remaining defect complexes which are completely not removed during annealing. The damage creation in ZnS is assumed to behave similar as in ZnO, which is valid due to the same ionicity of the bonding and similar melting points [99]. The implantation conditions for the samples with low Mn content can be compared to defect creation stages I and II, observed for irradiation of ZnO with similar ion masses and energies [310, 420]. A this stages, the damages scales with the ion fluence, but the defects can mainly recovered by annealing. The higher Mn fluences of the 0.14 at.% samples can

be compared to the defect creation stage III. Here, defect complexes are formed, which are more stable and not completely removed by annealing, thus resulting in a higher killer center density which remains after annealing. The higher Mn concentration results in a further reduction of the migration time to $\tau_{Migr} = 1.0$ ms, meaning that the energy transfer is more effective and therefore faster due to the small Mn distances.

Figure 6.2 (c) shows the transients of the green (centered at 2.4 eV) and the red (centered at 1.9 eV) defect bands. The temporal behaviour of the defects has been investigated, as these bands are superimposed to the Mn emission and therefore the major contribution of the background. The green defect emission is observed for all ZnS:Mn nanowire samples and dominates emission at early times up a few microseconds. The transient is non-exponential and the emission can be observed up to 100 µs. The treatment of the sample has a major influence on the band intensity: low temperature annealing as well as additional Ne implantation (see below) lead to an enhancement of the emission intensity, which can even exceed the Mn luminescence intensity. The origin of the band is not clear, as mentioned above: intrinsic defects like sulfur vacancies [519, 520] are probable as their amount should increase with ion irradiation and decrease with thermal treatment, as it is observed in the band emission intensity. On the other hand, extrinsic defects as origin of the band cannot be ruled out as Au was used as catalyst for the nanowire growth [140].

The red defect band occurs mainly for samples with low Mn content. The spectra show a large overlap of the Mn^{2+} and defect emission up to a few hundred microseconds. A feeding of the red defect emission from the excited Mn has not been observed. Similar to the green defect band, the intensity increases with Ne irradiation and decreases for thermal treatment. The sample with low Mn content implanted at 600°C shows the lowest contribution of the band; while the red defect emission dominates the spectrum up to a millisecond for Ne implanted samples (see below). A clear identification of the origin is missing up to now. A connection between Ne implantation and the occurrence of the band cannot be confirmed [521]. Instead, Zn in interstitial sites are supposed as possible explanation [521, 522], which is reasonable as the intensity increases with ion fluency. But the low intensity of the band at the high Mn content samples also allows an alternative interpretation: The nanowires, used for the high Mn content series, were processed directly after synthesis, while the nanowires of the low Mn series were exposed to air for some time. Therefore, surface oxidation could give an alternative explanation for the occurrence of the red band, especially at the low Mn series [515].

The interaction of the Mn ions with the defects takes place within the first microseconds. But the overlap with defect emissions limits the evaluation of the Mn transients at early times. Only spectra are regarded for the fit in which the Mn emission is clearly observed and can be separated from other contributions. The earlier data points are not regarded for the fit, especially for the low Mn content samples. The reasonable adjustment of the defect density in the fit relies on the data points at early times after the excitation pulse. This is reflected by the uncertainties of the defect line densities in the fit, which is typically $\pm$ 0.03 nm^{-1} ($\pm 4 \cdot 10^{15}$ cm^{-3}) for the low Mn content samples using $D = 1$. As the evaluation of earlier times is accessible for the high Mn content samples due to the increased Mn emission intensity, the uncertainty of the defect line density is smaller ($\pm$ 0.008 nm^{-1}), but the calculated volume value ($\pm 5 \cdot 10^{16}$ cm^{-3}) is higher due to the increased dimensionality $D = 2$ for these samples.

6.3.2 Defect induced changes of the Mn decay dynamics

Implantation at elevated temperatures The impact of an energetic ion into the target is accompanied by the creation of defects. Their number is strongly influenced by the temperature of the sample during implantation as the the recombination of the vacancy and interstitial pairs is a thermally activated process [420]. Implantation at elevated temperatures results in a high dynamic annealing, the number of remaining defects is assumed to decrease with higher implantation temperature and amorphization can be avoided e.g. for GaAs nanowires [68, 274]. This offers a smart way to control the defect concentration.

To investigate the effect on the temporal Mn behaviour, a set of ZnS nanowires was implanted with the low Mn fluence at 400°C and 600°C and investigated without further annealing treatment afterwards. The observed transients are shown in figure 6.3 (a). The Mn luminescence intensity decays faster for the sample implanted at 400°C compared to implantation at 600°C. This is in agreement with the expectation that more killer centers remain after implantation at low temperatures; therefore, the probability of non-radiative Mn ion de-excitation by energy transfer to killer centers is enhanced. The transient at later times is governed by the emission of isolated Mn ions therefore similar for both samples. The transients can be well fitted by fixing the parameters determined for the reference sample (table 6.1) and varying only the defect line density n. The evaluated value increases from $n = 0.37$ nm^{-1} for the 600°C implanted sample to $n = 0.61$ nm^{-1} for implantation at 400°C, which corresponds to a volume defect density of $7.8 \cdot 10^{16}$ cm^{-3} (+ 66 %). The mean defect distance decreases from 28 nm to 23 nm, but still is in a similar range compared to the mean Mn-Mn distance.

A similar result was achieved for the samples with high Mn content: as expected, the lower implantation temperature leads to a faster Mn decay. Again, more implantation related defects remain at the lower temperature, therefore it is more probable for an exited Mn ion to find a killer center and de-excite by non-radiative energy transfer. A reasonable fit of the transients could be achieved by fixing all parameters listed in table 6.1 and variation of only the defect line density. The evaluated defect line densities as a function of implantation temperature are plotted in figure 6.3 (c). The transient of the sample implanted at 600°C can be fitted with the lowest defect line density of $n = 0.175$ nm^{-1} corresponding to $\approx 6.1 \cdot 10^{17}$ cm^{-3}. The transients of the sample implanted at 500°C and 400°C can be fitted using an increased line density of $n = 0.187$ nm^{-1} and $n = 0.204$ nm^{-1} ($7.0 \cdot 10^{17}$ cm^{-3} (+ 14%) and $8.3 \cdot 10^{17}$ cm^{-3} (+ 36%), respectively). The defect concentration increase for implantation at lower temperature is not as strong as for the low Mn content sample. The explanation is given in the intrinsic higher defect concentration, which exceeds the defect concentration of the samples with low Mn content by one order of magnitude, even for the best preparation conditions. As mentioned before, the creation of defect complexes due to the high Mn fluence is assumed as origin [310]. Higher implantation temperatures would be needed to recover the crystal lattice from the defect complexes, but the maximum temperature is limited by the dissolution of the ZnS nanostructures at 700 °C in vacuum [480]. It is worth mentioning that the relative defect intensity decrease from 500°C to 600°C is smaller compared to implantation at 400°C. It can be assumed that some of the created defect complexes recombine only at temperatures well above 600°C; therefore, the recovery shows a slight deviation from a linear relation.

Post-implantation annealing An alternative approach to control the remaining defect concentration was performed by implantation at room temperature and post-implantation annealing. As for implantation at elevated temperatures, the remaining defect concentration should decrease for higher annealing temperatures while the Mn lifetime should increase.
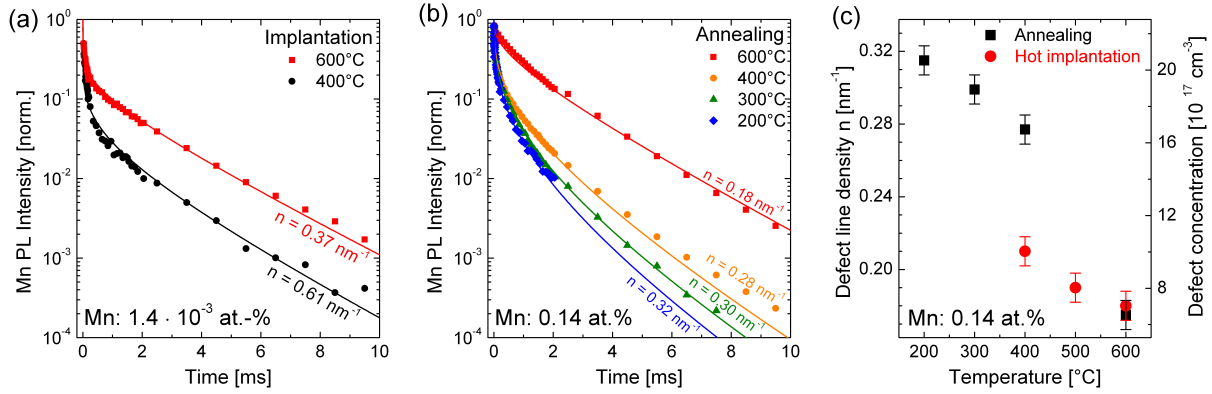
Figure 6.3: *(a) Transients of the ZnS:Mn ($1.4 \cdot 10^{-3}$ at.%) nanowires show a faster PL decay for lower implantation temperatures without further annealing. (b) Annealing at high temperatures leads to slower decay of the ZnS:Mn (0.14 at.%) luminescence. (c) The comparison of the evaluated defect concentrations for annealed and hot implanted samples (Mn 0.14 at.%) show a strong reduction upon thermal treatment.*

A sample with low Mn content was annealed between 400°C and 600°C in steps of 100 °C for 30 min each; thus, the overall annealing time increases with each step. The evaluated Mn transients nearly overlap, which is not shown as a figure. The reason is found in the strong emission of the red defect band, which superimpose Mn emission up to 750 µs. The normalization of the transients to this delay exclude the time range, which is necessary for a reliable fit of the defect line density. A defect line density of n = 0.45 nm^{-1} (corresponding to $5.7 \cdot 10^{16}$ cm^{-3}) was evaluated from the fit of the transient at 600°C annealing. Post-implantation annealing seems therefore less effective as implantation at the same temperature for the low Mn fluence. For implantation at room temperature, some defects can form complexes and remain even after annealing, which would have been otherwise directly recovered at elevated implantation temperatures due to the higher dynamic annealing rate. The absolute Mn emission intensity did even slightly decrease with longer annealing times while the defect band emission was strongly promoted. Although the samples were annealed in vacuum, oxygen is present in the residual gas and can substitute sulfur atoms close to the nanowire surface [523]. This creates defect levels responsible for the red defect band emission.

Annealing of a sample with high Mn content in vacuum was performed starting at 200°C to 400°C in steps of 100 °C for 30 min each, thus increasing the annealing time with each step. The obtained transients are compared to a sample annealed at 600°C for 30 min in figure 6.3 (b). For this sample, it is assumed that the majority of the created defects, except remaining defect complexes, were recovered [497]. Similar to the observed behaviour at different implantation temperatures, the Mn decay becomes slower for higher annealing temperatures, which can be related to a reduction of the defect concentration. Again, fitting of the transient was performed by fixing all parameter from table 6.1 and variation of only the defect line density. Reasonable fits were obtained for all annealing temperatures. For the sample annealed of 200°C, the Mn emission could be observed only up to 2 ms due to the low emission intensity. Nevertheless, the transient could be well fitted with the given parameters and a defect line density of n = 0.318 nm^{-1} (corresponding to $2.0 \cdot 10^{18}$ cm^{-3}) within this time range. The increased Mn emission intensity for higher annealing temperatures allows the observation at later times. This comes along with a strong reduction of the green defect band emission intensity. The defect line densities evaluated from the fits are plotted in figure 6.3 (c) as a function of annealing temperature. A non-linear correlation is found, as the defect reduction is enhanced for higher temperatures. This is obvious as the recombination of the vacancies and interstitials is a thermally activated process [420].
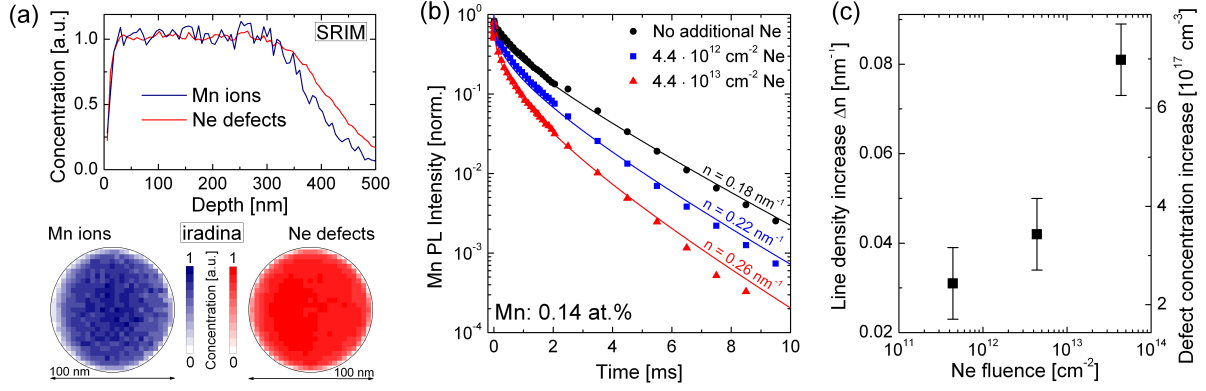
Figure 6.4: *(a) SRIM simulation of the overlapping Mn implantation and Ne damage profile. The overlap is in well agreement with iradina simulations calculated for a 100 nm ZnS nanowire (shown below). (b) The Mn decay is accelerated by additional defects created by Ne implantation. (c) The evaluated defect concentration increase relative to the unimplanted reference increases with Ne fluence.*

Annealing at 400°C results in a defect concentration of $n = 0.277$ nm^{-1} ($1.5 \cdot 10^{18}$ cm^{-3}), which is nearly twice the value compared to implantation at 400 °C. Post-implantation annealing seems not as efficient as implantation at elevated temperatures. As in the case of low Mn content, many defects already recover at elevated implantation temperatures due to the enhanced dynamic annealing rate before defect complexes can form.

Comparing the defect line densities for implantation and annealing at 600°C, the resulting defect line densities are about the same. The majority of vacancy-interstitial pairs have recombined and defect complexes are left, whose recovery is activated at temperatures exceeding the limits of the ZnS nanostructure. Here, post implantation annealing seems more favourable to high temperature implantation as the evaluated defect line density is slightly lower. At first sight, this is contrary to the behaviour observed before, but can be understood by a closer look at the implantation process parameters. The post implantation annealing is performed in 30 min, but the implantation can take longer (up to 90 min) due to the high Mn fluence and available ion currents. During this time, sulfur can dissolve from the ZnS nanowire surface, which results in the creation additional defect levels [524]. This was observed for the hot implanted sample, which shows a stronger emission of the green defect band. The Mn emission intensity exceeds the defect band upon 2 µs for the hot implanted sample. The post-implantation annealed sample shows this emission ration even at 100 ns after the excitation pulse.

Additional implantation of Ne ions A third approach to control the defect density was performed by implantation of noble gas ions. Ne was chosen as it is chemically inert; therefore, the implanted species forms no bonds within the crystal and the majority of the implanted Ne ions diffuses out at latest after irradiation [521]. Thus, only defects are generated, which act as killer centers and their density can precisely be controlled by the Ne fluence. Ar and heavier nobles gases would have the same effect, but due to their higher mass, the ion related damage is increased, limiting the precise control at the low fluences needed. Helium on the other hand is too light for sufficient damage creation.

For sample preparation, ZnS nanowires were implanted first with Mn and annealed at 600°C for 30 min in vacuum in order to achieve a sufficient crystal recovery. Next, the samples were irradiated with Ne ions at 20 - 200 keV without further annealing. The Ne damage profiles were calculated using SRIM (figure 6.4 (a)). The Ne ion energies and fluences were chosen to create a damage profile matching the Mn implantation profile. The simulations were confirmed later for the nanowire geometry using iradina as shown in figure 6.4 (a): the results show a good overlap

between Mn ions and Ne created defects for a 100 nm ZnS nanowire.

No change in the Mn decay transients was observed for the samples with low Mn content up to a Ne fluence of $1.3 \cdot 10^{11}$ cm^{-2}, corresponding to a theoretical value of $2 \cdot 10^{-4}$ dpa. The additional damage created by the Ne ions is probably below the intrinsic defect concentration after Mn implantation and annealing, so no additional influence is induced. Upon irradiation of $6.3 \cdot 10^{11}$ cm^{-2} Ne ($1 \cdot 10^{-3}$ dpa), the Mn decay gets faster due to the presence additional Ne created killer centers. A further irradiation up to a Ne fluence of $6.3 \cdot 10^{13}$ cm^{-2} (0.1 dpa) increases this effect, but unfortunately, the Mn emission intensity is reduced as well, especially for long times after the excitation pulse in the luminescence measurements. The defect line densities evaluated from the fits increased from n = 0.45 nm^{-1} (corresponding to $5.7 \cdot 10^{16}$ cm^{-3}) for the reference without Ne to n = 0.52 nm^{-1} ($6.6 \cdot 10^{16}$ cm^{-3}, + 15%) and n = 0.60 nm^{-1} ($7.6 \cdot 10^{16}$ cm^{-3}, + 33%) for the low and high Ne fluence. The increase is in the same range observed from the variation of the implantation temperature in chapter 6.3.2. Therefore, one can conclude that similar processes are involved in the defect creation.

Theoretical values for the defect concentration have been calculated assuming a background level of $5 \cdot 10^{16}$ cm^{-3} defects remaining from the Mn implantation after sufficient annealing [525]. The SRIM and iradina calculated defect concentrations are in the range of 10^{19} cm^{-3} for the low Ne fluence and up to 10^{21} cm^{-3} for the high Ne fluence, which is a significant deviation by several orders of magnitude from the evaluated values. Several reasons have to be taken into account to explain the observation: first, the low Ne fluence implantation can be compared to the defect creation stage I observed in ZnO [420], at which the defect creation is governed by point defects and scales linear with the fluence. Deviations from linear relation appear at high fluences with the beginning of the defect creation stage II [526]. The highest Ne fluence ($6.3 \cdot 10^{13}$ cm^{-2}) can still be set to the beginning defect creation stage II, thus nearly no defect complexes are formed. Second, a significant recombination of point defects was observed even below room temperature, therefore the majority of the Ne created defects already recombines during implantation. But the simulations completely neglect defect recombination and only show a reasonable agreement with experimental values for very low temperatures, at which the defect recombination is mainly suppressed [310, 420]. The theoretical calculations are therefore an overestimation for implantations at elevated temperatures. On the other hand, the defect concentrations evaluated from the fits take only defects into account, that participate in the Förster energy transfer and strongly depend on the chosen nanowire diameter. As mentioned above, this is on the other side an underestimation and only provides a lower limit of the real value.

Additional Ne implantation on samples with high Mn content was performed with fluences between $4.4 \cdot 10^{11}$ cm^{-2} and $4.4 \cdot 10^{13}$ cm^{-2}. The observed Mn decay transients are plotted in figure 6.4 (b). Again, the excited Mn ions decay faster as the additional defects are created by the Ne implantation. The fits could be well performed using D = 2 even for the highest Ne fluence and by adjusting only the defect line density. The increase of the defect line density with respect to the reference sample without Ne irradiation is plotted in figure 6.4 (c). The increase is low for small Ne fluences, but the relation scales non-linear for high Ne fluences. The evaluated defect line density increases from n = 0.206 nm^{-1} ($8.5 \cdot 10^{16}$ cm^{-3}, + 34%) for the low Ne fluence to n = 0.256 nm^{-1} ($1.3 \cdot 10^{17}$ cm^{-3}, + 114%) at the high Ne fluence. Although the Ne fluences were nearly equivalent compared to the low Mn content series, the effect on the defect concentration is stronger. This might be due to the higher dimension and the projection of the line density to the volume defect concentration, but another reason is more likely: the higher Mn fluence already creates significantly more defects, resulting into a high background defect concentration of $\sim 6 \cdot 10^{17}$ cm^{-3}. Comparison to the situation of ZnO [420] shows that the annealed samples are already at defect creation stage III, at which extended defects occur. At this stage, the created

defects mainly do not recombine as in the case of the low Mn concentration, but are accumulated to extended defects. Additional Ne irradiation even extends those defects and hampers defect recovery, which explains the stronger effect of the Ne fluence on the high Mn content samples. The comparison to the theoretical calculated values is equivalent as for the low Mn content: The simulations give an overestimation ($\sim 10^{19}$ - 10^{21} cm^{-3} for low and high Ne fluence) of the real concentration; while, the value derived from the Förster model fits marks an lower limit.

All three approaches were successful in varying the defect concentration in Mn implanted ZnS nanowires. The Mn decay is accelerated by additional defects and the modified Förster model can successfully describe the tune of the Mn decay from a few microseconds up to several milliseconds for all chosen preparation conditions. This completely proofs the model for Mn implanted ZnS nanowires.

6.4 Tb implanted ZnS nanowires

As-grown ZnS nanowire ensembles were implanted with terbium (Tb) with ion energies of 20 - 380 keV to provide a homogeneous doping up to a nanowire diameter of 120 nm with a maximum ion range of about 210 nm. The Tb fluences of $1.4 \cdot 10^{12}$ - $1.4 \cdot 10^{16}$ ions/cm^2 resulted in nominal concentrations of $2 \cdot 10^{-4}$ - 2.0 at.%. The implantation related defects were recovered by annealing in high vacuum at temperatures up to 600°C and times of typically 30 min.

6.4.1 Morphology and Stoichiometry

Figure 6.5 (a) presents the typical morphology of the ZnS nanowires after implantation of $1.4 \cdot 10^{15}$ ions/cm^2 Tb (nominal 0.2 at.%) and annealing at 600°C for 30 min in high vacuum ($< 10^{-5}$ mbar). The nanowires mainly preserve their morphology compared to the as-grown ensemble (compare figure 6.1 (a)). A slight bending is observed, which was attributed to the crystal damage induced by ion implantation [273, 274], leading to compressive and tensile stress in the lattice (see chapter 5.2). Thinner nanowires show a stronger bending than thicker ones due to th ion range in respect to the nanowire diameter [274]. The implanted nanowires sometimes exhibit the tendency to stick together, which probably results from the evacuation and venting processes during ion implantation and annealing.

The crystal structure of the implanted ZnS nanowires was investigated using TEM. The ZnS nanowires show a strong inhomogeneous contrast in the TEM after implantation of $1.4 \cdot 10^{15}$ ions/cm^2 (nom. 0.2 at.% Tb) without further annealing (not shown). SAED and high resolution images show the presence of crystalline order but with a high degree of structural disorder originating from the nuclear stopping processes of the impinging ions [86]. The lattice is even more damaged after implantation of $1.4 \cdot 10^{16}$ ions/cm^2 (nom. 2.0 at.% Tb), but still no extended amorphous areas were observed;. however, the lattice structure becomes strongly polycrystalline with small crystallites. Figure 6.5 (b) presents a survey TEM micrograph of a ZnS nanowire after implantation such a high fluence and subsequent annealing at 600°C for 30 min in vacuum. The nanowire shows a strong inhomogeneous contrast. The surface is rough compared to the as-grown ZnS nanowires (see figure 6.1 (b)), which is attributed to the sputtering. The SAED pattern presented in the inset of figure 6.5 (b) confirms the polycrystalline lattice structure. The diffraction spots are arranged at circles around the central spot. The distance to the central spot matches the spacing of the {111} denoted planes of the cubic ZnS phase, which was found to be more stable after ion implantation and annealing, but residua of the wurtzite phase are also present [497]. The strong intensity of those diffraction spots in the direction of the nanowire axis reveal the preservation of a preferential orientation. The high resolution image (figure 6.5 (c))
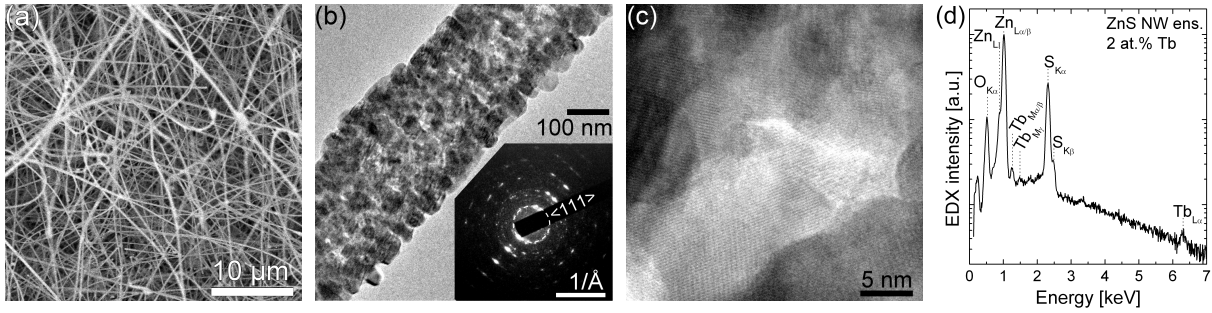
Figure 6.5: *(a) SEM image of Tb implanted ZnS nanowires (0.2 at.%) after annealing at 600°C. (b) The nanowires exhibit an irregular contrast in the survey TEM image. The surface is roughened due to sputter effects during the ion implantation. The inset presents the SAED pattern revealing the polycrystalline structure, but still a preferential orientation of the {111} lattice plains remains along the nanowire axis. (c) The HR-TEM image shows the high crystal quality of the crystallites. (d) EDX measurements verify the incorporation of Tb in the ZnS nanowires.*

shows the crystalline lattice structure. The crystallites are enlarged after the annealing treatment compared to the as-implanted state. The crystallites exhibit a high degree of structural order without the presence of extended defects. No evidence for Tb related clusters or secondary phases were found. A good recovery of the implantation related defects could be achieved by the annealing treatment.

The stoichiometry of the Tb implanted ZnS nanowires (nom. 2.0 at.%) was investigated by EDX in the SEM. The electron voltage was adjusted to 15 keV to excite mainly the implanted ZnS nanowires in the ensemble. The EDX spectrum in figure 6.5 (d) shows the presence of Zn and S by the appearance of the respective Zn L_I and $L_{\alpha/\beta}$ X-ray emission lines at 0.88 keV and 1.02 keV as well as the S $K_{\alpha/\beta}$ X-ray lines at 2.31 keV and 2.46 keV [453]. The quantification reveals a Zn:S ratio close to the stoichiometric composition within the experimental uncertainties. The X-ray emission at 0.21 keV and 0.53 keV are related to carbon and oxygen from contaminations on the surface. Successful doping is confirmed by the presence of the Tb $M_{\alpha/\beta}$ and M_γ X-ray emissions at 1.25 keV and 1.46 keV as well as the L_α emission at 6.27 keV. The evaluated Tb concentration matches the desired value and confirms that no outdiffusion occurred during annealing.

6.4.2 Tb^{3+} luminescence in ZnS nanowires

The optical emission properties of Tb implanted ZnS nanowire ensembles were investigated using PL and CL spectroscopy. Figure 6.6 presents the PL survey spectrum of implanted and annealed ZnS nanowires (nom. 0.2 at.% Tb) at low power cw excitation and T = 4 K. The emission consists of a series of sharp emission peaks in the range of 3.26 - 1.75 eV superimposed to the broad defect emission of the ZnS nanowires. The emission peaks can be clearly assigned to the Tb^{3+} intra-4f^8 emissions [485, 488, 527–529] by comparison of the emission peak energies and level spacings with the term scheme derived by with theoretical calculations [530, 531] and literature data [532, 533]. The Tb^{3+} emission peaks originate from the excited $^5D_3$ and $^5D_4$ to the ^7F_J (J=0..6) multiplet, as sketched in figure 6.6 (b). The transitions originating from the $^5D_4$ term are generally stronger than those from the $^5D_3$ term, as this excited level can relax non-radiatively into the lower $^5D_4$ term. According to the selection rules of the Judd-Ofelt theory [193, 194], electric dipole transitions can be induced from the $^5D_4$ term to the complete ^7F_J multiplet and magnetic dipole transitions are allowed from the $^5D_4$ to the $^7F_{5,4,3}$ terms for good quantum numbers [534]. The assignment of the $^5D_3 \rightarrow ^7F_1/^7F_0$ and the $^5D_4 \rightarrow ^7F_6$ transition is not completely conclusive, as those emission lines overlap. A strong contribution of the
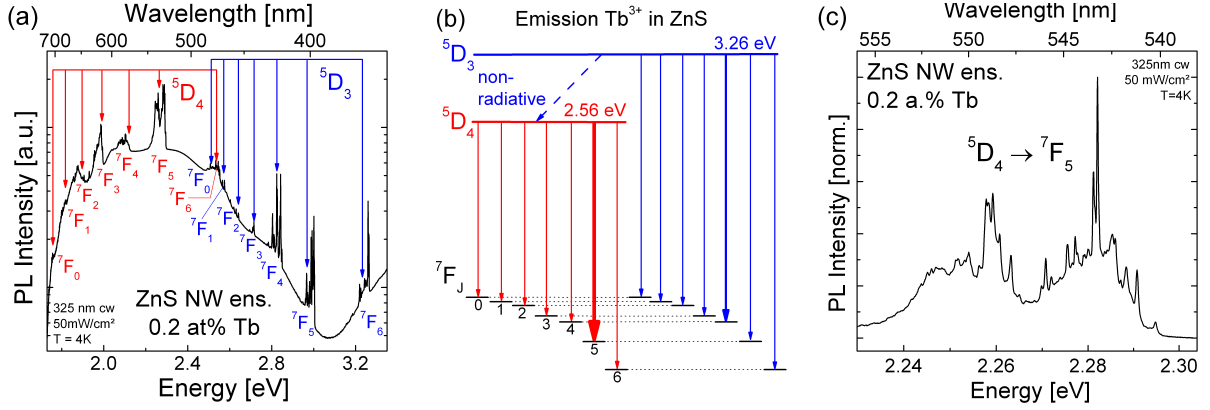
Figure 6.6: *(a) The PL survey spectra of Tb implanted ZnS nanowires (0.2 at.%) show the intense Tb^{3+} related emission peaks superimposed to the ZnS defect emission. (b) The Tb^{3+} intra-$4f^8$ transitions originate from the excited $^5D_3$ and $^5D_4$ to the lower ^7F_J multiplet. (c) The high resolution PL spectra unfold the sharp emission peaks originating from the strong Stark level splitting of the $^5D_4$ ($^5D_3$) to $^7F_5$ transition.*

$^5D_4 \rightarrow {}^7F_6$ transition in the emission can be expected as the $^5D_3 \rightarrow {}^7F_0$ should have a low transition probability according to the selection rules [194]. The Tb emission bands and a possible assignment is listed in the appendix in table B.11.

Figure 6.6 (c) presents a high resolution spectrum of the most intense $^5D_4 \rightarrow {}^7F_5$ transition. Multiple very sharp emission lines (FWHM < 0.14 meV, limited by the resolution of the spectrometer) are observed in the range of 2.22 - 2.30 eV, which result from the the Stark level splitting of the $^5D_4$ and the $^7F_5$ terms in the presence of the crystal field . For Tb^{3+} ions incorporated on Zn lattice sites (C_{3v} symmetry), the 9-fold degenerated $^5D_4$ term splits into three non-degenerated and three double-degenerated sub-levels, while the 11-fold $^7F_5$ term splits into three non-generated and four double-degenerated sub-levels [535]. The selection rules allow 38 electronic transitions between those Stark levels [535]. However, fewer emission lines should be observed, as only lower Stark levels are populated at low temperatures [91]. However, more than the allowed emission lines are observed in the luminescence spectra in figure 6.6 (c), which indicates that the Tb^{3+} ions occupy more than one site in the ZnS lattice [536]. The assumption of several different sites is reasonable, as the ZnS nanowires exhibit both the cubic as well as the wurtzite lattice structure and the ZnS lattice can accommodate Tb^{3+} ions on interstitial sites in both cases [535]. An additional source of disturbance is introduced by (implantation) defects located in the surrounding of the Tb^{3+} ions, which are necessary for the charge compensation and the activation of the rare earth ion in the trivalent state [536].

6.4.3 Optimization of the annealing conditions and Tb concentration

The recovery of the ZnS and activation of the implanted Tb ions was investigated for a ZnS nanowire ensemble doped with nominal 0.2 at.% Tb. The sample was split into several parts, which were annealed at temperatures between 200 - 700°C for 30 min each in high vacuum. The CL spectra of the Tb implanted and subsequently annealed ZnS nanowire ensembles are plotted in figure 6.7 (a). The as-implanted sample shows no ZnS related emission, as the optical properties of the ZnS nanowires are governed by defects in the crystal lattice at this stage. However, broad Tb^{3+} related emission peaks of low intensity could observed in the spectrum. Some Tb ions were already incorporated in the trivalent state and could be directly excited by the hot electrons in CL [528, 537]. No fine splitting of the Tb emission was observed, which is attributed to the high degree of disorder in the surrounding. The partial recrystallization of the ZnS lattice starts after annealing at 400°C, as a low intense ZnS defect emission was observed. A fine splitting
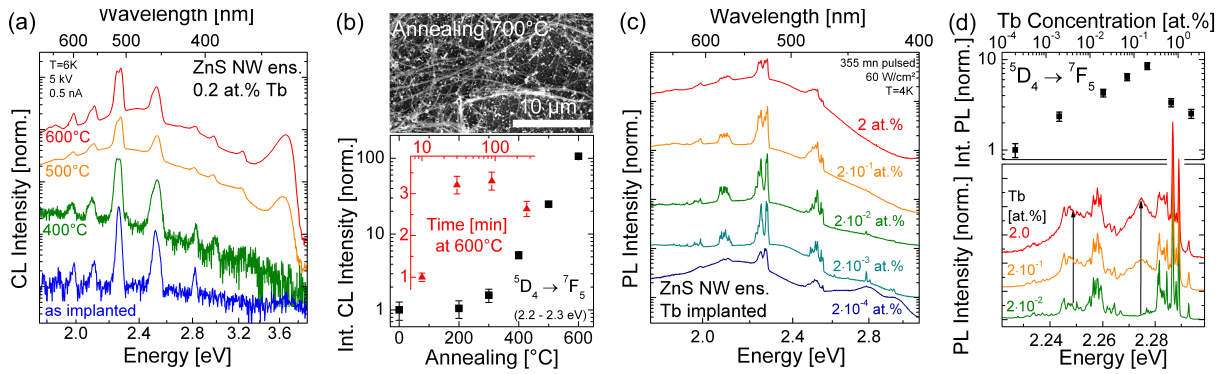
Figure 6.7: *(a) The Tb^{3+} luminescence can be observed directly after implantation in CL spectra. The ZnS crystal lattice recovered at annealing above 400°C. (b) The intensity of the Tb^{3+} $^5D_4 \rightarrow ^7F_5$ transition can be strongly enhanced by annealing at 600°C. Higher annealing temperatures lead to the decomposition of the ZnS nanowires (SEM inset). (c) PL survey spectra of ZnS nanowires implanted with $2 \cdot 10^{-4}$ - 2 at.%. (d) The Tb^{3+} emission intensity increase sublinear and shows a strong quenching above 0.2 at.%. The high resolution PL spectra shown below indicate additional broad emission lines in the $^5D_4 \rightarrow ^7F_5$ transition, which probably originate from Tb ions in a surrounding with higher disorder.*

in the $^5D_4 \rightarrow ^7F_5$ transition occurred, which was attributed to the incorporation of a fraction of the implanted Tb ions on Zn lattice sites [538]. The recovery of the ZnS lattice is strongly enhanced after annealing at 500°C, which is manifested in the reappearance of the excitonic emission around 3.7 eV as well as the pronounced defect emission. Annealing at 600°C could further improve the crystal quality, so that the excitonic emission became more intense while the defect emission decreased in intensity. The Tb^{3+} intra-4f emission dominated the spectra and a strong Stark splitting was observed in the high resolution spectra, as already discussed in figure 6.6 (c). The change in the Stark level splitting can be attributed to the recovery of the ZnS host lattice: more Tb ions are on Zn lattice sites in an undisturbed surrounding [539] due to the mobility of the Zn vacancies at this temperature [538, 540]. But also the lattice strain introduced by e.g. interstitial atoms is reduced by the thermal annealing [541], leading to a change of the crystal field at the Tb ion sites and thus an altered Stark splitting.

The intensity of the Tb^{3+} $^5D_4 \rightarrow ^7F_5$ transition was extracted from the CL spectra and is plotted as a function of the annealing temperature in figure 6.7 (b). A strong increase of the emission intensity was observed above 400°C, which is related to the recovery of the ZnS host matrix. The course of the emission intensity was equal for all Tb transitions [480]. The Tb emission could be enhanced by a factor of 100 compared to the as-implanted sample. The intensity enhancement for ZnS:Tb nanowires is about a factor 3 - 5 stronger than for sputtered ZnS:Tb films [534, 542]. The excitation of the Tb^{3+} ions by energy transfer from the ZnS host matrix strongly depends on the crystal quality, as a high defect concentration would reduce the transfer efficiency [505]. The observation can be explained by the higher crystal quality of the ZnS:Tb nanowires compared to the sputtered films.

Annealing above 600°C leaded to the decomposition of the ZnS nanowires, which is shown in the SEM image in figure 6.7 (b). This probably resulted from the desorption of sulphur in the high vacuum atmosphere [543]. An enhanced oxidation of the surface was observed for the Zn rich nanostructures [544, 545] determined by EDX (not shown). The annealing temperature for ZnS nanowires in vacuum ambient is therefore limited to 600°C.

The influence of the annealing time was investigated for a sample annealed at 600°C in vacuum. After 10 min annealing, Tb and ZnS defect emission was observed while the excitonic emission was still missing (CL spectra not shown). Longer annealing at 30 min to 90 min enhanced the NBE emission intensity, while the Tb related emission increased by a factor of 3. Longer annealing times of 270 min leaded to a further enhanced excitonic emission, which results from an

improved ZnS lattice quality, but the Tb intra-4f emission decreased, as shown in the red inset of figure 6.7 (b). An outdiffusion of Tb at this temperature is not expected [542]. The better recovery of the lattice structure probably reduced the amount of defects in the Tb surrounding, which are necessary for charge compensation and the activation of Tb in the trivalent state [536]. The influence of the Tb concentration on the emission properties was investigated for ZnS nanowire ensembles doped with Tb in the range $2 \cdot 10^{-4}$ - 2.0 at.%. The normalized PL survey spectra presented in figure 6.7 (c) show low Tb related intra-4f emission bands superimposed to the ZnS defect emissions at the lowest concentration of $2 \cdot 10^{-4}$ at.%. The intra-4f emission clearly dominates the spectrum for increasing the Tb content by one to two orders of magnitude. A further raise of the Tb concentration also increases slightly the ZnS defect emission, especially for the highest Tb concentration of 2 at.%. However, the defect emission is effectively suppressed at lower Tb concentrations, as the majority of the electron-hole pairs recombine at the rare earth centers [505]. The increase of the defect emission intensity at high Tb concentrations resulted from the ion irradiation with high ion fluences, yielding into the creation of extended defects, which cannot be removed by the thermal annealing treatment [310, 420].

High resolution PL spectra of the $^5D_4 \rightarrow {}^7F_5$ transition are shown in figure 6.7 (d). For the moderate Tb concentration of $2 \cdot 10^{-2}$ at.%, the transition consists of a series of very sharp emission peak, which occur between 2.275 - 2.292 eV on the high energy side and 2.230 - 2.269 eV on the low energy side. Increasing the Tb concentration, additional broad bands raised around 2.248 eV, 2.275 eV and 2.283 eV and ascend in intensity with concentration, while the intensity of the sharp emission lines at 2.259 eV and 2.282 eV decrease. The change of the Stark level emission fine structure is related to the location of the Tb ions in the ZnS host. For low Tb fluences ($\leq 2 \cdot 10^{-2}$ at.%), the majority of the Tb^{3+} ions is expected to be incorporated on a Zn lattice site with nearly undisturbed surrounding, resulting in the sharp emission lines due to the similar crystal field splitting for those ions. With increasing Tb content, a higher fraction of the implanted Tb ions exhibit a stronger disturbed surrounding, as defects remain after annealing [310]. The resulting broad emission bands originate from the superposition of several different surroundings of the Tb ions, each leading to a different Stark level splitting [505].

The emission intensity of the $^5D_4 \rightarrow {}^7F_5$ transition was extracted from the survey PL spectra and is plotted as a function of the Tb concentration above the high resolution PL spectra in figure 6.7 (d). The Tb emission intensity increases sublinear by a factor of 10 up to 0.2 at.% resulting from a higher number of Tb centers contributing to the intra-4f emission. The deviation from a linear increase originates from the concentration of the higher killer center, which are simultaneously introduced by the ion implantation process and are expected to increase in the same manner as the Tb concentration. The presence of killer centers/defects causes a less efficient excitation of the Tb ions [505]. Additionally, the shrinking mean Tb-killer center distance enhances the energy transfer rate resulting in a higher fraction of non-radiative de-excitation at killer centers. The strong intensity decrease above 0.2 at.% is attributed to concentration quenching [546], as the ions are spaced so close to each other, that fast non-radiative and resonant energy transfer between Tb ions becomes more probable than radiative emission. This strongly promotes fast de-excitation to killer centers, which explains the quenching of the radiative Tb emission [233]. A similar behaviour was observed for ZnS:Tb thin films [505, 547], for which the optimum Tb concentration was also in the range of 0.2 - 0.4 at.% for excitation with photons above the ZnS band gap, which fits well with the present results for ZnS:Tb nanowires. But the concentration for the most intense Tb emission depended on the excitation [547]: For ZnS:Tb and ZnS:Tb,F films in electroluminescence devices, the maximum emission intensity was observed for Tb concentrations of 1 - 2 at.% [233, 488, 547, 548] and attributed to the different excitation mechanism (impact excitation by hot electrons) [547]. Although a strong contribution of non-radiative de-excitation
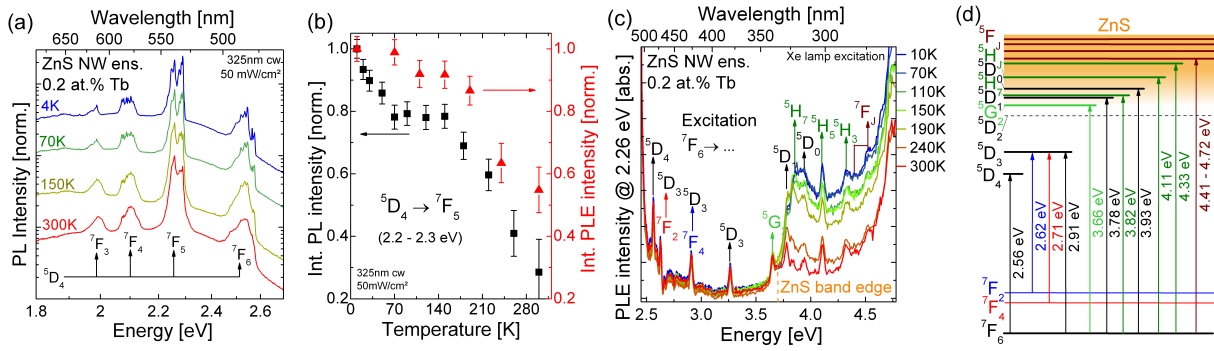
Figure 6.8: *(a) PL survey spectra of a Tb doped ZnS nanowire ensemble at different sample temperatures. The spectra shape of the Tb emission changed at elevated temperatures due to the fractional thermal population of the Stark levels. The emission is broadened due to the increased interaction with phonons. (b) The integrated intensity of the $^5D_4 \to {}^7F_5$ transition is plotted as a function of temperature. The integrated PLE intensity is displayed in the same scale for comparison. (c) PLE spectra of a Tb implanted ZnS nanowire ensemble at temperatures between 10 - 300 K. The ions can be directly excited via higher Tb^{3+} levels, but also energy transfer from the ZnS host became important at lower temperatures. (d) Scheme of the possible excitation pathways and assignment of the excited Tb levels.*

by energy transfer is already present above 0.2 at.%, the excitation efficiency was determined by the electron scattering length for hot electron excitation, which becomes too short for Tb concentrations above 1 - 2 at.% [505].

6.4.4 Dependence on temperature and excitation of Tb ions

The influence of the sample temperature on the Tb luminescence of the implanted ZnS nanowire ensemble was investigated on the range of 4 - 300 K. Figure 6.8 presents the PL survey spectra of a doped nanowire ensemble with 0.2 at.% at excitation above the band edge. The sharp Tb emission peaks, which are observed at low temperatures, broaden at elevated temperatures, which can be attributed to an increased interaction with phonons [91]. At a close look to the $^5D_4 \to {}^7F_5$ transition, the spectral shape changed significantly as the Stark level transitions with lower emission energies increased in intensity at elevated temperatures, while the intensity of the high energy side declined. Due to the strong phonon interaction within the excited multiplet, the fractional thermal population of the excited $^5D_4$ Stark levels favored a population of lower energetic excited levels [223].

The integrated intensity of the $^5D_4 \to {}^7F_5$ transition is plotted as a function of temperature in figure 6.8 (b). The strongest emission intensity was detected at a temperature of 4 K. Increasing of sample temperature to 70 K leads to an intensity decrease of $\sim$ 30%, but remains about constant up to 150 K. A thermal quenching of the emission intensity down to 30% was observed at room temperature, which is still a relatively weak quenching compared to e.g. RE elements in ZnO nanowires [62].

The observed temperature dependence cannot be simply explained by a stronger de-excitation due to an increased phonon interaction [91]. A similar temperature dependence was evaluated for a ZnS:Tb thin film for excitation with photon energies above the ZnS band gap, but a stronger Tb intensity decrease was observed for excitation below the ZnS band gap [549]. From those results, it was concluded that the temperature behaviour is more related to temperature dependent excitation efficiency than to thermal induced non-radiative de-excitation [505]. For a deeper understanding of this phenomena, PLE spectroscopy of a Tb implanted ZnS nanowire ensemble (0.2 at.%) was performed at sample temperatures between 10 - 300 K. The emission intensity was monitored at the maximum of the $^5D_4 \to {}^7F_5$ transition at 2.26 eV as a function of the excitation energy in the range of 2.48 - 4.7 eV. Several sharp peaks appear in the PLE

spectra in figure 6.8 at energies between 2.56 eV to 3.65 eV, which are assigned to the direct excitation of the $^7F_6$ to the $^5D_4$ and $^5D_3$ terms [505, 550–554]. The line width of the peaks was broadened by the spectral bandwidth of the excitation source. The peaks at 2.63 eV and 2.91 eV do not match any transition from the $^7F_6$ level, but the energies fit to transitions from the excited $^7F_2$ and $^7F_4$ to the $^5D_3$ term determined from PL data. The peak at 3.65 eV is attributed to the $^7F_6 \rightarrow ^5D_2$ transition from comparison with the theoretical calculated energetic positions of the upper levels [530]. Above 3.7 eV, the PLE intensity increased as broad band, which can be attributed to the excitation of the ZnS host above the band edge [505, 554], followed by energy transfer to the Tb ions and excitation 4f electrons [535, 546]. Several sharp peaks were observed in this energy range, which could be assigned to direct excitations of the $^5D_{1/0}$, ^5H_J from the $^7F_6$ ground term [530, 551, 554]. The assignment to the $^7F_6 \rightarrow ^5F_{5/4}$ transition at 4.41 eV and 4.53 eV is not completely conclusive, as the $^5I_{8/7}$ levels have nearly the same energetic spacing to the ground term and cannot be separated in the spectra [530]. A possible assignment of the excitation pathways of the Tb^{3+} ions in ZnS nanowires is sketched in figure 6.8 (d). The assignment of the upper Tb levels and the respective energies above $^7F_6$ ground term are listed in the appendix in table B.12.

The presence of several excited Tb^{3+} terms above the the ZnS band edge explains the good excitation efficiency for the Tb luminescence by excitation of the ZnS host and energy transfer to the Tb ions [505]. In the case of cathodoluminescence, the Tb ions can be additionally excited by inelastic scattering with hot electrons (impact excitation) [485, 488, 528, 546]. The excited Tb 4f-levels exhibit a fast non-radiative de-excitation to the $^5D_3$ and $^5D_4$ [535, 546]. The strong intensity of the $^5D_4$ transitions for moderate to high Tb concentrations can be explained by a cross-relaxation process [233, 234, 505], in which the $^5D_3$ term decays fast to a high ^7F_J level, followed by non-radiative energy transfer to a Tb ion in the surrounding. The acceptor Tb is resonantly excited from the ground term to the $^5D_4$, followed by radiative emission. This process is possible due to the small energetic mismatch between the $^5D_3 \longleftrightarrow ^5D_4 \sim 0.7$ eV and the $^7F_0 \longleftrightarrow ^7F_6 \sim 0.71$ eV terms [551]. The remaining energy mismatch can be bridged by phonons [220, 221].

Resonant excitation via excited Tb terms is nearly independent on the sample temperature, as observed from the PLE spectra in figure 6.8 (c). But a strong increase of the PLE contribution above the ZnS band edge was observed for decreasing temperatures down to 150 K. The PLE intensity remained about constant upon cooling down to 110 K and was further enhanced in the temperature range of 70 - 10 K. The integrated PLE intensity is plotted in comparison to the PL emission intensity in figure 6.8 (b). A similar temperature dependence is observed for both excitation and emission of the $^5D_4 \rightarrow ^7F_5$ transition. The intensity decrease of the PL emission in the range between 4 - 70 K is probably related to an enhanced non-radiative de-excitation due to the stronger interaction with phonons, while the excitation efficiency remained nearly constant in this temperature range. Above 70 K, the PL and PLE intensity showed the same temperature behaviour up to room temperature. This observation leaded to the conclusion, that the decrease of the PL emission intensity is more related to the reduced excitation efficiency of the Tb ions from the ZnS host rather than the non-radiative de-excitation in this temperature range [505].

6.4.5 Temporal decay of the Tb luminescence

ZnS nanowire ensembles dispersed on clean Si substrates were implanted with $1.4 \cdot 10^{15}$ ions/cm^2 and $1.4 \cdot 10^{16}$ ions/cm^2 Tb (nom. 0.2 and 2.0 at.%) and annealed at 600°C for 30 min in vacuum. The samples were investigated by TRPL spectroscopy using moderate excitation by 355 nm nanosecond pulses of a frequency-tripled Nd:YAG laser and sample temperatures between
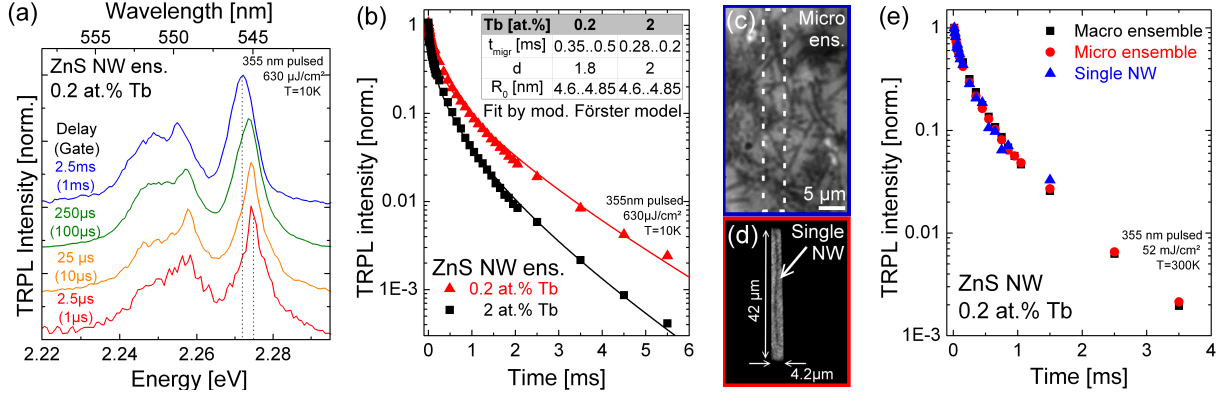
Figure 6.9: *(a) The normalized PL spectra of the Tb^{3+} $^5D_4 \rightarrow {}^7F_5$ transition at different delay times after the excitation show a red-shift of the emission peaks, caused by the de-excitation of higher stark level. (b) The transients of the ZnS nanowires doped with 0.2 and 2 at.% Tb can be fitted using the modified Förster model [9]. (c) Optical images taken by the TV camera of the µPL setup used for the TRPL investigation of the microscopic ensemble. (d) Optical image of one single Tb implanted ZnS nanowire aligned at the monochromator entrance slit. (e) The transients of the microscopic ensemble and the single nanowire exhibit the decay as the macroscopic nanowire ensemble. Data published in [482, 483].*

10 K and room temperature.

The Tb^{3+} $^5D_3 \rightarrow {}^7F_J$ (J = 6..4) transitions could be observed 50 ns after the excitation pulse (not shown). The luminescence consists of a series of sharp peaks, which decayed very fast within about hundred nanoseconds after the excitation. This very fast decay is probably related to the cross-relaxation mechanism [233, 234] described above. This also explained the weak intensity of the $^5D_3$ transitions in the PL spectra at pulsed excitation. Using cw excitation, the intensity of the $^5D_3$ transitions was stronger due to constant re-excitation.

The $^5D_4 \rightarrow {}^7F_J$ transitions can be observed in a very long time range up to more than 10 milliseconds after the excitation pulse. The emission spectra are comparable to the low temperature steady state spectra presented in figure 6.8 (a). An equal decay behaviour was found for all $^5D_4$ to ^7F_J transitions within the observed time range, meaning that the transition probabilities to the ^7F_J multiplet are stationary and independent of time. The temporal decay was investigated in detail for the most intense $^5D_4 \rightarrow {}^7F_5$ transition. High resolution spectra are compared at different delay times after the excitation in figure 6.9 (a). The spectral shape of the emission remains similar within the investigated time range, but a small red-shift of about 2.8 meV is observed. This originates form the temporal depopulation of higher $^5D_4$ Stark levels by acoustic phonons [221, 222], thus lowering the emission energy.

The integrated emission intensity of the $^5D_4 \rightarrow {}^7F_5$ transition is plotted as a function of time in figure 6.9 (b). The transient is described by a fast strongly non-exponential decay shortly after the excitation pulse, resulting from the energy transfer from Tb ions to killer centers. The intensity decrease follows a nearly single exponential decay at delay times above 2 ms, as only isolated ions were present in this time range and contribute by spontaneous emission to the luminescence. A radiative life time of the Tb ions was determined to $\tau_{Tb} = 2.06 \pm 0.12$ ms for the 0.2 at.% sample by fitting the decay with a single exponential function in the range of 2 - 10 ms. The radiative Tb lifetime in ZnS nanowires is in reasonable agreement with the lifetime of Tb doped ZnS crystals ($\tau \sim 3$ ms) [527] and Tb doped ZnS bulk samples ($\tau_{1/10} \sim 1.15$ ms) [552, 555]. The transient of the 0.2 at.% sample can be well described in the complete time range using the modified Förster dipole-dipole transfer model (equation 6.1) assuming a defect line density of $n = 0.26$ nm^{-1}, which corresponds to a defect volume concentration of $n_{bulk} = 3.3 \cdot 10^{16}$ cm^{-3}. This is actually a very low defect density for implanted ZnS nanowires [497] and reflects the high crystal quality, as observed in the TEM investigations above. Nevertheless, the evaluated defect

concentration marks the lower limit of the real defect concentration, because only those defects are regarded, which act as an acceptor for the energy transfer (compare previous section 6.3). The transients can be reasonably fitted with the determined defect line density for the low(high) Tb concentration assuming a dimensionality of $d = 1.8(2)$. A larger dimensionality has to be employed compared to the fit of transients of Mn implanted ZnS nanowires of comparable morphology and similar Mn concentration (see section 6.3 and [482]). Although the mean ion-ion distance is equal, the smaller Förster radius of the Tb ions reduced the mobility of the excitation energy in the Tb sublattice compared to the Mn sublattice [482]. This originated from the higher shielding of the 4f- compared to 3d-electrons from the surrounding. The exact determination of $R_{0,Tb}$ is not exactly possible from these fits, as the Förster radius and the energy migration in the Tb subsystem are not independent from each other. A smaller radius would cause a decreased energy transfer rate, thus elongating the migration time τ_{migr}. The Förster radius of Mn was estimated as upper limit for the Tb case and a migration time of $\tau_{migr,Mn} = 0.2$ ms marked the lower limit for the transient of the 2 at.% Tb nanowires [482]. The Tb Förster radius was estimated to be within the small range of $R_{0,Tb} = 4.6$ - 4.85 nm using this assumptions. A reasonable fit could be performed using migration times of $\tau_{migr,Tb} = 0.35$ - 0.5 ms for 0.2 at.% Tb concentration and $\tau_{migr,Tb} = 0.2$ - 0.28 ms for 2 at.% Tb, respectively. The short migration times compared to the determined radiative lifetime indicate the strong contribution of energy transfer processes in the temporal behaviour. The good agreement of the experimental data with the fit conclude that the modified Förster model is also applicable to describe the temporal decay of Tb ions in ZnS nanostructures.

The TRPL measurements presented in this and the previous chapter are based on the investigation of an macroscopic nanowire ensemble, from which the luminescence of about 10^2 - 10^3 nanowires was collected in the TRPL measurements. The parameters for the model were determined by the statistics assuming a large number of luminescent ions. However, all kinds of fluctuations may occur within these macroscopic measurements, like e.g. the arrangement of the implanted ions and the killer centers in the nanowires. Possible dependencies on the nanowire diameter are lost. Thus, TRPL measurements were performed on microscopic ensembles ($\sim$ 10 nanowires) and even single nanowires in order to clarify, whether single nanowires exhibit an identical or different temporal behaviour compared to the ensemble. A µPL setup was established at the TRPL setup in Marburg similar to the µPL setup described in chapter 3.3.2. The Nd:YAG laser beam was partially reflected by a beam splitter and focussed by a 60x microscope objective onto the sample. The emitted luminescence was collected by the same objective, passed the beam splitter and was imaged either on a TV camera or the spectroscopic TRPL detection system. All µTRPL measurements were performed at room temperature. Figure 6.9 (c) presents the TV image of a microscopic ensemble. The dotted frame marks the area on the sample, from which the luminescence signal was collected. Depending on the nanowire density at the examined spot, the microscopic ensemble contained about 10 - 20 nanowires. If the temporal decay would be strongly determined by the individual properties of the nanowires, the random distribution should induce differences between the microscopic ensemble measurements. The evaluated transients of a typical microscopic ensemble is compared to the macroscopic ensemble measured at comparable excitation conditions in the standard TRPL setup in figure 6.9 (e). Although several measurements have been performed on various microscopic ensembles, the evaluated transients were always identical and very similar to the transient of the macroscopic ensemble within the experimental errors. Additionally, a single nanowire could be investigated, which was aligned parallel to the monochromator entrance slit, as shown in the optical image in figure 6.9 (d). The luminescence intensity of the single nanowire was significantly less, so the temporal decay could only be investigated for about 1.5 orders of magnitude in luminescence intensity. Again,

the evaluated transient is identical to the microscopic and macroscopic ensemble. The temporal decay of the Tb ions is therefore not determined by the individual nanowire properties. This becomes clear by assuming a typical 100 nm diameter nanowire of 50 µm length, which was doped with 0.2 at.% Tb. Already about $8 \cdot 10^6$ Tb ions are present in such a nanowire, which make it clear, why all the different nanowires show the same temporal behaviour. The large number of dopants already include all possible ion-ion and ion-killer center arrangements within one single nanowire. The statistics of the luminescence decay is therefore independent on the individual nanowire properties and already covered by each single nanowire [482].

6.4.6 Emission properties of single ZnS:Tb nanowires

The emission homogeneity of the Tb implanted ZnS nanowires was investigated using monochromatic CL imaging. Nanowires from the implanted ensemble were transferred by imprint to a clean Si substrate and investigated at low temperatures. Figure 6.10 (a) presents the comparison of the SEM and the monochromated CL emission observed at 2.26 eV with a bandpass of 0.1 eV. The single ZnS nanowires showed intense CL emission. The ZnS defect emission at 2.38 eV was significantly less intense (image not shown); therefore, it can be concluded that the observed CL emission at 2.26 eV mainly originates from the Tb $^5D_4 \rightarrow ^7F_5$ transition. Within the uncertainties of the method, no inhomogeneities in the CL emission were observed from the implanted ZnS nanowires; thus, a homogeneous Tb doping and optical activation was achieved.

The CL emission spectra of single Tb doped ZnS nanowires of different diameter taken at moderate excitation power and low temperature are shown in figure 6.10 (b). Although the results were not as obvious as for ZnO:Co nanowires, a trend was observed that the luminescence was dominated by Tb intra-4f emission and only a low intense ZnS defect emission was present even for nanowires up to 500 nm diameter. This observation was surprising, as a homogeneous Tb doping was only present to 120 nm with a maximum ion range of 210 nm, so that even the thinnest investigated nanowire (260 nm diameter) should not have been completely implanted. The sputter yield was calculated to be in the order of 12 atoms/ion, which is significantly higher due to the heavy mass of Tb compared to the transition metals. For the implanted Tb fluence of $1.4 \cdot 10^{15}$ ions/cm^2 (nom. 0.2 at.%), the sputtering should result in the removal of about 8-10 monolayers, which corresponds to about 5 nm of ZnS. Thus, the sputter effect cannot induce a significant thinning of the nanowires. A partial explanation is given by the electron voltage of 5 kV, which limited the penetration depth of electrons in ZnS to about 300 nm, thus mainly the implanted part of the nanowires was excited. But still does not completely explain the observation of the strong Tb luminescence for thick nanowires, as a dependency on the nanowire diameter would have been expected as for ZnO:Co nanowires. It is supposed that the excited carriers can diffuse through the ZnS crystal at low temperatures and are bound to the Tb impurities much more effective compared to the ZnO:Co system. This efficient energy transfer from the host was already observed by the PLE measurements (compare figure 6.8 (c)). The carrier diffusion and efficient energy transfer to the Tb ions can explain the observation at least for thinner nanowires. As nanowires were transferred after the implantation, the implanted side is randomly orientated to the electron beam. Due to the limited diffusion length, which is expected to be in the range of a few hundred nanometers [94, 556], the carriers recombine before they reach the Tb implanted part and are trapped by the impurities, explaining the increased contribution of the excitonic emission in the CL spectra for thick ZnS nanowires.

The CL emission properties of one single Tb implanted ZnS nanowires (diameter $\sim$ 480 nm, length = 9.3 µm, 0.2 at.% Tb) at different excitation powers are shown in figure 6.10 (c). The integrated emission intensities are plotted as a function of the excitation power in figure 6.10 (d).
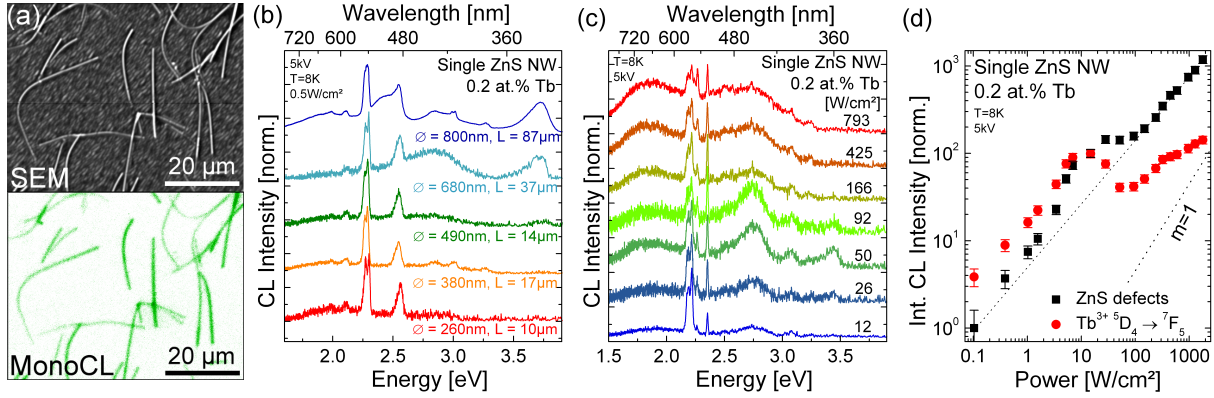
Figure 6.10: *(a) The comparison of the SEM and the monochromatic SEM image at 2.26 eV ($^5D_4{\rightarrow}^7F_5$) shows the homogeneous intra-4f emission of the transferred nanowires. (b) CL spectra of single nanowires show comparable emission features for the nanowires up to 500 nm diameter. (c) CL spectra of a single ZnS nanowire (diameter = 480 nm, length = 9.3 µm) at different excitation powers. (d) The integrated CL intensity of the ZnS defect and Tb $^5D_4{\rightarrow}^7F_5$ emission shows a complicated power dependency.*

At low excitation powers, the emission is dominated by the Tb intra-4f emission with a low intense ZnS defect luminescence. The sharp emission peak at 2.37 eV is related to the luminescence of an undetermined contamination, which solidified on the sample surface at low temperatures (see SEM image in figure 6.10 (a)) and probably originated from the residual gas. The emission intensity of the Tb and ZnS defect emission increases about linear with the excitation power up to 3 W/cm². At higher excitation, the ZnS defect emission increases more than linear, which was observed in the spectra by the appearance of an additional band at 2.75 eV. The emission energy suggests that the band is related to a self-activated (SA) defect center [497, 557]. The SA band gained strongly in intensity above 30 W/cm², while the Tb luminescence was quenched by a factor of about 3 up to 100 W/cm². At excitation powers above, the defect related emission band at 1.8 eV raised relative to the Tb and SA defect emission at 2.75 eV and a linear intensity increase of the ZnS defect and the Tb emission occurred up to 300 W/cm². The Tb luminescence saturated at higher excitation powers, while the ZnS defect emission ascended further linear.

The complicated emission behaviour of the Tb luminescence and the deviation of the otherwise linear power dependence of the ZnS defect emission is probably linked to the self activated defect emission band at 2.75 eV. Its occurrence could be related to the degradation of the ZnS nanowires induced by the intense electron beam due to the formation of defects in the ZnS matrix [558–560]. The assumption is reasonable and can explain why reversible measurements were only possible up to 3 W/cm². The quenching of the Tb luminescence could therefore result from a less effective excitation of the $^5D_4$ term and energy transfer processes from excited Tb ions to the self-activated center around 10 W/cm² and above. After saturation of the band at about 100 W/cm², the intensity of the Tb and the ZnS defect emission increased linear again with excitation power.

The spectral shape of the Tb $^5D_4{\rightarrow}^7F_5$ transition showed a strong dependence on the excitation power. The intra-4f luminescence is characterized by two bands of sharp emission lines in the range of 2.23 - 2.29 eV (compare figure 6.6 (c)) at low excitation powers. Increasing the power, the Tb emission was blue-shifted and broadened due to an additional emission at 2.32 eV, which can be attributed to the population of higher $^5D_4$ Stark levels. The intensity increase of the 2.32 eV emission above 300 W/cm² is correlated to the saturation behaviour of the Tb emission at this excitation power. Due to the long lifetime of ∼ 2 ms, lower $^5D_4$ Stark level are completely populated, so that the additional excitation results in the stronger population of energetically higher levels, which are not populated at low excitation powers. A similar blue-shift of the Tb emission was observed for µPL measurements at 1 kW/cm² cw excitation (not shown). However,

the self-activated defect band did not occur in the µPL measurements even at higher excitation levels, but the ZnS defect band at 1.8 eV was strongly enhanced and the Tb luminescence also showed saturation effects, comparable to the CL measurements.

6.5 Summary

ZnS nanowires were successfully doped with desired Mn concentrations via ion implantation. The Mn implanted nanowires exhibit a strong Mn intra-3d luminescence after annealing. The temporal decay was examined by TRPL spectroscopy at low temperatures. The transients can be described using a modified Förster model, which takes the nanowire geometry into account. Three approaches were conducted to influence the defect density in the ZnS:Mn nanowires: 1) implantation at elevated temperatures, 2) post-implantation annealing and 3) implantation of additional Ne ions. In all three approaches, a faster decay of the Mn luminescence was observed, which can be attributed to an enhanced non-radiative excitation of the excited Mn ions to killer centers. The transients of all samples could be well fitted using the modified Förster model with fixed parameter determined from the best recovered sample and adjusting only the defect line density n. The experiments conclude that the modified Förster model describes correctly all aspects of the temporal behaviour of Mn in ZnS nanowires.

Further on, ZnS nanowires were successfully doped by Tb ion implantation. A roughening of the surface was observed for high ion fluences and the nanowires exhibit a polycrystalline lattice structure. The crystal quality was significantly improved by annealing at 600°C in vacuum. A weak Tb related luminescence was observed directly after implantation, which could be enhanced by a factor of 100 due to the recovery of the ZnS lattice. The Tb luminescence could be assigned to intra-4f transitions of the $^5D_3$ and $^5D_4$ to the ^7F_J multiplet. The Tb emission intensity increased up to a concentration of 0.2 at.%, strong concentration quenching occurred above. The intra-4f luminescence is most intense at low temperatures and shows only slight thermal quenching up to room temperature. The temperature dependence is related to the different excitation efficiencies by energy transfer from the ZnS host, which could be proven by PLE measurements. The temporal decay of the Tb luminescence is non-exponential and faster for high Tb concentrations. A Tb lifetime of $\tau = 2.06 \pm 0.12$ ms was extracted from the nearly single exponential tail at long times after the excitation pulse. The transient can be successfully described by the modified Förster model using a reduced Förster radius, which proves the general applicability of the model for TM and RE implanted ZnS nanostructures. Microscopic ensembles and single ZnS:Tb nanowires were investigated by TRPL and identical transients were observed. One single nanowire therefore already exhibits the same temporal decay statistics as the nanowire ensemble, which was attributed to the large number of dopant ions and related ion-ion and ion-defect arrangements in the nanowire. The emission properties of single ZnS:Tb nanowires were examined by CL spectroscopy. A strong and homogeneous Tb emission was observed at low excitation powers. Power dependent measurements showed a quenching of the Tb intensity above 10 W/cm^2, which is related to non-radiative de-excitation and energy transfer to a self-activated defect band. After saturation of the defect band at 100 W/cm^2, the Tb luminescence increased linear with power, but saturated at 300 W/cm^2.

7 Summary and conclusion

Semiconductor nanowires exhibit unique optical properties, which are based on light emission, strong light confinement and light amplification, possible by gain from the semiconductor material and the resonator structure offered by the morphology of the nanowire. The combination of these properties enables the realization of nanoscaled light sources with small footprint and high spatially localized light emission. For the successful integration of nanowires into optoelectronic devices, three key challenges have to be investigated: 1) The emission properties of single nanowires have to be correlated to the morphology in order to determine the physical size limits for efficient nanowire emitters. 2) The emission properties of the semiconductor nanowires have to be tailored by doping. Transition metals and rare earth elements are suitable optical active impurities and offer extraordinary properties in the combination with nanowires. 3) The efficiency limiting processes, which result from the interaction of the nanowire and the impurities with defects, have to be investigated and understood. As the nanowire interacts with its surrounding, external influences have to be considered as well. This thesis reports on the lasing properties and doping of semiconductor nanowires and the presented experiments address all three key challenges. A µPL setup was developed, installed and established in the scope of this thesis, which provides the technical base for the investigation of the optical properties of individual nanowires.

The experiments on undoped ZnO and CdS nanolasers concentrate on the first key challenge in order to uncover the emission properties of the individual nanowire and fundamental size limits. ZnO and CdS nanowires were synthesized via the VLS mechanism. The structural properties of the nanowires were investigated using electron microscopy techniques. The nanowires exhibit a single crystalline structure and no extended defects were observed. The nanowires grow along the [0001] axis of the respective wurtzite crystal phases. This could be unambiguously identified for CdS nanowires by comparison of SAED patterns taken from selected directions of the crystal lattice. The optical properties of single ZnO and CdS nanowires were investigated using µPL at room temperature and moderate cw excitation. A saturation of the defect emission was observed at low power densities, which points out the superior optical quality of the synthesized nanowires. µPL measurements using pulsed excitation could observe a broad excitonic emission at moderate power levels, yielding into amplified spontaneous emission by increasing the laser power. Sharp, equidistant spaced peaks appear and dominate the emission at high pumping levels. The evaluated power dependency showed a linear increase in the moderate excitation regime, followed by a super linear slope above, which is typical for amplified spontaneous emission. The power dependence returned to a linear slope at high power levels, which is the definite proof for lasing oscillations in ZnO as well as CdS nanowires at room temperature. The experimental data of the respective power dependences were fitted using an analytic model for multi-mode lasers [360]. A threshold of 300 kW/cm^2 was determined for ZnO nanolasers, which is in well agreement with literature [51]. The threshold for CdS nanolasers was determined to be in the order of 10 kW/cm^2, which is significantly lower compared to their ZnO counterparts. µPL measurements in a "head-on" geometry were able to collect the direct emission from the CdS nanowire end facet and allowed to judge the slope efficiency in the lasing regime to 5 - 10 %, which is also a higher value compared to ZnO nanowires. Further on, the head-on µPL setup enabled the investigation of the excitation polarization on the nanowire lasing. The mode spacing of the CdS nanolaser emission verified the Fabry-Pérot type resonator. The lasing ability of CdS nanowires was correlated to their morphology in order to determine the physical size limites for CdS nanolasers. No lasing oscillations occured in nanowires below 175 nm diameter independent of the length,

which can be explained by the reduced light confinement at smaller diameters. For thicker nanowires, lasing was observed for nanowires longer than 7 μm, representing the minimum length of the CdS nanowire cavity to achieve sufficient gain to compensate the losses. The results were compared to size limits of ZnO nanolasers, leading to the conclusion that the lasing ability of semiconductor nanowires is governed material properties (emission energy, refractive index and material gain) and morphology (diameter, length and shape of facet ends). A strong influence of the substrate was found on the emission properties of the nanowires. The choice of a low index substrate (SiO_2) could drastically reduce the leakage of the guided modes from the nanowires into the substrate, which was found for CdS nanowires on Si by FDTD simulations. The comparison of the emission properties of ZnO and CdS nanowires could finally identify the origin of the lower lasing threshold of CdS nanolasers as a combination of several factors: the reflection was increased by the remaining Au calatyst dot attached to the end of many CdS nanowires, which were missing for the majority of the ZnO nanowires. Additionally, CdS has larger exciton bohr radius, so that the critical concentration of electron-hole pairs necessary to establish the electron-hole plasma, which is expected to be the gain mechanism, is reached at lower pumping powers in CdS nanolasers.

Future investigation should characterize the emission polarization of the nanolasers in the head-on setup, which will help to determine the fundamental lasing modes in combination with FDTD simulations. Modifications of the nanowire morphology (e.g. at deformed facet ends) could improve the quality of the resonator and enable the tuning of the emission properties and lasing at even lower thresholds.

The experiments on doping of ZnO nanowires by ion implantation with cobalt address the second key challenge. The modification of the doped ZnO nanowires with the ion beam was investigated using electron microscopy techniques and could be related to the interaction with the ion beam. The nanowires experienced a roughening of the surface. Bending occurred due to the created defects at high ion fluences. Nanowires in contact to the substrate suffer from enhanced sputter effects compared to free-standing nanowires. The stoichiometric investigation of single Co implanted nanowires could verify the successful and homogeneous doping in desired concentrations. Lateral resolved XAS spectroscopy could observe the good recovery of the crystal structure by annealing. The Co^{2+} ions occupy Zn lattice sites in a nearly undisturbed surrounding for a concentration of 0.3 at.%.

PL and CL spectroscopy prove the optical activation of the implanted Co ions after annealing. Intense Co^{2+} intra-3d emissions were observed in the VIS and IR range. The $^2E(G) \rightarrow {}^4A_2(F)$ transition at 1.88 eV showed the strongest intensity and was studied in detail. The Co ions were excited via energy transfer from the ZnO host, but also near-resonant excitation is possible with a high efficiency. The Co luminescence intensity increases for higher Co concentrations. However, the crystal quality was significantly reduced at concentrations above 1 at.% due to the creation of extended defects in the nanowire structure, which cannot be recovered by annealing. An improvement of the Co emission intensity by one order of magnitude could be achieved by adjusted annealing conditions and implantation at elevated substrate temperatures. The bending of the nanowires could be suppressed by implantation at 700°C, as the created defects can recombine directly during implantation by enhanced dynamic annealing. The strong Co emission was observed up to 150 K. Thermal quenching reduced the emission intensity at higher temperatures, but the Co^{2+} intra-3d emission is not completely quenched at room temperature. TRPL measurements could determine a radiative lifetime of $\tau_{Co} \sim 8$ ns.

CL and μPL investigations on single doped nanowires show the dominant Co luminescence. Monochromatic CL imaging proves the homogeneous impurity emission. The contribution of the

ZnO to the nanowire emission was found to depend on the nanowire diameter in relation to the ion range. Power dependent µPL investigation on a single doped ZnO nanowire showed a linear increase of the Co emission intensity at moderate cw excitation. The diameter of the investigated nanowire was below the critical diameter for efficient waveguiding, which could be observed for doped nanowires with large diameters > 400 nm. Only a low intense Co^{2+} emission was detected at µPL measurements using pulsed excitation, which is probably related to the short lifetime of the Co ions.

The temporal decay of the Co ions in ZnO nanowires should be further investigated with a TRPL system with better time resolution on nanowires with large diameters. Those measurements should be performed as a function of the nanowire diameter and varying pump intensities in order to detect gain mechanisms of the impurities by the shortening of the lifetime. The TRPL measurements could be compared to equally prepared ZnO single crystals in order to judge the influence of the nanostructure on the temporal decay of the impurity luminescence. Additional investigation on the temporal coherence of the impurity emission by $g^{(2)}(\tau)$ auto-correlation measurements could be helpful to detect light amplification mechanisms of the excited impurities. The realization of nanowire impurity LEDs could be performed by adding electrical contacts to the doped ZnO nanowires and investigation of the electroluminescence properties.

The experiments on Mn implanted ZnS nanowires examine the interaction of Mn impurities with defects and are directly related to the third key challenge. The temporal decay of the Mn ions is influenced by the energy transfer between Mn ions (mean Mn-Mn distance) and the distance to killer centers (defect concentration). An additional influence arises from the ratio of these lengths to the nanowire diameter. The radiative Mn decay can be fitted using a Förster dipole-dipole model [229], which was modified for 1D and 2D sample geometries [9]. The model could be successfully verified for different Mn concentrations and ZnS nanostructure morphologies [183]. In the experiments presented in this thesis, the defect concentration is varied in a controlled manner by three different approaches. The modified Förster model is tested for its ability to describe the Mn-defect interaction. First, ZnS nanowires were implanted with different Mn fluences in order to establish low and high doping conditions with minor and major energy transfer in the Mn sublattice, respectively. After annealing, the radiative Mn decay was investigated by TRPL and the experimental transients were fitted with the model. In the next step, the defect concentrations in the ZnS nanowires were modified by a) implantation at elevated temperatures, b) post-implantation annealing and c) additional implantation of Ne ions. The creation of defects leaded to a faster decay of the Mn luminescence due to the non-radiative de-excitation of Mn ions in all cases. The evaluated transients were fitted using the modified Förster model. The fit parameter determined for the best recovered sample were fixed and only the defect line density was varied to fit the data. In all cases, the model delivered a reasonable fit for the data. This points out that the modified Förster model is capable to describe the Mn-defect interaction correctly and could be experimentally verified for all fit parameters.

The experiments on implantation of ZnS nanowires with terbium display a second approach for the key challenge of nanowire doping. The morphology of the implanted ZnS nanowires was characterized by electron microscopy techniques. The crystal structure is polycrystalline after the implantation, but the crystal quality could be improved by annealing. EDX measurements verify the incorporation of Tb in the desired concentration.

Intense Tb intra-4f luminescence was observed from implanted and subsequent annealed ZnS nanowire ensembles. The emission peaks could be assigned to transitions from the excited $^5D_3$ and $^5D_4$ to the ^7F_J multiplet. The activation of the Tb ions in the ZnS nanowires was investigated by annealing at temperatures between 200 - 700°C in vacuum. A strong Tb emission increase

was observed after annealing above 400°C, which can be correlated to the recovery of the ZnS lattice. The emission intensity could be increased by a factor of 100 after annealing at 600°C compared to the as-implanted state. The ZnS nanowires dissolved at higher temperatures in vacuum. The terbium concentration was optimized in the range of $2 \cdot 10^{-4}$ - 2 at.%. A sublinear PL intensity increase was observed up to 0.2 at.%. Higher Tb concentrations yielded into a strong concentration quenching of the luminescence. The temperature dependent emission intensity was investigated in the range of 4 K to room temperature. Only a minor thermal quenching was observed for the Tb luminescence. PLE measurements at different sample temperatures could uncover the temperature dependent excitation efficiency for energy transfer from the ZnS host, which explain well the temperature emission dependence. The temporal luminescence decay was observed by TRPL measurements on ZnS:Tb nanowire ensembles. A strong non-exponential decay occurred at short times after the excitation, which was determined by the interaction with defects. From the nearly single-exponential tail at late times, a radiative lifetime of $\tau_{Tb} = 2.06$ ms could determined as only isolated ions contributed by spontaneous emission. The transients of the 0.2 and 2 at.% Tb nanowire ensembles could be reasonably fitted using the modified Förster model with a reduced Förster radius. The smaller interaction distance can be attributed to the higher shielding of the 4f-electrons in the rare earth ions compared to the 3d-electrons in transition metals. TRPL measurements were performed on microscopic ensembles and even single doped nanowires to investigate, if the temporal decay depend on the properties of the individual nanowire. The evaluated transients were in every measurement equal to the ensemble measurement, which could be attributed to the high number of dopants present in one nanowire at the chosen preparation conditions. CL measurements in single ZnS:Tb nanowires confirm a homogeneous impurity emission. The emission characteristics of individual nanowires depend on the ratio of the diameter to the Tb ion range. Although nanowires below 600 nm are not completely implanted, the Tb emission dominated the CL spectra, which can be attributed to the diffusion of excited carriers to the Tb impurity centers, pointing out the high efficient of the energy transfer from the ZnS matrix into the Tb subsystem. A complicated power dependence was observed for CL measurements on single ZnS:Tb nanowire. The deviations from a linear dependence can be attributed to a self-activated defect center created by the irradiation with the intense electron beam. Saturation of the Tb emission intensity was observed above 300 W/cm^2. The results of experiments on ZnS:Tb nanowires contain the optimization of the preparation parameters and the conclusive characterization of the nanowire emission properties. In the next step, ZnS:Tb nanowire based electroluminescence devices should be realized by adaption of the concepts for thin film electroluminescence devices [233, 505].

The successful realization of nanoscaled light sources is linked to the understanding of the fundamental optical properties of semiconductor nanowires. This creates the need to investigate the physical size limits and correlate the emission properties of the individual nanowire with its morphology. The approaches for the doping of nanowires with suitable impurities have to be developed and of the influence of defects on the emission efficiency needs to be investigated. The experiments in this thesis address all the mentioned key challenges: The knowledge of the physical size limits is crucial for the future integration of CdS nanolasers into devices. Doping of semiconductor nanowires can be successfully achieved by ion implantation and subsequent annealing using optimized preparation conditions, which enables to tailor the optical properties of the nanowires. Time resolved PL spectroscopy was proven as a tool to investigate the interaction of the nanowires and impurities with defects. The results of the experiments presented in this thesis provide a valuable contribution for the future realization of nanoscaled light sources.

A Properties of the luminescence setups

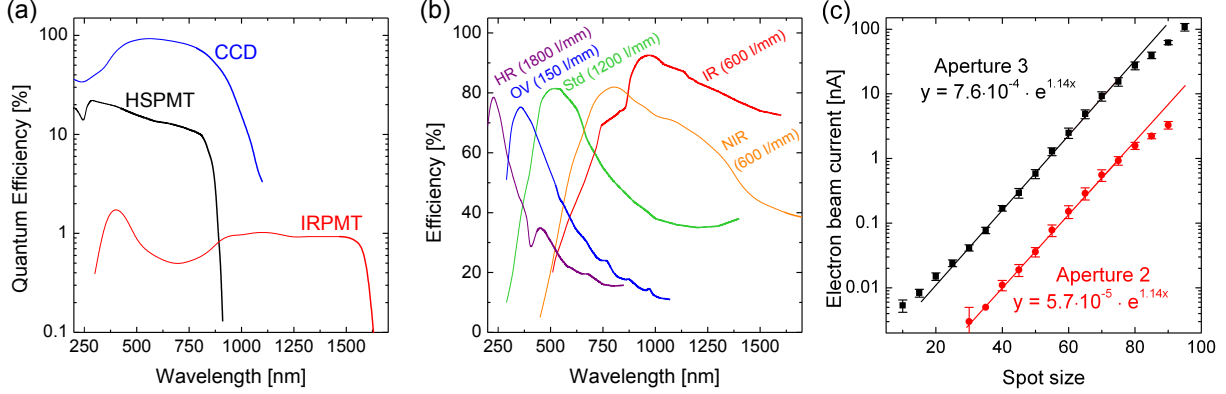## A.1 Details of the cathodoluminescence setup

Figure A.1: *(a) Quantum efficiencies of the CL detectors. Data taken from Gatan Inc. [561]. (b) Efficiencies of the dispersion gratings at 45° polarization (S- and P-component of the incident light have equal intensity.) Data taken from Newport [562]. (c) The SEM electron beam current can be varied by the spot size from below 0.01 to 100 nA. The relation between the spot size and the electron current can be fitted using a simple exponential function.*

The focussed electron beam of the JEOL JSM-6490 excites the sample. The luminescence light is collected by a parabolic Al mirror (PM) from the focal spot (diameter $\sim$ 30 µm) and guided by the retractable light guide to the detection system, as shown in figure 3.2 in chapter 3.3.2. A long pass filter (F) can be inserted to block higher order diffractions. In *panchromatic* mode, the luminescence intensity is detected by the photomultiplier as a function of the excitation position. In *monochromatic* mode, the luminescence light is guided by mirrors (M) and focussed by a lens (L) onto the monochromator entrance slit (S). A 1200 l/mm grating is installed as standard in the 300 mm Czerny-Turner type monochromator, a second grating can be exchanged according to the specific application. The spectrally dispersed light is detected by the photomultiplier or CCD. Two photomultipliers are available: a peltier cooled GaAs photomultiplier provides high sensitivity in the UV-VIS range (HSPMT, Hamamatsu R943, 200 - 900 nm). For investigations in the IR range, the light is detected by a liquid nitrogen cooled InGaAs photomultiplier (IRPMT, Hamamatsu R5509-43, 300 - 1700 nm). Fast parallel acquisition can be performed using the a back-illuminated peltier cooled CCD (Roper Scientific Spec-10, 200 - 1100 nm). The quantum efficiencies of the detectors and the available gratings are shown in figure A.1. Further properties of the gratings are listed in table A.1. The excitation intensity can varied by the beam current, which is related to the spot size (SS) and the beam aperture of the SEM. An increase of 5 in spot size is about a doubling of the electron current. The mid-sized aperture 2 is useful

Table A.1: *Details of the available CL gratings.*

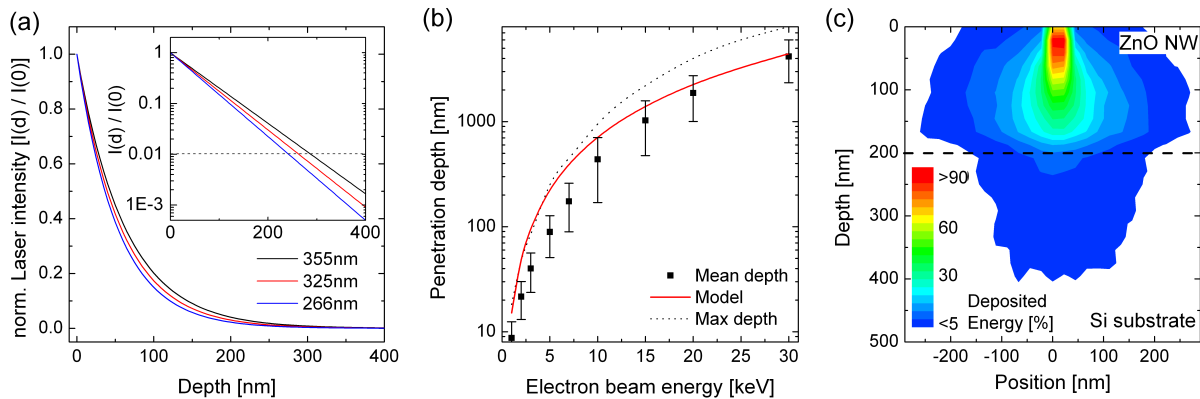| Grating	Grooves [l/mm]	Blaze [nm]	Coverage on CCD [nm]	Dispersion [nm/mm]	Min. Resolution [nm] @ 20 µm Slit
Overview	150	300	567	21.6	1.08
NIR	600	800	134	5.03	0.27
IR	600	1600	134	5.03	0.27
VIS (Std.)	1200	500	60	2.7	0.14
UV HR	1800	250	34	1.8	0.09

Figure A.2: *(a) Absorption of photons in ZnO for excitation with different UV lasers. (b) Mean penetration depth of electrons in ZnO as a function of the acceleration voltage simulated by CASINO. The Kanaya-Okayama model [563] overestimates the penetration depth for small voltages. (c) Distribution of the deposited energy of 10 keV electrons impinging on a 200 nm ZnO nanowire on Si.*

for imaging, while the larger aperture 3 offers a factor of 10 higher beam currents at a reduced SEM resolution. This allows a beam current variation within ~ 10 pA (at SS 20, aperture 2) to more than 100 nA (SS 90, aperture 3), as shown in figure A.1 (c). It has to be noted that the available beam currents are highly dependent on the adjustment of the electron gun. The beam current can be measured using the Faraday cup of the retractable beam blanker (Xenos XeBase) and a pico-ammeter (Keithley 485).

Several improvements were installed to the commercial system: nitrogen venting of the monochromator was installed to prevent condensation of water vapour on the CCD window. The thermoelectric cooler of the CCD was converted to liquid cooling as the fan introduced strong vibration, limiting the SEM performance. A long pass filter was installed to suppress the second diffraction order and therefore allows investigations in a broader spectral range.

A.2 Excitation depth in II-VI semiconductors

II-VI semiconductors exhibit a strong absorption of photons with energies larger than respective the band gap due to the creation of electron-hole pairs, which leads to limited excitation depth of the laser light in the material. Assuming that the absorption follows the simple Lambert-Beer law [566], nearly all of the incoming light is absorbed within the 300 nm of the semiconductor, as shown in figure A.2 (a) for the example of ZnO. The excitation depth is in the typical range of the nanowire diameters. The absorption coefficients at room temperature and the excitation depth (at 99% absorption) are listed in table A.2 for common UV lasers used in photoluminescence spectroscopy of II-VI semiconductors.

The excitation depth of hot electrons strongly depends on kinetic energy, determined by the acceleration voltage of the electron gun. Upon penetration of the target, the electrons are de-accelerated due to the interaction with the target electrons and nuclei in form of elastic and

Table A.2: *Absorption coefficient and penetration depth of UV lasers in II-VI semiconductors at room temperature.*

Material (Citation)	Absorption @ 355nm	coefficient @ 325nm	α [10^5 cm^{-1}] @ 266nm	99% @ 355nm	absorption @ 325nm	at depth [nm] @ 266nm
ZnO ([564])	1.6	1.7	1.9	290	262	240
ZnS ([565])	0.2	1.4	2.8	2300	330	165
CdS ([390])	1.6	2.2	3.8	288	210	120

inelastic scattering, thereby creating $\sim E/3E_G$ electron-hole pairs per electron [291, 292]. The penetration depth of the electrons in the semiconductor material therefore depends on their kinetic energy E and can be estimated by $R_e = \left(0.0276A/(\rho \cdot Z^{0.889})\right) E^{1.67}$ [563], with A being the atomic weight, ρ is the material density and Z is the the atomic number. This empirical formula developed by Kanaya and Okayama was found to be in good agreement with experimental data for several semiconductors [291].

The penetration depth of electrons in ZnO was simulated in the energy range of 1 - 30 keV using the Monte-Carlo code *CASINO* [293–296]. The mean as well as the maximum penetration depth is plotted in figure A.2 (b) as a function of the acceleration voltage. The data follow the Kanaya-Okayama model for high energies, but the model overestimates the penetration depth at small energies. The distribution of the deposited energy was also simulated with *CASINO* for 10 keV. The result is displayed for a 200 nm diameter ZnO nanowire on a Si substrate along the nanowire axis in figure A.2 (c). At these conditions, the electrons deposit more than 85 % of their energy in the nanowire. For the investigation of semiconductor nanowires with typical diameters of 100 - 500 nm, an electron acceleration voltage of 5-10 keV is therefore a reasonable choice.

A.3 Properties of the (micro-)photoluminescence setup

In the scope of this work, a (micro-)photoluminescence setup was developed and installed. The concept includes a setup, which allows the investigation of single wide band gap semiconductor nanostructures as well as the fast characterization of thin film semiconductors used for photovoltaics. The detection range should span from the UV (200nm) up to IR (1650nm) and sample temperatures between 4 K to 300 K should be available. In addition, time resolved detection down to ns resolution and a tunable light source for wavelength selective excitation complete the setup.

A.3.1 Sample mounting and cooling

For investigations at room temperature, a sample holder can be mounted on a 3-axis stage (Thorlabs LT3) with 50 mm moving range in every direction. Each axis is equipped with differential screw drives, which allow a fast movement as well as high accuracy positioning with a resolution better than 1 µm. A rotation stage (Thorlabs MSRP01) can be mounted on top, which allows angle adjustment with a resolution better than 0.5°.

For investigations at low temperatures, the samples can be installed into a helium flow microscopy cryostat (Janis ST-500), which allows sample temperatures from 3.5 K up to 475 K. The cryostat can be cooled using liquid helium (consumption $\sim$ 1 l LHe per hour @ 5 K) or with liquid nitrogen (consumption $\sim$ 0.1 l LN$_2$ per hour @ 80 K) with a temperature stability of about 0.05 K. A rotary pump (Oerlikon Sogevac 10) introduces low pressure down to some mbar in the system and draws the coolant from the reservoir through the cryostat. The coolant flow is regulated using a fine valve installed at the LHe transfer tube, suitable pressures for the lowest base temperature (3.3 K with LHe) were found at a pressure of 180 - 220 mbar in the system. The cool down time from 300 K to 4 K is approximately 20 min, stable operation at a base temperature below 4 K is reached after 15 min. The cryostat is equipped with a patron heater in combination with a temperature controller (LakeShore 331), which allows software controlled variation of the sample temperature between 4 K and 475 K. Heating from 4 K to 300 K can be performed in $\sim$ 45 min.

For characterization of many or large samples, a macro sample holder (diameter 50 mm) is avail-

able in combination with a large UV fused silica front window (3 mm thickness). Several holders are available for a sample thickness up to 3.5 mm. For µPL measurements, a micro sample holder (diameter 20 mm) can be used in combination with a microscopy UV fused silica window (0.5 mm thickness), which allows work distances of less than 2.0 mm. Several holders for a sample thickness between 0.5 and 3.5 mm are available.

A 10 point electrical feed through is available for contacting samples inside the cryostat, thus allowing electroluminescence measurements or characterization of LEDs and FET structures under illumination. A sample holder with a 28 pin SMD PLCC chip socket was designed to fast and reliable integration of pre-contacted samples.

The cryostat is mounted on a high precision 3-axis stage (Thorlabs LNR50DD), which provides high stability and positioning with 50 mm movement range in each direction; therefore, every position on the sample holders can be addressed. Each axis is equipped with differential drives for fast position movement and high accuracy positioning with a resolution better 1 µm. Although the cryostat and related parts introduce a vertical load of almost 10 kg, only negligible position drift and angular tilt is observed.

A.3.2 Excitation sources

Several excitation sources are available to match the experimental conditions: a HeCd laser (Kimmon IK3301R-G) emitting at 325.0 nm with 33 mW in single mode (TEM_{00}) and a HeNe laser (Polytec PL-750) emitting at 632.8 nm with 5 mW (TEM_{00}) are available for continuous wave excitation. A Nd:YAG laser (Innolas DPSS10-100) delivers nanosecond pulsed excitation (pulse width FWHM 9 ns) at a frequency up to 200 Hz. The fundamental wavelength 1064 nm (10 mJ) can be frequency doubled (532 nm, 5 mJ), tripled (355 nm, 2.5 mJ) and quadrupled (266 nm, 0.7 mJ). The delay of the pocket cell as well as the hold-off voltage of the Q-switch can be altered to adjust the pulse energy. The intensity of the laser beams can be further attenuated using a $\lambda/2$ wave plate in combination with a Brewster window (Eksma 990-0071) optimized for the specific wavelength. The attenuation range is variable between 200:1. External synchronization of the laser with e.g. an intensified CCD camera can be established.

The lasers are mounted on an optical table and optical shielding suppresses stray light. The laser beams are guided using flippable dielectric high power laser mirrors (reflectivity > 99.5 %) onto a Pellin-Broca UV fused silica prism, which disperses the desired wavelength under an exit angle of 90° towards the incoming direction. Other wavelength (e.g. from higher harmonics) are blocked by the iris aperture. The laser beam is aligned to pass trough two iris apertures, therefore every wavelength can be delivered at the same laser beam axis. Switching between different wavelength is performed by turning of the Pellin-Broca prism and re-adjustment of the mirrors, which can be typically performed in less than 10 min. The intensity of all lasers can be adjusted by reflective neutral density filters in a filter wheel. The range spans more than eight orders of magnitude (around hundred pW up to tens of mW).

A tunable excitation source is provided by a 75 W Xe high pressure lamp, which is mirror coupled to a 200 mm monochromator (Optical Building Blocks Tunable PowerArc Illuminator, f/4). The system is computer controlled and provides light in the range between 250 to 1000 nm. Two 1200 l/mm gratings optimized for UV (blaze 300 nm) and VIS (blaze 500 nm) are available. The minimum bandwidth is 0.25 nm at 20 µm slit with maximum power of 5 µW/nm at 470 nm. The highest output power of 5 mW at 470 nm is achieved at 10 nm bandwidth (5 mm slit). The tunable light source can be coupled to a 900 µm UV-VIS optical fiber and focused by a spherical lens onto the sample.

For on-line power monitoring, an uncoated UV fused silica beam splitter (Reflection ~ 8 %)
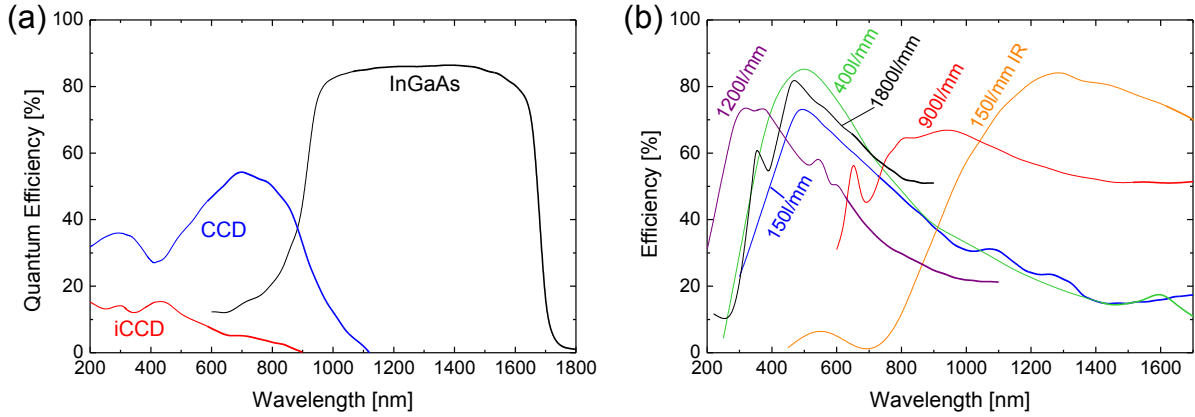
Figure A.3: *(a) Quantum efficiencies of the PL detectors. Data taken from Princeton Instruments [567]. (b) Efficiencies of the dispersion gratings at 45° polarization (S- and P-component of the incident light have equal intensity.) Data taken from Newport [562].*

can be inserted into the laser beam. The intensity of the reflected beam is determined by a Si photo diode (Thorlabs S130VC, 200-1100 nm, 1 nW - 50 mW cw) suitable for cw and low power pulsed lasers (up to a mean power of 2 µW). A thermopile sensor (Thorlabs S302C, 190 nm - 25 µm, 10 µW - 2 W) is available for high power pulsed lasers. Both sensors are monitored using the Thorlabs PM100USB module on the computer. Higher laser powers can be measured using neutral density filters in front of the sensors.

A.3.3 Detection hardware

The luminescence light is focussed by a 150 mm lens (f/6) onto the 500 mm Czerny-Turner imaging monochromator (Princeton Instruments SP-2500i, f/6.5), which is equipped with two entrance ports. This enables two different experiments to use the same detection hardware without re-arrangement of optical equipment. Both ports provide a full software controlled filter wheel (6 positions), entrance slit (5 µm - 12 mm, 5 µm step), mechanical shutter as well as internal switching between the ports via a movable mirror. The luminescence light is dispersed at one of the three dispersive gratings on the installed turret and focussed by a toroidal mirror onto the detector. Two grating turrets are available, turret 1 optimized for UV-VIS operation and turret 2 for NIR and ultra-high resolution VIS. The efficiencies of the installed gratings are shown in figure A.3, further details are listed in table A.3.

A liquid nitrogen cooled (-120°C) front-illuminated CCD camera (Princeton Instruments Spec-10:256E/LN, open electrode chip) is installed at the front exit port. The open electrode CCD chip offers light detection sensitive 200 - 1100 nm with a peak quantum efficiency of 55 %. Although this sensor type offers lower quantum efficiencies compared to back-illuminated devices, it is completely free of the etalon effect. Etaloning causes a modulation of the light intensity due to thin film interference effects on the back-thinned chip, and thus allows disturbance free recording of spectra over the complete sensitivity range.

This camera can be exchanged to an intensified CCD camera (iCCD, Princeton Instruments PI-MAX 3), which allows time-resolved recording of luminescence spectra. The detector (18 mm Gen2 intensifier, photocathode RB fast) is sensitive between 200 - 900 nm (Peak QE 16 %) with a minimum gate width of 2.7 ns. The software controlled build-in timing generator allows pulse series from ns to ms with a timing accuracy of 40 ps and an insertion delay of 27 ns. External synchronization to a pulsed laser is available. The intensifier is capable of up to 5 MHz aquisition rate and is therefore suitable in combination with high repetition lasers.

On the side exit port, a liquid nitrogen cooled (-100°C) InGaAs array detector (Princeton instru-
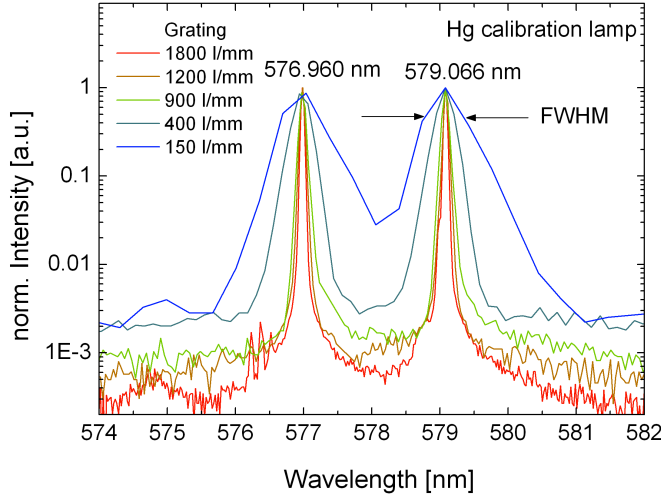
Figure A.4: *The resolution of the PL detection system was measured by the FWHM of the 576.960 nm and 579.066 nm emission of the Hg calibration lamp using different gratings and the CCD detector (20 µm slit). A minimum resolution of 0.059 nm (0.18 meV at 579 nm) can be achieved with the 1800 l/mm grating.*

ments OMA V:1024-1.7) is mounted for light detection in the NIR (800 - 1700 nm). The 1024 pixel array has a peak QE of 85 %. The quantum efficiency curves for the decectors are shown in figure A.3. A movable mirror is used to switch between the detectors.

All functions of the monochromator and the detectors are controlled a the Winspec acquisition software, which also allows step&glue acquisition as well as gluing of recorded spectra. More accessories for the monochromator are available, e.g. a combined Hg/Ar and Ne calibration lamp which can be directly attached to the side entrance of the monochromator. Further on, this port can be reassembled with a fiber connector, which includes a mirror based f-matcher for maximum collection efficiency without chromatic abberations.

The spectral resolution of detection was determined by detection of the 579.066 nm emission line of the Hg calibration lamp with the CCD camera at 20 µm slit width (figure A.4). The integration time was adjusted to achieve comparable signal intensities. The resolution was determined by fitting the 579.066 nm emission line with a Gaussian function and evaluation of the full width at half maximum (FWHM). The minimum resolutions using the 1800 lines/mm grating was determined to 0.059 nm, which equals 0.18 meV at the used emission wavelength. For higher wavelength, the energetic resolution is even better. The observed minimum resolution for each grating is listed in table A.3.

Table A.3: *Properties of the available dispersion gratings on the UV-VIS optimized turret (1) and the IR optimized turret (2). The resolution was determined using the Hg calibration lamp emission line at 579.066 nm and 20 µm slit width.*

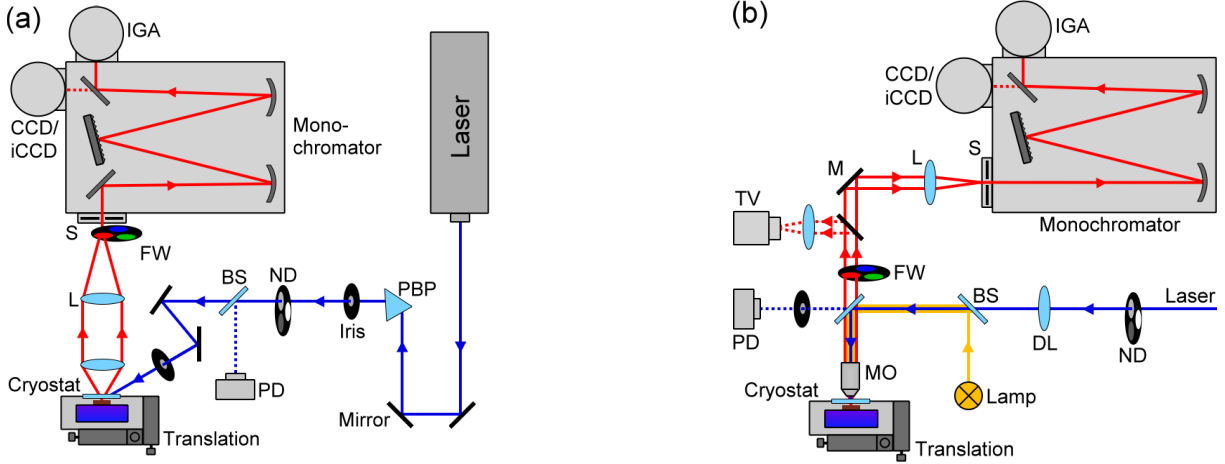| Turret	Grooves [l/mm]	Blaze [nm]	Coverage on CCD [nm]	Dispersion [nm/mm]	Min. Resolution @ 20µm Slit [nm]
1	150	500	350	13.1	0.67
1	400	550	120	4.7	0.24
1	1200	300	40	1.5	0.08
2	150	1250	350	13.1	0.67
2	900	Holo-IR	50	1.9	0.09
2	1800	500	24	0.9	0.05

Figure A.5: *(a) Scheme of the macro PL setup: The excitation laser (cw or pulsed) is guided by mirrors (M) through a pellin-broca prism (PBP) to separate the excitation wavelength from other harmonics. The laser intensity can be adjusted by neutral density filters (ND) and a part of the laser beam is guided by a beam splitter (BS) to a power diode (PD) for on-line monitoring. The luminescence from the sample mounted in a cryostat is collected by lenses (L) and focused onto the monochromator entrance. The laser and higher order diffractions are suppressed by a long pass filter wheel (FW). The dispersed luminescence is detected either by a CCD(iCCD) or an InGaAs array (IGA). (b) Scheme of the μPL setup used for the investigation of single nanowires: The laser beam is guided by a beam splitter and focused by a microscope objective (MO) onto the sample. The luminescence light is collected in backscatter geometry, passes the beam splitter and the filter wheel and is detected either by a TV camera (TV) for imaging or the detectors attached to the monochromator for spectral acquisition. White light can be coupled to the beam path for bright field illumination.*

A.3.4 Macro PL setup

For fast sample characterization, a macro photoluminescence setup is installed at the side entrance port of the monochromator. The scheme is presented in figure A.5 (a). The laser beam is guided by two UV enhanced Al mirrors onto the sample under an angle of 55° to the sample surface normal. This angle was chosen as it is close to the Brewster angle of the cryostat front window (UV fused silica) and thus minimizes the reflections at the window surfaces. The beam diameter is determined by an iris aperture to minimum 1.0 mm which helps for an reproducible adjustment of the laser beam. The luminescence light is collected by a plano-convex lens with a focal length of $f_1 = 30$ mm (collection angle $\sim 50°$, NA = 0.42) and focussed by a $f_2 = 150$ mm plano-convex lens on the monochromator. The focal length of the second lens matches the f-number of the monochromator. Depending on the experiment, three sets of lenses are available:

Table A.4: *Available long pass filters for the PL setup. [M]Dielectric filters may introduce a modulation of the PL signal.*

Filter	Type	$\Delta\lambda$ [nm]	Range [nm]	Blocks 266	laser 325	[nm] 355	532	633
WG305	Absorbive	35	315-1700	✓	X	X	X	X
ASA350	Dielectric[M]	20	355-1700	✓	✓	X	X	X
SEM355	Dielectric[M]	5	360-800	✓	✓	✓	X	X
GG385	Absorbive	35	400-1700	✓	✓	✓	X	X
FEL550	Dielectric[M]	15	570-1700	✓	✓	✓	✓	X
OG590	Absorbive	35	610-1700	✓	✓	✓	✓	X
FEL650	Dielectric[M]	15	670-1650	✓	✓	✓	✓	✓
OG715	Absorbive	35	730-1700	✓	✓	✓	✓	✓
OG850	Absorbive	35	900-1700	✓	✓	✓	✓	✓

a pair of uncoated UV fused silica provides the largest transmission range from 200 - 1700 nm. The anti-reflex coated BK7 lens pair maximizes the throughput in the VIS range (350 - 800 nm). The focusing and chromatic abberation can be enhanced using a NUV achromat lens instead of the $f = 150$ mm BK7 lens. For NIR investigations, a set of NIR anti-reflex coated achromats (800 - 1700 nm) performs best. A set of six longpass filters in the filter wheel in front of the monochromator entrance suppresses the laser beam or second order diffractions. A list of the available filters is given in table A.4.

A.3.5 Micro PL setup

The micro-photoluminescence setup described in chapter 3.3.2 works like a epifluorescence microscope. The scheme is displayed in figure A.5 (b). A UV fused silica plate beam splitter (Transmission/Reflection 80/20 between 250 - 400 nm) splits the laser beam and the reflected part is focussed by a microscope objective onto the sample. Good focusing of the laser beam results at a laser spot of < 800 nm in diameter for a 100x objective and up to 5 µm for a 15x objective. A list of the available objectives and their properties is given in table A.5. The luminescence light is collected by the same objective, passes the beam splitter in transmission. The reflected laser can be suppressed by a longpass filter in the beam path behind the beam splitter. A UV enhanced Al mirror guides the luminescence on a monochromatic TV camera (Watec WAT-120N+). The microscope image is displayed on a small CRT monitor and can be captured by a video grabber. A white light source (Thorlabs OSL1) can be coupled into the light path by an uncoated UV fused silica beam splitter (Transmission/Reflection 90/10 between 200 - 1700 nm). This allows illumination of the sample for focusing and sample positioning, similar to a bright field microscope. Using dimmable self-built LED ring, dark field illumination can be realised, which is sometimes better suited for the investigation of small nanostructures.

Flipping apart the mirror in front of the TV camera, the luminescence light guided by another mirror and focussed on the front entrance slit of the monochromator. The main advantage of this configuration is that the possibility to adjust the same point in the center of the TV camera and at the entrance slit of the monochromator. This allows fast switching between optical imaging and spectral data collection from the same sample position. In addition, the mirror allows a fine shift of the microscope image on the entrance slit without the need of mechanical repositioning of the sample. The sample image on the CCD detector can be shifted with an accuracy better than

Table A.5: *Details for the microscope objectives available at the µPL setup.*

Manufacturer	Type	Magnification	NA	WD [mm]	Transmission [nm]
Newport$^{(UV,C)}$	Reflective	15x	0.40	20.3	200 - 2000
Newport$^{(UV,C)}$	Reflective	36x	0.52	10.4	200 - 2000
Zeiss$^{(355,C)}$	Refractive	10x	0.25	~ 6	400 - 800
Zeiss$^{(355,C)}$	Refractive	15x	0.30	~ 5	355 - 800
Zeiss	Refractive	25x	0.50	< 2	400 - 800
Zeiss	Refractive	40x	0.65	< 1	400 - 800
LOMO$^{(355)}$	Refractive	40x	0.75	< 1	355 - 800
Zeiss	Refractive	63x	0.80	<1	400 - 800
LOMO$^{(355)}$	Refractive	90x	1.25	<1	355 - 800
Zeiss	Refractive	100x	1.30	<1	400 - 800
Mitutoyo$^{(C)}$	Refractive	100x	0.52	13.0	480 - 1700

$^{(UV)}$*Objective suitable for 266 and 325 nm UV laser.* $^{(355)}$ *Objective suitable for 355 nm laser.* $^{(C)}$ *Objective suitable for cryostat.*

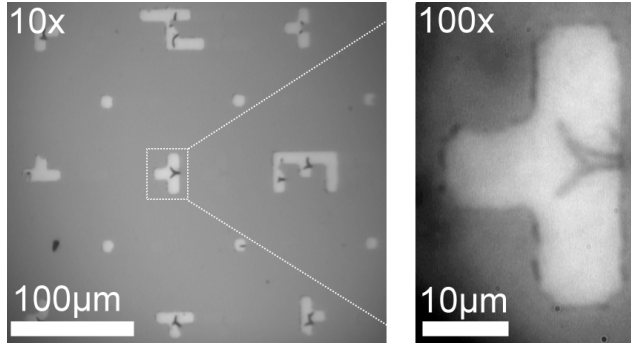| Objective Type	TV Cam [µm/px]	CCD [µm/px]
Zeiss 10x	0.60	2.11
Zeiss 15x	0.53	1.82
Newport 15x	0.48	1.48
Newport 36x	0.19	0.78
Lomo 40x	0.15	0.63
Zeiss 100x	0.09	0.35

Figure A.6: *Optical images of the marker substrates obtained with the 10x and 100x microscope objective and the TV camera.*

Table A.6: *Scale factors of the µPL system determined for the TV camera and the CCD detector.*

1 pixel ($\sim$ 600 nm using the 40x objective), which is more accurate as movement of the stage ($\sim$ 1 - 2 µm). On-line power monitoring is available by measurement of the transmitted laser beam behind the beam splitter with the power meter. The program "BeamPower" written by Steffen Milz allows the determination of the laser spot size from TV camera images and the evaluation of the calibration factor for the reflected laser beam. This allows the on-line evaluation of the actual laser power in the focus spot during the measurements. Optical shielding are installed at both the micro and macro PL setup in order to suppress stray light and allow low light level measurements of single nanowires.

A.3.6 Optical resolution of the µPL

The optical resolution of the self-build microscope was determined for several objectives. Images of the marker substrate with known marker sizes were recorded with bright-field illumination. The distance per pixel was evaluated using the markers as reference. All refractive microscope objectives up to 40x magnification deliver a nearly diffraction limited optical performance, the imaging of the reflective objectives is slightly more unsharp in direct comparison. Images taken with the 100x objective are limited by diffraction effects, as e.g. the edges of the markers blur on the images (see figure A.6). The scale factors (distance/pixel) were evaluated for the TV and the CCD camera (see table A.6). The optical resolution of the system is sufficient to resolve single nanowires. Please note: the evaluated factors may change by the use of different lenses and lens positions in front of the detectors.

A.3.7 Laser spot size

The focus of the laser beams was tested by direct imaging of the laser spot on the TV camera at high attenuation. The spot size typically depends on the coupling of the laser beam and the wavelength. The refractive objectives deliver a good performance and allow sharp focal spots with nearly Gaussian intensity distributions (inset of figure A.7 (a)). The minimum diameter was determined to $\sim$ 0.8 (2) µm for the 100x (40x) objective using the 633 nm laser. The reflective objectives are free of chromatic abberation and have a larger working distance and broad spectral range, but their laser focusing ability is limited by the disturbing influence of the holders for the second mirror. This results in a distortion of the spot shape, as it is presented in the inset of figure A.7 (c). The intensity distribution is more inhomogeneous compared to the refractive objectives and the minimum laser spot diameter is 6 (10) µm with 36x (15x) reflective objective. For lasing experiments, the laser spot of the refractive objective can be defocussed by a $f = 300$
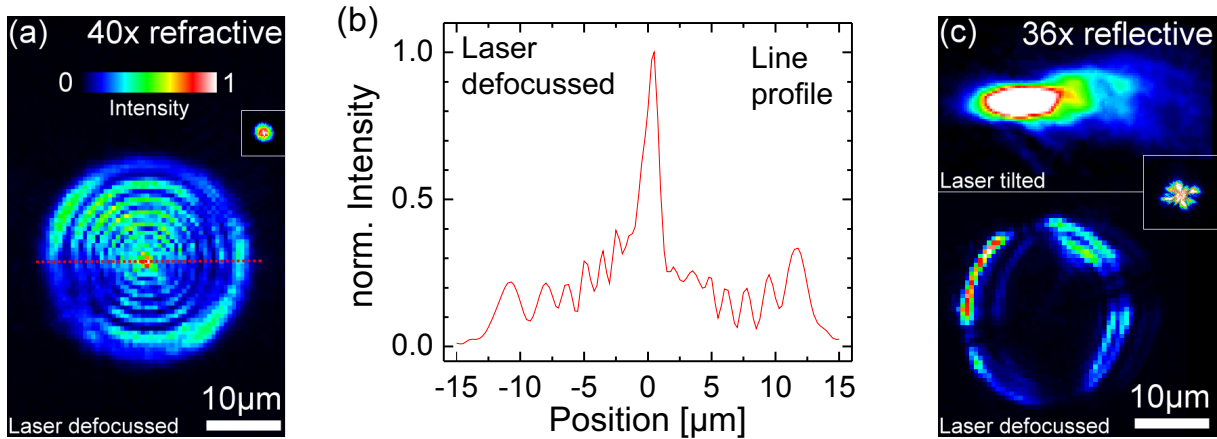
Figure A.7: *(a) Optical image of the defocussed laser spot using the 40x refractive objective. The spot has ∼ 25 µm diameter. The intensity is plotted by the colour scale. The inset shows the focussed laser spot at equal scale for comparison. (b) The line profile of the defocussed spot (marked in (a) as red line) reveals a relatively homogeneous intensity around the main peak. (c) Defocussing the laser beam using the 36x reflective objective results in an inhomogeneous intensity profile. The small inset shows the focussed spot. A slight tilt of the laser beam provides a more homogeneous spot profile (top image).*

mm UV fused silica plano-convex lens in the laser path (see figure A.7 (a)). The defocussed laser spot is variable between 15 - 25 µm in diameter and allows a more homogeneous excitation of a complete nanowire, which increases the damage threshold. The intensity distribution is in first approximation an Airy disk for good focus conditions. A line plot of the intensity distribution is shown in figure A.7 (b). Unfortunately, defocussing is not available for reflective objectives, as the secondary mirror blocks the central ray path (for details see [302]). This results in a strongly inhomogeneous defocussing of the spot (figure A.7 (c)). Alternatively, the laser beam can be slightly tilted off-axis by the beam splitter (upper inset of figure A.7 (c)).

A.3.8 Polarization dependent measurements

The lasers offer a polarized excitation source, which can be used for polarization dependent excitation measurements. The polarization axis of the 355 nm and the 325 nm laser can be rotated using a $\lambda/2$ wave plate (Eksma, low order at 355 nm), as it is used e.g. in the Head-On setup. The polarization ratio for the S- and P-component for the 355 nm Nd:YAG was analyzed after the wave plate using a Glan-Thompson polarizer (10 x 10 mm^2, transmission 350 - 2000 nm),
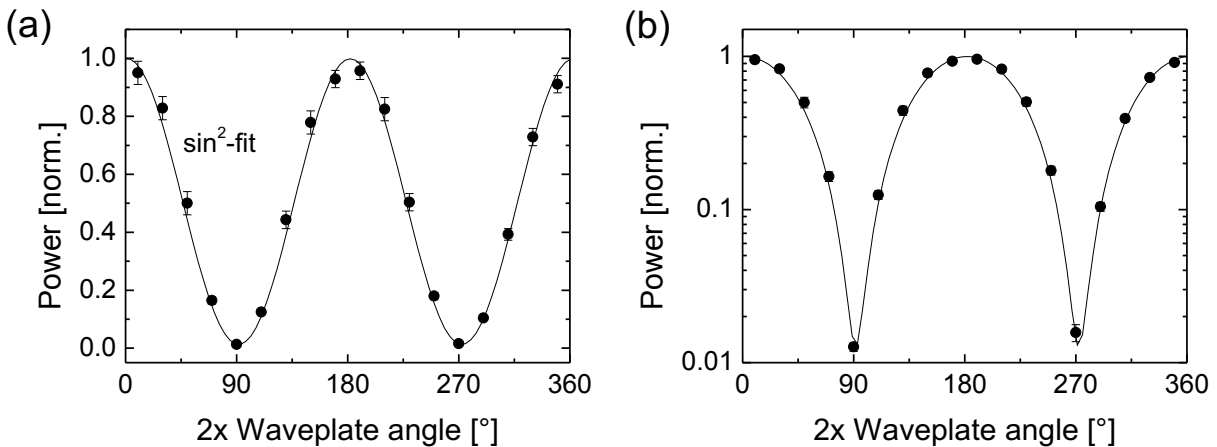

Figure A.8: *(a) The polarization axis of the 355 nm laser was rotated by the $\lambda/2$ wave plate and the transmitted laser power determined behind the Glan-Thompson polarizer. (a) The data follow the expected $\sin^2$-dependency. (b) The maximum polarization ratio is 100:1.*

which offers an extinction ratio of $10^5 : 1$. Wave plate and polarizer were aligned to maximum transmission and the power of the transmitted laser beam was measured by the Si photo diode as a function the rotation angle of the wave plate. The data shown in figure A.8 follow the expected $\sin^2$-dependency. The maximum polarization ratio was determined to $100 : 1$, which is limited by the polarization of the laser and the dynamic range of the photo diode.

Polarization sensitive emission measurements can be performed using the Glan-Thompson polarizer. The extra-ordinary ray is transmitted while the ordinary ray is blocked. In order to exclude corruptions of the PL signal intensity due to the polarization sensitive gratings in the monochromator, a $\lambda/4$ wave plate (Eksma, low order at 515 nm) is inserted into the beam path. The polarized PL signal is converted to circular polarization at an wave plate angle of 45° towards the polarizaiton axis, which eliminates disturbing effects of the detection hardware.

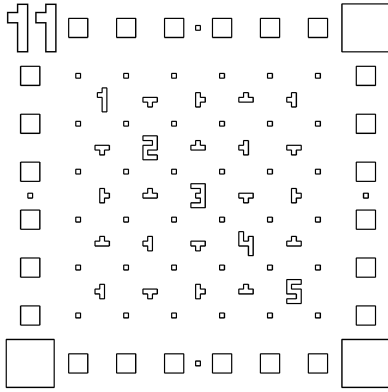## A.4 Marker substrates for µPL investigations

Figure A.9: *Scheme of the coordinate system of the marker substrates produced by photolithography. The upper left corner is marked with two digits marking the field number. The corner squares have 100 µm egde length, the border squares 40 µm and the smallest squares 10 µm edge length.*

The investigation of single nanowires using different methods brings the need for a reliable and reproducible relocation of the nanowire position. An elegant solution is the introduction of a coordinate system using markers on the sample substrates, which were introduced within the scope of this thesis. UV photolithography in the cleanroom of the IFK was used to copy the marker structures from the lithography mask to the photoresist covered substrates. Details for the lithography process are given in [271, 568]. After the lithography steps and developing of the structures, metals (Ti and/or Au) were electron beam evaporated onto the substrates forming the markers. The photoresist was finally removed in a lift-off process leaving the metal markers and a clean surface behind. Ti proved to give a sufficient contrast in the optical microscope, while the contrast in the SEM was rather poor. An Au film provides a better contrast in the SEM, but decomposes to droplets if the sample should be annealed after nanowire transfer.

The markers are rectangular structures of 1000 x 1000 µm^2 as schematically shown in figure A.4, an optical image is presented in figure A.6. The upper left corner is marked with a two digit number for the identification of the field. Inside each field, a system of corner and border squares (100 and 40 µm edge length) as well as smaller squares (10 µm edge length) and "T"-shaped structures in combination with numbers (1 - 5) provide an precise coordinate system which was proven to work for a reproducible relocation of single nanowires. In addition, the marker structures can be used for a scale calibration of the optical microscope.

B Information on samples and experiments

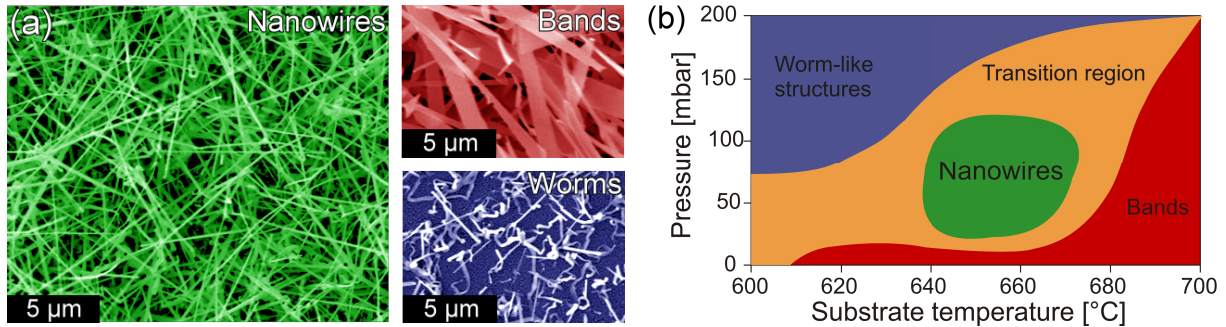## B.1 Synthesis and morphology of CdS nanowires

Figure B.1: *(a) SEM images of typical as-grown CdS nanowires, bands and worm-like structures. (b) Temperature and pressure have been correlated with the morphology of the nanostructures to extract the growth phase diagram. (Image from [270, 303].)*

CdS nanowires were synthesized by a CVD method using a horizontal tube furnace. The used process is similar to the synthesis of ZnO nanowires. Figure B.1 (a) shows SEM images of typical as-grown CdS nanostructures. Temperature and transport gas pressure were systematically varied and the morphology was correlated to the growth conditions, as shown in figure B.1 (b). No growth occurs above 720°C marking the upper limit for CVD grown CdS nanostructures as significant condensation of CdS is probably suppressed by the high temperature [312, 569]. Below 600°C, it is likely that the Au layer does not melt to form the liquid droplets necessary for the VLS catalyst function [570]. In between these limits, several morphology types are present: band-like structures ("nanobands") with a thickness of 100-300 nm, width between 1 - 10 µm and length up to 100 µm grow at high temperature and pressure. These conditions offer a rich CdS vapor supply which not only enables the fast VLS growth along the band axis, but also slower VS growth perpendicular to it at energetically favorable crystal sides [365, 571, 572]. At low growth temperatures, bands only occurred at low gas pressure.

Straight nanowires with diameters between 50-700 nm and lengths up to 50 µm grow at temperatures around 650°C and pressure between 50-100 mbar. The lower temperature and intermediate pressure induces a reduced CdS vapour supply which seems favourable for a suppression of tapering and VS side growth [569]. A remaining catalyst dot is observed on top of many nanowires revealing the VLS growth [257, 312]. Lower temperatures and higher pressures lead to the formation of highly irregular formed structures ("nanoworms"). Growth conditions in between the distinct areas lead to a mixture of the described morphologies, like e.g. tapered nanowires occur at conditions between nanowire and band growth.

B.2 Casperson multimode laser model

The nanowire resonator is not selective for a longitudinal and transversal lasing modes, therefore the cavity has to be assumed as multimode system in which several lasing modes compete for gain. The excitation dependent emission intensity can be described by the model developed by Casperson et al. [361] for multimode laser systems. The overall intensity x_t of the competing laser modes impinging on the resonator mirror, which is directly proportional to the overall
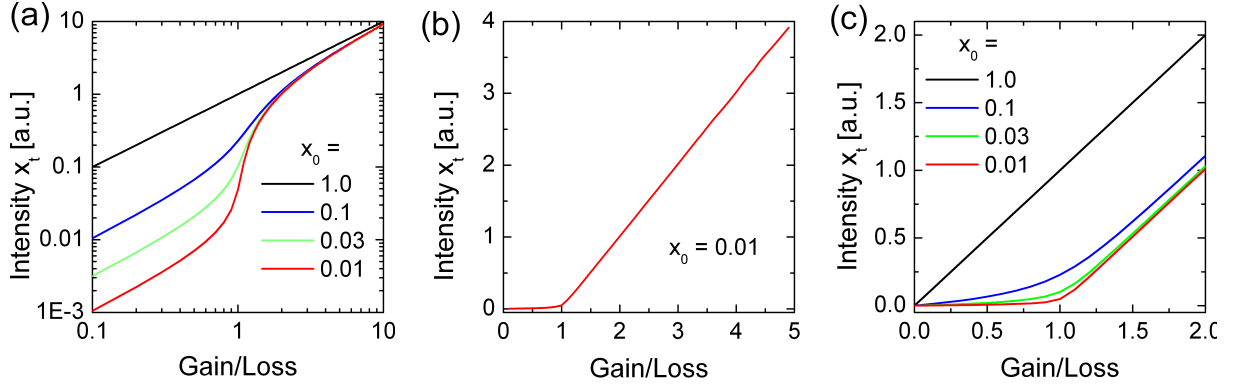
Figure B.2: *(a) Double logarithmic plot of the calculated (homogeneously broadened) intensity of a multimode laser system [361] as a function of the gain/loss ratio for different x_0 values. (b) The model displays at $x_0 = 0.01$ the typical laser emission characteristic with a strong linear intensity increase above the threshold. (c) The steepness of the kink at the lasing threshold (gain/loss = 1) increases for smaller x_0 values.*

emission intensity, is given by

$$x_t = \frac{r(1+x)^{-1}x_0}{[1 - r(1+x)^{-1}]^{1/2}} \tag{B.1}$$

including the parameter r as the ratio of gain to loss per resonator cycle. x_0 determines the fraction of spontaneous emission in the lasing emission. The parameter x is determined for every value of r by an implicit relation (equation B.2), which is valid for the assumption that the mode spacing of the longitudinal modes is small against the width of the gain profile. This condition is fulfilled for nanowire lasers.

$$x = x_0 \left[\left(\frac{1+x}{1+x-r} \right)^{1/2} - 1 \right] \tag{B.2}$$

The overall intensity x_t is plotted as a function of the gain/loss ratio r for different x_0 values. From the double logarithmic plot in figure B.2 (a), it can be seen that $x_0 = 1$ presents the case of pure spontaneous emission. The emission intensity scales purely linear with the gain/loss ratio. Smaller x_0 values correspond to less spontaneous emission in the output laser emission, the slope is therefore stronger s-shaped with a more pronounced kink at a gain/loss ratio $r = 1$. Figure B.2 (b) presents the calculated dependency for $x_0 = 0.01$ in linear scale. The curve follows the typical laser output intensity which is characterized by a strong increase of the emission intensity above the threshold. Figure B.2 (c) displays the dependency around gain/loss = 1 for different x_0 values.

B.3 Simulation of the CdS nanowire waveguide

To gain further insights into the waveguide properties, a CdS nanowire (refractive index $n = 2.76$ at 515 nm [110]) surrounded by air ($n = 1$) was modelled with a spherical cross section of 500 nm diameter in three dimensions by Robert Buschlinger from the group of Prof. Ulf Peschel at the MPI for the physics of light, Erlangen. A Gaussian shaped excitation profile was employed for the simulation. The distribution of the electric field component and its intensity was calculated by solving the Maxwell equations using finite-difference time-domain (FDTD) codes of the software package *Lightwave*. Figure B.3 (a) shows the distribution and intensity of the electric field in a CdS nanowire with a length extended to infinity by periodic boundary conditions. The spherical symmetry of the CdS nanowire is reflected by the equal electric field
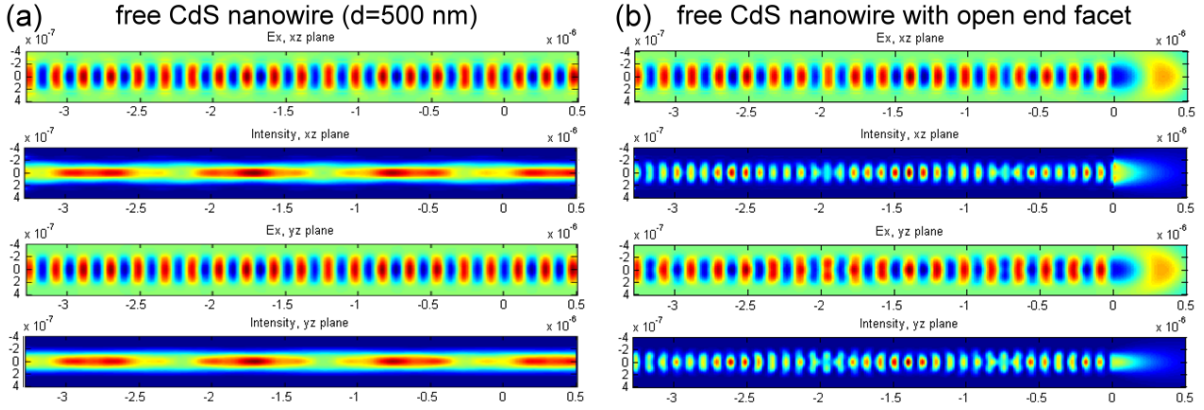
Figure B.3: *(a) Visualization of the FDTD simulation of a CdS nanowire (d = 500 nm) surrounded by air with length extended to infinity showing the distribution of the electric field component and it's intensity in the xz and yz plane. (b) The facet end at z = 0 µm breaks the symmetry, leading to partial reflection of the guided electromagnetic field and interference of the reflected with the incoming field.*

distribution in the xz and yz plane. The electric field is completely confined in the nanowire, pointing out it's excellent properties as optical waveguide. Several modes are excited and guided at a nanowire diameter of 500 nm, which is reflected by the intensity distribution.

In figure B.3 (b), one open facet end at z = 0 µm is included in the simulation, which breaks the symmetry along the x direction. The electric field partially expands as evanescent field up to 500 nm into the surrounding air while it's intensity decreases strongly outside the nanowire. The difference of the refractive index between the CdS nanowire and the surrounding medium leads to a partial reflection of the incoming electric field. The reflected field interferes with the incoming field, as it can be observed from the intensity distribution.

The modelling of the nanowire in three dimensions allows the simulation of all relevant situations influencing the nanowire waveguide properties. The calculation of the polarization the electric field and the reflectivity at the nanowire end e.g. as a function of the diameter can be easily calculated by a post procession step using the results from the FDTD simulation. This will allow the identification of the guided modes in smaller diameter CdS nanolasers. The model is capable to simulate the absorption properties for different polarizations, which will help to gain a deeper understanding of the physics of the excitation of nanowire laser. Further on, the influence of different substrates can be investigated, as it was shown in chapter 4.3.3 for a CdS nanowire on a Si substrate. In addition, a gold cap can be included at the nanowire facet end to study the influence of the remaining Au catalyst dot on the waveguide properties, as this is expected to increase the reflectivity at the nanowire facet end.

B.4 Material parameter used for ion implantation simulation

Table B.1: *Values and parameter of ZnO and ZnS used for SRIM and iradina simulations.*

Property	ZnO	ZnS
Density [g/cm^3]	5.61	4.01
Molar weight [g/mol]	81.39	97.46
# of atomic species	2	2
# atoms in 1 cm^3	$8.30 \cdot 10^{22}$	$4.95 \cdot 10^{22}$
Displacement energy [eV]	18.5 (Zn), 44.1 (O) from [343]	9.7 (Zn), 15.4 (S) from [573]

B.5 Near band edge recombinations in ZnO

Table B.2: *Emissions due to recombinations of free and bound excitons in the near band edge emission of ZnO. The donor bound exciton transitions (D^0X) are labelled by the common I_x assignment. * labels ionized donor bound exciton transitions (D^-X). AX labelled acceptor bound exciton transitions, DAP is used for donor-acceptor-pair transitions. TES names two-electron-satellite transitions. The energy of the longitudinal optical (LO) phonon is 71.9 meV [98].*

Recombination	Energy [eV]	Wavelength [nm]	Binding energy [meV]	Origin	Citation
Band edge	3.4376	360.671			[106]
A_L	3.3772	367.151	Longitudinal	free A-exciton	[99]
A_T	3.3759	367.263	Transversal	free A-exciton	[99]
I_0	3.3725	367.662			[102, 317]
I_1	3.3718	367.709		Ga	[574]
I_1a	3.3679	368.165			[102, 317]
I_2^*	3.3674	368.190			[102, 317]
SX	3.3670	368.263	Surface	exciton	[179, 320]
I_3^*	3.3665	368.288			[102]
I_3a	3.3660	369.030	37	Zn_i	[102]
I_4	3.3628	368.723	46.1	H	[102]
I_5	3.3614	368.877			[316]
I_6	3.3608	368.942	51.6	Al	[316]
I_6a	3.3604	369.030	53	Al	[316, 317]
I_7	3.3600	369.030			[316]
I_8	3.3598	369.052	54.6	Ga	[317, 574]
I_8a	3.3593	369.360			[574]
I_9	3.3567	369.393	63.2	In	[316, 317]
AX	3.3550	369.580			[575]
I_10	3.3531	369.790	72.6		[316]
I_11	3.3484	370.309			[316]
ADX (Y)	3.3330	372.020	Structural	defects	[102]
TES (I_6)	3.3200	373.476			[102, 324]
AX/DAP	3.3150	374.010	Acceptor =	Na or Li	[576, 577]
A,e	3.3100	374.605	Free electron	- acceptor	[577]
TES (I_9)	3.3064	374.982			
FX-1LO	3.3052	375.149			
DX-1LO	3.2880	377.111			
TES (I_6) -1LO	3.2480	381.755			
FX-2LO	3.2332	383.503			
DAP	3.2300	383.883	Acceptor =	N	[316]
DX-2LO	3.2160	385.554			
TES (I_6) -2LO	3.1760	390.410			
FX-3LO	3.1612	392.238			
DAP-1LO	3.1580	392.635			
DX-3LO	3.1440	394.383			

B.6 Near band edge recombinations in CdS and ZnS

Table B.3: *Emissions due to radiative recombinations of free and bound excitons in the near band edge emission of CdS. The donor bound exciton transitions (D^0X) are labelled by I_2. * labels ionized donor/acceptor bound exciton transitions. The acceptor bound excitons (AX) are I_1. The energy of the longitudinal optical (LO) phonon is 37.8 meV [578].*

Recombination	Energy [eV]	Wavelength [nm]	Citation
FX_C	2.6290	471.602	[369]
FX_B	2.5680	482.804	[369]
I_{2B}	2.5626	483.822	[121]
I_{2B}	2.5600	484.313	[369]
Y	2.5521	485.820	[121]
X	2.5513	485.970	[121]
I_{1B}	2.5504	486.136	[121]
FX_A	2.5500	486.212	[369]
I_3	2.5499	486.231	[121]
I_{1B^*}	2.5491	486.376	[121]
I_{1B}	2.5489	486.428	[121]
I_2	2.5471	486.766	[121]
SX / I_3	2.5460	486.976	[579]
I_2	2.5430	487.551	[369]
I_1	2.5360	488.906	[121]
I_1a	2.5330	489.476	[369]
I_1	2.5310	489.862	[369]
I_{2B} - 1 LO	2.5230	491.416	[369]
FX - 1 LO	2.5122	493.528	[369]
DX - 1 LO	2.5052	494.907	[369]
I_1a - 1 LO	2.4952	496.891	[369]
I_1 - 1 LO	2.4932	497.289	[369]
D,h	2.4770	500.542	[369]
FX - 2 LO	2.4744	501.068	[369]
DX - 2 LO	2.4674	502.489	[369]
I_1a - 2 LO	2.4574	504.534	[369]
I_1 - 2 LO	2.4554	504.945	[369]
Y	2.4440	507.300	[369]
I_1 - 3 LO	2.4176	512.840	[369]
DAP_1	2.4140	513.605	[369]
DAP_2	2.3970	517.247	[369]
DAP_1 - 1 LO	2.3762	521.775	[369]
DAP_2 - 1 LO	2.3592	525.535	[369]
DAP_1 - 2 LO	2.3384	530.209	[369]

Table B.4: *Emissions due to recombinations of free and bound excitons in the near band edge emission of ZnS. The energy of the longitudinal optical (LO) phonon is 43 meV [126].*

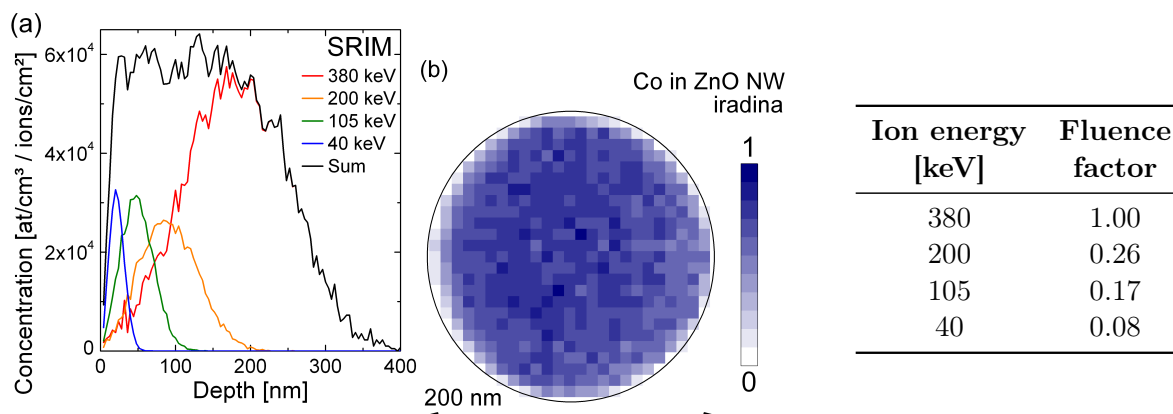| Recombination	Energy [eV]	Wavelength [nm]	Citation
FX_w	3.872	320.207	[106]
DX^*	3.82	324.566	[507]
FX_c	3.82	324.566	[123]
DX (I_2)	3.78	328.001	[122, 507, 508]
AX	3.73	332.397	[122, 507, 508]
A,e	3.66	338.755	[122, 508]

B.7 Details for Co implanted ZnO nanowires

Figure B.4: *Superposition of the Co implantation profiles calculated by SRIM (a) and iradina (b).*
Table B.5: *Ion energies and fluence factors for Co implantation in ZnO nanowires.*

Ion energy [keV]	Fluence factor
380	1.00
200	0.26
105	0.17
40	0.08

Table B.6: *Implantation and annealing parameter of Co implanted ZnO nanowire samples.*

| Sample	Energy [keV]	Implantation T [°C]	tot. Fluence [ions/cm²]	nom. Conc. [at.%]	Annealing
Co005	40-380	RT	$7.75 \cdot 10^{14}$	0.05	750°C 120min Air
Co01	40-380	RT	$1.55 \cdot 10^{15}$	0.10	750°C 120min Air
Co025	40-380	RT	$3.88 \cdot 10^{15}$	0.25	750°C 120min Air
Co05	40-380	RT	$7.75 \cdot 10^{15}$	0.5	750°C 120min Air
Co1	40-380	RT	$1.55 \cdot 10^{16}$	1.0	750°C 120min Air
Co1HT300	40-380	300°C	$1.55 \cdot 10^{16}$	1.0	700°C 30min Air
Co1HT500	40-380	500°C	$1.55 \cdot 10^{16}$	1.0	700°C 30min Air
Co1HT700	40-380	700°C	$1.55 \cdot 10^{16}$	1.0	700°C 30min Air
Co2	40-3800	RT	$3.10 \cdot 10^{16}$	2.0	750°C 120min Air
Co4	40-380	RT	$6.20 \cdot 10^{16}$	4.0	750°C 120min Air
Co8	40-380	RT	$1.24 \cdot 10^{17}$	8.0	750°C 120min Airr

B.8 Details for Mn implanted ZnS nanowires
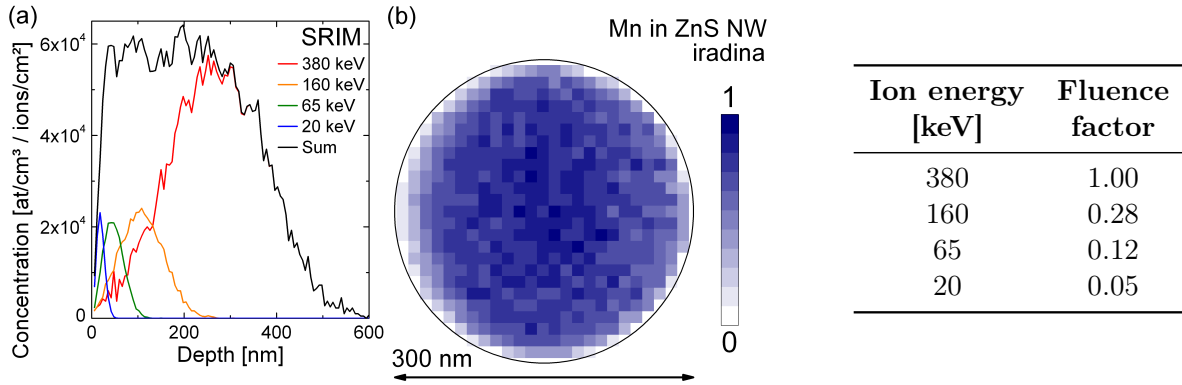
Figure B.5: *Superposition of the Mn implantation profiles calculated by SRIM (a) and iradina (b).*
Table B.7: *Ion energies and fluence factors for Mn implantation in ZnS nanowires.*

Table B.8: *Implantation and annealing parameter of Mn implanted ZnS nanowire samples.*

Sample	Mn conc. [at.%]	Implantation / Annealing	Ne [Ions/cm^2]
Mn2HT400	$1.4 \cdot 10^{-3}$	Hot implantation 400°C	none
Mn2HT500	$1.4 \cdot 10^{-3}$	Hot implantation 500°C	none
Mn2HT600	$1.4 \cdot 10^{-3}$	Hot implantation 600°C	none
Mn2Ta550	$1.4 \cdot 10^{-3}$	Annealing 400°C - 550°C	none
Mn2Ne5	$1.4 \cdot 10^{-3}$	Annealing 600°C	$4.47 \cdot 10^{11}$
Mn2Ne6	$1.4 \cdot 10^{-3}$	Annealing 600°C	$8.47 \cdot 10^{11}$
Mn2Ne7	$1.4 \cdot 10^{-3}$	Annealing 600°C	$4.38 \cdot 10^{12}$
Mn2Ne8	$1.4 \cdot 10^{-3}$	Annealing 600°C	$8.47 \cdot 10^{13}$
Mn2Ne9	$1.4 \cdot 10^{-3}$	Annealing 600°C	$4.38 \cdot 10^{13}$
Mn2aHT600Ne5	$2.0 \cdot 10^{-3}$	Hot implantation 600°C	$4.47 \cdot 10^{11}$
Mn2aHT600Ne7	$2.0 \cdot 10^{-3}$	Hot implantation 600°C	$4.38 \cdot 10^{12}$
Mn2aHT600Ne9	$2.0 \cdot 10^{-3}$	Hot implantation 600°C	$4.38 \cdot 10^{13}$
Mn2aHT600Ne10 (Ne5)	$2.0 \cdot 10^{-3}$	Hot implantation 600°C	$1.45 \cdot 10^{14}$
Mn2aHT600Ne11 (Ne7)	$2.0 \cdot 10^{-3}$	Hot implantation 600°C	$4.38 \cdot 10^{14}$
Mn2aHT600Ne12 (Ne9)	$2.0 \cdot 10^{-3}$	Hot implantation 600°C	$1.45 \cdot 10^{15}$
Mn2aNe9	$2.0 \cdot 10^{-3}$	Annealing 600°C	$4.38 \cdot 10^{14}$
Mn2aHT400	$2.0 \cdot 10^{-3}$	Hot implantation 400°C	none
Mn4aTa300	$1.4 \cdot 10^{-1}$	Annealing 200°C - 500°C	none
Mn4aHT400	$1.4 \cdot 10^{-1}$	Hot implantation 400°C	none
Mn4aHT500	$1.4 \cdot 10^{-1}$	Hot implantation 500°C	none
Mn4aHT600	$1.4 \cdot 10^{-1}$	Hot implantation 600°C	none
Mn4aNe5	$1.4 \cdot 10^{-1}$	Annealing 600°C	$4.47 \cdot 10^{11}$
Mn4aNe7	$1.4 \cdot 10^{-1}$	Annealing 600°C	$4.38 \cdot 10^{12}$
Mn4aNe9	$1.4 \cdot 10^{-1}$	Annealing 600°C	$4.38 \cdot 10^{13}$

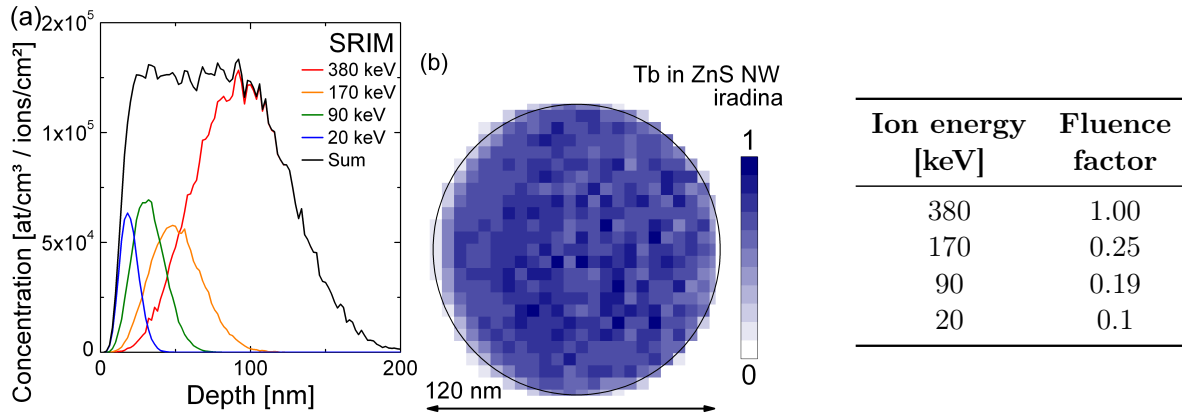## B.9 Details for Tb implanted ZnS nanowires

Figure B.6: *Superposition of the Tb implantation profiles calculated by SRIM (a) and iradina (b).*
Table B.9: *Ion energies and fluence factors for Tb implantation in ZnS nanowires.*

Ion energy [keV]	Fluence factor
380	1.00
170	0.25
90	0.19
20	0.1

Table B.10: *Implantation and annealing parameter of Tb implanted ZnS nanowire samples.*

Sample	Tb Implantation		Annealing	
	Tb [at.%]	Fluence [cm^{-2}]	Temp. [°C]	Time [min]
Tb02AnHV200	0.2	$1.36 \cdot 10^{15}$	200/300	30
Tb02AnHV400	0.2	$1.36 \cdot 10^{15}$	400/500	30
Tb02AnHV600	0.2	$1.36 \cdot 10^{15}$	600/700	30
Tb02Ant10	0.2	$1.36 \cdot 10^{15}$	600	10
Tb02Ant30	0.2	$1.36 \cdot 10^{15}$	600	30
Tb02Ant90	0.2	$1.36 \cdot 10^{15}$	600	90
Tb02Ant270	0.2	$1.36 \cdot 10^{15}$	600	270
Tb2	2.0	$1.38 \cdot 10^{16}$	600	30
Tb02	0.2	$1.36 \cdot 10^{15}$	600	30
Tb002	$2.0 \cdot 10^{-2}$	$1.36 \cdot 10^{14}$	600	30
Tb2E-3	$2.0 \cdot 10^{-3}$	$1.36 \cdot 10^{13}$	600	30
Tb2E-4	$2.0 \cdot 10^{-4}$	$1.35 \cdot 10^{12}$	600	30

B.9.1 Emission energies and excited level of Tb in ZnS nanowires

Table B.11: *Emission energies and assignment of Tb^{3+} intra-4f transitions in ZnS nanowires derived from PL and CL spectra. Assignment derived by comparison with theoretical calculations [530, 531] and literature data [532, 533].*

Emission [eV]	Assingment	Splitting [meV]	Spacing above lower ^7F_J level [meV]
3.266 - 3.215	$^5D_3 \rightarrow {}^7F_6$	51	296
3.006 - 2.919	$^5D_3 \rightarrow {}^7F_5$	87	159
2.85 - 2.76	$^5D_3 \rightarrow {}^7F_4$	90	100
2.717 - 2.66	$^5D_3 \rightarrow {}^7F_3$	57	103
2.644 - 2.557	$^5D_3 \rightarrow {}^7F_2$	87	30
2.55 - 2.527	$^5D_3 \rightarrow {}^7F_1$	24	53
2.474 - 2.50	$^5D_3 \rightarrow {}^7F_0$	27	0
2.549 - 2.498	$^5D_4 \rightarrow {}^7F_6$	51	286
2.301 - 2.212	$^5D_4 \rightarrow {}^7F_5$	89	205
2.131 - 2.007	$^5D_4 \rightarrow {}^7F_4$	124	64
1.998 - 1.943	$^5D_4 \rightarrow {}^7F_3$	55	100
1.911 - 1.843	$^5D_4 \rightarrow {}^7F_2$	68	49
1.830 - 1.794	$^5D_4 \rightarrow {}^7F_1$	30	43
1.776 - 1.751	$^5D_4 \rightarrow {}^7F_0$	15	0

Table B.12: *Assignment of possible excitations of Tb in ZnS nanowires.*

Energy [eV]	Ground term		Excited Level	Citation
4.72	$^7F_6$	$\rightarrow$	$^5F_1$	[530]
4.64	$^7F_6$	$\rightarrow$	$^5F_3$	[530]
4.53	$^7F_6$	$\rightarrow$	$^5F_4, {}^5I_7$	[530]
4.41	$^7F_6$	$\rightarrow$	$^5F_5, {}^5I_8$	[530]
4.33	$^7F_6$	$\rightarrow$	$^5H_3$	[530]
4.11	$^7F_6$	$\rightarrow$	$^5H_5$	[530]
3.94	$^7F_6$	$\rightarrow$	$^5D_0$	[530, 554]
3.87	$^7F_6$	$\rightarrow$	$^5H_7$	[530]
3.78	$^7F_6$	$\rightarrow$	$^5D_1$	[551]
3.70	ZnS		Band edge	[505, 554]
3.65	$^7F_6$	$\rightarrow$	$^5G_2$	[530]
3.26	$^7F_6$	$\rightarrow$	$^5D_3$	[505, 551, 552, 554]
2.91	$^7F_4$	$\rightarrow$	$^5D_3$	PL Data, [530]
2.63	$^7F_2$	$\rightarrow$	$^5D_3$	PL Data, [530]
2.56	$^7F_6$	$\rightarrow$	$^5D_4$	[550, 551]

List of Figures

List of Tables

Bibliography

[1] ITRS. *International technology roadmap for semiconductors - 2011 edition - Executive summary*

[2] D. Stichtenoth, C. Ronning, T. Niermann, L. Wischmeier, T. Voss, C.-J. Chien, P.-C. Chang und J. G. Lu. *Optical size effects in ultrathin ZnO nanowires.* Nanotechnology, **18**(43): (2007) 435701–

[3] C. P. Dietrich, M. Lange, F. J. Klupfel, H. von Wenckstern, R. Schmidt-Grund und M. Grundmann. *Strain distribution in bent ZnO microwires.* Applied Physics Letters, **98**(3): (2011) 031105–3

[4] F. Flory, L. Escoubas und G. Berginc. *Optical properties of nanostructured materials: A review.* Journal of Nanophotonics, **5**(1): (2011) 052502–052502

[5] Y. Wan, J. Sha, B. Chen, Y. Fang, Z. Wang und Y. Wang. *Nanodevices Based on Silicon Nanowires.* Recent Patents on Nanotechnology, **3**(1): (2009) 1–9

[6] G. Guisbiers und S. Pereira. *Theoretical investigation of size and shape effects on the melting temperature of ZnO nanostructures.* Nanotechnology, **18**(43): (2007) 435710–7

[7] S. B. Qadri, E. F. Skelton, D. Hsu, A. D. Dinsmore, J. Yang, H. F. Gray und B. R. Ratna. *Size-induced transition-temperature reduction in nanoparticles of ZnS.* Physical Review B, **60**(13): (1999) 9191–9193

[8] W. Nawrocki. *Electrical and Thermal Properties of Nanowires in Quantum Regimes.* Reviews on Advanced Materials Science, **23**: (2010) 107–112

[9] L. Chen, T. Niebling, W. Heimbrodt, D. Stichtenoth, C. Ronning und P. J. Klar. *Dimensional dependence of the dynamics of the Mn $3d^5$ luminescence in (Zn, Mn)S nanowires and nanobelts.* Physical Review B, **76**(11): (2007) 115325–7

[10] Y. Cui, X. Duan, Y. Huang und C. M. Lieber. *Nanowires and Nanobelts, Vol 1: Metal and Semiconductor Nanowires*, Kap. Nanowires as Building Blocks for Nanoscale Science and Technology. Kluwer Academic Publishers, Norwell, MA (2003)

[11] C. M. Lieber und Z. L. Wang. *Functional nanowires.* MRS Bulletin, **32**(2): (2007) 99–108

[12] Z. Wang. *Nanobelts, Nanowires, and Nanodiskettes of Semiconducting Oxides - From Materials to Nanodevices.* Advanced Materials, **15**(5): (2003) 432–436

[13] Y. Cui, Z. Zhong, D. Wang, W. U. Wang und C. M. Lieber. *High Performance Silicon Nanowire Field Effect Transistors.* Nano Letters, **3**(2): (2003) 149–152

[14] P.-H. Yeh, Z. Li und Z. L. Wang. *Schottky-Gated Probe-Free ZnO Nanowire Biosensor.* Advanced Materials, **21**(48): (2009) 4975–4978

[15] R. Wehrspohn. *Powered by Nanowires.* ChemSusChem, **1**(3): (2008) 173–174

[16] C. H. Peters, A. R. Guichard, A. C. Hryciw, M. L. Brongersma und M. D. McGehee. *Energy transfer in nanowire solar cells with photon-harvesting shells.* Journal of Applied Physics, **105**(12): (2009) 124509–6

[17] A. Hochbaum und P. D. Yang. *Semiconductor Nanowires for Energy Conversion.* Chemical Reviews, **110**(1): (2010) 527–546

[18] Y. Yang, X. W. Sun, B. K. Tay, G. F. You, S. T. Tan und K. L. Teo. *A p-n homojunction ZnO nanorod light-emitting diode formed by As ion implantation.* Applied Physics Letters, **93**(25): (2008) 253107–3

[19] M. A. Zimmler, D. Stichtenoth, C. Ronning, W. Yi, V. Narayanamurti, T. Voss und F. Capasso. *Scalable Fabrication of Nanowire Photonic and Electronic Circuits Using Spin-on Glass.* Nano Letters, **8**(6): (2008) 1695–1699

[20] T. Voss, G. Svacha, E. Mazur, S. Müller, C. Ronning, D. Konjhodzic und F. Marlow. *High-Order Waveguide Modes in ZnO Nanowires.* Nano Letters, **7**(12): (2007) 3675–3680

[21] M. A. Zimmler, F. Capasso, S. Müller und C. Ronning. *Optically pumped nanowire lasers: invited review.* Semiconductor Science and Technology, **25**(2): (2010) 024001–12

[22] Y. Zhang und W. Ge. *Behavior of nitrogen impurities in III-V semiconductors.* Journal of Luminescence, **85**(4): (2000) 247–260

[23] C. Borchers, S. Müller, D. Stichtenoth, D. Schwen und C. Ronning. *Catalyst-Nanostructure Interaction in the Growth of 1-D ZnO Nanostructures.* Journal of Physical Chemics B, **110**(4): (2006) 1656–1660

[24] D. Stichtenoth, D. Schwen, S. Müller, C. Borchers und C. Ronning. *Growth and properties of zincsulfide nanowires.* Functional Properties of Nanostructured Materials, **223**: (2005) 407–410

[25] M. Willander, O. Nur, Q. X. Zhao, L. L. Yang, M. Lorenz, B. Q. Cao, J. Z. PÃ©rez, C. Czekalla, G. Zimmermann, M. Grundmann, A. Bakin, A. Behrends, M. Al-Suleiman, A. El-Shaer, A. C. Mofor, B. Postels, A. Waag, N. Boukos, A. Travlos, H. S. Kwack, J. Guinard und D. L. S. Dang. *Zinc oxide nanorod based photonic devices: recent progress in growth, lightÂ emitting diodes and lasers.* Nanotechnology, **20**(33): (2009) 332001–41

[26] A. Mikkelsen, N. Skold, L. Ouattara, M. Borgstrom, J. N. Andersen, L. Samuelson, W. Seifert und E. Lundgren. *Direct imaging of the atomic structure inside a nanowire by scanning tunnelling microscopy.* Nature Materials, **3**(8): (2004) 519–523

[27] C. Gutsche, I. Regolin, K. Blekker, A. Lysov, W. Prost und F. J. Tegude. *Controllable p-type doping of GaAs nanowires during vapor-liquid-solid growth.* Journal of Applied Physics, **105**(2): (2009) 024305–5

[28] S.-G. Ihn, J.-I. Song, Y.-H. Kim, J. Y. Lee und I.-H. Ahn. *Growth of GaAs Nanowires on Si Substrates Using a Molecular Beam Epitaxy.* Nanotechnology, IEEE Transactions on, **6**(3): (2007) 384–389

[29] Y. Qin, X. Wang und Z. L. Wang. *Microfibre-nanowire hybrid structure for energy scavenging.* Nature, **451**(7180): (2008) 809–813

[30] Z. L. Wang. *Nanowires and Nanobelts - Material, Properties and Devices: Vol. I: Metal and Semiconductor Nanowires.* Kluver Academic Publishers (2004)

[31] B. Mandl, J. Stangl, T. Martensson, A. Mikkelsen, J. Eriksson, L. S. Karlsson, G. Bauer, L. Samuelson und W. Seifert. *Au-Free Epitaxial Growth of InAs Nanowires.* Nano Letters, **6**(8): (2006) 1817–1821

[32] A. Lugstein, M. Steinmair, C. Henkel und E. Bertagnolli. *Scalable Approach for Vertical Device Integration of Epitaxial Nanowires.* Nano Letters, **9**(5): (2009) 1830–1834

[33] P. J. Pauzauskie und P. Yang. *Nanowire photonics.* Materials Today, **9**(10): (2006) 36–45

[34] R. Agarwal und C. M. Lieber. *Semiconductor nanowires: optics and optoelectronics.* Applied Physics A, **83**(3): (2006) 209–215

[35] J. Johnson, H. Yan, R. Schaller, P. Petersen, P. Yang und R. Saykally. *Near-Field Imaging of Nonlinear Optical Mixing in Single Zinc Oxide Nanowires.* Nano Letters, **2**(4): (2002) 279–283

[36] T. Voss, I. Kudyk, L. Wischmeier und J. Gutowski. *Nonlinear optics with ZnO nanowires.* Physica Status Solidi (b), **246**(2): (2009) 311–314

[37] T. Voss, J.-P. Richters und A. Dev. *Surface effects and nonlinear optical properties of ZnO nanowires.* Physica Status Solidi (b), **247**(10): (2010) 2476–2487

[38] Q. Zhang, X.-Y. Shan, X. Feng, C.-X. Wang, Q.-Q. Wang, J.-F. Jia und Q.-K. Xue. *Modulating Resonance Modes and Q Value of a CdS Nanowire Cavity by Single Ag Nanoparticles.* Nano Letters, **11**(10): (2011) 4270–4274

[39] Y. Huang, X. Duan und C. Lieber. *Nanowires for Integrated Multicolor Nanophotonics.* Small, **1**(1): (2005) 142–147

[40] M. Willander, Q. X. Zhao und O. Nur. *Zinc oxide nanostructures at the forefront of new white light-emitting technology.* SPIE

[41] J.-P. Richters, A. Dev, S. Müller, R. Niepelt, C. Borschel, C. Ronning und T. Voss. *Influence of metallic coatings on the photoluminescence properties of ZnO nanowires.* Physica Status Solidi (RRL) - Rapid Research Letters, **3**(5): (2009) 166–168

[42] J.-P. Richters, T. Voss, L. Wischmeier, I. Ruckmann und J. Gutowski. *Influence of polymer coating on the low-temperature photoluminescence properties of ZnO nanowires.* Applied Physics Letters, **92**(1): (2008) 011103–3

[43] X. J. Chen, G. Perillat-Merceroz, D. Sam-Giao, C. Durand und J. Eymery. *Homoepitaxial growth of catalyst-free GaN wires on N-polar substrates.* Applied Physics Letters, **97**(15): (2010) 151909–3

[44] J. Bao, M. Zimmler, F. Capasso, X. Wang und Z. Ren. *Broadband ZnO Single-Nanowire Light-Emitting Diode.* Nano Letters, **6**(8): (2006) 1719–1722

[45] M. Law, D. J. Sirbuly, J. C. Johnson, J. Goldberger, R. J. Saykally und P. Yang. *Nanoribbon Waveguides for Subwavelength Photonics Integration.* Science, **305**(5688): (2004) 1269–1273

[46] J. Johnson, H. Yan, P. Yang und R. Saykally. *Optical Cavity Effects in ZnO Nanowire Lasers and Waveguides.* Journal of Physical Chemics B, **107**(34): (2003) 8816–8828

[47] L. K. van Vugt, B. Piccione und R. Agarwal. *Incorporating polaritonic effects in semiconductor nanowire waveguide dispersion.* Applied Physics Letters, **97**(6): (2010) 061115–3

[48] C. Sturm, H. Hilmer, R. Schmidt-Grund und M. Grundmann. *Observation of strong exciton-photon coupling at temperatures up to 410 K.* New Journal of Physics, **11**(7): (2009) 073044–13

[49] R. F. Oulton, V. J. Sorger, T. Zentgraf, R.-M. Ma, C. Gladden, L. Dai, G. Bartal und X. Zhang. *Plasmon lasers at deep subwavelength scale.* Nature, **461**(7264): (2009) 629–632

[50] Y.-J. Lu, J. Kim, H.-Y. Chen, C. Wu, N. Dabidian, C. E. Sanders, C.-Y. Wang, M.-Y. Lu, B.-H. Li, X. Qiu, W.-H. Chang, L.-J. Chen, G. Shvets, C.-K. Shih und S. Gwo. *Plasmonic Nanolaser Using Epitaxially Grown Silver Film.* Science, **337**(6093): (2012) 450–453

[51] M. A. Zimmler, J. Bao, F. Capasso, S. Müller und C. Ronning. *Laser action in nanowires: Observation of the transition from amplified spontaneous emission to laser oscillation.* Applied Physics Letters, **93**(5): (2008) 051101–3

[52] T. Nobis und M. Grundmann. *Low-order optical whispering-gallery modes in hexagonal nanocavities.* Physical Review A, **72**(6): (2005) 063806–11

[53] C. Czekalla, T. Nobis, A. Rahm, B. Cao, J. Zaiga-Parez, C. Sturm, R. Schmidt-Grund, M. Lorenz und M. Grundmann. *Whispering gallery modes in zinc oxide micro- and nanowires.* Physica Status Solidi (b), **247**(6): (2010) 1282–1293

[54] C. F. Klingshirn. *Semiconductor Optics.* Springer, 2nd edition Aufl. (2005)

[55] A. Maslov und C. Ning. *Modal gain in a semiconductor nanowire laser with anisotropic bandstructure.* IEEE Journal of Quantum Electronics, **40**(10): (2004) 1389–1397

[56] J. P. Richters, J. Kalden, M. Gnauck, C. Ronning, C. P. Dietrich, H. von Wenckstern, M. Grundmann, J. Gutowski und T. Voss. *Modal gain and its diameter dependence in single-ZnO micro- and nanowires.* Semiconductor Science and Technology, **27**(1): (2012) 015005–6

[57] Y. K. Liu, J. A. Zapien, C. Y. Geng, Y. Y. Shan, C. S. Lee, Y. Lifshitz und S. T. Lee. *High-quality CdS nanoribbons with lasing cavity.* Applied Physics Letters, **85**(15): (2004) 3241–3243

[58] A. Pan, R. Liu, Q. Yang, Y. Zhu, G. Yang, B. Zou und K. Chen. *Stimulated Emissions in Aligned CdS Nanowires at Room Temperature.* The Journal of Physical Chemistry B, **109**(51): (2005) 24268–24272

[59] B. Cao, Y. Jiang, C. Wang, W. Wang, L. Wang, M. Niu, W. Zhang, Y. Li und S. Lee. *Synthesis and Lasing Properties of Highly Ordered CdS Nanowire Arrays.* Advanced Functional Materials, **17**(9): (2007) 1501–1506

[60] C. Z. Ning. *Semiconductor nanolasers.* Physica Status Solidi (b), **247**(4): (2010) 774–788

[61] S. Müller, M. Zhou, Q. Li und C. Ronning. *Intra-shell luminescence of transition-metal-implanted zinc oxide nanowires.* Nanotechnology, **20**(13): (2009) 135704–8

[62] S. Geburt, D. Stichtenoth, S. Müller, W. Dewald, C. Ronning, J. Wang, Y. Jiao, Y. Rao, S. Hark und Q. Li. *Rare Earth doped Zinc Oxide Nanowires.* Journal of Nanoscience and Nanotechnology, **8**: (2008) 244–251

[63] A. Colli, A. Fasoli, C. Ronning, S. Pisana, S. Piscanec und A. C. Ferrari. *Ion Beam Doping of Silicon Nanowires.* Nano Letters, **8**(8): (2008) 2188–2193

[64] D. Stichtenoth, K. Wegener, C. Gutsche, I. Regolin, F. J. Tegude, W. Prost, M. Seibt und C. Ronning. *P-type doping of GaAs nanowires.* Applied Physics Letters, **92**(16): (2008) 163107–3

[65] P. Das Kanungo, R. Koegler, N. Zakharov, P. Werner, R. Scholz und W. Skorupa. *Characterization of Structural Changes Associated with Doping Silicon Nanowires by Ion Implantation.* Crystal Growth & Design, **11**(7): (2011) 2690–2694

[66] S. Milz. *Konzepte zur Realisierung von einfachen Nanodrahtbauelementen für die Energiegewinnung.* Diplomarbeit, Friedrich-Schiller-Universität Jena (2010)

[67] P. M. Wu, W. Paschoal, S. Kumar, C. Borschel, C. Ronning, C. M. Canali, L. Samuelson, H. Pettersson und H. Linke. *Thermoelectric Characterization of Electronic Properties of GaMnAs Nanowires.* Journal of Nanotechnology, **2012**: (2012) 480813–5

[68] C. Borschel, M. E. Messing, M. T. Borgström, W. Paschoal, J. Wallentin, S. Kumar, K. Mergenthaler, K. Deppert, C. M. Canali, H. Pettersson, L. Samuelson und C. Ronning. *A new route toward semiconductor nanospintronics: highly Mn-doped GaAs nanowires realized by iIon-implantation under dynamic annealing conditions.* Nano Letters, **11**(9): (2011) 3935–3940

[69] Z. H. Zhang, H. Wang, X. Wang, J. B. Xu, S. Müller, C. Ronning und L. Quan. *Evidence of intrinsic ferromagnetism in individual dilute magnetic semiconducting nanostructures.* Nature Nanotechnology, **4**(8): (2009) 523–527

[70] W. Liang, B. D. Yuhas und P. Yang. *Magnetotransport in Co-Doped ZnO Nanowires.* Nano Letters, **9**(2): (2009) 892–896. PMID: 19170557

[71] D. J. Newman und B. Ng. *Crystal Field Handbook*. Cambridge University Press (2000)

[72] B. Cheng, Y. Xiao, G. Wu und L. Zhang. *Controlled Growth and Properties of One-Dimensional ZnO Nanostructures with Ce as Activator/Dopant*. Advanced Functional Materials, **14**(9): (2004) 913–919

[73] S.-J. Whang, S. Lee, D.-Z. Chi, W.-F. Yang, B.-J. Cho, Y.-F. Liew und D.-L. Kwong. *B-doping of vapour-liquid-solid grown Au-catalysed and Al-catalysed Si nanowires: effects of B 2 H 6 gas during Si nanowire growth and B-doping by a post-synthesis in situ plasma process*. Nanotechnology, **18**(27): (2007) 275302–5

[74] D. Lide (Hg.). *CRC Handbook of Chemistry and Physics*. CRC Press, Boca Raton, Florida, USA (1996)

[75] T. Hirate, S. Sasaki, W. Li, H. Miyashita, T. Kimpara und T. Satoh. *Effects of laser-ablated impurity on aligned ZnO nanorods grown by chemical vapor deposition*. Thin Solid Films, **487**(1-2): (2005) 35–39

[76] C. Xu, J. Chun, B. Chon, T. Joo und D. E. Kim. *In situ fabrication and blueshifted red emission of GaN:Eu nanoneedles*. Nanotechnology, **18**(1): (2007) 015703–6

[77] Z. Hou, Z. Cheng, G. Li, W. Wang, C. Peng, C. Li, P. Ma, D. Yang, X. Kang und J. Lin. *Electrospinning-derived $Tb_2(WO_4)_3$:Eu^{3+} nanowires: energy transfer and tunable luminescence properties*. Nanoscale, **3**(4): (2011) 1568–1574

[78] A. Ishizumi und Y. Kanemitsu. *Structural and luminescence properties of Eu-doped ZnO nanorods fabricated by a microemulsion method*. Applied Physics Letters, **86**(25): (2005) 253106–3

[79] A. Ishizumi, Y. Taguchi, A. Yamamoto und Y. Kanemitsu. *Luminescence properties of ZnO and Eu^{3+}-doped ZnO nanorods*. Thin Solid Films, **486**(1-2): (2005) 50–52

[80] A. Ishizumi, Y. Takahashi, A. Yamamoto und Y. Kanemitsu. *Fabrication and optical properties of Eu^{3+}-doped ZnO nanospheres and nanorods*. Materials Science and Engineering: B, **146**(1-3): (2008) 212–215

[81] S.-M. Liu, F.-Q. Liu und Z.-G. Wang. *Relaxation of carriers in terbium-doped ZnO nanoparticles*. Chemical Physics Letters, **343**(5-6): (2001) 489–492

[82] S.-M. Liu, F.-Q. Liu, H.-Q. Guo, Z.-H. Zhang und Z.-G. Wang. *Correlated structural and optical investigation of terbium-doped zinc oxide nanocrystals*. Physics Letters A, **271**(1-2): (2000) 128–133

[83] J. Sadowski, P. Dulewski, S. Kret, E. Janik, E. Lusakowska, J. Kanski, A. Presz, F. Terki, S. Charar und D. Tang. *GaAs:Mn Nanowires Grown by Molecular Beam Epitaxy of (Ga,Mn)As at MnAs Segregation Conditions*. Nano Letters, **7**(9): (2007) 2724–2728

[84] P. Xie, Y. Hu, Y. Fang, J. Huang und C. M. Lieber. *Diameter-dependent dopant location in silicon and germanium nanowires*. Proceedings of the National Academy of Sciences, **106**(36): (2009) 15254–15258

[85] J. Ziegler. *Ion Implantation Technology*. North-Holland Publishing, Amsterdam (1992)

[86] J. F. Ziegler, J. P. Biersack und U. Littmark. *The Stopping and Range of Ions in Solids*. Pergamon Press (1985)

[87] J. Wang, S. Hark und Q. Li. *Electronic Structure and Luminescence Properties of Er Doped ZnO Nanowires*. Microscopy and Microanalysis, **12**: (2006) 748–749

[88] U. Kaiser. *Dipol-Dipol-Transfer in Mangan-dotierten Zinksulfid-Nanodrähten*. Diplomarbeit, Philipps-Universität Marburg (2010)

[89] D. Kim, K. Kim, Y. Shin, D. Kang, B. Kim, Y. Kim, Y. Park und T. Kim. *Defect engineering for 650nm high-power AlGaInP laser diodes*. Physica B: Condensed Matter, **376–377**(0): (2006) 610–613

[90] M. Gutierrez, M. Hopkinson, H. Liu, M. Herrera, D. Gonzalez und R. Garcia. *Characterization of structure and defects in dot-in-well laser structures*. Materials Science and Engineering: C, **25**(5–8): (2005) 793–797

[91] R. Boyn. *4f-4f Luminescence of Rare-Earth Centers in II-VI Compounds*. Physica Status Solidi (b), **148**(1): (1988) 11–47

[92] J. Hader, J. V. Moloney und S. W. Koch. *Density-activated defect recombination as a possible explanation for the efficiency droop in GaN-based diodes*. Applied Physics Letters, **96**(22): (2010) 221106–3

[93] J. Hader, J. V. Moloney und S. W. Koch. *Density-activated defect recombination as a possible explanation for the efficiency droop in GaN-based diodes*. Seite 79540

[94] C. Gutsche, R. Niepelt, M. Gnauck, A. Lysov, W. Prost, C. Ronning und F.-J. Tegude. *Direct Determination of Minority Carrier Diffusion Lengths at Axial GaAs Nanowire p-n Junctions*. Nano Letters, **12**(3): (2012) 1453–1458

[95] E. Schlenker, A. Bakin, T. Weimann, P. Hinze, D. H. Weber, A. Gölzhäuser, H.-H. Wehmann und A. Waag. *On the difficulties in characterizing ZnO nanowires*. Nanotechnology, **19**(36): (2008) 365707–8

[96] Y. R. Do, D.-H. Park, Y.-C. Kim und Y.-D. Huh. *Improved Cathodoluminescence Output Coupling of ZnS:Tb Thin-Film Phosphors Deposited on 2D SiO[sub 2] Corrugated Glass Substrate*. Journal of Electrochemical Society, **150**(11): (2003) H260–H265

[97] U. Ozgur, Y. I. Alivov, C. Liu, A. Teke, M. A. Reshchikov, S. Dogan, V. Avrutin, S.-J. Cho und H. Morkoc. *A comprehensive review of ZnO materials and devices*. Journal of Applied Physics, **98**(4): (2005) 041301–103

[98] U. Rössler (Hg.). *Landolt-Börnstein -Group III: Vol. 17B, 22, 41B: Crystal and Condensed Matter Physics*, Kap. Semiconductors, Seiten 85–124. Springer, Berlin (1999)

[99] U. Rössler. *Landolt-Börnstein -Group III/22a: Crystal and Condensed Matter Physics*, Kap. Intrinsic properties, Seiten 160–166. Springer, Berlin (1990)

[100] Z. Wang. *Nanopiezotronics*. Advanced Materials, **19**(6): (2007) 889–892

[101] I. Ivanov und J. Pollmann. *Electronic structure of ideal and relaxed surfaces of ZnO: A prototype ionic wurtzite semiconductor and its surface properties*. Physical Review B, **24**(12): (1981) 7275–7296

[102] B. K. Meyer, H. Alves, D. M. Hofmann, W. Kriegseis, D. Forster, F. Bertram, J. Christen, A. Hoffmann, M. Straßburg, M. Dworzak, U. Haboeck und A. V. Rodina. *Bound exciton and donor-acceptor pair recombinations in ZnO*. Physica Status Solidi (b), **241**(2): (2004) 231–260

[103] Y. S. Park und J. R. Schneider. *Index of Refraction of ZnO*. Journal of Applied Physics, **39**(7): (1968) 3049–3052

[104] O. Mandelung (Hg.). *Landolt-Börnstein*. Springer, Berlin (1984)

[105] J. C. Miklosz und R. G. Wheeler. *Exciton Structure and Magneto-Optical Effects in ZnS*. Physical Review, **153**(3): (1967) 913–923

[106] O. Mandelung (Hg.). *Landolt-Börnstein - Group III/22a - Semiconductors: Intrinsic properties of group IV elements and II-V and II-VI compounds*, Kap. Semiconductors: Intrinsic properties of group IV elements and II-V and II-VI compounds. Springer Berlin (1987)

[107] U. Hotje, C. Rose und M. Binnewies. *Lattice constants and molar volume in the system ZnS, ZnSe, CdS, CdSe*. Solid State Sciences, **5**(9): (2003) 1259–1262

[108] D. Theis. *Wavelength-modulated reflectivity spectra of ZnSe and ZnS from 2.5 to 8 eV*. Physica Status Solidi (b), **79**(1): (1977) 125–130

[109] M. Cardona und G. Harbeke. *Optical Properties and Band Structure of Wurtzite-Type Crystals and Rutile*. Physical Review, **137**(5A): (1965) A1467–A1476

[110] M. Bass (Hg.). *Handbook of Optics*. McGraw-Hill, New York (2010)

[111] L. V. Titova, T. B. Hoang, H. E. Jackson, L. M. Smith, J. M. Yarrison-Rice, J. L. Lensch und L. J. Lauhon. *Low-temperature photoluminescence imaging and time-resolved spectroscopy of single CdS nanowires*. Applied Physics Letters, **89**(5): (2006) 053119–3

[112] G. H. Wannier. *The Structure of Electronic Excitation Levels in Insulating Crystals*. Physical Review, **52**(3): (1937) 191–197

[113] Mollwo. *Landolt-Börnstein - Group III/17b - Semiconductors: Intrinsic properties of group IV elements and II-V and II-VI compounds*, Kap. Zinc oxide, Seiten 35–60. Springer, Berlin (1982)

[114] Nelkowski und Schulz. *Landolt-Börnstein - Group III/17b - Semiconductors: Intrinsic properties of group IV elements and II-V and II-VI compounds*, Kap. Zinc sulfide, Seiten 61–126. Springer, Berlin (1982)

[115] D. G. Thomas und J. J. Hopfield. *Exciton Spectrum of Cadmium Sulfide*. Physical Review, **116**(3): (1959) 573–582

[116] T. Koida, S. F. Chichibu, A. Uedono, A. Tsukazaki, M. Kawasaki, T. Sota, Y. Segawa und H. Koinuma. *Correlation between the photoluminescence lifetime and defect density in bulk and epitaxial ZnO*. Applied Physics Letters, **82**(4): (2003) 532–534

[117] D. Reynolds, D. Look, B. Jogai, J. Hoelscher, R. Sherriff, M. Harris und M. Callahan. *Time-resolved photoluminescence lifetime measurements of the Γ_5 and Γ_6 free excitons in ZnO*. Journal of Applied Physics, **88**: (2000) 2152–2153

[118] R. Heitz, A. Hoffmann und I. Broser. *Exciton dynamics in Ni-activated CdS*. Physical Review B, **49**(20): (1994) 14307–14314

[119] J. J. Hopfield. *Theory of the Contribution of Excitons to the Complex Dielectric Constant of Crystals*. Physical Review, **112**(5): (1958) 1555–1567

[120] C. Klingshirn, M. Grundmann, A. Hoffmann, B. Meyer und A. Waag. *Zinkoxid - ein neuer, alter Halbleiter*. Physik Journal, **1**: (2006) 33–39

[121] D. G. Thomas und J. J. Hopfield. *Optical Properties of Bound Exciton Complexes in Cadmium Sulfide.* Physical Review, **128**(5): (1962) 2135–2148

[122] N. Morozova, I. Karetnikov, V. Plotnichenko, E. Gavrishchuk, . Yashina und V. Ikonnikov. *Transformation of luminescence centers in CVD ZnS films subjected to a high hydrostatic pressure.* Semiconductors, **38**(1): (2004) 36–41

[123] S. Nakamura, S. Pearton und G. Fasol. *The Blue Laser Diode.* Springer (1997)

[124] D. R. Vij (Hg.). *Luminescence in Solids.* Plenum Publishing Coporation (1998)

[125] T. C. Damen, S. P. S. Porto und B. Tell. *Raman Effect in Zinc Oxide.* Physical Review, **142**(2): (1966) 570–574

[126] W. Klein. *Exzitonenemission von hexagonalem ZnS bei Anregung mit 50-keV-Elektronen.* Journal of Physics and Chemistry of Solids, **26**(9): (1965) 1517–1521

[127] R. C. C. Leite, J. F. Scott und T. C. Damen. *Multiple-Phonon Resonant Raman Scattering in CdS.* Physical Review Letters, **22**(15): (1969) 780–782

[128] C. Klingshirn. *ZnO: Material, Physics and Applications.* ChemPhysChem, **8**(6): (2007) 782–803

[129] C. Kittel. *Introduction to Solid State Physics.* Wiley & Sons (1995)

[130] Y. Jiang, X.-M. Meng, J. Liu, Z.-R. Hong, C.-S. Lee und S.-T. Lee. *ZnS nanowires with wurtzite polytype modulated structure.* Advanced Materials, **15**(14): (2003) 1195–1198

[131] D. Denzler, M. Olschewski und K. Sattler. *Luminescence studies of localized gap states in colloidal ZnS nanocrystals.* Journal of Applied Physics, **84**(5): (1998) 2841–2845

[132] M. Reshchikov, H. Morkoc, B. Nemeth, J. Nause, J. Xie, B. Hertog und A. Osinsky. *Luminescence properties of defects in ZnO.* Physica B: Condensed Matter, **401-402**: (2007) 358–361

[133] A. B. Djurisic, Y. H. Leung, K. H. Tam, Y. F. Hsu, L. Ding, W. K. Ge, Y. C. Zhong, K. S. Wong, W. K. Chan, H. L. Tam, K. W. Cheah, W. M. Kwok und D. L. Phillips. *Defect emissions in ZnO nanostructures.* Nanotechnology, **18**(9): (2007) 095702–8

[134] A. Janotti und C. G. Van de Walle. *Native point defects in ZnO.* Physical Review B, **76**(16): (2007) 165202–22

[135] F. A. Kröger. *Imperfection chemistry of crystalline solids.* North-Holland Publishing Company (1974)

[136] A. Janotti und C. G. Van de Walle. *New insights into the role of native point defects in ZnO.* Journal of Crystal Growth, **287**(1): (2006) 58–65

[137] W. G. Becker und A. J. Bard. *Photoluminescence and photoinduced oxygen adsorption of colloidal zinc sulfide dispersions.* Journal of Chemical Physics, **87**(24): (1983) 4888–4893

[138] R. Dingle. *Luminescent Transitions Associated With Divalent Copper Impurities and the Green Emission from Semiconducting Zinc Oxide.* Physical Review Letters, **23**(11): (1969) 579–581

[139] N. Y. Garces, L. Wang, L. Bai, N. C. Giles, L. E. Halliburton und G. Cantwell. *Role of copper in the green luminescence from ZnO crystals.* Applied Physics Letters, **81**(4): (2002) 622–624

[140] Y. Wang, L. Zhang, C. Liang, G. Wang und X. Peng. *Catalytic growth and photoluminescence properties of semiconductor single-crystal ZnS nanowires.* Chemical Physics Letters, **357**: (2002) 314–318

[141] J. Hu, G. Wang, C. Guo, D. Li, L. Zhang und J. Zhao. *Au-catalyst growth and photoluminescence of zinc-blende and wurtzite ZnS nanobelts via chemical vapor deposition.* Journal of Luminescence, **122–123**: (2007) 172–175

[142] K. Huang und A. Rhys. *Theory of Light Absorption and Non-Radiative Transitions in F-Centres.* Proceedings of the Royal Society of London. Series A. Mathematical and Physical Sciences, **204**(1078): (1950) 406–423

[143] J. I. Pankove. *Optical Processes in Semiconductors.* Prentice-Hall Englewood Cliffs (1971)

[144] A. M. Stoneham. *Non-radiative transitions in semiconductors.* Reports on Progress in Physics, **44**(12): (1981) 1251–1295

[145] C. B. À la Guillaume, J.-M. Debever und F. Salvan. *Radiative Recombination in Highly Excited CdS.* Physical Review, **177**(2): (1969) 567–580

[146] C. Klingshirn. *The Luminescence of ZnO under High One- and Two-Quantum Excitation.* Physica Status Solidi (b), **71**(2): (1975) 547–556

[147] H. Priller, J. Brückner, T. Gruber, C. Klingshirn, H. Kalt, A. Waag, H. J. Ko und T. Yao. *Comparison of linear and nonlinear optical spectra of various ZnO epitaxial layers and of bulk material obtained by different experimental techniques.* Physica Status Solidi (b), **241**(3): (2004) 587–590

[148] W. Wünstel und C. Klingshirn. *Tunable laser-emission from Wurtzite-type II-VI compounds.* Optics Communications, **32**(2): (1980) 269–273

[149] J. M. Hvam, G. Blattner, M. Reuscher und C. Klingshirn. *The Biexciton Levels and Nonlinear Optical Transitions in ZnO.* Physica Status Solidi (b), **118**(1): (1983) 179–189

[150] T. V. Butkhuzi, T. G. Chelidze, A. N. Georgobiani, D. L. Jashiashvili, T. G. Khulordava und B. E. Tsekvava. *Exciton photoluminescence of hexagonal ZnO.* Physical Review B, **58**(16): (1998) 10692–10695

[151] D. Magde und H. Mahr. *Exciton-Exciton Interaction in CdS, CdSe, and ZnO.* Physical Review Letters, **24**(16): (1970) 890–893

[152] C. Klingshirn, J. Fallert, H. Zhou, J. Sartor, C. Thiele, F. Maier-Flaig, D. Schneider und H. Kalt. *65 years of ZnO research: old and very recent results.* Physica Status Solidi (b), **247**(6): (2010) 1424–1447

[153] C. Klingshirn und H. Haug. *Optical properties of highly excited direct gap semiconductors.* Physics Reports, **70**(5): (1981) 315–398

[154] R. Hauschild, H. Priller, M. Decker, J. Brückner, H. Kalt und C. Klingshirn. *Temperature dependent band gap and homogeneous line broadening of the exciton emission in ZnO.* Physica Status Solidi (c), **3**(4): (2006) 976–979

[155] P. Vashishta und R. K. Kalia. *Universal behavior of exchange-correlation energy in electron-hole liquid.* Physical Review B, **25**(10): (1982) 6492–6495

[156] R. Zimmermann. *Nonlinear Optics and the Mott Transition in Semiconductors.* Physica Status Solidi (b), **146**(1): (1988) 371–384

[157] R. Leheny, J. Shah und G. Carina Chiang. *Exciton-contribution to the reflection spectrum at high excitation intensities in CdS.* Solid State Communications, **25**(9): (1978) 621–624

[158] K. Bohnert, G. Schmieder, S. El-Dessouki und C. Klingshirn. *Gain spectroscopy and plasma recombination in CdS.* Solid State Communications, **27**(3): (1978) 295–299

[159] A. Beer. *Bestimmung der Absorption des rothen Lichts in farbigen Flüssigkeiten.* Annalen der Physik und Chemie, **86**: (1852) 78–88

[160] H. Saito und E. O. Göbel. *Picosecond spectroscopy of highly excited CdS.* Physical Review B, **31**(4): (1985) 2360–2369

[161] J. A. Fallert. *Stimulierte Emission in Zinkoxid-Nanostrukturen.* Dissertation, Universität Karlsruhe (2009)

[162] K. Bohnert, G. Schmieder und C. Klingshirn. *Gain and Reflection Spectroscopy and the Present Understanding of the Electron-Hole Plasma in II-VI Compounds.* Physica Status Solidi (b), **98**(1): (1980) 175–188

[163] A. Siegmann. *Lasers.* University Science Books, Sausalito (1986)

[164] L. A. Coldren. *Diode lasers and photonic integrated circuits.* Wiley, New York (1982)

[165] Y. Chen, N. T. Tuan, Y. Segawa, H.-j. Ko, S.-k. Hong und T. Yao. *Stimulated emission and optical gain in ZnO epilayers grown by plasma-assisted molecular-beam epitaxy with buffers.* Applied Physics Letters, **78**(11): (2001) 1469–1471

[166] A. Pan, D. Liu, R. Liu, F. Wang, X. Zhu und B. Zou. *Optical Waveguide through CdS Nanoribbons.* Small, **1**(10): (2005) 980–983

[167] S. Rühle, L. K. van Vugt, H.-Y. Li, N. A. Keizer, L. Kuipers und D. Vanmaekelbergh. *Nature of Sub-Band Gap Luminescent Eigenmodes in a ZnO Nanowire.* Nano Letters, **8**(1): (2008) 119–123

[168] F. Urbach. *The Long-Wavelength Edge of Photographic Sensitivity and of the Electronic Absorption of Solids.* Physical Review, **92**(5): (1953) 1324–1324

[169] M. Zimmler. *Physics and Applications of Semiconductor Nanowire Photonic Devices.* Dissertation, Harvard University (2009)

[170] M. H. Huang, S. Mao, H. Feick, H. Yan, Y. Wu, H. Kind, E. Weber, R. Russo und P. Yang. *Room-Temperature Ultraviolet Nanowire Nanolasers.* Science, **292**(5523): (2001) 1897–1899

[171] R. Agarwal, C. J. Barrelet und C. M. Lieber. *Lasing in Single Cadmium Sulfide Nanowire Optical Cavities.* Nano Letters, **5**(5): (2005) 917–920

[172] J. Johnson, H. Yan, R. Schaller, L. Haber, R. Saykally und P. Yang. *Single Nanowire Lasers.* Journal of Physical Chemics B, **105**(46): (2001) 11387–11390

[173] S. F. Yu, C. Yuen, S. P. Lau, W. I. Park und G.-C. Yi. *Random laser action in ZnO nanorod arrays embedded in ZnO epilayers.* Applied Physics Letters, **84**(17): (2004) 3241–3243

[174] H.-C. Hsu, C.-Y. Wu und W.-F. Hsieh. *Stimulated emission and lasing of random-growth oriented ZnO nanowires.* Journal of Applied Physics, **97**(6): (2005) 064315–4

[175] X. Han, G. Wang, Q. Wang, L. Cao, R. Liu, B. Zou und J. G. Hou. *Ultraviolet lasing and time-resolved photoluminescence of well-aligned ZnO nanorod arrays.* Applied Physics Letters, **86**(22): (2005) 223106

[176] J. X. Ding, J. A. Zapien, W. W. Chen, Y. Lifshitz, S. T. Lee und X. M. Meng. *Lasing in ZnS nanowires grown on anodic aluminum oxide templates.* Applied Physics Letters, **85**(12): (2004) 2361–2363

[177] L. Wischmeier. *ZnO-Nanodrähte: Optische Eigenschaften und Ladungsträgerdynamik.* Dissertation, Universität Bremen (2007)

[178] J. Grabowska, A. Meaney, K. K. Nanda, J.-P. Mosnier, M. O. Henry, J.-R. Duclere und E. McGlynn. *Surface excitonic emission and quenching effects in ZnO nanowire/nanowall systems: Limiting effects on device potential.* Physical Review B, **71**(11): (2005) 115439–7

[179] L. Wischmeier, T. Voss, S. Börner und W. Schade. *Comparison of the optical properties of as-grown ensembles and single ZnO nanowires.* Applied Physics A: Materials Science & Processing, **84**(1): (2006) 111–116

[180] J.-P. Richters, T. Voss, L. Wischmeier, I. Rückmann und J. Gutowski. *Near-Band-Edge Photoluminescence Spectroscopy of ZnO Nanowires Embedded in Polymers.* Journal of Korean Physical Society

[181] J.-P. Richters, T. Voss, D. S. Kim, R. Scholz und M. Zacharias. *Enhanced surface-excitonic emission in ZnO/Al_2O_3 core-shell nanowires.* Nanotechnology, **19**(30): (2008) 305202–

[182] U. C. Schröder. *Biofunktionalisierung von ZnO-Nanodrähten für die Nukleinsäuresensorik.* Diplomarbeit, Friedrich-Schiller-Universität Jena (2010)

[183] L. Chen, T. Niebling, W. Heimbrod, P. J. Klar, D. Stichtenoth und C. Ronning. *Energy Transfer and Dynamics of the Mn $3d^5$ Luminescence in Low Dimensional (Zn,Mn)S Nanostructures.* Journal of the Korean Physical Society, **53**(5): (2008) 2830–2834

[184] J. Jensen und A. Mackintosh. *Rare Earth Magnetism: Structures and Excitation.* Clarendon Press, Oxford (1991)

[185] S. Hüfner. *Optical spectra of transparent rare earth compounds.* Academic Press (1978)

[186] A. Kaminskij (Hg.). *Laser crystals: Their Physics and Properties.* Springer (1990)

[187] H. N. Russell und F. A. Saunders. *New Regularities in the Spectra of the Alkaline Earths.* Astrophysical Journal, **61**

[188] J. Becquerel. *Untersuchungen über die magneto-optischen Erscheinungen in Kristallen.* Physikalische Zeitung, **8**: (1908) 632

[189] R. Tomaschek und O. Deutschbein. *Über den Zusammenhang der Emissions- und Absorptionsspektren der Salze der Seltenen Erden im festen Zustand.* Zeitschrift für Physik A Hadrons and Nuclei, **V82**(5): (1933) 309–327

[190] J. H. V. Vleck. *The Puzzle of Rare-earth Spectra in Solids.* Journal of Physical Chemics, **41**(1): (1937) 67–80

[191] O. Laporte und W. F. Meggers. *Some rules of spectral structure.* Journal of the Optical Society of America, **11**(5): (1925) 459–464

[192] H. Bethe. *Termaufspaltung in Kristallen.* Annalen der Physik, **395**(2): (1929) 133–208

[193] B. R. Judd. *Optical Absorption Intensities of Rare-Earth Ions.* Physical Review, **127**(3): (1962) 750–761

[194] G. S. Ofelt. *Intensities of Crystal Spectra of Rare-Earth Ions.* Journal of Chemical Physics, **37**(3): (1962) 511–520

[195] G. H. Dieke. *Spectra and Energy levels of Rare Earth Ions in Crystals.* Interscience Publishers (1968)

[196] K. A. Gschneidner. *Handbook on the Physics and Chemistry of Rare Earth.* North-Holland Publiching Company (1978)

[197] D. Garcia und M. Faucher. *Handbook on the Physics and Chemistry of Rare Earth*, Kap. Crystal fiels in non-metallic (rare earth) compounds, Seiten 263–304. Elsevier Science B.V. (1995)

[198] C. Görller-Walrand und K. Binnemans. *Handbook on the Physics of Rare Earths Vol. 23*, Kap. 155: 'Rationalization of Crystal-Field Parametrization', Seiten 121–283. Elsevier Sience B.V. (1996)

[199] C. Görller-Walrand und K. Binnemans. *Handbook on the Physics of Rare Earths Vol. 25*, Kap. 167: 'Spectral Intensities of f-f Transitions', Seiten 101–264. Elsevier Sience B.V. (1998)

[200] J. F. Moulder, W. F. Stickle, P. E. Sobol und K. D. Bomben. *Handbook of X Ray Photoelectron Spectroscopy.* Eden Prairie, Minnesota : Physical Electronics (1995)

[201] G. Racah. *Theory of Complex Spectra. I.* Physical Review, **61**(3-4): (1942) 186–198

[202] G. Racah. *Theory of Complex Spectra. II.* Physical Review, **62**(9-10): (1942) 438–463

[203] G. Racah. *Theory of Complex Spectra. III.* Physical Review, **63**(9-10): (1943) 367–383

[204] G. Racah. *Theory of Complex Spectra. IV.* Physical Review, **76**(9): (1949) 1352–1366

[205] K. Rajnak und B. G. Wybourne. *Configuration Interaction Effects in l^N Configurations.* Physical Review, **132**(1): (1963) 280–290

[206] B. R. Judd. *Three-Particle Operators for Equivalent Electrons.* Physical Review, **141**(1): (1966) 4–14

[207] B. R. Judd, H. M. Crosswhite und H. Crosswhite. *Intra-Atomic Magnetic Interactions for f-Electrons.* Physical Review, **169**(1): (1968) 130–138

[208] Z. B. Goldschmidt, A. Pasternak und Z. H. Goldschmidt. *Magnetic interactions in heavy atoms.* Physics Letters A, **28**(4): (1968) 265–266

[209] R. S. Mulliken. *Report on Notation for the Spectra of Polyatomic Molecules.* Journal of Chemical Physics, **23**: (1955) 1997

[210] H. A. Kramers. Proceedings of the Amsterdam Academy, **33**: (1930) 959

[211] J. Griffith. *The Theory of Transition-Metal Ions.* Cambridge University Press (1961)

[212] H. A. Jahn und E. Teller. *Stability of Polyatomic Molecules in Degenerate Electronic States. I. Orbital Degeneracy.* Proceedings of the Royal Society of London. Series A, Mathematical and Physical Sciences, **161**(905): (1937) 220–235

[213] S. Sugano, Y. Tanabe und H. Kamimura. *Multiplets of transition-metal ions in crystals.* In *Pure and Applied Physics*, Bd. 33. Academic Press, New York (1970)

[214] R. S. Anderson. *Lattice-Vibration Effects in the Spectra of ZnO:Ni and ZnO:Co.* Physical Review, **164**(2): (1967) 398–405

[215] E. Malguth, A. Hoffmann und M. R. Phillips. *Fe in III-V and II-VI semiconductors.* Physica Status Solidi (b), **245**(3): (2008) 455–480

[216] A. Hoffmann und U. Scherz. *Jahn-teller effect and zero-phonon line isotope shifts of transition metals in II-VI compounds.* Journal of Crystal Growth, **101**: (1990) 385–392

[217] P. Koidl, O. F. Schirmer und U. Kaufmann. *Near-Infrared Absorption of Co^{2+} in ZnS: Weak Jahn-Teller Coupling in the $^4T_2$ and $^4T_1$ States.* Physical Review B, **8**(11): (1973) 4926–4934

[218] M. Klintenberg. *Rare-earth Polarized Absorption Spectra as a Structural Tool.* Acta Universitatis Upsaliensis (1997)

[219] P. Y. Yu und M. Cardona. *Fundamentals of Semiconductors: Physics and Materials Properties.* Springer (2001)

[220] F. Auzel. *Multiphonon-assisted anti-Stokes and Stokes fluorescence of triply ionized rare-earth ions.* Physical Review B, **13**(7): (1976) 2809–2817

[221] F. Auzel und F. Pelle. *Concentration and excitation effects in multiphonon non-radiative transitions of rare-earth ions.* Journal of Luminescence, **69**(5-6): (1996) 249–255

[222] T. Miyakawa und D. L. Dexter. *Phonon sidebands, multiphonon relaxation of excited states, and phonon-assisted energy transfer between ions in solids.* Physical Review B, **1**(7): (1970) 2961–2969

[223] L. A. Riseberg und H. W. Moos. *Multiphonon Orbit-Lattice Relaxation of Excited States of Rare-Earth Ions in Crystals.* Physical Review, **174**(2): (1968) 429–438

[224] M. Godlewski und K. Swiatek. *Excitonic processes in II-VI compounds doped with transition metal and rare earth impurities.* Journal of Crystal Growth, **117**(1-4): (1992) 634–639

[225] M. Godlewski, K. Swiatek und B. Monemar. *Recombination processes of rare earth bound excitons.* Journal of Luminescence, **58**(1-6): (1994) 303–306

[226] Y. Jiaqi und S. Yongrong. *Calculation of the impact cross section of rare-earth centres in solids.* Journal of Physics C: Solid State Physics, **21**: (1988) 3381–3386

[227] E. Bringuier. *Impact excitation in ZnS-type electroluminescence.* Journal of Applied Physics, **70**(8): (1991) 4505–4512

[228] K. Swiatek, A. Suchocki und M. Godlewski. *Impact ionization mechanism in rare earth activated sulfides.* Applied Physics Letters, **56**(2): (1990) 195–197

[229] T. Förster. *Zwischenmolekulare Energiewanderung und Fluoreszenz.* Annalen der Physik, **437**: (1948) 55–75

[230] D. L. Dexter. *A theory of sensitized luminescence in solids.* Journal of Chemical Physics, **21**(5): (1953) 836–850

[231] F. Auzel. *Radiationless processes.* Plenum Press, New York (1980)

[232] Y. E. Perlin und A. A. Kaminskii. *Nonradiative Transitions of the Trivalent Lanthanides in Insulating Laser Crystals.* Physica Status Solidi (b), **132**(1): (1985) 11–40

[234] A. D. Pearson, G. E. Peterson und W. R. Northover. Tb^{3+} *Fluorescence and Nonradiative Energy Transfer from Gd^{3+} to Tb^{3+} in Borate Glass.* Journal of Applied Physics, **37**(2): (1966) 729–734

[233] H. Kobayashi, S. Tanaka, V. Shanker, M. Shiiki, T. Kunou, J. Mita und H. Sasakura. *Multicolor electroluminescent ZnS thin films doped with rare earth fluorides.* Physica Status Solidi (a), **88**(2): (1985) 713–720

[235] J. Langer, A. Suchocki, L. Van Hong, P. Ciepielewski und W. Walukiewicz. *Auger effect at localized impurities in semiconductors.* Physica B+C, **117–118, Part 1**(0): (1983) 152–154

[236] J. W. Allen. *Impact excitation and Auger quenching of luminescent centres in crystals, with special reference to ZnS:Mn.* Journal of Physics C: Solid State Physics, **19**(31): (1986) 6287–6295

[237] M. Inokuti und F. Hirayama. *Influence of Energy Transfer by the Exchange Mechanism on Donor Luminescence.* Journal of Chemical Physics, **43**(6): (1965) 1978–1989

[238] E. M. Omel'janovskij und V. I. Fistul. *Transition metal impurities in semiconductors.* Hilger Bristol (1986)

[239] H. A. Weakliem. *Optical Spectra of Ni^{2+}, Co^{2+}, and Cu^{2+} in Tetrahedral Sites in Crystals.* Journal of Chemical Physics, **36**(8): (1962) 2117–2140

[240] H.-J. Schulz und M. Thiede. *Optical spectroscopy of $3d^7$ and $3d^8$ impurity configurations in a wide-gap semiconductor (ZnO:Co,Ni,Cu).* Physical Review B, **35**(1): (1987) 18–34

[241] R. Heitz, A. Hoffmann und I. Broser. Fe^{3+} *center in ZnO.* Physical Review B, **45**(16): (1992) 8977–8988

[242] H. Schmid, M. T. Björk, J. Knoch, S. Karg, H. Riel und W. Riess. *Doping Limits of Grown in situ Doped Silicon Nanowires Using Phosphine.* Nano Letters, **9**(1): (2008) 173–177

[243] M. T. Borgström, E. Norberg, P. Wickert, H. A. Nilsson, J. Trägardh, K. A. Dick, G. Statkute, P. Ramvall, K. Deppert und L. Samuelson. *Precursor evaluation for in situ InP nanowire doping.* Nanotechnology, **19**(44): (2008) 445602–7

[244] J. Wallentin und M. T. Borgström. *Doping of semiconductor nanowires.* Journal of Materials Research, **26**(17): (2011) 2142–2156

[245] D. Perea, E. Wijaya, J. Lensch-Falk, E. Hemesath und L. Lauhon. *Tomographic analysis of dilute impurities in semiconductor nanostructures.* Journal of Solid State Chemistry, **181**(7): (2008) 1642–1649

[246] D. E. Perea, E. R. Hemesath, E. J. Schwalbach, J. L. Lensch-Falk, P. W. Voorhees und L. J. Lauhon. *Direct measurement of dopant distribution in an individual vapour-liquid-solid nanowire.* Nature Nanotechnology, **4**(5): (2009) 315–319

[247] Y. Yang, H. Lai, H. Xu, C. Tao und H. Yang. *Morphology & luminescence correlations in europium-doped ZnO nanomaterials.* Journal of Nanoparticle Research, **12**(1): (2010) 217–225

[248] Y. Yang, H. Lai, C. Tao und H. Yang. *Correlation of luminescent properties of ZnO and Eu doped ZnO nanorods.* Journal of Materials Science: Materials in Electronics, **21**(2): (2010) 173–178

[249] C. Ronning, C. Borschel, S. Geburt, R. Niepelt, S. Müller, D. Stichtenoth, J. .-P. Richters, A. Dev, T. Voss, L. Chen, W. Heimbrodt, C. Gutsche und W. Prost. *Tailoring the properties of semiconductor nanowires using ion beams.* Physica Status Solidi (b), **10**: (2010) 2329–2337

[250] C. Ronning, C. Borschel, S. Geburt und R. Niepelt. *Ion beam doping of semiconductor nanowires.* Materials Science and Engineering: R: Reports, **70**(3-6): (2010) 30–43

[251] C. Ronning, P. X. Gao, Y. Ding, Z. L. Wang und D. Schwen. *Manganese-doped ZnO nanobelts for spintronics.* Applied Physics Letters, **84**(5): (2004) 783–785

[252] J. Wang, M. J. Zhou, S. K. Hark, Q. Li, D. Tang, M. W. Chu und C. H. Chen. *Local electronic structure and luminescence properties of Er doped ZnO nanowires.* Applied Physics Letters, **89**(22): (2006) 221917–3

[253] L. Chen, J. Zhang, X. Zhang, F. Liu und X. Wang. *Optical properties of trivalent europium doped ZnO:Zn phosphor under indirect excitation of near-UV light.* Optical Express, **16**(16): (2008) 11795–11801

[254] C. Borschel und C. Ronning. *Ion beam irradiation of nanostructures: A 3D Monte Carlo simulation code.* Nuclear Instruments and Methods in Physics Research Section B: Beam Interactions with Materials and Atoms, **269**(19): (2011) 2133–2138

[255] C. Borschel, R. Niepelt, S. Geburt, C. Gutsche, I. Regolin, W. Prost, F.-J. Tegude, D. Stichtenoth, D. Schwen und C. Ronning. *Alignment of semiconductor nanowires using ion beams.* Small, **5**(22): (2009) 2576–2580

[256] C. Borschel, S. Spindler, D. Lerose, A. Bochmann, S. H. Christiansen, S. Nietzsche, M. Oertel und C. Ronning. *Permanent bending and alignment of ZnO nanowires.* Nanotechnology, **22**(18): (2011) 185307–

[257] R. S. Wagner und W. C. Ellis. *Vapor-liquid-solid mechanism of single crystal growth.* Applied Physics Letters, **4**(5): (1964) 89–90

[258] H. Okamoto und T. Massalski. *The Au-S (Gold-Sulfur) system.* Journal of Phase Equilibria, **6**(6): (1985) 518–519

[259] H. Okamoto und T. Massalski. *The Au-Cd (Gold-Cadmium) system.* Journal of Phase Equilibria, **7**(1): (1986) 52–67

[260] H. Okamoto und T. Massalski. *The Au-Zn (Gold-Zinc) system.* Journal of Phase Equilibria, **10**(1): (1989) 59–69

[261] A. I. Persson, M. W. Larsson, S. Stenstrom, B. J. Ohlsson, L. Samuelson und L. R. Wallenberg. *Solid-phase diffusion mechanism for GaAs nanowire growth.* Nature Materials, **3**(10): (2004) 677–681

[262] B. A. Wacaser, K. A. Dick, J. Johansson, M. T. Borgström, K. Deppert und L. Samuelson. *Preferential Interface Nucleation: An Expansion of the VLS Growth Mechanism for Nanowires.* Advanced Materials, **21**(2): (2009) 153–165

[263] Z. L. Wang. *Zinc oxide nanostructures: growth, properties and applications.* Journal of Physics: Condensed Matter, **16**(25): (2004) R829–R858

[264] Z. L. Wang. *Nanostructures of Zinc Oxide.* Materials Today, **7**(6): (2004) 26–33

[265] S. Jebril, H. Kuhlmann, S. Müller, C. Ronning, L. Kienle, V. Duppel, Y. K. Mishra und R. Adelung. *Epitactically Interpenetrated High Quality ZnO Nanostructured Junctions on Microchips Grown by the Vapor-Liquid-Solid Method.* Crystal Growth & Design, **10**(7): (2010) 2842–2846

[266] C. Ronning und D. Schwen. *Nanodrähte, Nanosägen, Nanospiralen. Eindimensionale Materialien aus Halbleitern.* Physik in unserer Zeit, **37**(1): (2006) 34–40

[267] D. Stichtenoth. *Wachstum und Modifikation von Halbleiternanodrähten.* Diplomarbeit, II. Physikalisches Institut, Universität Göttingen (2005)

[268] S. Müller. *Wachstum von ZnO-Nanodrähten und deren Dotierung durch Ionenstrahlen.* Diplomarbeit, II. Physikalisches Institut, Universität Göttingen (2005)

[269] C. Borchers, D. Stichtenoth, S. Müller, D. Schwen und C. Ronning. *Catalyst nanostructure interaction and growth of ZnS nanobelts.* Nanotechnology, **17**(4): (2006) 1067–1071

[270] M. Kozlik. *Synthese von Halbleiternanodrähten für die Photonik.* Diplomarbeit, Friedrich-Schiller-Universität Jena, Institut für Festkörperphysik (2009)

[271] M. Gnauck. *Elektrische Kontaktierung von ZnO-Nanostrukturen und deren Verwendung für sensorische Zwecke.* Diplomarbeit, Friedrich-Schiller-Universität Jena (2010)

[272] J. Kühnel. *Cathodoluminescence probing of semiconducting nanowires and plasmonic nanostructures.* Diplomarbeit, University of Jena (2011)

[273] S. Spindler. *Morphologieänderungen und Ausrichtung von Halbleiternanodrähten durch Ionenbeschuss.* Diplomarbeit, Friedrich-Schiller Universität Jena (2011)

[274] C. Borschel. *Ion-solid interaction in semiconductor nanowires.* Dissertation, Friedrich-Schiller-Universität Jena (2011)

[275] J. Goldstein, D. E. Newbury, P. Echlin, D. C. Joy, A. D. J. Roming, C. E. Lyman, C. Foori und E. Lifhin. *Scanning Electron Microscopy and X-ray Microanalysis.* Plenum Press, New York (1992)

[276] L. Reimer. *Scanning Electron Microscopy.* Springer Berlin (1998)

[277] D. Williams und C. Carter. *Transmission Electron Microscopy - I Basics.* Plemum Press, New York (1996)

[278] D. Williams und C. Carter. *Transmission Electron Microscopy - II Diffraction.* Plemum Press, New York (1996)

[279] D. Williams und C. Carter. *Transmission Electron Microscopy - III Imaging.* Plemum Press, New York (1996)

[280] D. Williams und C. Carter. *Transmission Electron Microscopy - IV Spectrometry.* Plemum Press, New York (1996)

[281] V. Solé, E. Papillon, M. Cotte, P. Walter und J. Susini. *A multiplatform code for the analysis of energy-dispersive X-ray fluorescence spectra.* Spectrochimica Acta Part B: Atomic Spectroscopy, **62**(1): (2007) 63–68

[282] L. Tröger, D. Arvanitis, K. Baberschke, H. Michaelis, U. Grimm und E. Zschech. *Full correction of the self-absorption in soft-fluorescence extended x-ray-absorption fine structure.* Physical Review B, **46**(6): (1992) 3283–3289

[283] A. Somogyi, R. Tucoulou, G. Martinez-Criado, A. Homs, J. Cauzid, P. Bleuet, S. Bohic und A. Simionovici. *ID22: a multitechnique hard X-ray microprobe beamline at the European Synchrotron Radiation Facility.* Journal of Synchrotron Radiation, **12**(2): (2005) 208–215

[284] R. Tucoulou, G. Martinez-Criado, P. Bleuet, I. Kieffer, P. Cloetens, S. Laboura, T. Martin, C. Guilloud und J. Susini. *High-resolution angular beam stability monitoring at a nanofocusing beamline.* Journal of Synchrotron Radiation, **15**(4): (2008) 392–398

[285] M. Salomé, P. Bleuet, S. Bohic, J. Cauzid, E. Chalmin, P. Cloetens, M. Cotte, V. D. Andrade, G. Martinez-Criado, S. Petitgirard, M. Rak, J. A. S. T. andJ Szlachetko, R. Tucoulou und J. Susini. *Fluorescence X-ray micro-spectroscopy activities at ESRF.* Journal of Physics: Conference Series, **186**(1): (2009) 012014–4

[286] G. Martinez-Criado, R. Tucoulou, P. Cloetens, P. Bleuet, S. Bohic, J. Cauzid, I. Kieffer, E. Kosior, S. Laboure, S. Petitgirard, A. Rack, J. A. Sans, J. Segura-Ruiz, H. Suhonen, J. Susini und J. Villanova. *Status of the hard X-ray microprobe beamline ID22 of the European Synchrotron Radiation Facility.* Journal of Synchrotron Radiation, **19**(1): (2012) 10–18

[287] D. C. Koningsberger und R. Prins. *X-Ray Absorption: Principles, Applications, Techniques of EXAFS, SEXAFS and XANES.* Wiley-Interscience; (1988)

[288] G. Bunker. *Introduction to XAFS.* Cambridge University Press (2010)

[289] Newville und Matthew. *IFEFFIT : interactive XAFS analysis and FEFF fitting.* Journal of Synchrotron Radiation, **8**(2): (2001) 322–324

[290] B. Valeur und M. N. Berberan-Santos. *A Brief History of Fluorescence and Phosphorescence before the Emergence of Quantum Theory.* Journal of Chemical Education, **88**(6): (2011) 731–738

[291] B. G. Yacobi und D. B. Holt. *Cathodoluminescence scanning electron microscopy of semiconductors.* Journal of Applied Physics, **59**(4): (1986) R1–R24

[292] B. G. Yacobi und D. B. Holt. *Cathodoluminescence microscopy of inorganic solids.* Plenum Press, New York (1990)

[293] D. Drouin, A. R. Couture, D. Joly, X. Tastet, V. Aimez und R. Gauvin. *CASINO V2.42 - A Fast and Easy-to-use Modeling Tool for Scanning Electron Microscopy and Microanalysis Users.* Scanning, **29**(3): (2007) 92–101

[294] D. Drouin, P. Hovington und R. Gauvin. *CASINO: A new monte carlo code in C language for electron beam interactions - part II: Tabulated values of the mott cross section.* Scanning, **19**(1): (1997) 20–28

[295] P. Hovington, D. Drouin und R. Gauvin. *CASINO: A new monte carlo code in C language for electron beam interaction - part I: Description of the program.* Scanning, **19**(1): (1997) 1–14

[296] P. Hovington, D. Drouin, R. Gauvin, D. C. Joy und N. Evans. *CASINO: A new monte Carlo code in C language for electron beam interactions - part III: Stopping power at low energies.* Scanning, **19**(1): (1997) 29–35

[297] H. Demers, N. Poirier-Demers, A. R. Couture, D. Joly, M. Guilmain, N. de Jonge und D. Drouin. *Three-dimensional electron microscopy simulation with the CASINO Monte Carlo software*. Scanning, **33**(3): (2011) 135–146

[298] M. R. Phillips. *Cathodoluminescence Microscopy and Spectroscopy of Opto-Electronic Materials*. Microchemica Acta, **155**(1): (2006) 51–58

[299] A. Gustafsson. *Cathodoluminescence studies of nanostructured semiconductors*. Journal of Microscopy, **224**(1): (2006) 72–78

[300] B. Dierre, X. Yuan und T. Sekiguchi. *Low-energy cathodoluminescence microscopy for the characterization of nanostructures*. Science and Technology of Advanced Materials, **11**(4): (2010) 043001–11

[301] S. Müller. *Structural and optical impact of transition metal implantation into zinc oxide single crystals and nanowires*. Dissertation, Universität Göttingen (2009)

[302] A. Thielmann. *Aufbau einer Mikrophotolumineszenzapparatur und Lasingeigenschaften von ZnO- und CdS-Nanodrähten*. Diplomarbeit, Friedrich-Schiller-Universität Jena (2011)

[303] A. McDonnell. *Synthesis and Characterisation of CdS Nanowires*. Batchelorarbeit, Friedrich-Schiller-Universität Jena (2009)

[304] R. Röder. *Modifikation der Lasingeigenschaften von CdS Nanodrähten*. Masterarbeit, Friedrich-Schiller Universität Jena (2012)

[305] S. Geburt, A. Thielmann, R. Röder, C. Borschel, A. McDonnell, M. Kozlik, J. Kühnel, K. A. Sunter, F. Capasso und C. Ronning. *Low threshold room-temperature lasing of CdS nanowires*. Nanotechnology, **23**(36): (2012) 365204–6

[306] C. Barrelet, A. Greytak und C. Lieber. *Nanowire Photonic Circuit Elements*. Nano Letters, **4**(10): (2004) 1981–1985

[307] D. Banerjee, J. Rybczynski, J. Huang, D. Wang, K. Kempa und Z. Ren. *Large hexagonal arrays of aligned ZnO nanorods*. Applied Physics A: Materials Science & Processing, **80**(4): (2005) 749–752

[308] M. A. Zimmler, T. Voss, C. Ronning und F. Capasso. *Exciton-related electroluminescence from ZnO nanowire light-emitting diodes*. Applied Physics Letters, **94**(24): (2009) 241120–3

[309] T. Voss, G. T. Svacha, E. Mazur, S. Müller und C. Ronning. *The influence of local heating by nonlinear pulsed laser excitation on the transmission characteristics of a ZnO nanowire waveguide*. Nanotechnology, **20**(9): (2009) 095702–6

[310] E. Wendler, O. Bilani, K. Gärtner, W. Wesch, M. Hayes, F. Auret, K. Lorenz und E. Alves. *Radiation damage in ZnO ion implanted at 15 K*. Nuclear Instruments and Methods in Physics Research Section B: Beam Interactions with Materials and Atoms, **267**(16): (2009) 2708–2711

[311] X. Duan, Y. Huang, R. Agarwal und C. M. Lieber. *Single-nanowire electrically driven lasers*. Nature, **421**: (2003) 241–245

[312] T. Zhai, X. Fang, L. Li, Y. Bando und D. Golberg. *One-dimensional CdS nanostructures: synthesis, properties, and applications*. Nanoscale, **2**(2): (2010) 168–187

[313] X. Wang, C. Summers und Z. Wang. *Large-Scale Hexagonal-Patterned Growth of Aligned ZnO Nanorods for Nano-optoelectronics and Nanosensor Arrays*. Nano Letters, **4**(3): (2004) 423–426

[314] H. J. Fan, W. Lee, R. Scholz, A. Dadgar, A. Krost, K. Nielsch und M. Zacharias. *Arrays of vertically aligned and hexagonally arranged ZnO nanowires: a new template-directed approach*. Nanotechnology, **16**: (2005) 913–917

[315] J.-S. Lee, K. Park, M.-I. Kang, I.-W. Park, S.-W. Kim, W. K. Cho, H. S. Han und S. Kim. *ZnO nanomaterials synthesized from thermal evaporation of ball-milled ZnO powders*. Journal of Crystal Growth, **254**(3-4): (2003) 423–431

[316] B. K. Meyer, J. Sann, D. M. Hofmann, C. Neumann und A. Zeuner. *Shallow donors and acceptors in ZnO*. Semiconductor Science and Technology, **20**(4): (2005) S62–S66

[317] B. K. Meyer, J. Sann, S. Lautenschlager, M. R. Wagner und A. Hoffmann. *Ionized and neutral donor-bound excitons in ZnO*. Physical Review B, **76**(18): (2007) 184120–4

[318] Y. Sun und H. Wang. *The electronic properties of native interstitials in ZnO*. Physica B: Condensed Matter, **325**: (2003) 157–163

[319] J. Sann, J. Stehr, A. Hofstaetter, D. M. Hofmann, A. Neumann, M. Lerch, U. Haboeck, A. Hoffmann und C. Thomsen. *Zn interstitial related donors in ammonia-treated ZnO powders*. Physical Review B, **76**(19): (2007) 195203–6

[320] V. V. Travnikov, A. Freiberg und S. F. Savikhin. *Surface excitons in ZnO crystals.* Journal of Luminescence, **47**(3): (1990) 107–112

[321] L. Wischmeier, C. Bekeny, T. Voss, S. Börner und W. Schade. *Optical properties of single ZnO nanowires.* Physica Status Solidi (b), **243**(4): (2006) 919–923

[322] S. Müller, D. Stichtenoth, M. Uhrmacher, H. Hofsäss, C. Ronning und J. Roder. *Unambiguous identification of the PL-I$_9$ line in zinc oxide.* Applied Physics Letters, **90**(1): (2007) 012107–3

[323] Alfa Aesar. *ZnO powder properties: contaminations* (2008)

[324] D. C. Reynolds, D. C. Look, B. Jogai, C. W. Litton, T. C. Collins, W. Harsch und G. Cantwell. *Neutral-donor & bound-exciton complexes in ZnO crystals.* Physical Review B, **57**(19): (1998) 12151–5

[325] D. Stichtenoth. *Dimensionseffekte in Halbleitern.* Dissertation, Universität Göttingen (2008)

[326] Y. Varshni. *Temperature dependence of the energy gap in semiconductors.* Physica, **34**(1): (1967) 149–154

[327] X. L. Wu, G. G. Siu, C. L. Fu und H. C. Ong. *Photoluminescence and cathodoluminescence studies of stoichiometric and oxygen-deficient ZnO films.* Applied Physics Letters, **78**(16): (2001) 2285–2287

[328] R. Kuhnert und R. Helbig. *Vibronic structure of the green photoluminescence due to copper impurities in ZnO.* Journal of Luminescence, **26**(1-2): (1981) 203–206

[329] K. Vanheusden, C. H. Seager, W. L. Warren, D. R. Tallant und J. A. Voigt. *Correlation between photoluminescence and oxygen vacancies in ZnO phosphors.* Applied Physics Letters, **68**(3): (1996) 403–405

[330] K. Vanheusden, W. L. Warren, C. H. Seager, D. R. Tallant, J. A. Voigt und B. E. Gnade. *Mechanisms behind green photoluminescence in ZnO phosphor powders.* Journal of Applied Physics, **79**(10): (1996) 7983–7990

[331] F. Leiter, H. Zhou, F. Henecker, A. Hofstaetter, D. M. Hofmann und B. K. Meyer. *Magnetic resonance experiments on the green emission in undoped ZnO crystals.* Physica B: Condensed Matter, **308-310**: (2001) 908–911

[332] F. Leiter, H. Alves, D. Pfisterer, N. G. Romanov, D. M. Hofmann und B. K. Meyer. *Oxygen vacancies in ZnO.* Physica B: Condensed Matter, **340-342**: (2003) 201–204

[333] E. G. Bylander. *Surface effects on the low-energy cathodoluminescence of zinc oxide.* Journal of Applied Physics, **49**(3): (1978) 1188–1195

[334] A. F. Kohan, G. Ceder, D. Morgan und C. G. Van de Walle. *First-principles study of native point defects in ZnO.* Physical Review B, **61**(22): (2000) 15019–15027

[335] S. Müller, M. Lorenz, C. Czekalla, G. Benndorf, H. Hochmuth, M. Grundmann, H. Schmidt und C. Ronning. *Intense white photoluminescence emission of V-implanted zinc oxide thin films.* Journal of Applied Physics, **104**(12): (2008) 123504–7

[336] D. Reynolds, D. Look, B. Jogai und H. Morkoc. *Similarities in the bandedge and deep-centre photoluminescence mechanisms of ZnO and GaN.* Solid State Communications, **101**: (1997) 643–646

[337] D. C. Reynolds, D. C. Look und B. Jogai. *Fine structure on the green band in ZnO.* Journal of Applied Physics, **89**(11): (2001) 6189–6191

[338] W. B. Fowler. *Physics of color centers.* Academic Press, New York (1968)

[339] T. Ogino und M. Aoki. *Mechanism of Yellow Luminescence in GaN.* Japanese Journal of Applied Physics, **19**(12): (1980) 2395–

[340] M. A. Reshchikov, F. Shahedipour, R. Y. Korotkov, B. W. Wessels und M. P. Ulmer. *Photoluminescence band near 2.9 eV in undoped GaN epitaxial layers.* Journal of Applied Physics, **87**(7): (2000) 3351–3354

[341] P. Xu, Y. Sun, C. Shi, F. Xu und H. Pan. *Native Point Defect States in ZnO.* Chinese Physics Letters, **18**(9): (2001) 1252–1253

[342] C. G. Van de Walle. *Defect analysis and engineering in ZnO.* Physica B: Condensed Matter, **308–310**: (2001) 899–903

[343] D. C. Look, J. W. Hemsky und J. R. Sizelove. *Residual Native Shallow Donor in ZnO.* Physical Review Letters, **82**(12): (1999) 2552–2555

[344] B. Lin, Z. Fu und Y. Jia. *Green luminescent center in undoped zinc oxide films deposited on silicon substrates.* Applied Physics Letters, **79**(7): (2001) 943–945

[345] Q. X. Zhao, P. Klason, M. Willander, H. M. Zhong, W. Lu und J. H. Yang. *Deep-level emissions influenced by O and Zn implantations in ZnO.* Applied Physics Letters, **87**(21): (2005) 211912–3

[346] E. Rita, U. Wahl, J. G. Correia, E. Alves, J. C. Soares und I. Collaboration. *Lattice location and thermal stability of implanted Fe in ZnO*. Applied Physics Letters, **85**(21): (2004) 4899–4901

[347] U. Wahl, J. G. Correia, E. Rita, E. Alves, J. C. Soares, B. D. Vries, V. Matias, A. Vantomme und the ISOLDE collaboration. *Recent Emission Channeling studies in Wide Band Gap Semiconductors*. Hyperfine Interactions, **159**: (2004) 363–372

[348] S. A. Studenikin, N. Golego und M. Cocivera. *Fabrication of green and orange photoluminescent, undoped ZnO films using spray pyrolysis*. Journal of Applied Physics, **84**(4): (1998) 2287–2294

[349] H. von Wenckstern, G. Benndorf, S. Heitsch, J. Sann, M. Brandt, H. Schmidt, J. Lenzner, M. Lorenz, A. Kuznetsov, B. Meyer und M. Grundmann. *Properties of phosphorus doped ZnO*. Applied Physics A: Materials Science & Processing, **88**(1): (2007) 125–128

[350] B. T. Adekore, R. F. Davis und D. W. Barlage. *Electrical and optical properties of ZnO (000$\bar{1}$) wafers implanted with Argon*. Journal of Applied Physics, **101**(2): (2007) 024902–9

[351] A. Pöppl und G. Völkel. *ESR and Photo-ESR Investigations of Zinc Vacancies and Interstitial Oxygen Ions in Undoped ZnO Ceramics*. Physica Status Solidi (a), **125**: (1991) 571–581

[352] X. H. Zhang, S. J. Chua, A. M. Yong, H. Y. Yang, S. P. Lau, S. F. Yu, X. W. Sun, L. Miao, M. Tanemura und S. Tanemura. *Exciton radiative lifetime in ZnO nanorods fabricated by vapor phase transport method*. Applied Physics Letters, **90**(1): (2007) 013107–3

[353] A. Teke, . Özgür, S. Dogan, X. Gu, H. Morkoç, B. Nemeth, J. Nause und H. O. Everitt. *Excitonic fine structure and recombination dynamics in single-crystalline ZnO*. Physical Review B, **70**(19): (2004) 195207–10

[354] L. Rui-Bin, P. An-Lian, W. Fei-Fei und Z. Bing-Suo. *Optical processes in the formation of stimulated emission from ZnO nanowires*. Chinese Physics, **16**(4): (2007) 1129–6

[355] M. A. Reshchikov. *Defects in bulk ZnO studied by steady-state and time-resolved photoluminescence*. MRS Online Proceedings Library, **1035**

[356] J. C. Johnson, H. Yan, H.-J. Choi, K. P. Knutsen, P. B. Petersen, M. Law, P. Yang und R. J. Saykally. *Single nanowire lasers and waveguides*. In *Proc. SPIE*, Bd. 5223, Seiten 187–196. SPIE, San Diego, CA, USA (2003)

[357] M. V. Kurik. *Urbach rule*. Physica Status Solidi (a), **8**(1): (1971) 9–45

[358] B. E. A. Saleh und M. C. Teich. *Fundamentials of photonics*. Wiley Interscience (2007)

[359] D. M. Bagnall, Y. F. Chen, Z. Zhu, T. Yao, S. Koyama, M. Y. Shen und T. Goto. *Optically pumped lasing of ZnO at room temperature*. Applied Physics Letters, **70**: (1997) 2230–2232

[360] L. W. Casperson und S. D. Lunnam. *Gaussian Modes in High Loss Laser Resonators*. Applied Optics, **14**(5): (1975) 1193–1199

[361] L. W. Casperson. *Threshold characteristics of multimode laser oscillators*. Journal of Applied Physics, **46**(12): (1975) 5194–5201

[362] T. Shih, E. Mazur, J.-P. Richters, J. Gutowski und T. Voss. *Ultrafast exciton dynamics in ZnO: Excitonic versus electron-hole plasma lasing*. Journal of Applied Physics, **109**(4): (2011) 043504. Journal article

[363] M. A. M. Versteegh, D. Vanmaekelbergh und J. I. Dijkhuis. *Room-Temperature Laser Emission of ZnO Nanowires Explained by Many-Body Theory*. Physical Review Letters, **108**(15): (2012) 157402–5

[364] O. Mandelung (Hg.). *Semiconductors - Basic data*. Springer, Berlin (1996)

[365] S. Kar und S. Chaudhuri. *Shape Selective Growth of CdS One-Dimensional Nanostructures by a Thermal Evaporation Process*. The Journal of Physical Chemistry B, **110**(10): (2006) 4542–4547

[366] A. Imada, S. Ozaki und S. Adachi. *Photoreflectance spectroscopy of wurtzite CdS*. Journal of Applied Physics, **92**(4): (2002) 1793–1798

[367] S. Seto. *Photoluminescence, Reflectance and Photoreflectance Spectra in CdS Epilayers on Si(111) Substrates*. Japanese Journal of Applied Physics, **44**(8): (2005) 5913–5

[368] D. G. Thomas und J. J. Hopfield. *Bound Exciton Complexes*. Physical Review Letters, **7**(8): (1961) 316–319

[369] X. Xu, Y. Zhao, E. J. Sie, Y. Lu, B. Liu, S. A. Ekahana, X. Ju, Q. Jiang, J. Wang, H. Sun, T. C. Sum, C. H. A. Huan, Y. P. Feng und Q. Xiong. *Dynamics of Bound Exciton Complexes in CdS Nanobelts*. ACS Nano, **5**(5): (2011) 3660–3669

[370] K. M. Ip, C. R. Wang, Q. Li und S. K. Hark. *Excitons and surface luminescence of CdS nanoribbons*. Applied Physics Letters, **84**(5): (2004) 795–797

[371] S. W. Koch, H. Haug, G. Schmieder, W. Bohnert und C. Klingshirn. *Stimulated Intrinsic Recombination Processes in II-VI Compounds.* Physica Status Solidi (b), **89**(2): (1978) 431–440

[372] G. Shen, J. H. Cho, J. K. Yoo, G.-C. Yi und C. J. Lee. *Synthesis of Single-Crystal CdS Microbelts Using a Modified Thermal Evaporation Method and Their Photoluminescence.* The Journal of Physical Chemistry B, **109**(19): (2005) 9294–9298

[373] B. A. Kulp. *Displacement of the Cadmium Atom in Single Crystal CdS by Electron Bombardment.* Physical Review, **125**(6): (1962) 1865–1869

[374] N. Susa, H. Watanabe und M. Wada. *Effects of Annealing in Cd or S Vapor on Photoelectric Properties of CdS Single Crystals.* Japanese Journal of Applied Physics, **15**(12): (1976) 2365–2370

[375] M. Agata, H. Kurase, S. Hayashi und K. Yamamoto. *Photoluminescence spectra of gas-evaporated CdS microcrystals.* Solid State Communications, **76**(8): (1990) 1061–1065

[376] K.-T. Chen, Y. Zhang, S. Egarievwe, M. George, A. Burger, C.-H. Su, Y.-G. Sha und S. Lehoczky. *Post-growth annealing of CdS crystals grown by physical vapor transport.* Journal of Crystal Growth, **166**(1-4): (1996) 731–735

[377] B. A. Kulp und R. H. Kelley. *Displacement of the Sulfur Atom in CdS by Electron Bombardment.* Journal of Applied Physics, **31**(6): (1960) 1057–1061

[378] J. Aguilar-Hernández, G. Martinez-Criado, V. D. Andrade, G. Contreras-Puente, A. Morales-Acevedo, O. Vigil-Galán, F. Cruz-Gandarilla, J. Vidal-Larramendi, A. Escamilla-Esquivel, H. Hernández-Contreras, M. Hesiquio-Garduño, A. Arias-Carbajal, M. Chavarría-Castañeda und G. Arriaga-Mejía. *Photoluminescence and structural properties of cadmium sulphide thin films grown by different techniques.* Semiconductor Science and Technology, **18**(2): (2003) 111–114

[379] R. J. Collins. *Mechanism and Defect Responsible for Edge Emission in CdS.* Journal of Applied Physics, **30**(8): (1959) 1135–1140

[380] R. Heitz, C. Fricke, A. Hoffmann und I. Broser. *Picosecond energy transfer between excitons and defects in II-VI semiconductors.* Material Science Forum, **83-87**: (1992) 1241–1246

[381] J. Puthussery, A. Lan, T. H. Kosel und M. Kuno. *Band-Filling of Solution-Synthesized CdS Nanowires.* ACS Nano, **2**(2): (2008) 357–367

[382] L. K. van Vugt, B. Piccione, C.-H. Cho, C. Aspetti, A. D. Wirshba und R. Agarwal. *Variable Temperature Spectroscopy of As-Grown and Passivated CdS Nanowire Optical Waveguide Cavities.* Journal of Chemical Physics A, **115**(16): (2011) 3827–3833

[383] T. Fischer und J. Bille. *Recombination processes in highly excited CdS.* Journal of Applied Physics, **45**(9): (1974) 3937–3942

[384] J. Wang, M. S. Gudiksen, X. Duan, Y. Cui und C. M. Lieber. *Highly Polarized Photoluminescence and Photodetection from Single Indium Phosphide Nanowires.* Science, **293**(5534): (2001) 1455–1457

[385] Z. Fan, P.-c. Chang, J. G. Lu, E. C. Walter, R. M. Penner, C.-h. Lin und H. P. Lee. *Photoluminescence and polarized photodetection of single ZnO nanowires.* Applied Physics Letters, **85**(25): (2004) 6128–6130

[386] R. Zhou, H.-C. Chang, V. Protasenko, M. Kuno, A. K. Singh, D. Jena und H. G. Xing. *CdSe nanowires with illumination-enhanced conductivity: Induced dipoles, dielectrophoretic assembly, and field-sensitive emission.* Journal of Applied Physics, **101**(7): (2007) 073704–9

[387] J. Giblin, V. Protasenko und M. Kuno. *Wavelength Sensitivity of Single Nanowire Excitation Polarization Anisotropies Explained through a Generalized Treatment of Their Linear Absorption.* ACS Nano, **3**(7): (2009) 1979–1987

[388] N. S. Han, H. S. Shim, S. Lee, S. M. Park, M. Y. Choi und J. K. Song. *Light-matter interaction and polarization of single ZnO nanowire lasers.* Physical Chemistry Chemical Physics, **14**(30): (2012) 10556–10563

[389] M. Wojdyr. *Fityk: a general-purpose peak fitting program.* Journal of Applied Crystallography, **43**(5): (2010) 1126–1128

[390] S. Ninomiya und S. Adachi. *Optical properties of wurtzite CdS.* Journal of Applied Physics, **78**(2): (1995) 1183–1190

[391] L. D. Landau, E. M. Lifshitz und L. P. Pitaevskii. *Electrodynamics of continous media.* Pergamon Press, Oxford (1984)

[392] A. V. Maslov und C. Z. Ning. *Reflection of guided modes in a semiconductor nanowire laser.* Applied Physics Letters, **83**(6): (2003) 1237–1239

[393] R. Paschotta. *Q factor.* Encyclopedia of Laser Physics and Technology, RP Photonics (2004)

[394] Y. Ma, X. Li, Z. Yang, H. Yu, P. Wang und L. Tong. *Pigtailed CdS nanoribbon ring laser.* Applied Physics Letters, **97**(15): (2010) 153122–3

[395] D. E. Aspnes und A. A. Studna. *Dielectric functions and optical parameters of Si, Ge, GaP, GaAs, GaSb, InP, InAs, and InSb from 1.5 to 6.0 eV.* Physical Review B, **27**(2): (1983) 985–1009

[396] A. Gruzintsev, G. Emelchenko, A. Redkin, W. Volkov, E. Yakimov und G. Visimberga. *Mode structure of laser emission from ZnO Nanorods with one metal mirror.* Semiconductors, **44**(9): (2010) 1235–1240

[397] D. Meschede (Hg.). *Gerthsen Physik.* Springer Verlag, Berlin, 24. edition Aufl. (2010)

[398] H. E. Swoboda, F. A. Majumder, V. G. Lyssenko, C. Klingshirn und L. Banyai. *The Electron-Hole plasma in CdS between 5 K and room temperature.* Zeitschrift für Physik B Condensed Matter, **70**(3): (1988) 341–348

[399] M. H. Chu, J. Segura-Ruiz, G. Martinez-Criado, P. Cloetens, I. Snigireva, S. Geburt und C. Ronning. *Synchrotron fluorescence nanoimaging of a single Co-implanted ZnO nanowire.* Physica Status Solidi (RRL) - Rapid Research Letters, **5**(8): (2011) 283–285

[400] J. Segura-Ruiz, G. Martinez-Criado, M. H. Chu, S. Geburt und C. Ronning. *Nano-X-ray Absorption Spectroscopy of Single Co-Implanted ZnO Nanowires.* Nano Letters, **11**(12): (2011) 5322–5326

[401] W. Jadwisienczak, H. Lozykowski und P. B. *Visible Emission from ZnO Doped with Rare-Earth Ions.* Journal of Electronic Materials, **31**: (2002) 776–784

[402] S. Bachir, K. Azuma, J. Kossanyi, P. Valat und J. C. Ronfard-Haret. *Photoluminescence of polycrystalline zinc oxide co-activated with trivalent rare earth ions and lithium. Insertion of rare-earth ions into zinc oxide.* Journal of Luminescence, **75**(1): (1997) 35–49

[403] S. Bhushan, A. N. Pandey und B. R. Kaza. *Photo- and electroluminescence of undoped and rare earth doped ZnO electroluminors.* Journal of Luminescence, **20**(1): (1979) 29–38

[404] J. Kossanyi, D. Kouyate, J. Pouliquen, J. C. Ronfard-Haret, P. Valat, D. Oelkrug, U. Mammel, G. P. Kelly und F. Wilkinson. *Photoluminescence of semiconducting zinc oxide containing rare earth ions as impurities.* Journal of Luminescence, **46**(1): (1990) 17–24

[405] D. Kouyate, J. C. Ronfard-Haret und J. Kossanyi. *Electroluminescence of rare earths-doped semiconducting zinc oxide electrodes : Kinetic aspects of the energy transfer between Sm^{3+} and Eu^{3+}.* Journal of Luminescence, **55**(4): (1993) 209–216

[406] J. C. Ronfard-Haret, P. Valat, V. Wintgens und J. Kossanyi. *Triboluminescence of trivalent rare earth ions inserted in polycrystalline zinc oxide.* Journal of Luminescence, **91**(1-2): (2000) 71–77

[407] T. Monteiro, M. Soares, A. Neves, S. Pereira, M. Correia, M. Peres, E. Alves, D. Rogers, F. Teherani, V. Munoz-SanJose, T. Trindade und A. Pereira. *Optical active centres in ZnO samples.* Journal of Non-Crystalline Solids, **352**(9-20): (2006) 1453–1456

[408] Z. Yang, Z. Feng und Z. Jiang. *Upconversion emission in multi-doped glasses for full colour display.* Journal of Physics D: Applied Physics, **38**(10): (2005) 1629–1632

[409] V. X. Quang, N. Q. Liem, N. C. Tzhanh, T. V. Choung und L. T. L. Thanh. *Photoluminescence of rare-earth centers in ZnO phosphors.* Physica Status Solidi (a), **78**: (1983) K161–K165

[410] W. E. Fenwick, M. H. Kane, R. Varatharajan, T. Zaidi, Z. Fang, B. Nemeth, D. J. Keeble, H. El-Mkami, G. M. Smith, J. Nause, C. J. Summers und I. T. Ferguson. *Transition metal and rare earth-doped ZnO: a comparison of optical, magnetic, and structural behavior of bulk and thin films.* In *Proceedings SPIE International Society of Optical Engineering*, Bd. 6474, Seiten 64741Q–8. SPIE, San Jose, CA, USA (2007)

[411] J. E. Geusic, H. M. Marcos und L. G. Van Uitert. *Laser Oscillations in Nd-doped Yttrium Aluminium, Yttrium Gallium and Gadolinium Garnets.* Applied Physics Letters, **4**(10): (1964) 182–184

[412] P. F. Moulton. *Ti-doped sapphire: tunable solid-state laser.* Optics News, **8**(6): (1982) 9–13

[413] P. F. Moulton. *Spectroscopic and laser characteristics of $Ti:Al_2O_3$.* Journal of the Optical Society of America B, **3**(1): (1986) 125–133

[414] P. G. Kryukov. *Ultrashort-pulse lasers.* Quantum Electronics, **31**(2): (2001) 95–119

[415] C. Bates, W. White und R. Roy. *The solubility of transition metal oxides in zinc oxide and the reflectance spectra of Mn^{2+} and Fe^{2+} in tetrahedral fields.* Journal of Inorganic and Nuclear Chemistry, **28**(2): (1966) 397–405

[416] S. K. Mandal, A. K. Das, T. K. Nath und D. Karmakar. *Temperature dependence of solubility limits of transition metals (Co, Mn, Fe, and Ni) in ZnO nanoparticles.* Applied Physics Letters, **89**(14): (2006) 144105–3

[417] B. Aleman, Y. Ortega, J. A. Garcia, P. Fernandez und J. Piqueras. *Fe solubility, growth mechanism, and luminescence of Fe doped ZnO nanowires and nanorods grown by evaporation-deposition.* Journal of Applied Physics, **110**(1): (2011) 014317

[418] D. R. Lide (Hg.). *Handbook of Chemistry and Physics.* CRC Press, Boca Raton (2008)

[419] B. D. Yuhas, D. O. Zitoun, P. J. Pauzauskie, R. He und P. Yang. *Transition-Metal Doped Zinc Oxide Nanowires.* Angewandte Chemie, **118**(3): (2006) 434–437

[420] K. Lorenz, E. Alves, E. Wendler, O. Bilani, W. Wesch und M. Hayes. *Damage formation and annealing at low temperatures in ion implanted ZnO.* Applied Physics Letters, **87**(19): (2005) 191904–3

[421] C. Coskun, D. C. Look, G. C. Farlow und J. R. Sizelove. *Radiation hardness of ZnO at low temperatures.* Semiconductor Science and Technology, **19**(6): (2004) 752–754

[422] T. Yoshiie, H. Iwanaga, N. Shibata, K. Suzuki, M. Ichihara und S. Takeuchi. *Irradiation damage of II-VI compounds in a high-voltage electron microscope.* Philosophical Magazine A, **47**(3): (1983) 315–329

[423] P. Koidl. *Optical absorption of Co^{2+} in ZnO.* Physical Review B, **15**(5): (1977) 2493–2499

[424] C. Y. Lin, W. H. Wang, C.-S. Lee, K. W. Sun und Y. W. Suen. *Magnetophotoluminescence properties of Co-doped ZnO nanorods.* Applied Physics Letters, **94**(15): (2009) 151909–3

[425] J. Hays, K. M. Reddy, N. Y. Graces, M. H. Engelhard, V. Shutthanandan, M. Luo, C. Xu, N. C. Giles, C. Wang, S. Thevuthasan und A. Punnoose. *Effect of Co doping on the structural, optical and magnetic properties of ZnO nanoparticles.* Journal of Physics: Condensed Matter, **19**(26): (2007) 266203–25

[426] L. Zhu, Y. Yang und N. Bing. *Synthesis and Optical Properties of Co-doped ZnO Nanoparticles:.* Chemistry Letters, **40**(4): (2011) 390–392

[427] J. Cui, Q. Zeng und U. J. Gibson. *Synthesis and magnetic properties of Co-doped ZnO nanowires.* Journal of Applied Physics, **99**(8): (2006) 08M113–3

[428] P. Lommens, P. F. Smet, C. de Mello Donega, A. Meijerink, L. Piraux, S. Michotte, S. Mátéfi-Tempfli, D. Poelman und Z. Hens. *Photoluminescence properties of Co^{2+}-doped ZnO nanocrystals.* Journal of Luminescence, **118**(2): (2006) 245–250

[429] T. Dietl, H. Ohno, F. Matsukura, J. Cibert und D. Ferrand. *Zener Model Description of Ferromagnetism in Zinc-Blende Magnetic Semiconductors.* Science, **287**(5455): (2000) 1019–1022

[430] T. Dietl. *A ten-year perspective on dilute magnetic semiconductors and oxides.* Nature Materials, **9**(12): (2010) 965–974

[431] K. Sato und H. Katayama-Yoshida. *First principles materials design for semiconductor spintronics.* Semiconductor Science and Technology, **17**(4): (2002) 367–376

[432] D. P. Norton, S. J. Pearton, A. F. Hebard, N. Theodoropoulou, L. A. Boatner und R. G. Wilson. *Ferromagnetism in Mn-implanted ZnO:Sn single crystals.* Applied Physics Letters, **82**(2): (2003) 239–241

[433] C. Fitzgerald, M. Venkatesan, J. Lunney, L. Dorneles und J. Coey. *Cobalt-doped ZnO - a room temperature dilute magnetic semiconductor.* Applied Surface Science, **247**(1–4): (2005) 493–496

[434] S. Pearton, D. Norton, M. Ivill, A. Hebard, J. Zavada, W. Chen und I. Buyanova. *Ferromagnetism in Transition-Metal Doped ZnO.* Journal of Electronic Materials, **36**(4): (2007) 462–471

[435] F. Pan, C. Song, X. Liu, Y. Yang und F. Zeng. *Ferromagnetism and possible application in spintronics of transition-metal-doped ZnO films.* Materials Science and Engineering: R: Reports, **62**(1): (2008) 1–35

[436] S. J. Pearton, W. H. Heo, M. Ivill, D. P. Norton und T. Steiner. *Dilute magnetic semiconducting oxides.* Semiconductor Science and Technology, **19**(10): (2004) R59–R74

[437] S. J. Pearton, D. P. Norton, K. Ip, Y. W. Heo und T. Steiner. *Recent progress in processing and properties of ZnO.* Superlattices and Microstructures, **34**(1-2): (2003) 3–32

[438] K. Potzger, S. Zhou, Q. Xu, A. Shalimov, R. Groetzschel, H. Schmidt, A. Mücklich, M. Helm und J. Fassbender. *Ferromagnetic structurally disordered ZnO implanted with Co ions.* Applied Physics Letters, **93**(23): (2008) 232504–3

[439] K. Potzger. *Ion-beam synthesis of magnetic semiconductors.* Nuclear Instruments and Methods in Physics Research Section B: Beam Interactions with Materials and Atoms, **272**(0): (2012) 78–87

[440] S. Geburt. *Lanthanoid-dotierte ZnO-Nanodrähte.* Diploma thesis, Universität Göttingen (2008)

[441] P. Sigmund. *Theory of Sputtering. I. Sputtering Yield of Amorphous and Polycrystalline Targets.* Physical Review, **184**(2): (1969) 383–416

[442] C. Q. Chen, Y. Shi, Y. S. Zhang, J. Zhu und Y. J. Yan. *Size Dependence of Young's Modulus in ZnO Nanowires.* Physical Review Letters, **96**(7): (2006) 075505–4

[443] S. Hoffmann, F. Östlund, J. Michler, H. J. Fan, M. Zacharias, S. H. Christiansen und C. Ballif. *Fracture strength and Young's modulus of ZnO nanowires.* Nanotechnology, **18**(20): (2007) 205503–

[444] A. Desai und M. Haque. *Mechanical properties of ZnO nanowires.* Sensors and Actuators A: Physical, **134**(1): (2007) 169–176

[445] R. Agrawal, B. Peng, E. E. Gdoutos und H. D. Espinosa. *Elasticity Size Effects in ZnO Nanowires - A Combined Experimental-Computational Approach.* Nano Letters, **8**(11): (2008) 3668–3674

[446] I. E. Dzyaloshinskii, E. M. Lifshitz und L. P. Pitaevskii. *General Theory of Van Der Waals' Forces.* Soviet Physics Uspekhi, **4**(2): (1961) 153–

[447] T. D. de la Rubia, R. S. Averback, R. Benedek und W. E. King. *Role of thermal spikes in energetic displacement cascades.* Physical Review Letters, **59**(17): (1987) 1930–1933

[448] K. Nordlund, M. Ghaly, R. S. Averback, M. Caturla, T. Diaz de la Rubia und J. Tarus. *Defect production in collision cascades in elemental semiconductors and fcc metals.* Physical Review B, **57**(13): (1998) 7556–

[449] L. Liao, J. C. Li, D. F. Wang, C. Liu, M. Z. Peng und J. M. Zhou. *Size dependence of Curie temperature in Co^+ ion implanted ZnO nanowires.* Nanotechnology, **17**(3): (2006) 830–833

[450] S. Chatterjee, A. K. Behera, A. Banerjee, L. C. Tribedi, T. Som und P. Ayyub. *Nanometer-scale sharpening and surface roughening of ZnO nanorods by argon ion bombardment.* Applied Surface Science, **258**(18): (2012) 7016–7020

[451] M. Schumm. *ZnO-based semiconductors studied by Raman spectroscopy: semimagnetic alloying, doping and nanostructures.* Dissertation, Universität Würzburg (2008)

[452] M. Schumm, M. Koerdel, S. Müller, C. Ronning, E. Dynowska, Z. Golacki, W. Szuszkiewicz und J. Geurts. *Secondary phase segregation in heavily transition metal implanted ZnO.* Journal of Applied Physics, **105**(8): (2009) 083525–9

[453] J. A. Bearden. *X-Ray Wavelengths.* Review of Modern Physics, **39**(1): (1967) 78–124

[454] M. H. Yoon, S. H. Lee, H. L. Park, H. K. Kim und M. S. Jang. *Solid solubility limits of Ga and Al in ZnO.* Journal of Materials Science Letters, **21**(21): (2002) 1703–1704

[455] M. Komatsu, N. Ohashi, I. Sakaguchi, S. Hishita und H. Haneda. *Ga, N solubility limit in co-implanted ZnO measured by secondary ion mass spectrometry.* Applied Surface Science, **189**(3–4): (2002) 349–352

[456] W. B. Jian, Z. Y. Wu, R. T. Huang, F. R. Chen, J. J. Kai, C. Y. Wu, S. J. Chiang, M. D. Lan und J. J. Lin. *Direct observation of structure effect on ferromagnetism in $Zn_{1-x}Co_xO$ nanowires.* Physical Review B, **73**(23): (2006) 233308–6

[457] J. Stöhr. *NEXAFS Spectroscopy.* Springer Berlin (1992)

[458] A. Ney, K. Ollefs, S. Ye, T. Kammermeier, V. Ney, T. C. Kaspar, S. A. Chambers, F. Wilhelm und A. Rogalev. *Absence of Intrinsic Ferromagnetic Interactions of Isolated and Paired Co Dopant Atoms in $Zn_{1-x}Co_xO$ with High Structural Perfection.* Physical Review Letters, **100**(15): (2008) 157201–4

[459] G. Martinez-Criado, A. Segura, J. A. Sans, A. Homs, J. Pellicer-Porres und J. Susini. *X-ray absorption of $Zn_{1-x}Co_xO$ thin films: A local structure study.* Applied Physics Letters, **89**(6): (2006) 061906–3

[460] T. Büsgen, M. Hilgendorff, S. Irsen, F. Wilhelm, A. Rogalev, D. Goll und M. Giersig. *Colloidal Cobalt-Doped ZnO Nanorods: Synthesis, Structural, and Magnetic Properties.* The Journal of Physical Chemistry C, **112**(7): (2008) 2412–2417

[461] A. L. Ankudinov, B. Ravel, J. J. Rehr und S. D. Conradson. *Real-space multiple-scattering calculation and interpretation of X-ray-absorption near-edge structure.* Physical Review B, **58**(12): (1998) 7565–7576

[462] G. Cicero, A. Ferretti und A. Catellani. *Surface-induced polarity inversion in ZnO nanowires.* Physical Review B, **80**(20): (2009) 201304–4

[463] J. Geurts, M. Schumm, M. Koerdel, C. Ziereis, S. Müller, C. Ronning, E. Dynowska, Z. Golacki und W. Szuszkiewicz. *Annealing effects and generation of secondary phases in ZnO after high-dose transition metal implantation.* Physica Status Solidi (b), **247**(6): (2010) 1469–1471

[464] F. Decremps, F. Datchi, A. M. Saitta, A. Polian, S. Pascarelli, A. Di Cicco, J. P. Itia und F. Baudelet. *Local structure of condensed zinc oxide.* Physical Review B, **68**(10): (2003) 104101–

[465] E. Alves, E. Rita, U. Wahl, J. G. Correia, T. Monteiro, J. Soares und C. Boemare. *Lattice site location and optical activity of Er implanted ZnO.* Nuclear Instruments and Methods in Physics Research Section B: Beam Interactions with Materials and Atoms, **206**: (2003) 1047–1051

[466] E. Rita, U. Wahl, A. Lopes, J. Araújo, J. Correia, E. Alves, J. Soares und the ISOLDE Collaboration. *Lattice Site Location Studies of Rare-Earths Implanted in ZnO Single-Crystals.* Material Research Society Symposium Proceedings, **744**

[467] T. Monteiro, C. Boemare, M. J. Soares, E. Rita und E. Alves. *Photoluminescence and damage recovery studies in Fe-implanted ZnO single crystals.* Journal of Applied Physics, **93**(11): (2003) 8995–9000

[468] R. O. Kuzian, A. M. Dareacute, P. Sati und R. Hayn. *Crystal-field theory of Co^{2+} in doped ZnO.* Physical Review B, **74**(15): (2006) 155201–12

[469] S. Mitra und J. Bryant. *Raman spectrum of ZnO.* Journal of Physics France, **26**(11): (1965) 610–610

[470] R. Cusco, E. Alarcon-Llado, J. Ibanez, L. Artus, J. Jimenez, B. Wang und M. J. Callahan. *Temperature dependence of Raman scattering in ZnO.* Physical Review B, **75**(16): (2007) 165202–11

[471] M. D. Sturge. *Jahn-Teller Effect in the $^4T_{2g}$ Excited State of V^{2+} in MgO.* Physical Review, **140**(3A): (1965) A880–A891

[472] M. Wang, Y. Zhou, Y. Zhang, E. J. Kim, S. H. Hahn und S. G. Seong. *Near-infrared photoluminescence from ZnO.* Applied Physics Letters, **100**(10): (2012) 101906–4

[473] E. Sonder, R. A. Zuhr und R. E. Valiga. *Annealing of damage and stability of implanted ions in ZnO crystals.* Journal of Applied Physics, **64**(3): (1988) 1140–1144

[474] F. Tuomisto, D. Look und G. Farlow. *Defect studies in electron-irradiated ZnO and GaN.* Physica B: Condensed Matter, **401–402**(0): (2007) 604–608

[475] T. Molholt, R. Mantovan, H. Gunnlaugsson, K. Bharuth-Ram, M. Fanciulli, H. Gaslason, K. Johnston, Y. Kobayashi, G. Langouche, H. Masenda, D. Naidoo, S. Alafsson, R. Sielemann und G. Weyer. *Temperature and dose dependence of defect complex formation with ion implanted Mn/Fe in ZnO.* Physica B: Condensed Matter, **404**(23–24): (2009) 4820–4822

[476] R. M. Macfarlane und J. C. Viala. *Saturation spectroscopy and fluorescence in ZnO: Co^{2+}.* Material Science Forum, **10–12**: (1986) 845–852

[477] J. Donegan, T. Glynn und G. Imbusch. *FLN study of $LiGa_5O_8$:Co^{2+}.* Journal of Luminescence, **45**(1–6): (1990) 23–25

[478] B. Wen, J. E. Sader und J. J. Boland. *Mechanical Properties of ZnO Nanowires.* Physical Review Letters, **101**(17): (2008) 175502–

[479] Y. Zhou und G.-Z. Zhang. *Measurement of Photoluminescence from Cu_2O at 2K.* Chinese Physics Letters, **23**(5): (2006) 1276

[480] F. Riedel. *Terbiumdotierte Zinksulfidnanodrähte.* Diplomarbeit, Friedrich-Schiller-Universität Jena (2011)

[481] U. Kaiser, L. Chen, S. Geburt, C. Ronning und W. Heimbrodt. *Defect induced changes on the excitation transfer dynamics in ZnS/Mn nanowires.* Nanoscale Research Letters, **6**(1): (2011) 228–5

[482] U. Kaiser, S. Gies, S. Geburt, F. Riedel, C. Ronning und W. Heimbrodt1. *Luminescence and energy transfer processes in ensembles and single Mn or Tb doped ZnS nanowires.* submitted to Applied Physic Letters (2012)

[483] S. Gies. *Zeitaufgelöste Spektroskopie an ZnS:Tb-Nanodrähten.* Batchelorarbeit, Universität Marburg (2011)

[484] H. E. Gumlich, A. Zeinert und R. Mauch. *Luminescence of solids*, Kap. Electroluminescence, Seite 221. Plenum Press, New York (1998)

[485] D. Kahng. *Electroluminescence of Rare-Earth doped and Transition Metal Molecules in II-VI Compounds via Impact Excitation.* Applied Physics Letters, **13**(6): (1968) 210–212

[486] P. De Visschere und K. Neyts. *Concentration quenching and luminescent decay in AC thin-film ZnS:Mn electroluminescent devices.* Journal of Luminescence, **52**(5-6): (1992) 313–323

[487] K. Okamoto und Y. Hamakawa. *Bright green electroluminescence in thin-film $ZnS:TbF_3$.* Applied Physics Letters, **35**(7): (1979) 508–511

[488] D. C. Krupka und D. M. Mahoney. *Electroluminescence and Photoluminescence of Thin Films of ZnS Doped with Rare-Earth Metals.* Journal of Applied Physics, **43**(5): (1972) 2314–2320

[489] Y. A. Ono. *Materials for Full-Color Electroluminescence Displays.* Annual Review of Materials Research, **27**(1): (1997) 283–303

[490] M. Leskelä. *Rare earths in electroluminescent and field emission display phosphors.* Journal of Alloys and Compounds, **275–277**(0): (1998) 702–708

[491] T. Toyama, D. Adachi und H. Okamoto. *Full-color nanostructured thin-film electroluminescent device utilizing ZnS nanocrystals doped with activator-ions.* Physica Status Solidi (a), **205**(1): (2008) 15–18

[492] R. Bhargava, D. Gallagher und T. Welker. *Doped nanocrystals of semiconductors - a new class of luminescent materials.* Journal of Luminescence, **60-61**: (1994) 275–280

[493] A. Bol, R. van Beek und A. Meijerink. *On the Incorporation of Trivalent Rare Earth Ions in II-VI Semiconductor Nanocrystals.* Chemistry of Materials, **14**(3): (2002) 1121–1126

[494] R. N. Bhargava. *The role of impurity in doped nanocrystals.* Journal of Luminescence, **72-74**: (1997) 46–48

[495] H. Hu und W. Zhang. *Synthesis and properties of transition metals and rare-earth metals doped ZnS nanoparticles.* Optical Materials, **28**(5): (2006) 536–550

[496] L. Chen, J. Zhang, S. Lu, X. Ren und X. Wang. *On the energy transfer from nanocrystalline ZnS to Tb^{3+} ions confined in reverse micelles.* Chemical Physics Letters, **409**(1-3): (2005) 144–148

[497] D. Stichtenoth, D. Schwen, S. Müller, C. Borchers und C. Ronning. *Optical activation of implanted impurities in ZnS nanowires.* Journal of Vacuum Science and Technology A, **24**(4): (2006) 1356–1359

[498] A. A. Bol und A. Meijerink. *Long-lived Mn^{2+} emission in nanocrystalline $ZnS{:}Mn^{2+}$.* Physical Review B, **58**(24): (1998) R15997–R16000

[499] A. Cattell und A. Cullis. *The variation in the luminescent and structural properties of sputter-deposited ZnS:Mn thin films with post-deposition annealing.* Thin Solid Films, **92**(3): (1982) 211–217

[500] W. Busse, H.-E. Gumlich, B. Meissner und D. Theis. *Time resolved spectroscopy of ZnS : Mn by dye laser technique.* Journal of Luminescence, **12–13**: (1976) 693–700

[501] P. Benalloul, J. Benoit, R. Mach, G. Müller und G. Reinsperger. *Decay of ZnS:Mn emission in thin films - revisited.* Journal of Crystal Growth, **101**: (1990) 989–993

[502] H. E. Gumlich. *Electro- and photoluminescence properties of Mn^{2+} in ZnS and ZnCdS.* Journal of Luminescence, **23**(1-2): (1981) 73–99

[503] T. Förster. *Experimentelle und theoretische Untersuchung des zwischemmolekularen Übergangs von Elektronenanregungsenergie.* Zeitschrift Naturforschung Teil A, **4**: (1949) 321

[504] L. Chen, F. J. Brieler, M. Fröba, P. J. Klar und W. Heimbrodt. *Quantitative description of the temporal behavior of the internal $Mn3d^5$ luminescence in ensembles of $Zn_{0.99}Mn_{0.01}S$ quantum dots.* Physical Review B, **75**(24): (2007) 241303–4

[505] A. Mikami, T. Ogura, K. Taniguchi, M. Yoshida und S. Nakajima. *Excitation process of the Tb emission center in a ZnS:Tb,F thin-film electroluminescent device.* Journal of Applied Physics, **64**(7): (1988) 3650–3657

[506] G. C. Trigunayat und G. K. Chadha. *Progress in the study of polytypism in crystals (I).* Physica Status Solidi (a), **4**(1): (1971) 9–42

[507] T. K. Tran, W. Park, W. Tong, M. M. Kyi, B. K. Wagner und C. J. Summers. *Photoluminescence properties of ZnS epilayers.* Journal of Applied Physics, **81**(6): (1997) 2803–2809

[508] N. Lovergine, P. Prete, G. Leo, L. Calcagnile, R. Cingolani, A. M. Mancini, F. Romanato und A. V. Drigo. *MOVPE Growth of Wide Band-Gap II-VI Compounds for Near-UV and Deep-Blue Light Emitting Devices.* Crystal Research & Technology, **33**(2): (1998) 183–195

[509] Y. Kawakami, T. Taguchi und A. Hiraki. *Excitonic and edge emissions in MOCVD-grown ZnS films and ZnSe-ZnS superlattices.* Journal of Crystal Growth, **89**: (1988) 331–338

[510] R. Grasser und A. Scharmann. *Zur Lumineszenz und Lumineszenzzerstörung von ZnS-Leuchtstoffen.* Zeitschrift für Physik A Hadrons and Nuclei, **189**(4): (1966) 339–354

[511] T. Zhai, Z. Gu, Y. Ma, W. Yang, L. Zhao und J. Yao. *Synthesis of ordered ZnS nanotubes by MOCVD-template method.* Materials Chemistry and Physics, **100**: (2006) 281–284

[512] J. Gong, S. Yang, J. Duan, R. Zhang und Y. Du. *Rapid synthesis and visible photoluminescence of ZnS nanobelts.* Chemical Communications, (3): (2005) 351–353

[513] C. S. Kang, P. Beverley, P. Phipps und R. H. Bube. *Photoelectronic processes in ZnS single crystals.* Physical Review, **156**(3): (1967) 998–1009

[514] Y. Uehara. *Electronic structure of luminescence center of ZnS:Ag phosphors.* Journal of Chemical Physics, **62**(8): (1975) 2982–2994

[515] D. D. D. Ma, S.-T. Lee, P. Mueller und S. F. Alvarado. *Scanning tunneling microscope excited cathodoluminescence from ZnS nanowires.* Nano Letters, **6**(5): (2006) 926–929

[516] L. Chen, W. Heimbrodt, P. J. Klar, M. Fröba, C. Ronning und H.-A. K. von Nidda. *Optical and magnetic properties of quasi one-dimensional dilute magnetic ZnMnS and antiferromagnetic MnS.* Physica Status Solidi (b), **247**(10): (2010) 2522–2536

[517] M. Katiyar und A. H. Kitai. *Luminescence concentration quenching due to energy migration in ZnS:Mn with fixed trap density.* Journal of Luminescence, **46**(4): (1990) 227–234

[518] M. Katiyar und A. H. Kitai. *Effect of organized doping on concentration quenching in ZnS:Mn.* Journal of Luminescence, **52**(5–6): (1992) 309–312

[519] X. Zhang, Y. Zhang, Y. Song, Z. Wang und D. Yu. *Optical properties of ZnS nanowires synthesized via simple physical evaporation.* Physica E: Low-dimensional Systems and Nanostructures, **28**(1): (2005) 1–6

[520] J.-C. Lee und D.-H. Park. *Self-defects properties of ZnS with sintering temperature.* Materials Letters, **57**(19): (2003) 2872–2878

[521] Y. V. Bochkov, V. I. Demin, L. S. Lepnev und V. F. Tunitskaya. *Effect of irradiation of ZnS single crystals by neon ions on the photoluminescence band intensity.* Journal of Applied Spectroscopy, **33**(6): (1980) 1311–1314

[522] Y. V. Bochkov, Z. P. Ilyukhina, L. S. Lepnev und V. F. Tunitskaya. *Photoluminescence of zinc sulfide with ion-implanted neon impurity.* Journal of Applied Spectroscopy, **30**(2): (1979) 179–182

[523] T. Kryshtab, V. Khomchenko, J. Andraca-Adame, A. Savin, A. Kryvko, G. Juárez und R. Peña-Sierra. *Luminescence and structure of ZnO-ZnS thin films prepared by oxidation of ZnS films in air and water vapor.* Journal of Luminescence, **129**(12): (2009) 1677–1681

[524] Motlan, G. Zhu, K. Drozdowicz-Tomsia, K. McBean, M. Phillips und E. Goldys. *Annealing of ZnS nanocrystals grown by colloidal synthesis.* Optical Materials, **29**(12): (2007) 1579–1583

[525] M. Cui, X. Wu, L. Zhuge und Y. Meng. *Effects of annealing temperature on the structure and photoluminescence properties of ZnO films.* Vacuum, **81**(7): (2007) 899–903

[526] N. Hecking, K. Heidemann und E. Te Kaat. *Model of temperature dependent defect interaction and amorphization in crystalline silicon during ion irradiation.* Nuclear Instruments and Methods in Physics Research Section B: Beam Interactions with Materials and Atoms, **15**: (1986) 760–764

[527] R. N. Bhargava. *Doped nanocrystalline materials – Physics and applications.* Journal of Luminescence, **70**(1-6): (1996) 85–94

[528] D. C. Krupka. *Hot-Electron Impact Excitation of Tb^{3+} Luminescence in ZnS: Tb^{3+} Thin Films.* Journal of Applied Physics, **43**(2): (1972) 476–481

[529] E. W. Chase, R. T. Hepplewhite, D. C. Krupka und D. Kahng. *Electroluminescence of ZnS Lumocen Devices Containing Rare-Earth and Transition-Metal Fluorides.* Journal of Applied Physics, **40**(6): (1969) 2512–2519

[530] G. S. Ofelt. *Structure of the f^6 Configuration with Application to Rare-Earth Ions.* Journal of Chemical Physics, **38**(9): (1963) 2171–2180

[531] W. T. Carnall, P. R. Fields und K. Rajnak. *Spectral Intensities of the Trivalent Lanthanides and Actinides in Solution. II. Pm^{3+}, Sm^{3+}, Eu^{3+}, Gd^{3+}, Tb^{3+}, Dy^{3+}, and Ho^{3+}.* Journal of Chemical Physics, **49**(10): (1968) 4412–4423

[532] K. S. Thomas, S. Singh und G. H. Dieke. *Energy Levels of Tb^{3+} in $LaCl_3$ and Other Chlorides.* Journal of Chemical Physics, **38**(9): (1963) 2180–2190

[533] V. L. Levshin, S. A. Fridman, V. A. Chikhacheva und V. V. Shchaenko. *Rare earth elements as activators of zinc sulfide cathodoluminophors.* Journal of Applied Spectroscopy, **2**(2): (1965) 75–82

[534] A. Mikami, T. Ogura, K. Tanaka, K. Taniguchi, M. Yoshida und S. Nakajima. *Tb-F emission centers in ZnS:Tb,F thin-film electroluminescent devices.* Journal of Applied Physics, **61**(8): (1987) 3028–3034

[535] W. W. Anderson. *Tb^{3+} as a Recombination Center in ZnS.* Physical Review, **136**(2A): (1964) A556–A560

[536] W. W. Anderson, S. Razi und D. J. Walsh. *Luminescence of Rare-Earth-Activated Zinc Sulfide.* Journal of Chemical Physics, **43**(4): (1965) 1153–1160

[537] D. Hommel, H. Hartmann, M. Godlewski, J. M. Langer und A. Stapor. *Energy structure and recombination for ZnS bulk crystals doped with Tb, Er and Eu.* Journal of Crystal Growth, **72**(1-2): (1985) 346–350

[538] F. Bryant, J. Hogg und P. Jaffery. *Characterization of luminescence centres in neodymium implanted zinc sulphide.* Journal of Physics and Chemistry of Solids, **44**(6): (1983) 595–600

[539] C. C. Yu und F. J. Bryant. *Annealing studies of erbium-implanted zinc sulphide.* Philosophical Magazine Part B, **40**(3): (1979) 209–222

[540] A. Krier und F. Bryant. *Cathodoluminescence of laser-annealed erbium-implanted zinc selenide.* Journal of Physics and Chemistry of Solids, **47**(7): (1986) 719–725

[541] J. Mita, M. Koizumi, H. Kanno, T. Hayashi, Y. Sekido, I. Abiko und K. Nihei. *Difference in Electroluminescent ZnS:Tb, F Thin Films Prepared by Electron-Beam Evaporation and RF Magnetron Sputtering.* Japanese Journal of Applied Physics, **26**(Part 2, No. 7): (1987) L1205–L1207

[542] T. Ogura, A. Mikami, K. Tanaka, K. Taniguchi, M. Yoshida und S. Nakajima. *High-brightness green-emitting electroluminescent devices with ZnS:Tb,F active layers.* Applied Physics Letters, **48**(23): (1986) 1570–1571

[543] R. A. Rosenberg, G. K. Shenoy, F. Heigl, S.-T. Lee, P.-S. G. Kim, X.-T. Zhou und T. K. Sham. *Effects of in situ vacuum annealing on the surface and luminescent properties of ZnS nanowires.* Applied Physics Letters, **86**(26): (2005) 263115–3

[544] R. Wahab, S. Ansari, Y.-S. Kim, M. Dhage, H. Seo, M. Song und H.-S. Shin. *Effect of annealing on the conversion of ZnS to ZnO nanoparticles synthesized by the sol-gel method using zinc acetate and thiourea.* Metals and Materials International, **15**(3): (2009) 453–458

[545] G. Bulgarini. *Luminescence of single ZnS nanowires implanted with Mn and rare earths.* Masterarbeit, Friedrich-Schiller-Universität Jena (2009)

[546] Y. S. Chen, J. C. Burgiel und D. Kahng. *Photoluminescence of ZnS:TbF$_3$ Thin Films.* Journal of the Electrochemical Society, **117**(6): (1970) 794–797

[547] J. I. Pankove, M. A. Lampert, J. J. Hanak und J. E. Berkeyheiser. *Dependence of DC electroluminescence and host-excited photoluminescence on Tb^{3+} concentration in sputtered $ZnS : Tb^{3+}$ films.* Journal of Luminescence, **15**(3): (1977) 349–352

[548] P. Benalloul, J. Benoit und A. Geoffroy. *TbF$_3$ complex centre in ZnS ACTFEL devices.* Journal of Crystal Growth, **72**(1-2): (1985) 553–558

[549] A. Mikami, T. Ogura, K. Taniguchi, M. Yoshida und S. Nakajima. *Excitation processes of the Tb emission center in a ZnS:Tb,F thin film electroluminescent device.* Journal of Luminescence, **40–41**(0): (1988) 784–785

[550] D. Ananias, A. Ferreira, J. Rocha, P. Ferreira, J. P. Rainho, C. Morais und L. D. Carlos. *Novel Microporous Europium and Terbium Silicates.* Journal of the Americal Chemical Society, **123**(24): (2001) 5735–5742

[551] J. M. Sun, W. Skorupa, T. Dekorsy, M. Helm, L. Rebohle und T. Gebel. *Bright green electroluminescence from Tb_{3+} in silicon metal-oxide-semiconductor devices.* Journal of Applied Physics, **97**(12): (2005) 123513–7

[552] M. Ihara, T. Igarashi, T. Kusunoki und K. Ohno. *Preparation and Characterization of Rare Earth Activators Doped Nanocrystal Phosphors.* Journal of the Electrochemical Society, **147**(6): (2000) 2355–2357

[553] C. Tiseanu, R. K. Mehra, R. Kho und M. Kumke. *Comparative Study of Time-Resolved Photoluminescence Properties of Terbium-Doped Thiosalicylic-Capped CdS and ZnS Nanocrystals.* The Journal of Physical Chemistry B, **107**(44): (2003) 12153–12160

[554] M. Zalewska, B. Kuklinski, E. Grzanka, S. Mahlik, J. Jezierska, B. Palosz, M. Grinberg und A. M. Klonkowski. *Tb^{3+} ions in presence of $ZnS:Mn^{2+}$ nanocrystals immobilized on silica: Energy transfer ZnS $\rightarrow Tb^{3+}$ and coordination state of Mn^{2+} ions.* Journal of Luminescence, **129**(3): (2009) 246–250

[555] M. Ihara, T. Igarashi, T. Kusunoki und K. Ohno. *Cathodoluminescence and Photoluminescence of Nanocrystal Phosphors.* Journal of the Electrochemical Society, **149**(3): (2002) H72–H75

[556] R. Niepelt. *Characterisation and selective modification of semiconductor nanowire for electrical application.* Dissertation, Friedrich-Schiller-Universität Jena (2012)

[557] Q. Xiong, G. Chen, J. D. Acord, X. Liu, J. J. Zengel, H. R. Gutierrez, J. M. Redwing, L. C. Lew Yan Voon, B. Lassen und P. C. Eklund. *Optical Properties of Rectangular Cross-sectional ZnS Nanowires.* Nano Letters, **4**(9): (2004) 1663–1668

[558] J. S. Sebastian, H. C. Swart, T. A. Trottier, S. L. Jones und P. H. Holloway. *Degradation of ZnS field-emission display phosphors during electron-beam bombardment.* Journal of Vacuum Science and Technology A, **15**(4): (1997) 2349–2353

[559] K. Kajiwara. *Cross-sectional transmission electron microscopy investigation of the dead layer of ZnS:Ag,Al phosphors in field emission displays.* In *Journal of Vacuum Science and Technology A*, Bd. 19, Seiten 1083–1089. AVS, Boston, Massachusetts (USA) (2001)

[560] C. Ma, D. Moore, J. Li und Z. Wang. *Nanobelts, Nanocombs, and Nanowindmills of Wurtzite ZnS.* Advanced Materials, **15**(3): (2003) 228–231

[561] Gatan Inc. *Stand: 28.04.2012.* www.gatan.com

[562] Newport Corporation. *Stand: 26.05.2012.* http://gratings.newport.com.

[563] K. Kanaya und S. Okayama. *Penetration and energy-loss theory of electrons in solid targets.* Journal of Physics D: Applied Physics, **5**(1): (1972) 43–58

[564] J. F. Muth, R. M. Kolbas, A. K. Sharma, S. Oktyabrsky und J. Narayan. *Excitonic structure and absorption coefficient measurements of ZnO single crystal epitaxial films deposited by pulsed laser deposition.* Journal of Applied Physics, **85**(11): (1999) 7884–7887

[565] H. C. Ong, A. S. K. Li und G. T. Du. *Depth profiling of ZnO thin films by cathodoluminescence.* Applied Physics Letters, **78**(18): (2001) 2667–2669

[566] J. Lambert. *Photometry, or, On the measure and gradations of light, colors, and shade.* Augsburg ("Augusta Vindelicorum"), Germany: Eberhardt Klett, Seite 391

[567] Princeton Instruments. *Stand: 12.05.2012.* http://www.princetoninstruments.com

[568] I. Slowik. *Herstellung und Charakterisierung von ZnO-Nanodraht-Feldeffekttransistoren.* Batchelorarbeit, Friedrich-Schiller Universität Jena (2010)

[569] J. Ge und Y. Li. *Selective Atmospheric Pressure Chemical Vapor Deposition Route to CdS Arrays, Nanowires, and Nanocombs.* Advanced Functional Materials, **14**(2): (2004) 157–162

[570] T. Castro, R. Reifenberger, E. Choi und R. P. Andres. *Size-dependent melting temperature of individual nanometer-sized metallic clusters.* Physical Review B, **42**(13): (1990) 8548–8556

[571] Y. Wang, G. Wang, M. Yau, C. To und D. H. Ng. *Asymmetric growth on the polar surfaces of CdS ribbons.* Chemical Physics Letters, **407**(4-6): (2005) 510–515

[572] T. Gao und T. Wang. *Catalyst-Assisted Vapor-Liquid-Solid Growth of Single-Crystal CdS Nanobelts and Their Luminescence Properties.* The Journal of Physical Chemistry B, **108**(52): (2004) 20045–20049

[573] F. J. Bryant und S. A. Hamid. *Electron irradiation and trapping centres in zinc sulphide single crystals.* Physica Status Solidi (a), **2**(3): (1970) 597–605

[574] K. Johnston, M. O. Henry, D. McCabe, E. McGlynn, M. Dietrich, E. Alves und M. Xia. *Identification of donor-related impurities in ZnO using photoluminescence and radiotracer techniques.* Physical Review B, **73**(16): (2006) 165212–7

[575] H. J. Ko, Y. F. Chen, Z. Zhu, T. Yao, I. Kobayashi und H. Uchiki. *Photoluminescence properties of ZnO epilayers grown on CaF_2 (111) by plasma assisted molecular beam epitaxy.* Applied Physics Letters, **76**(14): (2000) 1905–1907

[576] H. Kato, M. Sano, K. Miyamoto und T. Yao. *Growth and characterization of Ga-doped ZnO layers on a-plane sapphire substrates grown by molecular beam epitaxy.* Journal of Crystal Growth, **237-239**: (2002) 538–543

[577] B. P. Zhang, N. T. Binh, Y. Segawa, K. Wakatsuki und N. Usami. *Optical properties of ZnO rods formed by metalorganic chemical vapor deposition.* Applied Physics Letters, **83**(8): (2003) 1635–1637

[578] B. Bendow, J. Birman, A. Ganguly, T. Damen, R. Leite und J. Scott. *Resonant Raman stokes scattering by LO-phonons in CdS.* Optics Communications, **1**(6): (1970) 267–270

[579] V. Travnikov. *Surface radiative recombination in CdS Crystals.* Journal of Crystal Growth, **101**(1-4): (1990) 579–583

List of Publications

Publications directly related to this thesis

1. *Rare Earth doped Zinc Oxide Nanowires*
   S. Geburt, D. Stichtenoth, S. Müller, W. Dewald, C. Ronning, J. Wang, Y. Jiao, Y.Y. Rao, S. H. Hark und Q. Li
   Journal of Nanoscience and Nanotechnology, 8, 244-251 (2008)

2. *Alignment of Semiconductor Nanowires Using Ion Beams*
   C. Borschel, R. Niepelt, **S. Geburt**, C. Gutsche, I. Regolin, F.J. Tegude, W. Prost, D. Stichtenoth, D. Schwen and C. Ronning
   Small 5, 2576 (2009)

3. *Ion beam doping of semiconductor nanowires*
   C. Ronning, C. Borschel, R. Niepelt and **S. Geburt**
   Materials Science and Engineering R 70, 30 (2010)

4. *Tailoring the properties of semiconductor nanowires using ion beams*
   C. Ronning, C. Borschel, R. Niepelt, **S. Geburt**, S. Müller, D. Stichtenoth, J.P. Richters, A. Dev, T. Voss, L. Chen, W. Heimbrodt, C. Gutsche and W. Prost
   physica status solidi b 247, 2329 (2010)

5. *Defect induced changes on the excitation-transfer dynamics in ZnS:Mn nanowires*
   U. Kaiser, L. Chen, **S. Geburt**, C. Ronning and W. Heimbrodt
   Nanoscale Research Letters 6, 228 (2011)

6. *Synchrotron flourescence nanoimaging of a single Co-implanted ZnO nanowires*
   M.H. Chu, J. Segura-Ruiz, G. Martinez-Criado, P. Cloetens, I Snigireva, **S. Geburt** and C. Ronning
   physica status solidi RRL 5, 283 (2011)

7. *Nano-X-ray Absorption Spectroscopy of Single Co Implanted ZnO Nanowires*
   J. Segura-Ruiz, G. Martínez-Criado, M.H. Chu, **S. Geburt** and C. Ronning
   Nano Letters 11, 5322 (2011)

8. *Low threshold room-temperature lasing of CdS nanowires*
   S. Geburt, A. Thielmann, R. Röder, C. Borschel, A. McDonnell, M. Kozlik, J. Kühnel, K. A. Sunter, F. Capasso and C. Ronning
   Nanotechnology 23, 365204 (2012)

9. *Luminescence and energy transfer processes in ensembles and single Mn or Tb doped ZnS nanowires*
   U. Kaiser, S. Gies, **S. Geburt**, F. Riedel, C. Ronning, and W. Heimbrodt
   Submitted to Applied Physics Letters (2012)

Further publications

1. *Determination of secondary ion mass spectrometry relative sensitivity factors for polar and non-polar ZnO*
   A. Laufer, N. Volbers, S. Eisermann, K. Potzger, **S. Geburt**, C. Ronning and B.K. Meyer
   Journal of Applied Physics 110, 094906 (2011)

2. *Quantification of impurity concentration in Cu_2O and CuO via secondary ion mass spectrometry*
   A. Laufer, D. Reppin, H. Metelmann, **S. Geburt**, C. Ronning, T. Leichtweiss, J. Janek and B.K. Meyer
   physica status solidi B (2012), accepted

3. *Extension of the cubic boron nitride thin film growth phase diagram*
   S. Weidner, **S. Geburt**, J. Ye, S. Ulrich and C. Ronning
   Diamond and Related Materials 22, 88 (2012)

4. *Significant stress reduction of cBN layers upon ion irradiation at elevated temperatures*
   S. Weidner, J. Ye, **S. Geburt**, C. Ronning and S. Ulrich
   Nuclear Instruments and Methods in Physics Research B 280 (2012)

5. *A CEMS search for precipitate formation in ^{57}Fe implanted ZnO*
   K. Bharuth-Ram, H. Masenda, T.B. Doyle, **S. Geburt**, C. Ronning and H.P. Gunnlaugsson
   Hyperfine Interactions (2012), accepted

Oral contributions at conferences, workshops and meetings

1. *Rare earth doped ZnO nanowires*
   S. Geburt, D. Stichtenoth, S. Müller, C. Ronning, J. Wang and Q. Li
   Seminar Talk at the Institute for Solid State Physics, University of Jena, November 2008

2. *Rare earth doped ZnO nanowires*
   S. Geburt and C. Ronning
   Talk at the Nanowire Symposium at the IPHT Jena, January 2009

3. *Ion beam induced bending of semiconductor nanowires*
   S. Geburt, C. Borschel, R. Niepelt, I. Regolin, C. Gutsche, W. Prost, F. T. Tegude, D. Stichtenoth, D. Schwen and C. Ronning
   Talk at the SPP1165 Meeting, Berlin, February 2009

4. *Conversion of rare earth doped ZnS to ZnO nanowires*
   S. Geburt, G. Bulgarini, C. Borschel and C. Ronning
   Talk at the DPG Spring Meeting, Session HL 13.12, Regensburg, March 2010

5. *Co implanted ZnO nanowires*
   S. Geburt and C. Ronning
   Seminar Talk at the Harvard School of Engineering and Applied Sciences, Harvard University, Cambridge (USA), July 2010

6. *Luminescence properties of single Co implanted ZnO nanowires*
   S. Geburt, C. Borschel and C. Ronning
   Seminar Talk at the Seminar of the Experimental Semiconductor Physics Group, University of Marburg, May 2011

7. *Intense intra-4f-emission of Tb doped single ZnS nanowires*
   F. Riedel, **S. Geburt**, C. Borschel, C. Ronning, U. Kaiser, S. Gies and W. Heimbrodt
   Talk at the MRS Fall Meeting, Session BB16.5, Boston (USA), November 2011

8. *Lasing and ion beam doping of semiconductor nanowires*
   S. Geburt and C. Ronning
   Invited Talk at Western Cape University, Cape Town (South Africa), February 2012

Theses of the Dissertation

Lasing and ion beam doping of semiconductor nanowires
(*Laseremission und Ionenstrahl-Dotierung von Halbleiter-Nanodrähten*)

by Sebastian Geburt

- High quality CdS nanowires can be synthesized reliably via the VLS mechanism. The emission properties of single CdS nanowires depend strongly on the excitation power, thus a characterization of the crystal quality from the luminescence properties is difficult.

- CdS nanowires show stimulated emission and sharp guided modes appear at elevated excitation powers. Laser oscillations are observed for nanowires with suitable morphology at excitation above the threshold.

- The morphology of the nanowires defines an optical Fabry-Pérot resonator.

- Semiconductor nanowires are the smallest possible photonic lasers. The fundamental limits for the occurrence of laser oscillations in ZnO and CdS nanowires are given by the materials properties (emission energy, refractive index) in combination with the morphology (length, diameter, shape of end facets).

- Semiconductor nanowires can be successfully doped with the desired concentration of optically active elements using ion implantation. The recovery of the lattice damage can be achieved by appropriate annealing procedures.

- The modification of the nanowire morphology upon ion irradiation is determined by the defect creation in the lattice as well as sputter effects. Adjusted preparation conditions enable the reduction of the morphological changes.

- The activation of the impurity emission is strongly coupled to the recovery of the host matrix by annealing. Using appropriate parameters, the intra-shell luminescence dominates the emission of implanted nanowires.

- The emission properties of single implanted semiconductor nanowires are dominated by the impurity emission and the contribution of the host matrix to the luminescence emission depends on the nanowire diameter and the ion range.

- The temporal luminescence decay of the impurity emission in ZnS nanowires depends in the ion-ion distance, the defect concentration as well as the ratio of the distances to the nanowire diameter. The modified Förster dipole-dipole energy transfer model is capable to describe the transient correctly from a few hundred nanoseconds up to several milliseconds after the excitation.

- Microscopic nanowire ensembles and single nanowires exhibit the same temporal decay characteristic as the macroscopic ensemble, which can be attributed to the large number of impurities in a single nanowire.

Thesen zur Dissertation

Laseremission und Ionenstrahl-Dotierung von Halbleiter-Nanodrähten

vorgelegt von Sebastian Geburt

- CdS Nanodrähte können über den VLS Mechanismus zuverlässig in hoher Kristallqualität synthetisiert werden. Die Emissionscharakteristik einzelner CdS Nanodrähte ist stark abhängig von der Anregungsleistung und eignet sich daher nur bedingt zur Bestimmung der Kristallqualität.

- CdS Nanodrähte zeigen unter hoher optischer Anregung stimulierte Emission sowie das Auftreten von geführten Moden. Bei geeingeter Nanodrahtmorphologie treten Laseroszillationen bei Raumtemperatur oberhalb einer Schwellintensität auf.

- Durch die Morphologie der CdS Nanodrähte entsteht ein optischen Resonator, welcher die Eigenschaften eines Fabry-Pérot Resonators besitzt.

- Halbleiter-Nanodrähte stellen die kleinst möglichen photonischen Laser dar. Die fundamentalen Größenbeschränkungen für das Auftreten von Laseroszillationen in CdS und ZnO Halbleiternanodrähten lassen sich auf die Materialeigenschaften (Emissionswellenlänge, Brechungsindex) in Verbindung mit der Morphologie (Länge, Durchmesser, Form der Endfacetten) zurückführen.

- Halbleiternanodrähte können erfolgreich über Ionenimplantation mit Leuchtzentren in der gewünschten Konzentration dotiert werden. Durch geeignete Temperverfahren kann die Kristallstruktur ausreichend wiederhergestellt werden.

- Die Veränderung der Morphologie der Nanodrähte durch die Ionenbestrahlung wird durch die Defektverteilung im Kristall sowie dem Abtrag von Oberflächenatomen bestimmt. Durch angepasste Präparationsbedingungen können die morphologischen Veränderungen deutlich reduziert werden.

- Die Aktivierung der Lumineszenz der optisch aktiven Leuchtzentren ist stark gekoppelt an die Ausheilung der Kristalldefekte im Wirtsgitter. Bei geeigneter Präparation dominieren die Leuchtzentren die Emission.

- Die Emissionseigenschaften einzelner implantierter Nanodrähte werden nach erfolgreicher Aktivierung von der Emission der optischen Zentren geprägt. Der Beitrag der Emission der Wirtsmatrix ist bestimmt vom Nanodrahtdurchmesser und der Ionenreichweite.

- Das zeitliche Abklingen der Leuchtzentren-Emission in ZnS Nanodrähten wird von dem Ionen-Abstand, der Defektkonzentration sowie dem Verhältnis der Abstände zum Drahtdurchmesser bestimmt und wird korrekt vom modifizierten Förster-Dipol-Dipol-Energietransfer-Modell im Zeitraum von wenigen hundert Nanosekunden bis zu einigen Millisekunden nach der Anregung beschrieben.

- Mikroskopische Nanodraht Ensemble und einzelne Nanodrähte zeigen das gleiche Lumineszenzabklingverhalten wie das makroskopische Ensemble, was sich auf die große Anzahl an Leuchtzentren im einzelnen Nanodraht zurückführen lässt.

Curriculum Vitae

Persönliche Daten

Name	Sebastian Geburt
Geburtsdatum	05.06.1982
Geburtsort	Göttingen

Bildungsweg

1988 - 1992	Johann-Joachim Quantz Grundschule in Scheden
1992 - 1994	Orientierungsstufe am Hohen Hagen in Dransfeld
1994 - 2001	Grotefend-Gymnasium Hann.Münden
2001	Abitur
2002 - 2008	Studium der Physik an der Georg-August Universität Göttingen
2008	Abschluss des Studiums an der Georg-August-Universität Göttingen als Diplom-Physiker
2008 - 2012	Wissenschaftlicher Mitarbeiter am Institut für Festkörperphysik der Friedrich-Schiller-Universität Jena mit dem Ziel der Promotion

Jena, den 10.10.2012

_____

(Sebastian Geburt)

Ehrenwörtliche Erklärung

Ich erkläre hiermit ehrenwörtlich, dass ich die vorliegende Arbeit selbständig, ohne unzulässige Hilfe Dritter und ohne Benutzung anderer als der angegebenen Hilfsmittel und Literatur angefertigt habe. Die aus anderen Quellen direkt oder indirekt übernommenen Daten und Konzepte sind unter Angabe der Quelle gekennzeichnet.

Bei der Auswahl und Auswertung folgenden Materials haben mir die nachstehend aufgeführten Personen in der jeweils beschriebenen Weise unentgeltlich geholfen:

- Der Aufbau und die Erweiterung der Mikrophotolumineszenz-Spektroskopieapparatur erfolgte in Zusammenarbeit mit Andreas Thielmann und Robert Röder.

- Die Synthese der ZnO Nanodrähte wurde zum Teil von Martin Gnauck, Michael Kozlik, Ulrich Schröder und Andreas Thielmann durchgeführt.

- CdS Nanostrukturen wurden von Amanda McDonnell, Micheal Kozlik, Julian Kühnel, Andreas Thielmann und Robert Röder synthetisiert.

- Die Experimente zum Lasing von ZnO und CdS Nanodrähten wurden mit Andreas Thielmann und Robert Röder durchgeführt. Die Ergebnisse wurden gemeinsam interpretiert.

- Die FDTD Simulationen von CdS Nanodrähten wurden von Robert Buschlinger in der Gruppe von Ulf Peschel am MPI für die Physik des Lichts an der Universität Erlangen durchgeführt.

- Die Ionenimplantationen wurde mit Hilfe von Gerald Lenk, Patrick Hoffmann und Ulrich Barth am Institut für Festkörperphysik durchgeführt.

- Die TEM-Bilder und TEM-EDX Spektren wurden am Institut für Materialwissenschaft und Werkstofftechnologie der FSU Jena mit der Hilfe von Christian Borschel und Steffen Milz aufgenommen.

- Die µXRF und µXAS Untersuchungen an Co dotierten ZnO Nanodrähten wurden von Gema Matrinez-Criado, Jaime Segura-Riuz und Manh-Hung Chu am ESRF in Grenoble durchgeführt.

- Die zeitaufgelösten PL Messungen sowie die PL Anregungsspektroskopie wurden von Limei Klar, Uwe Kaiser und Sebastian Gies in der Gruppe von Prof. Heimbrodt an der Philipps-Universität Marburg durchgeführt.

- ZnS Nanodrähte wurden von Michael Kozlik und Franziska Riedel hergestellt.

- Die Herstellung und Untersuchung von Tb dotierten ZnS Nanodrähten erfolgte gemeinsam mit Franziska Riedel.

- Im Übrigen waren jeweils die Koautoren der angeführten Veröffentlichungen (siehe Anhang List of Publications) an der Interpretation der Ergebnisse beteiligt.

Weitere Personen waren an der inhaltlich-materiellen Erstellung der vorliegenden Arbeit nicht beteiligt. Insbesondere habe ich hierfür nicht die entgeltliche Hilfe von Vermittlungs- bzw. Beratungsdiensten (Promotionsberater oder andere Personen) in Anspruch genommen. Niemand hat von mir unmittelbar oder mittelbar geldwerte Leistungen für die Arbeiten erhalten, die im Zusammenhang mit dem Inhalt der vorgelegten Dissertation stehen.

Die Arbeit wurde bisher weder im In- noch im Ausland in gleicher oder ähnlicher Form einer anderen Prüfungsbehörde vorgelegt. Die geltende Prüfungsordnung der Physikalisch-Astronomischen Fakultät ist mir bekannt.

Ich versichere ehrenwörtlich, dass ich nach bestem Wissen die reine Wahrheit gesagt und nichts verschwiegen habe.

Jena, den 10.10.2012

_____
(Sebastian Geburt)